ABSTRACT

Title of dissertation: OPTICAL TIME DOMAIN AND RADIO IMAGING ANALYSES OF THE DYNAMIC HEARTS OF AGN

Krista Lynne Smith, Doctor of Philosophy, 2017

Dissertation directed by: Professor Richard Mushotzky
Department of Astronomy

Active galactic nuclei (AGN) are among the most extreme objects in the universe: galaxies with a central supermassive black hole feeding on gas from a hot accretion disk. Despite their potential as powerful tools to study topics ranging from relativity to cosmology, they remain quite mysterious.

In the first portion of this thesis, we explore how an AGN may influence the formation of stars in its host galaxy. Using high-resolution 22 GHz radio imaging of an X-ray selected sample of radio-quiet AGN, we find that the far-infrared radio correlation for normal star forming galaxies remains valid within a few hundred parsecs of the central engine. Because the core flux is often spatially isolated from star formation, we can also determine that the radio emission in radio-quiet AGN is consistent with both coronal and disk-jet coupling models. Finally, we find that AGN with jet-like radio morphologies have suppressed star formation, possibly indicating ongoing feedback.

The second portion of this thesis uses optical AGN light curves to study the

physics of accretion. The *Kepler* spacecraft produces groundbreaking light curves, but its fixed field of view only contained a handful of known AGN. We conduct an X-ray survey of this field, yielding 93 unique X-ray sources identified by optical follow-up spectroscopy as a mixture of AGN and stars. For the AGN, we spectroscopically measure black hole masses and accretion rates.

We then analyze a sample of 22 *Kepler* AGN light curves. We develop a customized pipeline for AGN science with *Kepler*, a necessary step since the initial data was optimized for the unique goal of exoplanet detection. The light curves display an astonishing variety of behaviors in a new regime of optical variability inaccessible with previous facilities. We find power spectral slopes inconsistent with the damped random walk model, characteristic variability timescales, correlations of variability properties with physical parameters, and bimodal flux distributions possibly consistent with passing obscuring material. We also conclude that this regime of optical variability is not produced by simple X-ray reprocessing. Finally, we explain how this work supports future robust accretion studies with upcoming large timing surveys.

Optical Time-Domain and Radio Imaging Analyses of the Dynamic Hearts of AGN

by

Krista Lynne Smith

Dissertation submitted to the Faculty of the Graduate School of the
University of Maryland, College Park in partial fulfillment
of the requirements for the degree of
Doctor of Philosophy
2017

Advisory Committee:
Professor Richard Mushotzky, Chair/Advisor
Dr. Patricia Boyd
Professor Chris Reynolds
Professor Stuart Vogel
Professor Peter Shawhan, Dean's Representative

Preface

Readers of this thesis will notice that Chapter 2 and Chapters 3 and 4 address quite different scientific goals. Before setting out to read this document, it is perhaps helpful to understand the circumstances that led to its structure. The X-ray survey described in Chapter 3 was executed in 2012 and 2013 in the fixed field of view of the *Kepler* space telescope, with the ultimate plan of following up the sources discovered thereby with *Kepler*. By the time the survey was completed and just after we had submitted preliminary targets to *Kepler* in May 2013, the spacecraft unexpectedly suffered the loss of its final redundant reaction wheel and lost its ability to point, suspending operations and throwing the future of the mission into serious doubt. In this period of uncertainty, I began work on another thesis-worthy project: high-resolution radio imaging of star formation in AGN. This resulted in several interesting results and a paper, which manifests here as Chapter 2. Eventually, means were devised of repurposing the *Kepler* spacecraft as the K2 mission, which has different fields of view than the original. This was fortunate for the continuance of my X-ray survey, which has proceeded in these new fields, but this is not described here. Because the new AGN discovered in the X-ray survey were in the original field, only the preliminary handful were observed by *Kepler* before the failure, and the extensively-planned analysis could not be undertaken. Instead, a comprehensive analysis of a different sample of AGN in the original *Kepler* field, selected by another method, is described in Chapter 4 and will soon be submitted for publication.

Two of the chapters in this work have been published in *The Astrophysical Journal*. Chapter 2 is published as "Radio Properties of the BAT AGNs: the FIR-

radio Relation, the Fundamental Plane, and the Main Sequence of Star Formation" [Smith et al., 2016] and Chapter 3 is published as "KSwAGS: A Swift X-Ray and UV Survey of the Kepler Field. I." [Smith et al., 2015]. Portions of Chapter 2 were presented at the *Great Lakes Quasar Symposium* in London, Ontario (May 2016), the 15th Meeting of the High Energy Astrophysics Division of the AAS in Naples, Florida (April 2016) and the European Week of Astronomy and Space Science Symposium on Stellar and AGN Feedback in Athens, Greece (July 2016). Chapter 3 was presented as a poster at the *Swift: 10 Years of Discovery* Conference in Rome, Italy (December 2014). Portions of Chapter 3 and Chapter 4 were presented at the *Active Galactic Nuclei: What's In a Name?* Conference in Garching, Germany (June 2016), and are published in its proceedings. Preliminary results from Chapter 4 were presented at the 229th meeting of the American Astronomical Society in Grapevine, Texas (January 2017).

In addition to the work presented here, I have published a paper on the infrared selection of optically-elusive AGN as "An Infrared and Optical Analysis of a Sample of XBONGs and Optically Elusive AGNs" in *The Astrophysical Journal* [Smith, Koss & Mushotzky, 2014], as well as two first-author papers in my undergraduate studies [Smith et al., 2010, 2012]. I have also been a co-author on seven published works. Most relevant to this thesis are the discovery of a characteristic timescale in one of the first *Kepler* AGN which used a preliminary version of my *Kepler* pipeline [Edelson et al., 2014] and an investigation of the variability of the stellar X-ray sources discovered by the KSwAGS survey [Howell et al., 2016].

For my grandfather, Dr. Harold V. Freeman, who taught me to think, to doubt, and to learn.

Acts 8:30-31

Table of Contents

List of Tables

List of Figures

List of Abbreviations

2MASS	2-Micron All Sky Survey
ADAF	Advection-Dominated Accretion Flow
AGN	Active Galactic Nuclei/Nucleus
BAT	Burst Alert Telescope
CASA	Common Astronomy Software Applications
CBV	Cotrending Basis Vector
DCT	Discovery Channel Telescope
EPIC	Ecliptic Plane Input Catalog
FIR	Far-infrared
FIRST	Faint Images of the Radio Sky at Twenty-centimeters
FOV	Field of View
FFI	Full Frame Image
FWHM	Full Width at Half Maximum
GALEX	Galaxy Evolution Explorer
HRS	*Herschel* Reference Survey
IMBH	Intermediate Mass Black Hole
IR	Infrared
IRAS	Infrared Astronomical Satellite
(J)VLA	(Jansky) Very Large Array
KIC	*Kepler* Input Catalog
KSwAGS	*Kepler*-Swift Active Galaxies Survey
L	Luminosity
L_{Bol}	Bolometric Luminosity
L_{Edd}	Eddington Luminosity
λ_{Edd}	Eddington Ratio (L/L_{Edd})
LINER	Low-ionization Nuclear Emission Line Region
LSST	Large Synoptic Survey Telescope
M_{BH}	Black Hole Mass
$M_{\odot}$	Solar Mass
M_{*}	Stellar Mass of Galaxy
MRI	Magneto-Rotational Instability
NRAO	National Radio Astronomy Observatory
NUV	Near-Ultraviolet
NVSS	NRAO VLA Sky Survey

ν	Temporal Frequency
PIMMS	Portable Interactive Multi-Mission Simulator
PSD	Power Spectral Density
PSF	Point Spread Function
PTF	Palomar Transient Factory
QPO	Quasi-Periodic Oscillation
RFI	Radio Frequency Interference
RM	Reverberation Mapping
ROSAT	Röntgen Satellite (European X-ray Space Telescope)
S	Flux Density
SDSS	Sloan Digital Sky Survey
SED	Spectral Energy Distribution
SFR	Star Formation Rate
σ_*	Stellar Velocity Dispersion
TDE	Tidal Disruption Event
TESS	Transiting Exoplanet Survey Satellite
$\tau_{\rm char}$	Characteristic Timescale
UKIRT	United Kingdom Infrared Telescope
UV	Ultraviolet
UVOT	Ultraviolet-Optical Telescope
VLBI	Very Long Baseline Interferometry
WISE	Wide-field Infrared Survey Explorer
XBONG	X-ray Bright Optically Normal Galaxy
XRT	X-ray Telescope
z	Redshift
ZTF	Zwicky Transient Facility

Chapter 1: Introduction

1.1 Introduction

It is now well known that in the cores of all large galaxies, both spiral and elliptical, there dwells a black hole of enormous mass, reaching millions to billions of times the mass of the sun. Despite the prevalence of these so-called supermassive black holes, their discovery took many decades of circumstantial evidence and deductive reasoning, and was only possible because some black holes make themselves known by consuming gas from a hot, swirling disk of matter. Only about 10% of galaxies host black holes that are actively feeding, but these objects were the keys to discovering supermassive black holes in galactic cores generally. They were first discovered as a class by Carl Seyfert in 1943, when he found that a sample of galaxies with very bright central point sources exhibited optical spectral lines with very high excitations and widths indicating high rotational velocities. However, the importance of this discovery would have to wait until the astronomical community became caught up in the mystery of newly discovered "quasi-stellar objects" (QSOs) in the 1950s. These strange phenomena were first seen as star-like point sources on photographic plates, which spatially corresponded to bright radio sources and with optical spectra featuring emission lines at mysterious wavelengths. The somewhat

cumbersome phrase "quasi-stellar radio source" eventually morphed into shortcut "quasar." In an early attempt to understand QSOs, Lodewick Woltjer (1959) made this simple physical argument: since the point sources are not resolved, they must be quite small, and if the luminous matter is gravitationally bound, the nuclear mass must be extremely high. Quantitatively, he made the impressive point that a billion solar masses must occupy a space smaller than 100 parsecs. Rampant speculation arose on how this might be possible, with theories ranging from a chain reaction of supernovae in a very dense star cluster [Burbidge, 1961] to massive conglomerations of bare quarks [Pacini, 1966]. More intrigue was added to the picture when Schmidt [1963] identified the mysterious emission lines as the Balmer lines of hydrogen, but with a redshift of $z = 0.158$.

At a conference in 1964, Schmidt described the basic properties of QSOs as follows: starlike, with high ultraviolet flux, broad emission lines, variability over time, and large redshifts. The redshifts were not immediately assumed to be cosmological in origin; many believed that the QSOs were fast-moving objects within the Milky Way, although the complete non-detection of a *blue*shifted QSO complicated this picture. Further cataloguing soon made it clear that there was a large group of QSOs that did not have the characteristic radio emission, and that these "radio-quiet" QSOs in fact outnumbered the radio loud variety that had been discovered first.

While this speculation was ongoing, Matthews, Morgan & Schmidt [1964] and Zwicky [1965] had identified a new kind of object they called N-type galaxies. Their defining characteristic was that they appeared to be star-like, but upon closer

inspection had a very faint host galaxy that was almost outshined by the nuclear source. Slowly, the picture came together that QSOs, N-type galaxies, and the strange galactic centers with odd emission line properties discovered by Seyfert in 1943 were the same kind of objects at different points along a continuum of nuclear brightness. A term arose that encompassed all of these different types, which is still used today as the umbrella term: active galactic nuclei, or AGN.

Having established the cosmological nature of AGN, speculation on the physics that gave rise to such overwhelming nuclear emission continued. As already mentioned, variability was very early recognized to be a ubiquitous property among active galaxies. It was soon joined by X-ray emission [Elvis et al., 1978]; these two properties remain among the few properties of almost all classes of AGN.

The idea of gravitational accretion as a power source for AGN was in place quite early [Salpeter, 1964, Lynden-Bell, 1969], but competed stiffly with several other models. Variability was a key factor in solidifying a black hole as the source of the enormous observed energy output. If the flux varies by some amount in a time t, it sets a limit upon the size of the region in which the variability has taken place of $r \leq c \times t$, where c is the speed of light. The fastest-varying early sources were found to have size limits of approximately one light-day, or a few hundred astronomical units (AU). This restricted the possible sizes much further than the 100 parsec limit of the physical resolution discussed earlier, all the way down to solar-system size scales. There remained no other possible explanation: the massive energetic release was the result of the gravitational potential of a single object, which in such a small space must be a black hole. It is important to realize that all of this was taking place

while black holes were still mathematical theoretical constructs, before the discovery of the first stellar mass black hole in 1972 [Bolton, 1972, Webster & Murdin, 1972].

Over time, the evidence for supermassive black holes at galactic centers became overwhelming, culminating in direct dynamical studies of the stars and gas orbiting the black hole itself. In nearby galaxies, the group dynamics of stars and gas in the black hole's gravitational potential can be modelled and fitted to obtain a confident value for the mass of the black hole (see the review by Ferrarese & Ford [2005]). In the Milky Way, we can track the individual stars orbiting our own supermassive black hole [Genzel et al., 2010], enabling a confident mass measurement of $4.1 \times 10^6 M_\odot$. Of course, the Milky Way black hole is inactive, although there is evidence that it may have been an AGN as recently as a few million years ago [e.g., Zubovas & Nayakshin, 2012].

Although AGN are the most luminous non-transient objects in the cosmos and, through benefit of their vast energetic output, have relevance to both our own galaxy and the history and evolution of the universe, the engines that provide this enormous energy are still quite mysterious.

In this thesis we will examine two principal aspects of AGN. First, we study the properties of star formation very close to the nucleus to improve our understanding of the empirical relationship between the black hole and its host galaxy. Second, we study the optical variability of AGN as a probe of accretion disk physics.

In order to set the stage for the latter chapters, we must first introduce the necessary terminology. We will then briefly cover the motivation for studying the interrelationship between the environment of the supermassive black hole and the

host galaxy, as well as the history and motivation for the study of AGN variability. Finally, we introduce the major observing facilities that were used in these analyses before moving onto the main body of work. The sections that follow here are 1) a general introduction to AGN terminology, 2) a review of some important selection effects, 3) a phenomenological introduction to Chapter 2 on circumnuclear star formation in AGN, 4) a phenomenological introduction to Chapters 3 and 4, which describe two stages of the variability project, and 5) an introduction to the innovative space telescopes and ground-based facilities utilized in this thesis.

1.1.1 Types of AGN

This section will describe the physical classes of AGN in the current taxonomy. Due to the historical sequence described above, the term QSO or its radio-loud counterpart "quasar" is typically used for the most luminous objects, usually at high redshifts. Most of the work done here is on the less-luminous subclass of Seyfert galaxies, in which the nucleus is clearly active but the host galaxy is easily visible. There are two types of Seyfert galaxies, classified by the widths of the lines in their optical spectra. Seyferts with the characteristic broad lines that led to their original discovery are called Seyfert 1 AGN, or Type I AGN, abbreviated as Sy1. These broad components have widths of $10^3 - 10^4$ km/s, and only occur in the permitted lines (HI, HeI, and HeII, for example). In addition to the broad components, the hydrogen lines have a narrow component with several hundred km/s widths. Similarly, the forbidden lines, such as [O III] λ5007Å, also tend to

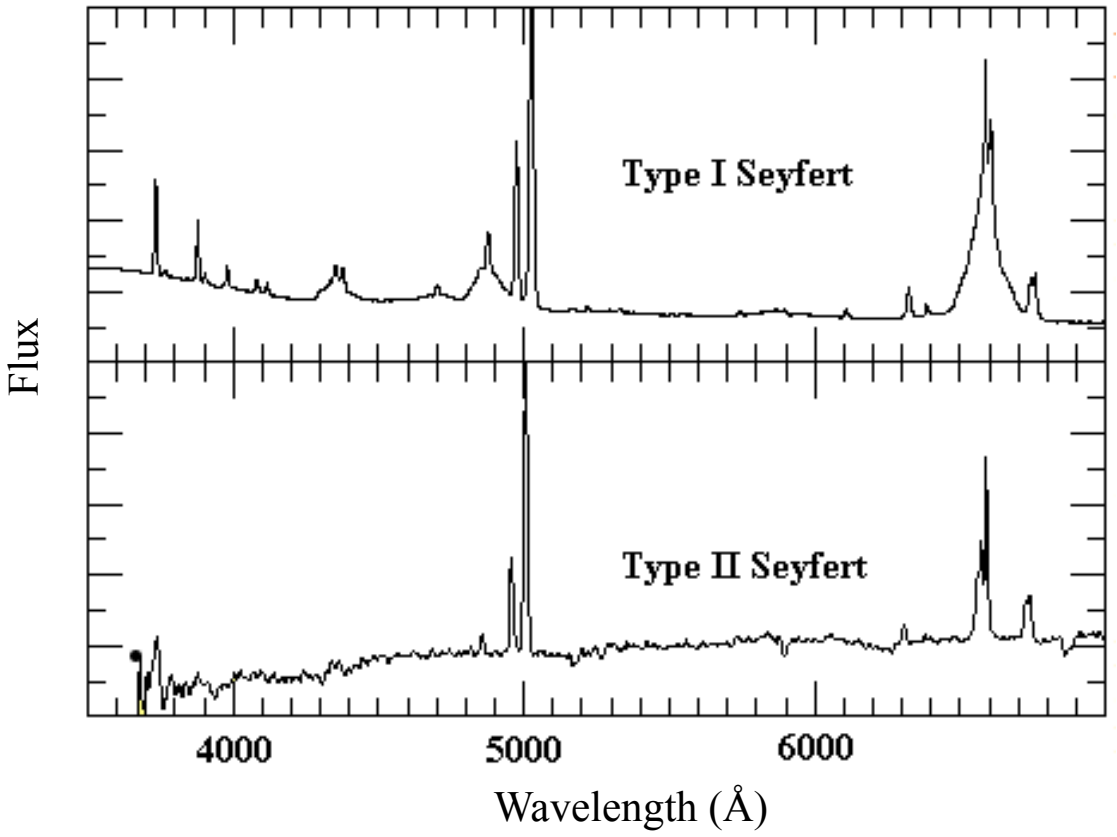

Figure 1.1: Sample spectra of a Seyfert 1 and Seyfert 2 type galaxy. Sy 1 galaxies have broad components on their permitted lines, while Sy2 galaxies do not. These spectra are taken from the astronomy slide collection of Bill Keel.

have widths of hundreds of km/s. Seyfert 2 AGN (or Type II, Sy2) have only the narrow components of the permitted lines, with no indication of broad bases. An example of each type of spectrum is shown in Figure 1.1.

This dichotomy in the spectra is attributed to viewing angle. In order to understand how, we must discuss the physical origin of the various components of the optical spectrum. First, the light of the continuum (the power-law which underlies the emission lines) is thought to come from the accretion disk. The disk

provides both the continuum emission in the optical spectrum, as well as the ionizing ultraviolet (UV) radiation that gives rise to both the broad and narrow emission lines. The permitted lines in Sy1 spectra are Doppler-broadened by their motion in the gravitational potential of the supermassive black hole, so the gas emits these lines is quite dense and quite near to the central engine. The narrow line-emitting gas is also ionized by accretion disk photons; however, the fact that the forbidden lines do not have broad bases means that the narrow-line gas is farther away from the black hole. The geometry of the central regions of an AGN is shown in Figure 1.2. The black hole is surrounded by the accretion disk. Sometimes, a jet is emitted perpendicular to the disk. This configuration is in turn surrounded at a greater distance by a thick torus of dust and gas. This torus is puffier than the disk, preventing edge-on viewers from seeing the accretion disk or the close-in broad line clouds. Such viewers would then see only the narrow lines, and essentially no AGN continuum. If, however, the viewer is looking at the AGN face-on, they will see the accretion disk and broad line clouds and the spectrum will have the characteristic power-law continuum shape and broad components on the permitted lines. In a very special and rare case, the viewer would be looking directly "down the barrel", along the jet axis. The optical spectrum in this case is a featureless continuum, and the object typically has extremely rapid variability and is radio-loud. These are called "BL Lacertae" spectra after the first such object discovered, often abbreviated as BL Lac or "blazar."

If a dusty torus-like structure is indeed the reason that Sy2 AGN spectra do not have broad lines, then one might expect to be able to see broad lines in the

infrared spectra, since infrared emission is less susceptible to dust extinction than optical. Infrared spectroscopy has indeed revealed broad permitted lines in many objects which optically appear to be Sy2 galaxies, implying a hidden Sy1 nucleus [DePoy et al., 1987]. This so-called "unified model" of AGN was most convincingly confirmed by the use of spectropolarimetry: emission from the obscured broad-line gas is scattered into the line of sight of an edge-on observer by material well above the disk plane and torus (see the dotted line in Figure 1.2). This light would be polarized due to the scattering. Antonucci & Miller [1985] found unambiguous broad emission lines in polarized optical spectra of Sy2 galaxies, lending strong support to the viewing-angle argument.

Although now widely accepted and used to interpret observations, the community realizes that this model is overly simplistic. Our concept of the torus is constantly evolving; for example, perhaps it is a clumpy collection of dust clouds [e.g., Krolik & Begelman, 1988] instead of a smooth, homogenous distribution [Pier & Krolik, 1992]. It has been proposed that some AGN may not have a population of broad-line emitting clouds at all [Bianchi et al., 2008]. Additionally, there are various types of AGN which we have not discussed here with peculiar emission line and obscuration properties (i.e., LINERs and XBONGs, as well as many others) that challenge the universality of the unified model. However, for the purposes of the analyses presented here, the basic model is a good reference point.

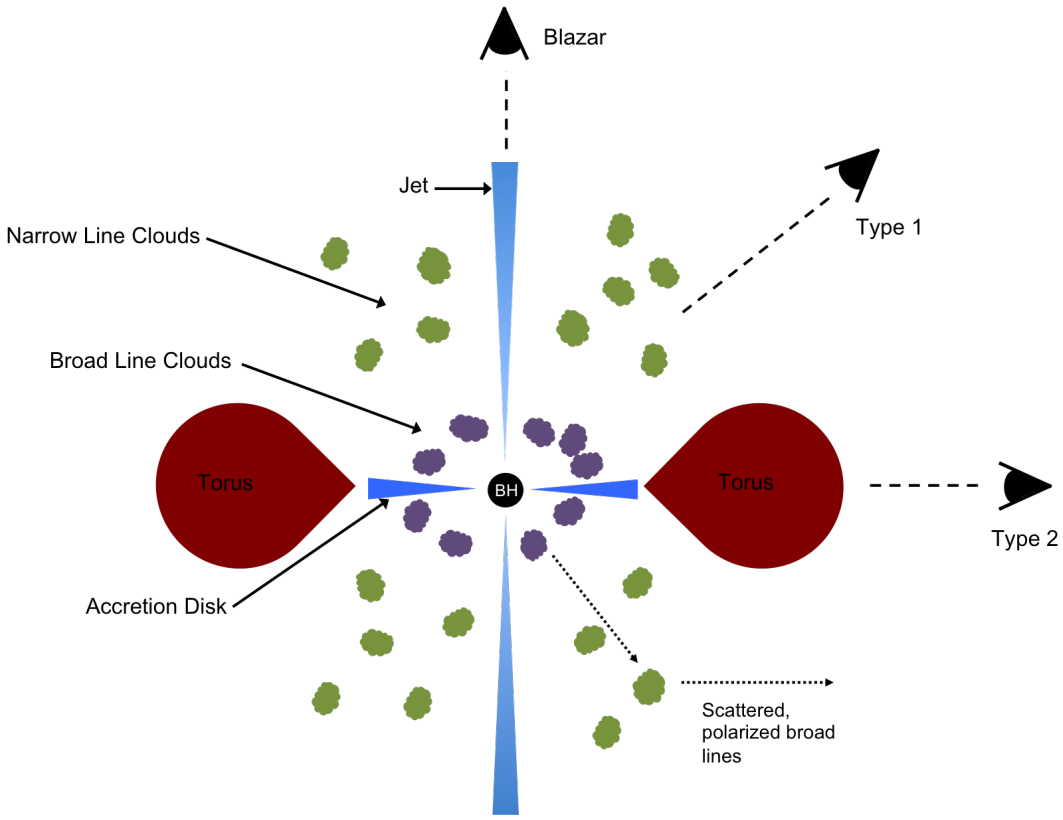

Figure 1.2: A cutaway diagram of an active nucleus, demonstrating the emitting region geometry and the resultant spectral types from different viewing angles.

1.1.2 Selection Effects in AGN Samples

Because AGN emit across the entire electromagnetic spectrum, selection techniques have been employed in every waveband. Different selection techniques introduce various biases in the sample. These must be borne in mind while interpreting results, as is comprehensively reviewed in Mushotzky [2004]. In this section we will briefly explore the consequences of selecting AGN in different wavebands, in order to motivate the X-ray selection of the parent sample for the objects discussed in Chapter 2, as well as the X-ray survey conducted in Chapter 3, and to introduce the infrared color selection applied in Chapter 4.

As already mentioned, the first quasars were discovered as bright radio sources associated with star-like optical sources. While this type of selection will undoubtedly find a relatively pure sample of quasars (especially if they are selected to have flat radio spectra) it will miss as much as 90% of the AGN population, which is radio-quiet [Smith & Wright, 1980, Sramek & Weedman, 1980]. Broad optical emission lines, the hallmark of optically-selected AGN, are indeed relatively rare in radio-selected samples [e.g., Kristian, Sandage & Katem, 1974, Sadler et al., 2002]. There is thus little overlap between radio and optically selected samples, a serious red flag for interpretation.

In the infrared, optical, and UV, color selection is a powerful tool. The technique is effective because the spectral energy distributions (SEDs) of AGN are slightly different from those of the host galaxy stellar population, and so one can use ratios of fluxes at different wavelengths to choose objects based on, essentially,

the shape of the continuum in any chosen band. In the infrared, the SED can be well-fit by a power law with $F_\nu \propto \nu^{-1}$ [Edelson & Malkan, 1986], generally thought to be the result of thermal re-radiation of the UV/optical disk continuum by dust. Stars, and therefore galaxies made up of stars without an AGN component, are not well described by a power law. There are numerous algorithms for selecting AGN based on this difference, made all the more useful by the publicly available all-sky surveys of infrared photometric colors by the Wide Field Infrared Survey Explorer (WISE) and 2-Micron All-Sky Survey (2MASS) satellites [e.g., Stern et al., 2012, Mateos et al., 2012]. However, these selection methods will fail on dust-obscured AGN, in which the infrared continuum is dominated by dust in the host galaxy at large, or on AGN with ongoing starbursts that may contribute to the infrared colors [Veilleux, 2002]. Edelson & Malkan [2012] improved on this technique by including a requirement for the photometrically-selected AGN candidate to be spatially coincident with an X-ray source, which helps to mitigate the presence of impostors in the sample, as we will shortly explore.

In the optical, detection of Doppler-broadened spectral emission lines is a definitive sign of an AGN. Although unfeasible in the early years due to the intensive process of obtaining spectra, recent databases like the Sloan Digital Sky Survey (SDSS), which collects optical spectra for hundreds of objects at a time, have enabled this technique en masse. However, one need only revisit Figure 1.2 to see why this would miss a large fraction of AGN: orientation effects would prevent all Sy 2 objects from being included. The same pitfall applies to selection by optical colors or an ultraviolet excess. Optical selection of AGN is a vast field with a rich literature, but

it is not a technique used widely in this thesis, so the discussion is deferred to the relevant portions of the upcoming chapters in which some context is necessary.

X-ray selection is perhaps the most complete way to assemble a sample of AGN, since X-ray emission is ubiquitous across almost all AGN types. Additionally, there are few confusing sources of X-rays, whereas stellar or dust emission can contaminate all other wavebands. Strong starbursts may contribute to the soft X-ray (0.2-5 keV) flux in some galaxies, and X-ray binaries can contribute to the hard (2-10 keV) X-ray flux. However, the ultra-hard (14-195 keV) X-ray band is devoid of contamination. Detection of a luminous point source in the ultra-hard band in a galactic center is a clear and unambiguous indicator of an AGN. Even better, hard X-rays are extremely penetrative, and so all but the very most obscured active nuclei are recovered by this technique. X-ray selection therefore assembles a nearly-complete sample of AGN with a wide range of black hole masses and accretion rates, as demonstrated by Hickox et al. [2009] and demonstrated in Figure 1.3.

1.1.3 The AGN - Host Galaxy Connection

The observed population of galaxies in the universe falls into two broad categories: red ellipticals that are no longer forming stars, and blue star-forming spirals. When galaxies first form, collapsing into disks, they begin forming stars. Young, hot stars are blue in color, and the host galaxies of starbursts are likewise blue. There is a dearth of galaxies in between these two populations in color-mass diagrams, as shown in Figure 1.4 [Schawinski et al., 2014]. This relatively empty region is often

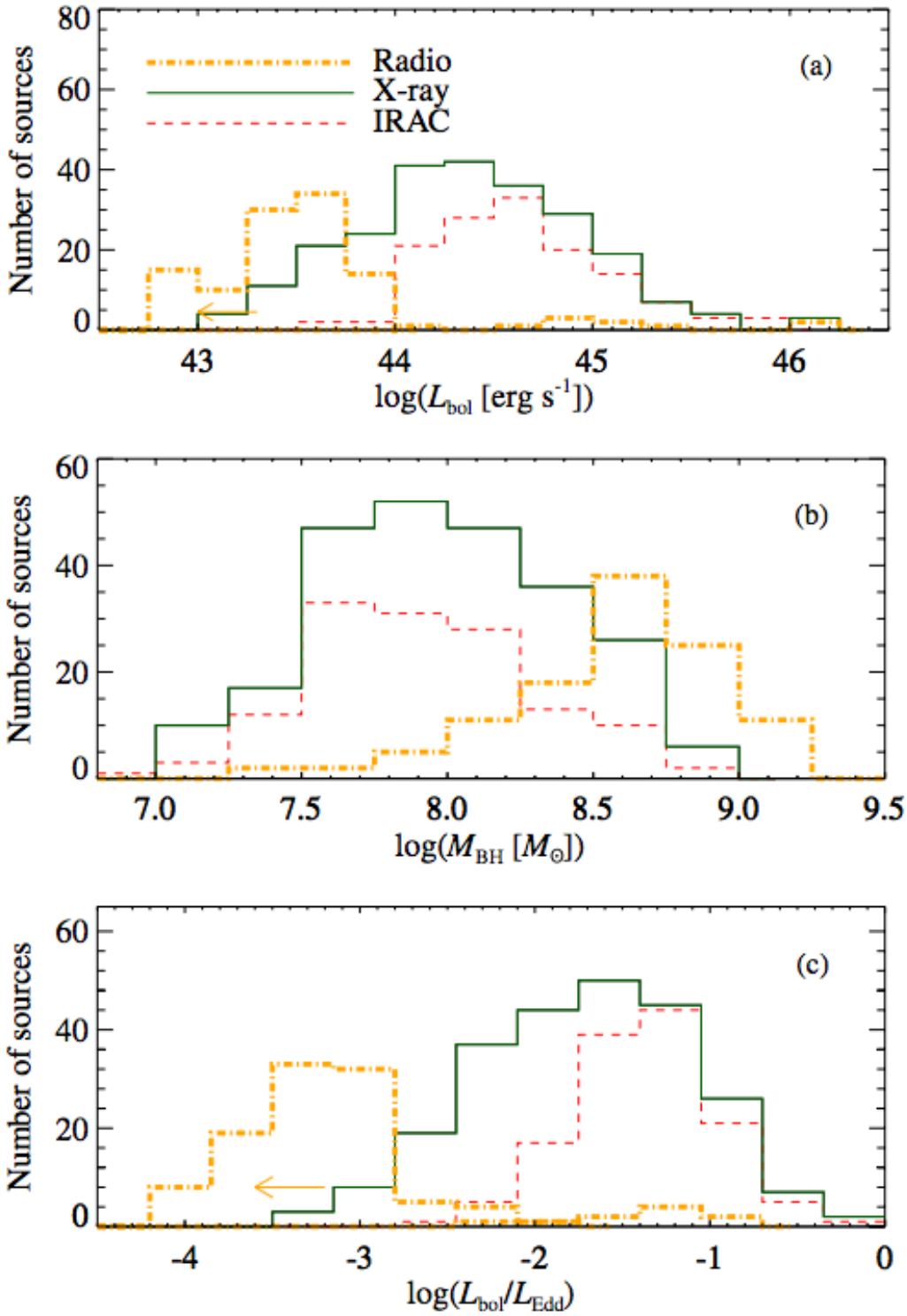

Figure 1.3: Distributions of bolometric luminosity (a), black hole mass (b) and Eddington ratios (accretion rates, c) for AGN selected by radio (yellow dot-dash), X-ray (green solid) and infrared (pink dashed) techniques. From Hickox et al. [2009].

called the "green valley." Some mechanism must be responsible for causing young, blue, star-forming galaxies into so-called "red and dead" ellipticals. Interestingly, AGN host galaxies tend to occupy the intermediate region of the diagram, implying that an AGN may be a phase of galaxy evolution responsible for shutting off star formation in the host [Nandra et al., 2007, Silverman et al., 2008, Cimatti et al., 2013]. The predominant idea is that the AGN produces powerful winds and radiative outflows, which evacuate gas and dust from the host galaxy and deplete the reservoir from which new stars can form. This outflow can take the form of radiation pressure on dust grains or can manifest as AGN-driven winds. The dust grains are slightly charged due to proximity to the quasar, allowing them to couple to ionized gas, which becomes entrained in the outflow. Such outflows and motions also serve to heat the gas, which further prevents the gravitational collapse necessary for star formation to begin. These processes are commonly referred to as "feedback."

There is ample evidence that galaxy-scale winds and outflows exist. For example, there is a class of quasars that exhibits broad, blue-shifted UV absorption lines that indicate fast-moving absorbing material along the line of sight [e.g., Ganguly et al., 2007]. We have also seen evidence of galactic "superwinds" emanating perpendicular to the galaxy plane, although whether these are more likely to be driven by AGN or by powerful starbursts depends on their outflow velocity [Heckman et al., 2000, Velleux, Cecil & Bland-Hawthorn, 2005].

There are a number of empirical results suggesting that despite a hundred-millionfold discrepancy in size, the central supermassive black hole and its host galaxy manage to affect one another (see the review by Fabian [2012]). The most

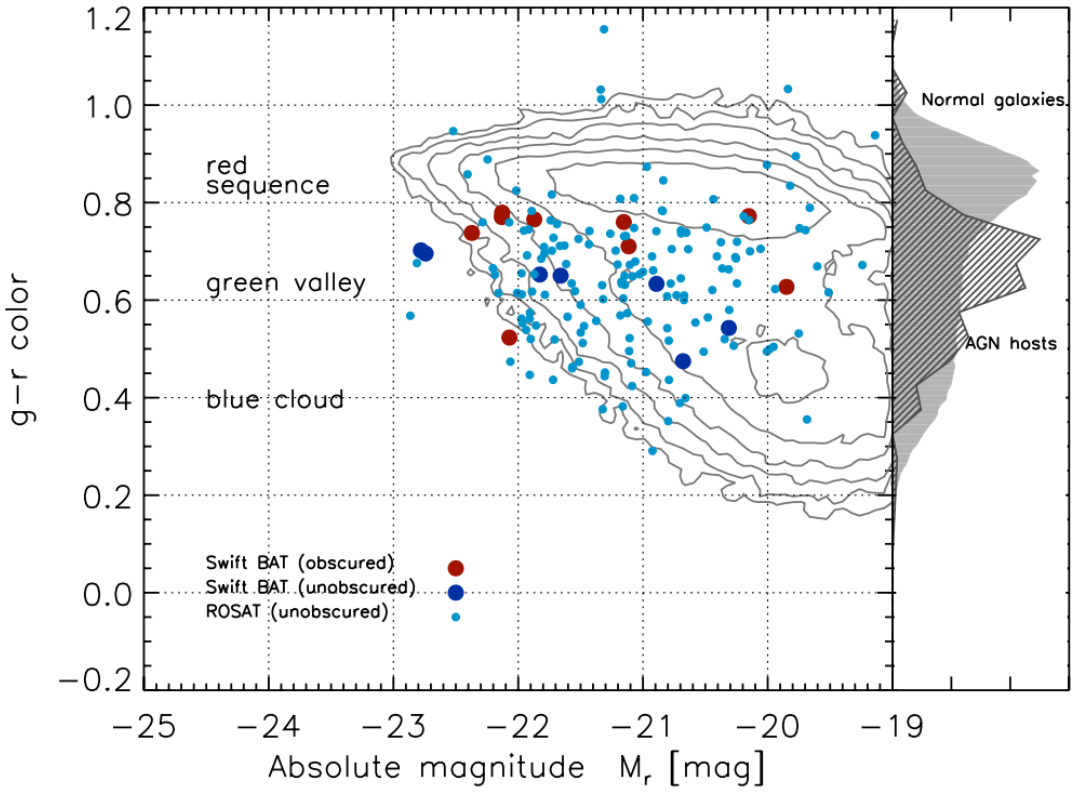

Figure 1.4: The distribution of galaxies from the Sloan Digital Sky Survey (SDSS) in $u-r$ color versus total stellar mass (contours). Elliptical galaxies occupy the red sequence, while star-forming spirals occupy the blue cloud. X-ray selected AGN host galaxies (colored symbols) occupy the intermediate region, often termed the "green valley." From Schawinski et al. [2009b] .

widely known is the strong correlation between the mass of the black hole ($M_{\rm BH}$) and the velocity dispersion of the stellar bulge of the host (σ_*) [Gebhardt et al., 2000]. This relationship holds for all types of host galaxy (elliptical and spiral) and across many orders of magnitude in mass, as shown in Figure 1.5, adapted from Gültekin et al. [2009]. Correlations have also been found between $M_{\rm BH}$ and the host luminosity and total stellar mass in the bulge [Magorrian et al., 1998, Marconi & Hunt, 2003]. The regulation of star formation via feedback is a natural explanation for such relationships. The theoretical work of Di Matteo, Springel & Hernquist [2005] has shown that including feedback from quasars in galaxy evolution simulations naturally reproduces the $M - \sigma_*$ relation. Additionally, negative feedback from quasars has been required in cosmological simulations to regulate the rapid growth of galaxies. Without it, the simulated universe includes too many large, blue, star-forming galaxies compared to what is observed [Ciotti, Ostriker & Proga, 2010]. Therefore, feedback from AGN seems to be required from both observational and theoretical standpoints.

Because of the many indications that the presence of an AGN affects the star formation in the host, it is prudent to examine how the properties of star formation differ between AGN hosts and quiescent galaxies. One relationship in particular has been critical to these examinations: the very strong correlation between far-infrared (FIR) and radio luminosity in normal, non-AGN star-forming galaxies. Originally discovered by van der Kruit [1971] and codified in the review by Condon [1992], the tightness and linearity of the FIR-radio correlation has been useful in confidently studying star forming galaxies out to high redshifts. The canonical plot

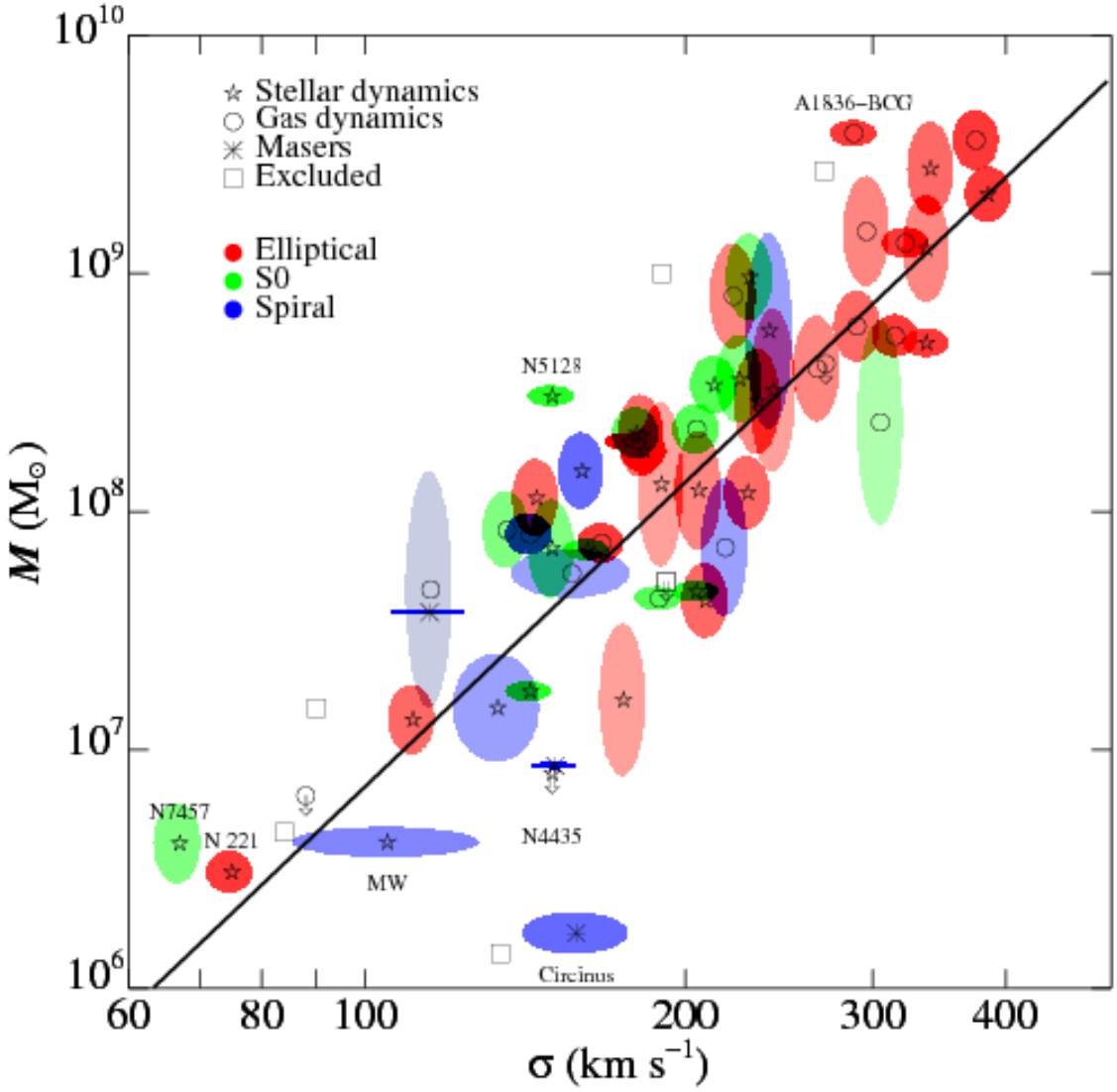

Figure 1.5: The empirical relationship between supermassive black hole mass and stellar bulge velocity dispersion, from Gültekin et al. [2009].

from Condon [1992] is shown in Figure 1.6. This correlation arises because both the FIR and radio emission is related to the star formation rate (SFR): the FIR is re-radiated emission from dusty H II regions, while the radio luminosity comes from synchrotron emission emitted by electrons accelerated in supernova remnants. The question of whether the FIR-radio relation holds in AGN is quite important, if we are to use either the FIR or the radio emission as a proxy for the star formation rate (SFR) in cosmological studies. If the AGN itself contributes significantly to either the FIR or the radio emission, then the relationship would no longer hold. The first step, then, is to determine whether or not the AGN contributes to the emission in these wavebands.

Of course, radio-loud AGN produce a large amount of radio emission that contaminates the relation. However, even studies of radio-quiet AGN have found that faint radio cores seem to be ubiquitous in sufficiently sensitive observations [e.g., Nagar et al., 2002, Maini et al., 2016]. The origin of nuclear radio emission in radio-quiet AGN is puzzling and remains an open question. We address this in our sample of 70 radio-quiet, X-ray selected Seyferts in Chapter 2.

Although originally assumed to be minimal, or at least overwhelmed by thermal re-radiation from star formation, the AGN contribution to the FIR emission has been shown to be as high as 50% at $60 - 70\mu$m [Mullaney et al., 2011, Shimizu et al., 2017]. Careful modeling of the FIR spectral energy distribution (SED) can remove the AGN component, leaving only the FIR emission expected from star formation. In order to remove the AGN contribution to the radio flux, we have turned to high-resolution spatial imaging of the nuclear source and the surrounding star for-

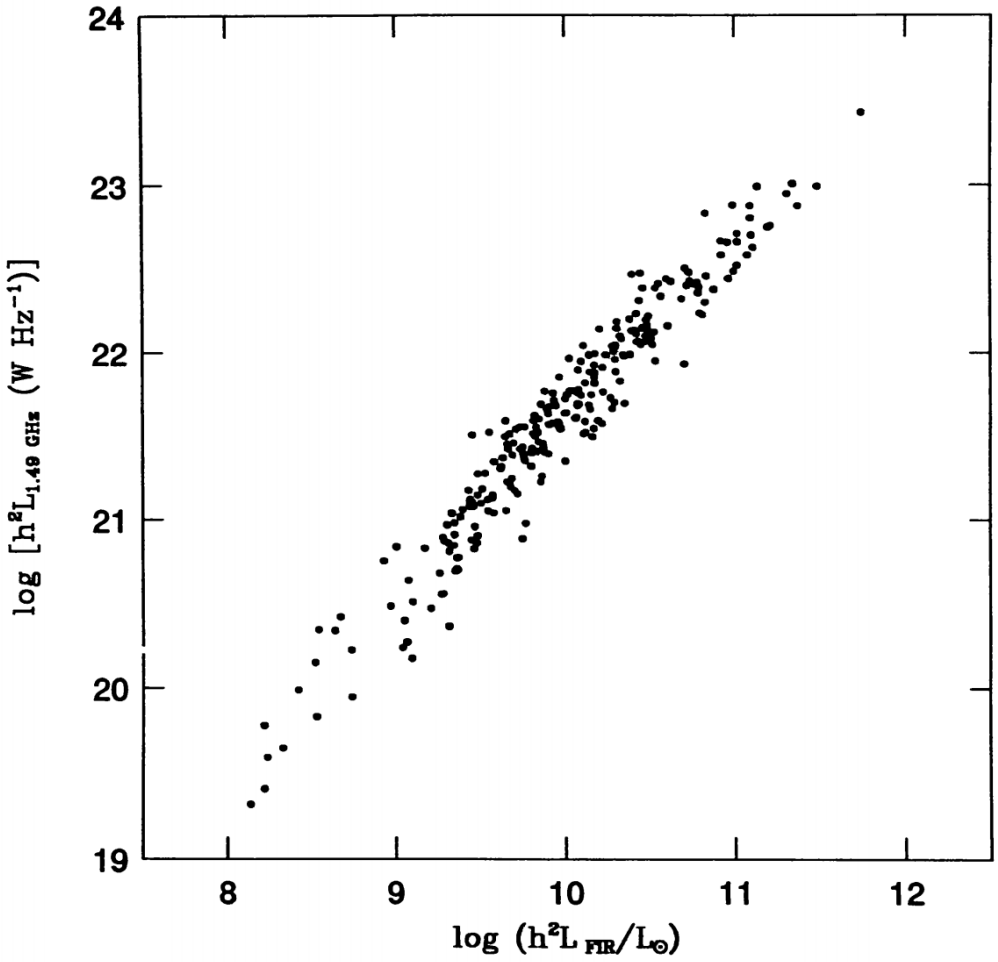

Figure 1.6: The linear relationship between 1.4 GHz radio luminosity and FIR luminosity for quiescent, normal star-forming galaxies from Condon [1992], referred to throughout the text as the FIR-radio correlation.

mation. The resolution of the Jansky Very Large Array (JVLA) enables us to isolate the star formation and AGN contributions to the radio flux, and together with the decomposed FIR emission, test the FIR/radio correlation in AGN (Chapter 2).

Many studies of large galaxy surveys have found that the SFR of blue, star-forming galaxies are correlated with the total stellar mass of the galaxy, M_*, along a narrow track called the "star formation main sequence," shown in Figure 1.7 [Brinchmann et al., 2004, Noeske et al., 2007, Rodighiero et al., 2010]. There has been much discussion about whether or not AGN hosts lie on this main sequence, or fall below it [Mullaney et al., 2012, Rosario et al., 2013]. Shimizu et al. [2015] found that a significant fraction of the ultra-hard X-ray selected *Swift*-BAT AGN lay well below the main sequence, implying that the AGN is suppressing star formation in its host. In Chapter 2, we follow up on this matter with our high-resolution radio imaging campaign, and find that objects with small, nuclear radio jets are most likely to lie below the main sequence. As evidence for feedback in action, this is currently tentative due to the small sample size, but in Chapter 5 we describe an ongoing observational program (PI Smith) designed to address this issue robustly.

1.1.4 AGN Variability and Accretion Physics

Optical flux variations were one of the very first properties of AGN to be recognized, and as described above, were the key with which the small size and thus identity of the central source was determined. Today, variability remains an important tool for studying physical processes that are beyond the reach of even

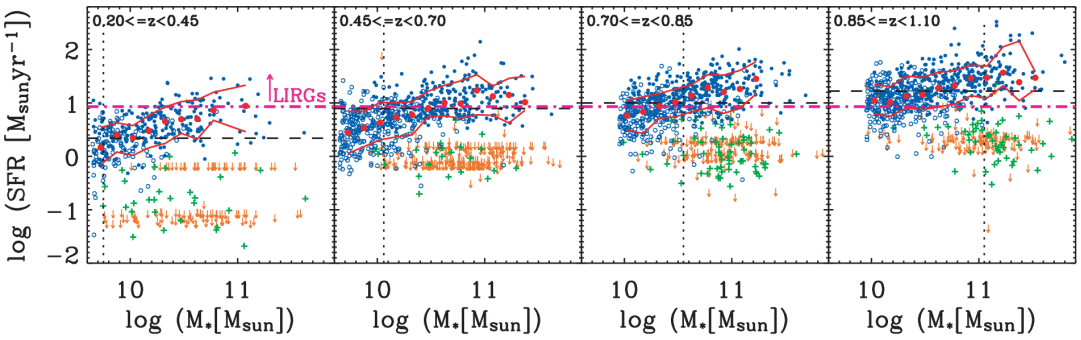

Figure 1.7: The relationship between SFR and stellar mass for $\sim$ 3000 galaxies in four different redshift groups (the four panels). The blue circles indicate objects with indications of star formation, including robust detection at 24μm, blue photometric color or emission lines. Green plus signs indicate galaxies with red colors and no 24μm detections, including objects with weak AGN-like line ratios. Orange arrows indicate objects with no 24μm detection and no emission lines, with elliptical morphologies. From Noeske et al. [2007].

our highest-resolution imaging instruments. Optical variations come from the accretion disk, which as we have noted is the origin of the optical continuum flux. A good average value for the size of an accretion disk is $\sim 10^{-2}$ parsecs, according to analytical arguments by Goodman [2003]. At the distances of AGN, this is impossible to directly image except in rare cases of microlensing, and will remain so for many generations of telescopes to come. So, optical flux variations offer one of the only means of probing the structure and behavior of the accretion disks around supermassive black holes.

In 1963, before the extragalactic nature of quasars was known, Matthews & Sandage [Matthews & Sandage, 1963] used optical plate comparisons to determine that the quasar 3C 48 varied by 0.4 magnitudes over 13 months. This was the very

first discovery of AGN variability. It was followed up by Smith & Hoffleit [1963] and Sharov & Efremov [1963] with more archival data. These studies found that the flux of 3C 48 would double or halve over the course of several years, but that changes also occurred on the scale of days to weeks. Sandage [1964] and several follow-up efforts searched for variability in the 8 quasars known at the time, and found evidence of 0.1 - 1.5 magnitude changes in all of them. It was recognized by the 1970s that all optically variable objects were broad-line quasars or Seyfert 1 galaxies, and that narrow-line quasars and Seyfert 2 galaxies did not vary, although it was not known why. This makes sense in view of the current unified model (see Figure 1.2), since the variability arises from the accretion disk, which is invisible in Sy 2 AGN.

It was clear from plots of quasar flux over time, called "light curves," that their variability was not periodic. Even characteristic timescales were elusive. The stochasticity of AGN light curves would go on to be seen in every variability survey conducted since. The earliest dedicated studies were monitoring campaigns of three AGN in the local universe: NGC 4151, NGC 5548, and 3C 273. Typically these campaigns consisted of monthly, weekly, or daily visits to the sources for a single photometric data point, over the course of several years; for example, the 7-year daily monitoring of NGC 5548 by Peterson [1994] shown in Figure 1.8. In the 1980s and 1990s, photometric surveys of larger samples of higher-redshift AGN began to proliferate, since a single wide-field telescope image can capture many of these AGN hosts at a time. Some examples of these surveys include the 16-month monitoring of 300 radio-quiet quasars with the South Galactic Pole telescope [Hook et al., 1994]

and a 10-year B-band monitoring program of 183 quasars in a region of the sky known as SA-94 [Cristiani, Vio & Andreani, 1990]. The history of such studies is well-reviewed by Ulrich, Maraschi & Urry [1997]. The modern era of AGN variability studies consists of many tens of thousands of objects, typically as byproducts of huge surveys dedicated to locating transient phenomena like supernovae and tidal disruptions of stars by supermassive black holes. The Panoramic Survey Telescope and Rapid Response System [Pan-STARRS; Kaiser et al., 2010], the Sloan Digital Sky Survey Stripe 82 [Sesar et al., 2007], and the Palomar Transient Factory [Law et al., 2009] are a few examples of surveys that have produced tens of thousands of AGN light curves, albeit typically with uneven sampling and large data gaps. A more extensive discussion of the current optical variability literature is undertaken in the latter sections of Chapter 4.

Variability of AGN is not confined to optical wavelengths. In fact, AGN have been seen to vary in every wavelength in which they have been studied, from radio to X-ray. X-ray variability studies are especially fruitful, as the X-ray emission is believed to come from very near the black hole. Many interesting clues have been seen in X-ray light curves, which due to their space-based nature are cleaner and more rapidly and evenly sampled than ground-based studies. Two properties of X-ray light curves of accreting black holes are particularly relevant for this work. First, the histograms of fluxes in a light curve are well-fit by lognormal distributions [Uttley & McHardy, 2005]. Second, the variability of a given light curve segment is linearly correlated with the average flux of that segment, in the so-called "rms-flux" relationship [Uttley & McHardy, 2001]. The sense of this very tight, linear

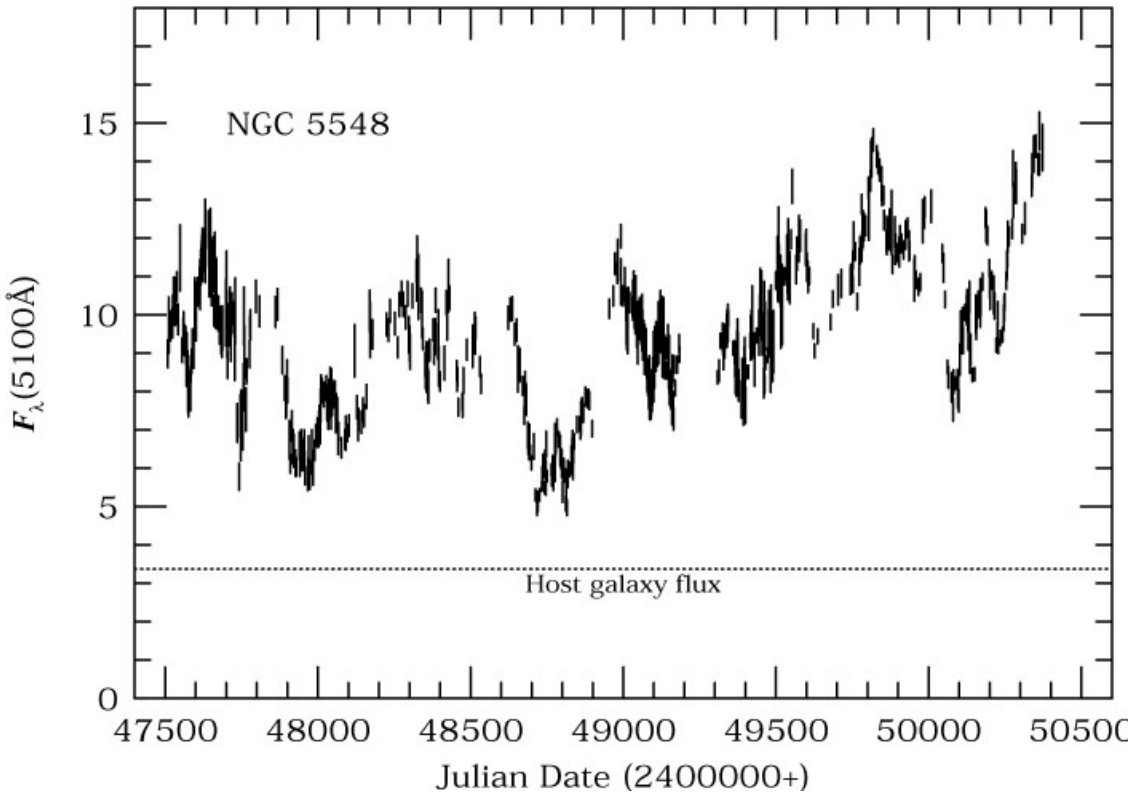

Figure 1.8: Optical light curve of NGC 5548 over approximately 7 years. From Peterson [1994].

relationship is that when a given object is brighter, it is more variable. As we will examine in Chapter 4, whether or not the optical light curves of AGN also exhibit these properties has implications for the relationship between the optical and X-ray emitting regions.

Although AGN variability has been long recognized and studied, the *cause* of the variability is still unknown. Intuitively, one might imagine that flux variations result from a changing mass accretion rate: perhaps we see a higher flux when the accretion rate is high, simply because more matter is being converted into energy, and less when it is low. However, simple arguments rule this option out. The fastest

that information can travel through the disk is the sound speed, and at the typical temperatures and densities of the plasma that we believe makes up the disk, it would take many years to decades for the bulk of the disk to "know" about an accretion rate increase. Such slow variations are at odds with both the observed fluctuations on hour-day timescales, as well as inconsistent with the observation that the UV and optical flux seem to vary almost simultaneously, not many years apart as one would expect from an outwardly-propagating energy release following an accretion surge.

It has also been proposed that the observed flux variations of quasars are not intrinsic to the AGN itself, but are instead the result of substellar-mass objects gravitationally lensing the quasars somewhere along our line of sight [Hawkins, 1993]. This phenomenon is known as microlensing, and while it enjoyed some early successes, it is now recognized that AGN variability is an intrinsic phenomenon. The most compelling piece of evidence for this is the now well-established fact that the broad emission lines also vary, and they do so in response to the continuum variations after some time lag. Measuring these lags has enabled us to effectively map out the location of the broad line emitting gas using light travel time considerations. The kinematics of the broad line gas can then be used to measure the mass of the central black hole quite effectively. This process is known as reverberation mapping [Peterson et al., 2004].

Another common explanation has been a shot noise model, in which the variability is due to the superposition of discrete flares randomly distributed in time [Cid Fernandes et al., 2000]. This description is quite general, as the origin of the

discrete flares could be caused by many types of instability within the accretion disk [Kawaguchi et al., 1998] or by more exotic explanations like stellar collisions or supernovae. In the early days before black holes were established as the central source in radio-quiet AGN, very dense nuclear star clusters were serious candidates [Terlevich et al., 1992]. In this framework, interpreting variability as a superposition of supernovae had some traction.

Of course, the generality of the shot noise model is also a pitfall, since even if the mathematical model fits the data well, the physical origin of accretion disk flares (or whatever else the discrete events may be due to) is not revealed. Lyubarskii [1997] proposed a model in which fluctuations in the instantaneous mass accretion rate form in the disk and propagate inwards. Because these fluctuations occur on timescales approximating or exceeding the viscous time, which decreases with smaller radii, long-timescale fluctuations in the outer disk acquire ever-shorter superpositions of fluctuations as they move inward. The observed rms-flux relationship and lognormal flux distributions seen in X-ray light curves arise naturally from this multiplicative process, so this description, commonly referred to as the model of "propagating fluctuations," is very attractive. Additional supporting evidence for this model comes from the discovery that variations in the observed flux in high energy X-ray bands tend to lag behind those in lower energy bands, indicating that the fluctuations underlying the variability first occur in the lower-temperature environments further out, and then move inwards to higher-temperature regimes [Nowak et al., 1999]. However, one requires a mechanism to drive the fluctuations.

The best current candidate for this driver is the magneto-rotational instability

(MRI). The instability of a viscous flow between annuli of a charged plasma was realized early by Chandrasekhar [1960], and extended to astrophysical disks by Balbus & Hawley [1991]. They showed that astrophysical accretion disks are unstable to axisymmetric perturbations if they are threaded with a weak magnetic seed field. The upshot is that disturbing a parcel of gas along the radial direction will result in a nonlinear dynamical instability. Many follow-up simulations have shown that this mechanism is effective at injecting and maintaining disk turbulence, allowing for angular momentum transport outwards and thus mass accretion rate inwards [Hawley & Balbus, 1991, Stone et al., 1996, Reynolds & Miller, 2009, Jiang, Stone & Davis, 2014]. Recent work by Hogg & Reynolds [2016] has found that propagating fluctuations remain a robust phenomenon even within the full machinery of magnetohydrodynamic (MHD) theory, and that the magnetic dynamo seen in most accretion disk simulations may be the driving mechanism.

Additionally, much modern research focuses on a mathematical model called the damped random walk, or Ornstein-Uhlenbeck process. Introduced as a statistical model for AGN variability by Kelly, Bechtold & Siemiginowska [2009], the damped random walk functions around a driving term which "kicks" stochasticity into a light curve around its mean value. After each kick, the perturbation decays exponentially back to the mean, resulting in overlapping of events and long-term correlations. The formalism can be found in Kelly, Bechtold & Siemiginowska [2009], with an improved treatment allowing for a linear combination of stochastic processes given by Kelly, Sobolewska & Siemiginowska [2011]. This theory makes the testable prediction that the power spectral density of variability should scale with temporal frequency as

$\propto \nu^{-2}$. As is reviewed more comprehensively in Chapter 4, most X-ray studies and some ground-based optical studies do find PSDs that are well-modelled by a power law with a slope of -2, with some important exceptions.

The work described in Chapter 4 addresses AGN variability using a new tool: light curves from the space-based timing telescope *Kepler*. The light curves from *Kepler* are the highest precision and most evenly sampled optical light curves ever obtained. However, the specificity of purpose with which *Kepler* was designed makes it quite difficult to use the data products for AGN science. Much of Chapter 4 is dedicated to addressing challenges that arose from *Kepler*'s data handling, which was optimized for exoplanet science.

In summary, the literature on AGN variability is still confusing, and the origin of the phenomenon is very much an open question. The work described in Chapter 4 takes the necessary initial steps to use space-based AGN light curves from the *Kepler* exoplanet-hunting satellite to probe a brand new realm of AGN variability, an avenue that will become more important after the launch of the Transiting Exoplanet Survey Satellite (TESS) in 2018. Chapter 5 will address some of the implications that the early *Kepler* work will have for TESS and other upcoming time domain surveys.

1.1.5 A Brief Summary of the Facilities

Most of these results could not have been obtained a decade ago, since the analyses leverage enormous improvements in observational facilities that have occurred in recent years. Each chapter discusses the relevant facilities in greater detail;

this discussion emphasizes the novelty of the work. First, the radio images of circumnuclear star formation in AGN that are used in Chapter 2 would not have been possible with the original Very Large Array (VLA). The array is a radio interferometer located in Soccoro, New Mexico, that consists of 27 radio antenna dishes that move along tracks to allow transitions between its largest (A) and smallest (D) configurations. Originally constructed in 1980, the array underwent a major upgrade beginning in 2001 to leverage the great technological improvements in signal processing over the previous two decades. Completed in 2012, the Expanded Very Large Array, later dubbed the Jansky Very Large Array (JVLA), had increased the instrument's overall bandwidth, improved spectral coverage, and greatly enhanced the spectral resolution. This can be read about in detail in Perley et al. [2011]. Without the resulting improvement in dynamic range from the JVLA upgrade, the radio images we use in Chapter 2 would have required unworkably long integration times. We were able to obtain each image in a matter of minutes, and the ongoing observations for this project, described in Chapter 5, leverage these improvements still further.

The X-ray and UV survey described in Chapter 3 was executed using the *Swift* spacecraft. *Swift* was designed to catch transient explosions known as gamma ray bursts, and provide near-instantaneous follow-up once the location of the transient had been identified. To this end, the spacecraft is outfitted with three telescopes. The first is the Burst Alert Telescope, or the BAT. The BAT is sensitive to very high energies ($14 - 195$ keV) and able to localize detections to within 4 arcminutes [Barthelmy et al., 2005]. Once the gamma ray burst is localized, the spacecraft

captures its afterglow using its other two instruments, the co-aligned X-ray Telescope (XRT) and the UV-Optical Telescope (UVOT). Although optimal for gamma ray burst science, we use this instrument for different purposes. The ultra-hard X-ray BAT is ideal for selecting a very complete sample of AGN. The latest *Swift*-BAT Catalog of ultra-hard X-ray sources was published by Baumgartner et al. [2013], and the AGN sample drawn from it has been used extensively due to its relatively unbiased nature with respect to luminosity, black hole mass, and accretion rate. This is the parent sample for the project described in Chapter 2. We also made use of *Swift*, this time with the XRT and UVOT, to conduct our own survey, described in Chapter 3, to locate new AGN in the field of view of the *Kepler* spacecraft.

Kepler represented an immense improvement over ground-based optical timing efforts. Designed to detect the parts-per-million signals of planets eclipsing other stars, it is the most accurate astronomical photometer ever built, capable of detecting variations in flux that were impossible in the past. Furthermore, it does it from space, which prevents the usual interruptions that plague ground-based variability studies (for example, weather and the diurnal cycle). To facilitate the discovery of exoplanets with orbits of ~ 1 year, the spacecraft stared at a fixed field of view near the galactic plane for the entirety of its 4-year mission, offering long, evenly sampled baselines. We have leveraged these capabilities to study AGN variability in a regime that was not accessible to any previous instruments. This, along with the technical challenges of adapting *Kepler* light curves for AGN science, is extensively discussed in Chapter 4.

We conclude by noting that the optical spectroscopy used in this thesis was

largely obtained at the brand new 4.3 meter Discovery Channel Telescope at Lowell Observatory, in which the University of Maryland is a major partner, which became operational in January 2015. Although the spectrograph is repurposed from another telescope, the projects described here are some of the very first optical spectroscopic observations obtained at this facility, which is now enabling the work of a large number of University of Maryland scientists and students.

Chapter 2: Radio Properties of the Burst Alert Telescope Active Galactic Nuclei: the Far Infrared-Radio Relation, the Fundamental Plane, and the Main Sequence of Star Formation

2.1 Introduction

The apparent ubiquity of the correlation between the mass of a galaxy's central supermassive black hole and the stellar velocity dispersion of its bulge, known as the $M_{BH} - \sigma$ relation [Gebhardt et al., 2000, Ferrarese & Merritt, 2000, Gültekin et al., 2009], has prompted a robust investigation of the mechanisms by which these regions may influence one another. The concept of feedback in active galactic nuclei (AGN) attempts to explain the correlation by proposing a positive or negative regulatory effect of the AGN on star formation. In negative feedback scenarios, the AGN quenches the near-nuclear star formation by expelling or heating gas in the central regions [e.g., Di Matteo, Springel & Hernquist, 2005, Hopkins et al., 2006, Dubois et al., 2013]. Positive feedback models suggest that AGN-driven jets or outflows generate turbulence and shocks which then trigger the collapse of giant molecular clouds and promote star formation [Klamer et al., 2004]. The relationships may

also be explained by co-evolution instead of ongoing interactions between the active nucleus and the nearby star-forming regions. Regardless of the physical method, it is now accepted that star formation and AGN activity are related phenomena.

There is a nearly linear, remarkably tight relationship between the infrared and radio emission found in normal star forming galaxies, called the far-infrared (FIR)-radio correlation [Condon, 1992], which is widely used in studies of star formation out to high redshifts. It would be convenient to be able to apply this relationship to studies of star formation in AGN. This is complicated by the fact that even radio-quiet AGN tend to have nuclear radio emission in addition to extended emission from star formation. Further, a number of necessary assumptions are often employed in applying the FIR-radio correlation to AGN, including the use of star formation spectral energy distribution (SED) templates which assume that the AGN does not contribute to the far-IR emission. Recent work has shown that this assumption is flawed [Lira et al., 2013]. It has also been shown that Seyferts have a wide variety of circumnuclear radio structures within the central kiloparsec, some attributable to star formation and some to linear structures resembling jets [e.g., Baum et al., 1993]. It is even possible that the star formation environment surrounding the active nucleus may be quite different from that in isolated star forming regions in the host galaxy, and that circumnuclear star formation in AGN may not follow the FIR-radio relation at all. It is known that Seyferts tend to depart from this relationship, showing a radio excess that can be attributed to the AGN in the core [Wilson, 1988, Roy et al., 1998, Morić et al., 2010]. Roy et al. [1992] and Baum et al. [1993] showed that subtraction of the core AGN emission significantly improved the relation, but

this was not borne out in the larger study by Roy et al. [1998].

In order to investigate this thoroughly, we have conducted a 22 GHz radio imaging program with the Karl G. Jansky Very Large Array (VLA) of 70 radio-quiet AGN from the ultra-hard X-ray *Swift*-BAT survey [Baumgartner et al., 2013]. With these high resolution (1″) radio images of a relatively unbiased AGN sample, we may spatially separate any emission due to star formation from the AGN core, and test the FIR-radio correlation using only the extended radio emission (beyond a few hundred parsecs).

These observations also enable us to address another important mystery: the origin of the core radio emission in radio-quiet AGN. There seem to be very few, if any, radio-silent active galaxies. Radio observations with sufficient sensitivity have found compact radio emission in the majority of radio-quiet AGN [e.g., Nagar et al., 2002, Panessa et al., 2010, Maini et al., 2016]. Ideas range from scaled-down versions of the powerful synchrotron jets seen in radio-loud AGN, to pure and highly compact star formation, to coronal synchrotron emission similar to that in active stars. Parsec-scale extended jet-like morphologies have been seen in some radio quiet AGN [e.g., Orienti & Prieto, 2010]; however, Laor & Behar [2008] found that the relationship between the X-ray and radio luminosities of radio quiet AGN was consistent with an extension of the same relationship for coronally active stars, and Baldi et al. [2015] observed millimeter-band variability in the radio quiet AGN NGC 7469 consistent with X-ray variability, implying a common physical origin (presumably the corona). Correlations have been observed between the radio and X-ray luminosities in AGN of all types, and both of these quantities seem to be

related to the supermassive black hole mass in a "fundamental plane of black hole activity" [Merloni et al., 2003]. The relationships between the X-ray luminosity, core radio luminosity and $M_{\rm BH}$ can place interesting constraints on accretion flow models and the geometry of the circumnuclear emitting regions. Using the same spatial decomposition that allows us to study the extended star formation in isolation, we see how the isolated AGN radio core properties of our sample fall on these relations.

The paper is organized as follows. In Section 2.2, we discuss the properties of the sample and describe the detailed observations and reduction techniques. Section 2.3 discusses flux density measurements. Section 2.4 focuses on the different star formation morphologies revealed by our high resolution maps. In Section 2.5.1, we describe our methodology for decomposing the infrared SED into AGN and star formation components, and Section 2.5.2 discusses our final results on the FIR-radio correlation. The fundamental plane and X-ray-radio correlation results are discussed in Section 2.6. Section 2.7 examines where our samples of various radio morphologies fall on the main sequence of star formation. We discuss final conclusions in Section 2.8.

Whenever redshifts and luminosities are discussed, we have assumed cosmological parameters $H_0 = 67.8$ kms^{-1}Mpc^{-1} and $\Omega_{\rm m} = 0.308$, consistent with the most recent results from *Planck* [Planck Collaboration XIII, 2015].

2.2 Observations and Reduction

2.2.1 Sample

Our parent sample is drawn from the 58-month version of the *Swift*-BAT all-sky survey [Baumgartner et al., 2013]. The survey was conducted in the ultra-hard X-ray band (14-195 keV). Because of its very high energy, this band is not affected by obscuration up to very high columns ($> 10^{24}$ cm^{-2}). By the survey's 58-month catalog, it had detected ~ 600 AGN of various types, many of which had never been detected as AGN at other wavebands. Hard X-ray selection is the least biased way to select AGN [Hickox et al., 2009, Koss et al., 2011a]; the vast majority of all AGN are hard X-ray sources. Since optical, radio, infrared, and ultraviolet properties of the source do not enter into the selection, the sample is chosen independent of galaxy mass, galaxy luminosity, dust properties, radio loudness, or star formation rate. Additionally, most of the BAT AGN are relatively nearby, so high angular resolution translates to high spatial resolution for most of our sample. Our original work on the star formation in the BAT AGN was done in Mushotzky et al. [2014], wherein we observed 313 of these objects with far-IR *Herschel* PACS 160 μm and 70 μm images either from our Cycle 1 open-time program or the Herschel Science Archive. Mushotzky et al. [2014] attempted to separate the star formation and AGN contributions to the infrared SED using *Herschel* imaging at 70 μm and 160 μm of a subset of the ultra-hard X-ray selected sample of *Swift*-BAT AGN, but were unable to spatially distinguish the components with *Herschel*'s 6″ resolution. It was clear

that spatial decomposition would require higher resolution images. However, the AGN and the star formation can also be disentangled spectrally. By decomposing the *Herschel* SED into AGN and star formation (SF) components, the methods in Shimizu et al. [2015] allow us to predict the radio emission expected from the FIR-radio correlation using the SF component of the FIR SED *only*, putting us in a position to test the FIR-radio correlation if we obtained radio images with sufficient resolution to spatially decompose the AGN core and extended star formation.

Many of the BAT AGN are detected in the FIRST [Becker et al., 1995] and NVSS [Condon et al., 1998] surveys at 1.4 GHz; however, these surveys have $\sim$5″ and 45″ resolution, respectively. As indicated by the unresolved *Herschel* images at 6″, higher resolution is needed to achieve the separation of the AGN and extended components. To this end, we initially obtained K-band (22 GHz) continuum observations of 45 of the *Swift*-BAT AGN with the VLA in C-array, which has an angular resolution of $\sim$1″. We chose our initial sample to be unresolved in the *Herschel* 70μm images, and to be radio-quiet. All of our targets have $L_{1.4\ \mathrm{GHz}} \leq 10^{23}$ W Hz^{-1}, based on archival NVSS data. Additionally, we obtained VLA B-array follow-up observations of 17 objects which were unresolved in C-array, or which had a significant unresolved core and were sufficiently bright that B-array observations were feasible regardless of source structure. These images have a resolution of $\sim$0.3″. Although the B-array provides higher angular resolution, it also requires longer integration times to reveal extended structure, limiting the sample size for which we could obtain images of sufficient sensitivity. As described in Section 2.4.2, the majority of our B-array follow-up observations did not alter the

morphological classification obtained with our C-array imaging. Finally, we obtained C-array observations in the following cycle for 25 new objects selected to be at low redshifts, to provide maximal spatial resolution and to supplement the original sample. Unlike the first set, this sample had no preselection to be unresolved in the *Herschel* images. The final total observed sample is 70 targets.

2.2.2 Observations and Reductions

All observations were conducted in the K-band, which has a central frequency of 22 GHz and a large 8 GHz bandwidth. We selected K-band (22 GHz) for our initial study rather than the more traditional lower frequency bands because we were aiming for 1″ angular resolution to spatially resolve the star formation and AGN emission, which was only possible at K-band in the available arrays (C and D arrays). We remained at K-band for our subsequent two sets of observations to provide a data set at a uniform frequency. The initial sample of 45 objects was observed in C-array in May 2013, the B-array sample was observed in September 2014, and the final low-redshift sample was observed in February 2015. Each object was observed in a one-hour block with 2-3 other objects. Each observing block began with attenuation scans, followed by flux and bandpass calibration on either 3C 48, 3C 138, or 3C 286, depending on sky position. Each object was observed for 3-8 minutes based on scheduling block constraints, and was followed before and after by a gain calibration scan.

The data were processed using the Common Astronomy Software Applica-

tions package (CASA) [McMullin et al., 2007], which was developed to process interferometric and single-dish data from radio astronomical telescopes and is hosted primarily by the National Radio Astronomy Observatory (NRAO)[1].

After passing the raw data through the standard VLA reduction pipeline, we split off each individual object from the main measurement set, averaging over all 64 channels within each spectral window, resulting in a single data point per window. This reduces the amount of processing time without compromising the data. Then, each object was imaged with Briggs weighting (robust=0.5) and cleaned to a 0.03 mJy threshold or the dynamic range limit, whichever was higher. The images were then assessed for systematic errors; some exhibited significant radio frequency interference (RFI) signatures, which we removed by flagging the affected spectral windows. Images with a peak flux density exceeding 1 mJy went through iterative rounds of phase-only (non-amplitude) self-calibration of their visibility data (sources with lower peak flux densities did not have high enough signal-to-noise in the self-calibration solutions). Although the fractional bandwidth (36%) of the observations is quite large, standard multi-frequency synthesis using the CASA task CLEAN worked well because the angular extent of emission is less than 10 to 20% of the primary beam width and because the achievable dynamic range of the data was modest (typically 100/1 or less). In most cases this is because our sources are fainter than 3 mJy (100 times the thermal noise, which is approximately 30μJy). For the few sources with peak flux densities higher than 3 mJy, the dynamic range was limited by factors such as gain calibration errors that we were unable to correct. In cases

[1]For more information on CASA, see www.casa.nrao.edu.

where the S/N warranted it, we specified two terms in the multi-frequency imaging, providing spectral index maps. In general the spatial spectral index variations were small and had no effect on the imaging. In the end, five images had to be discarded due to persistent RFI banding, and three objects were not detected at our sensitivity threshold (Mrk 653, Mrk 595, and 2MASX J0107-1139). The final sample of useful images consisted of 62 objects, and is tabulated in Table 2.1.

Lastly, we applied a Gaussian 6″ taper to the visibility data of each observation, to create a second image with resolution mimicking that of the original *Herschel* observations. In the end, we have 62 images at 1″ resolution and 62 at 6″ resolution, which we later use to compare extended and core emission (see Section 2.5.2).

Table 2.1: The *Herschel*-BAT Sample

Name	α J2000	δ J2000	z	Predicted Flux mJy	Core Flux mJy	Extended Flux mJy	Morphology
2MASX J0353+3714	58.427	37.235	0.018	0.74	0.32	0.48	compact
2MASX J0423+0408	65.9199	4.1338	0.045	0.33	0.58	6.41	jet
2MASX J0444+2813	71.0376	28.2168	0.011	1.26	2.91	1.23	compact
2MASX J1200+0648	180.2413	6.8064	0.036	0.49	0.82	0.42	extended
2MASX J1546+6929	236.6014	69.4861	0.038	0.11	0.27	1.21	jet
2MASX J1937-0613	294.388	-6.218	0.010	3.55	5.16	3.24	extended
2MASX J2010+4800	302.5725	48.0059	0.026	0.19	0.16	0.09	compact
2MFGC 02280	42.6775	54.7049	0.015	1.50	0.34	1.08	extended
ARK 347	181.1237	20.3162	0.022	0.19	0.42	0.48	compact
CGCG 122-055	145.52	23.6853	0.021	0.35	1.79	0.24	compact
CGCG 229-015	286.3581	42.461	0.028	0.08	0.20	0.20	compact
CGCG 420-015	73.3573	4.0616	0.029	0.34	0.83	0.34	compact
CGCG 493-002	324.639	32.085	0.025	0.20	1.18	0.26	extended
ESO 548-G081	55.5155	-21.2444	0.014	1.04	0.46	2.14	extended
ESO 549- G 049	60.607	-18.048	0.026	3.37	0.77	1.94	extended
IC 0486	120.0874	26.6135	0.027	0.79	0.77	1.03	extended
IC 2461	139.992	37.191	0.008	1.62	0.46	0.69	compact
IC 2637	168.457	9.586	0.029	2.70	2.01	3.32	extended
IGR J23308	352.696	71.336	0.037	0.41	0.11	0.40	compact
IRAS 05589	90.5446	28.4728	0.033	0.42	2.46	0.33	compact
MCG -01-30-041	178.159	-5.207	0.019	1.33	0.37	1.10	extended
MCG +02-57-002	335.938	11.836	0.029	0.14	0.38	0.14	extended
MCG +04-48-002	307.1461	25.7333	0.014	9.40	0.44	8.53	extended
MCG +06-16-028	108.5161	35.2793	0.016	2.33	2.24	1.17	extended
Mrk 18	135.493	60.152	0.011	1.90	3.45	1.68	extended
Mrk 198	182.3088	47.0583	0.024	0.79	0.83	0.47	extended
Mrk 279	208.2644	69.3082	0.030	0.63	3.03	0.05	compact
Mrk 359	21.8856	19.1788	0.017	1.31	0.53	0.28	compact
Mrk 477	220.1587	53.5044	0.038	1.01	5.45	0.65	compact
Mrk 590	33.64	-0.767	0.026	0.43	2.02	0.72	compact
Mrk 739E	174.122	21.596	0.030	1.76	0.31	1.05	extended

Table 2.1 – continued from previous page

Name	α J2000	δ J2000	z	Predicted Flux mJy	Core Flux mJy	Extended Flux mJy	Morphology
Mrk 766	184.6105	29.8129	0.013	3.20	4.60	0.24	compact
Mrk 79	115.6367	49.8097	0.022	0.94	1.45	0.94	extended
Mrk 817	219.092	58.7943	0.031	1.40	1.94	0.16	compact
Mrk 885	247.451	67.3783	0.025	0.44	0.23	0.07	compact
Mrk 926	346.1811	-8.6857	0.047	0.48	8.62	1.15	compact
Mrk 975	18.4626	13.2717	0.050	0.76	1.26	0.29	compact
NGC 1106	42.6688	41.6715	0.014	0.60	11.15	0.47	compact
NGC 1125	42.918	-16.651	0.011	2.49	6.14	0.28	compact
NGC 1194	45.9546	-1.1037	0.014	0.05	1.08	0.18	compact
NGC 2110	88.0474	-7.4562	0.008	4.73	42.17	23.93	jet
NGC 235A	10.72	-23.541	0.022	2.13	3.28	1.05	extended
NGC 2655	133.9072	78.2231	0.005	2.29	12.51	2.59	compact
NGC 2992	146.4252	-14.3264	0.008	8.63	12.49	16.78	extended
NGC 3081	149.8731	-22.8263	0.008	1.10	1.21	0.41	compact
NGC 3431	162.8127	-17.008	0.018	0.33	0.69	0.28	compact
NGC 3516	166.6979	72.5686	0.009	1.58	3.70	1.58	jet
NGC 3786	174.927	31.909	0.009	2.15	0.72	1.34	extended
NGC 4388	186.4448	12.6621	0.008	10.19	3.26	10.64	extended
NGC 513	21.1119	33.7995	0.020	2.92	0.87	4.33	compact
NGC 5231	203.951	2.999	0.022	0.76	0.64	0.47	compact
NGC 5273	205.5347	35.6542	0.004	0.64	0.55	0.14	compact
NGC 5548	214.4981	25.1368	0.017	0.80	1.44	3.08	jet
NGC 6552	270.0304	66.6151	0.026	2.10	4.76	0.59	compact
NGC 7679	352.1944	3.5114	0.017	8.55	0.46	6.76	extended
UGC 03478	98.1965	63.6737	0.013	1.34	0.97	0.44	compact
UGC 03601	103.9564	40.0002	0.017	0.36	1.26	0.32	compact
UGC 07064	181.1806	31.1773	0.025	1.77	0.61	0.54	extended
UGC 08327	198.822	44.4071	0.037	1.16	2.57	0.39	compact
UGC 11185	274.0487	42.6608	0.041	0.32	6.82	1.35	jet
UGC 12741	355.4811	30.5818	0.017	0.48	0.31	0.39	compact
UGC12282	344.7312	40.9315	0.017	1.24	0.44	0.48	compact

Note – Properties of the 22 GHz observations of our sample of BAT AGN. Columns are (1) object name, (2) right ascension, (3) declination, (4) redshift, (5) the 22 GHz flux density predicted from the star formation component of the *Herschel* SED using the FIR-radio relation (see Section 2.5.1), (6) the observed 22 GHz flux density in the compact core, (7) the observed 22 GHz flux density in full $6''$ resolution image minus the core component, thereby encompassing all the extended emission, and (8) the morphological classification based on the factors described in Section 2.4.

2.3 Flux Measurements

To measure the 22 GHz flux densities of unresolved or compact images and the compact cores of extended images, we used the CASA command `imfit` to fit an elliptical gaussian to our Stokes I image component. Although this method is questionable for use on extended sources, our compact sources are fitted very well by a single elliptical component. Each fit was inspected visually and manually re-done in the case that the elliptical was incorrectly fitted over an inappropriately large

area to include larger-scale flux.

A major objective in the project was to measure the extended emission in each image, which could be either star formation or an AGN-related jet or outflow. Although many of our 1″ resolution images exhibit large-scale structures even at very low surface brightness, we can be more confident of measuring this extended emission accurately by using our lower-resolution 6″ images. The extended flux in the higher resolution images is included in the 6″ beam in most cases. We can then use `imfit` on these unresolved large-scale images, and then subtract the core flux density as measured above in the full-resolution images, to calculate the value of extended flux only. In the handful of cases with extended flux visible in the 6″ images, it was measured manually in the CASA task `viewer`, using `imstat` on a box region drawn around the extent of the emission.

Of course, the emission inside the 1″ radio cores need not be exclusively caused by the AGN. For the full redshift range of our sample, 1″ resolution corresponds to 70 parsecs - 1 kiloparsec (see the following section). In order to be as conservative as possible, we measure the integrated flux density in the compact component of the image, rather than exclusively inside the unresolved beam, as the "core flux density." (Note that the compact component is sometimes larger than the beam, and so is resolved, despite being compact in morphology). This core flux density may still include unresolved star formation and jets, as well as the nuclear AGN component. By measuring the integrated flux density in the compact component to be subtracted off, we ensure our estimates of the extended star formation flux densities are conservative lower limits; including the core emission would provide an

upper limit.

2.4 Nuclear Star Formation Morphologies of BAT AGN

The sample has a wide variety of 22 GHz morphologies. The resolution of the VLA at 22 GHz in C-configuration is $\sim$1″. Our objects are relatively nearby with a redshift range of $0.003 \leq z \leq 0.049$. This corresponds to a spatial scale of 0.07 kpc to 1 kpc. The redshifts of our target objects are shown in Table 2.1. Of the 62 total objects, 34 are compact or unresolved, 22 show significant extension indicative of star formation or large outflows, and 6 are jet-like. We do not find any tendency for extended sources to be seen at lower redshifts, so this distribution is not a function of better resolution in nearby objects.

2.4.1 Core-Dominated Sources

All of our detected galaxies have an unresolved or nearly unresolved core component. Additionally, all of our galaxies have emission that is extended relative to the 1″ beam. However, in approximately half (34 out of 62) of our sources the extended emission is too weak at 1″ to be significantly detected in individual resolution elements, and the detection of extended structure only becomes significant with smoothing or integrating. We refer to the sources in which extended emission requires smoothing for significant detection as "core-dominated."

The origin of this core emission is discussed in more detail in Section 2.5.2 and Section 2.6. It is likely that many of our cores contain both AGN emission and

unresolved star formation.

2.4.2 Star Formation, Outflows and Jets

Twenty-two of our BAT AGN have extended, morphologically diverse 22 GHz emission that is not jet-related and six had jet-like morphologies. They are shown in Figure 2.1 and Figure 2.2, respectively. Among the non-jets are examples of smooth emission extending outwards from the core (e.g., CGCG 493-002), clumpy emission (e.g., ESO 549-G049), and star formation rings (e.g., IC 2637). Although we will show that the emission in these objects is due to star formation, it is important to note that AGN are capable of driving outflows other than classical, collimated radio jets. Such outflows can interact with the environment to produce radio emission. Two of our extended objects, NGC 2992 and NGC 4388 are known to be hosts to such outflows [Veilleux et al., 1999, 2001]. For consistency with the overall criteria described in this section, they remain in the "extended" sample.

Determining whether extended radio emission is due to star formation or to a jet/AGN-driven outflow thus requires more detailed analysis than a qualitative look at morphology. If a literature search does not indicate a known, well-studied outflow or jet, we overplot the radio emission on archival optical images. If the radio emission is located preferentially outside of and perpendicular to the galaxy plane, the object would most likely be an outflow. We also check whether the observed radio emission is roughly consistent with that expected from the star formation component of the infrared *Herschel* emission (see Section 2.5.1): a significant overage is indicative of a

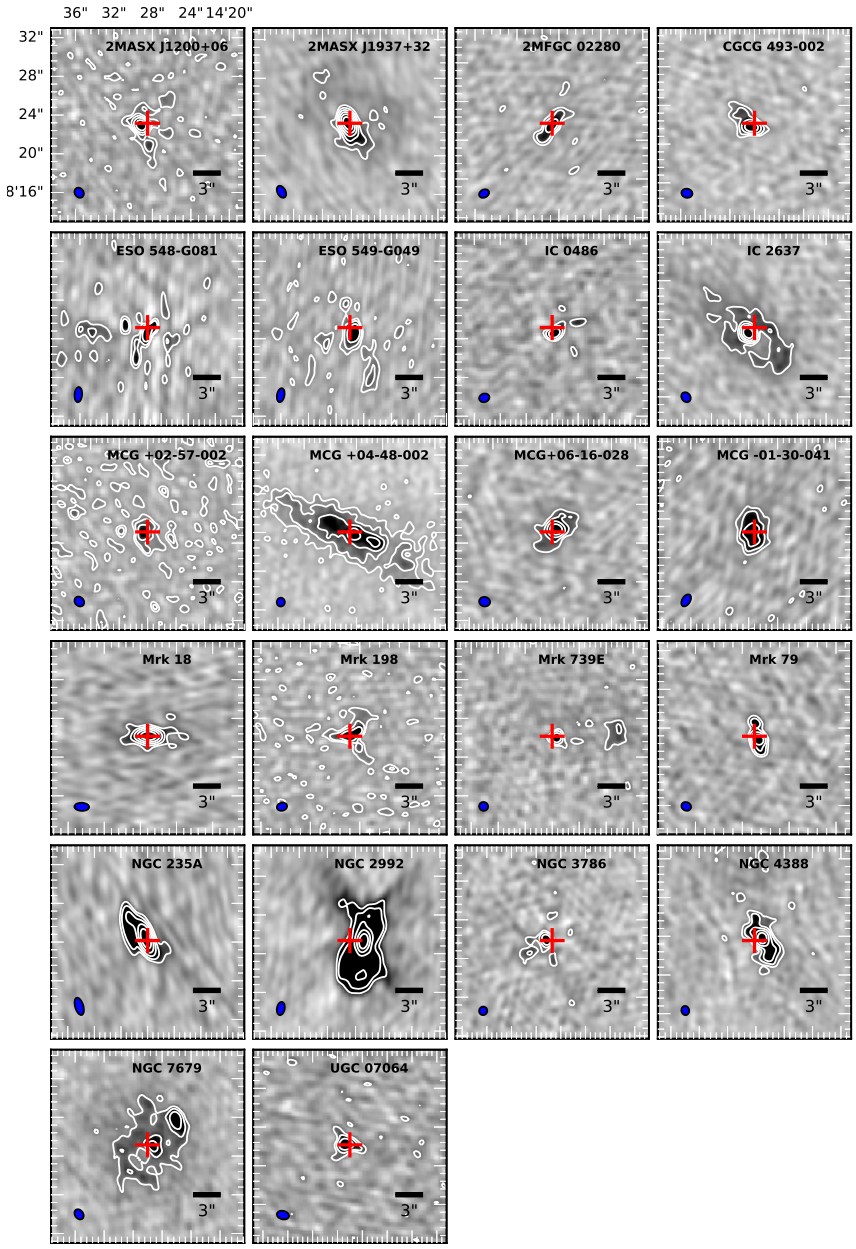

Figure 2.1: Radio continuum images at 22 GHz of the 22 radio-quiet BAT AGN with well-resolved, non-jetlike extended morphologies. The FWHM of the beam for each observation is shown in blue in the lower left corner of each image. Contours begin at 50% of the peak flux density, and decrease outwards by factors of two. A red cross is shown at the phase center of each image, as well as a 3″ scalebar. Major ticks correspond to 4″, as can be seen by the scale given in the first panel.

jet. Finally, we can look carefully at the higher ($\sim 0.3''$) resolution B-array images, if available, to further resolve the morphology.

Only six of our B-array follow-up images contained information which might affect the morphological classification of the objects in question. A comparison of the C-array and B-array images is shown in Figure 2.3. All but four of our sources categorized as core-dominated remained compact at the B-array's higher resolution. The four exceptions have slightly extended morphology in B-array: Mrk 279, Mrk 477, Mrk 766, and Mrk 926. For consistency with the rest of the analysis in which we have defined a core-dominated source as having no extended structure in our $1''$ resolution images, we do not alter their classification here. NGC 235A has a C-array morphology that could be interpreted as jet-like or star formation, while its B-array morphology shows significantly more clumping. Additionally, its extended radio flux density agrees with that predicted from the infrared star formation. These things together led us to classify it as an extended star formation object. Finally, UGC 11185 has ambiguous C-array morphology but is linear and jet-like in its B-array image, while also having an extended radio flux density in excess of the infrared star formation. We have therefore classified it as a jet.

There are two further objects that required greater scrutiny: 2MFGC 02280 and Mrk 79. Both have roughly linear structures that initially indicated a jet-like classification. However, their *Herschel* PSF-subtracted images have excess infrared emission roughly co-aligned with the radio structure, and their extended flux densities are consistent with that expected from star formation. These factors together led us to classify these as extended, rather than jet-like. However, the reader should

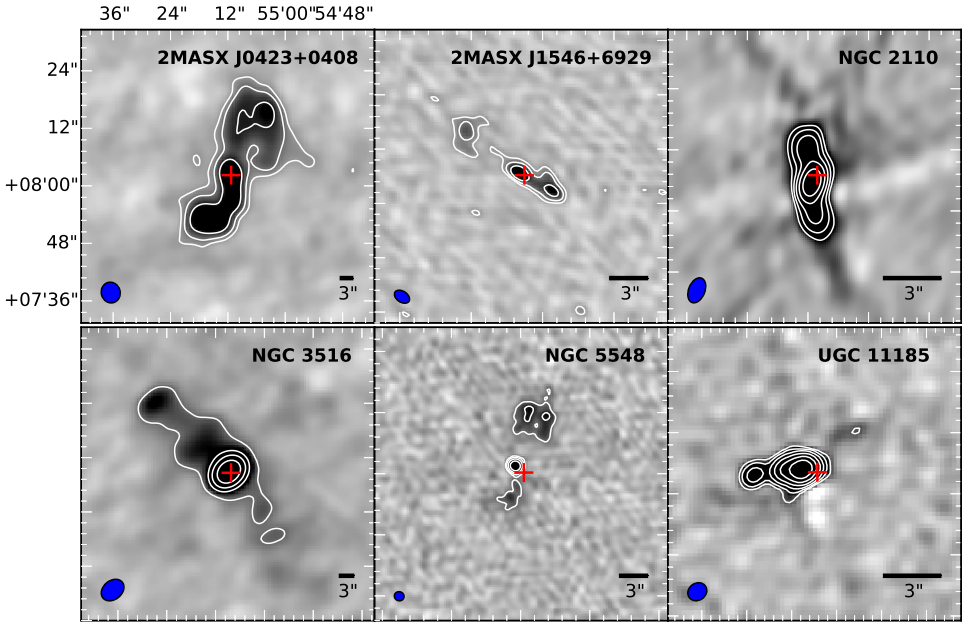

Figure 2.2: Radio continuum images at 22 GHz of the 6 radio-quiet BAT AGN with well-resolved, jetlike morphologies. The synthesized beam for each observation is shown in blue in the lower left corner of each image. Contours begin at 50% of the peak flux density, and decrease outwards by factors of two. 2MASX J0423+0408 and NGC 3516 are shown in 3″-tapered images to improve visibility of the jetlike structure. A 3″ scalebar is provided in each image, as different zooms were chosen based on the morphology. A red cross is shown at the phase center of each image.

bear in mind these considerations throughout the work.

We note that all objects with a significant excess of radio emission over that predicted from the infrared star formation have linear, jet-like morphologies (see Section 2.5.2). The amount of extended radio emission compared to that predicted from the *Herschel* observations was used to help classify only the small handful of cases where the morphology was not clearly jet-like or indicative of star formation, not as a primary classifying factor. We also note that while morphology cannot reliably differentiate between a jet and an AGN-driven wind [Harrison et al., 2015], we only wish to distinguish between radio emission from extended star formation and from AGN-related sources; those sources may be either jets or AGN-driven outflows without affecting our general analysis.

We conclude by noting that only six of our objects are host to arcsecond-scale jets. Importantly, this is only a small fraction of our sample; it is therefore inaccurate to assume that the unresolved emission in lower resolution surveys such as NVSS ($\theta \sim 45''$) and FIRST ($\theta \sim 5''$) is due entirely to scaled-down cousins of the large synchrotron jets of radio-loud AGN. See Section 2.6 for a more detailed discussion of our observations' implications for the origin of radio emission in radio-quiet AGN.

2.5 Testing the FIR-Radio Correlation

2.5.1 Radio and IR Flux Decomposition

Far-infrared (FIR) continuum flux is frequently used as a star formation tracer, and it is nearly always assumed that the FIR emission comes exclusively from star

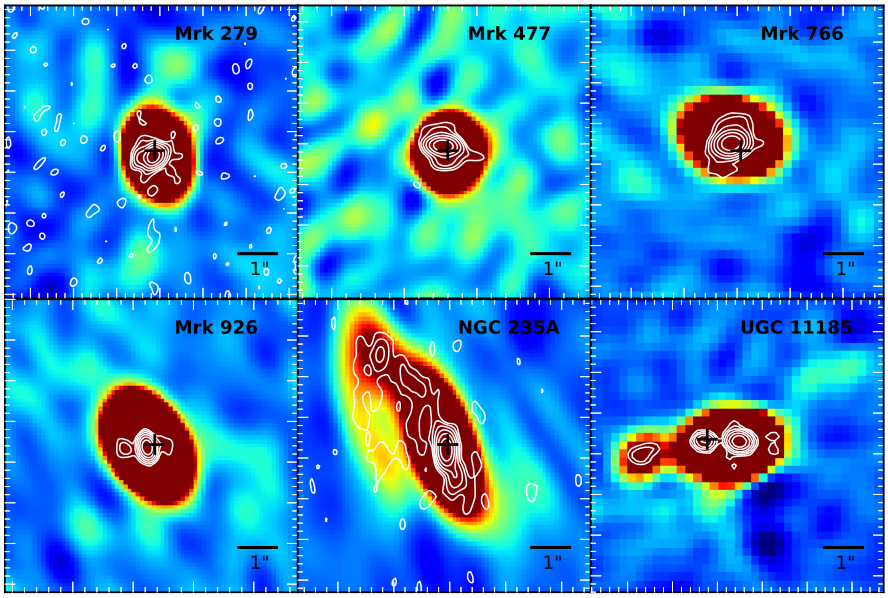

Figure 2.3: C-array images with 1″ resolution are shown in color in the background, while foreground contours show B-array 0.3″ resolution images overlaid. These six objects are those for which the B-array images added morphological information to that obtained from C-array. Scalebars are shown in the bottom right of each image, and a black plus sign is given at the phase center of each B-array observation.

formation, with no contribution from the AGN. However, our recent *Herschel* observations have shown that the AGN can contribute significantly to the mid-to-far IR *Herschel* SEDs. We have successfully separated the AGN and star formation components using SED decomposition for all 313 *Swift*-BAT AGN with *Herschel* data, which is discussed in detail in the appendix of Shimizu et al. [2015]. We provide a brief description here, including example SED fits for the reader.

Briefly, we are able to model the far-IR *Herschel* spectra using two components, following the methodology of Casey et al. [2012]. The first component is an exponentially cut-off mid-IR power law to model dust in the torus heated by the AGN as the superposition of many hot dust blackbodies, and has the form $F_\lambda \propto \lambda^\alpha \mathrm{e}^{-(\lambda/\lambda_{\mathrm{turn}})^2}$. The second component is a standard modified greybody, $F_\nu \propto \nu^\beta B_\nu(T)$, with dust emissivity spectral index β and temperature T, which models well the FIR emission from star formation. The fitting was done using a Levenberg-Marquardt χ^2-minimization algorithm and utilized all IR wavebands with at least a 5σ detection. As a sample of the fitting results, we show four of our BAT AGN SEDs in Figure 2.4.

To predict the 22 GHz emission due to star formation, we assume all of our sources follow the empirical FIR-radio correlation found by Condon [1992]. Equation 14 from Condon [1992] allows us to convert the FIR emission into a 1.4 GHz flux density. We use 60 and 100 μm flux densities based only on the best fit modified greybody component from our SED modeling. This removes any AGN contribution and provides a pure star-forming FIR flux density. In order to extrapolate from

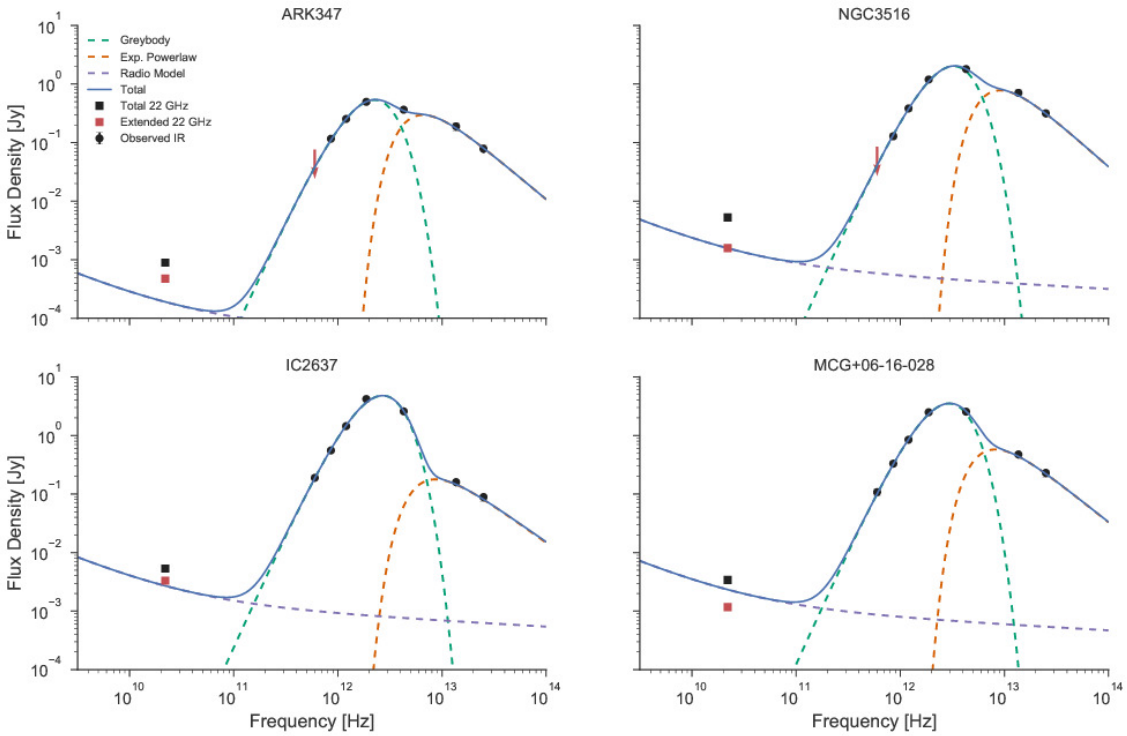

Figure 2.4: Decompositions of the *Herschel* FIR SEDs for four representative objects in our sample: Ark 347, a core-dominated object with higher radio flux than predicted with a likely AGN contribution to the core; NGC 3516 and IC 2637, extended cases where the model prediction matches the observed extended flux; and MCG+06-16-028, an extended object where there must be star formation within the compact core, since the extended emission alone falls below the prediction. The modeled AGN contribution is given as an orange dashed line, and the contribution from star formation is shown as a green dashed line. The purple dashed line shows the radio flux density predicted from the FIR-radio relation from the star formation component. Pink arrows denote upper limits. Error bars on the observed infrared points are smaller than the points in this log-log scaling.

1.4 GHz to 22 GHz, we first use the approximation of Condon & Yin [1990]:

$$\frac{S}{S_T} \sim 1 + 10(\frac{\nu}{\mathrm{GHz}})^{\alpha_{\mathrm{brem}}-\alpha_{\mathrm{synch}}} \tag{2.1}$$

to estimate the fraction of bremsstrahlung (S_T, thermal emission) and synchrotron radiation at 1.4 GHz. We then extrapolate both components to 22 GHz assuming a spectral index of α_{synch}=0.8 and α_{brem}=0.1 for the synchrotron and bremsstrahlung components, respectively, where flux density $S_\nu \sim \nu^{-\alpha}$.

As a sample of the fitting results, we show four cases in Figure 2.4: an object with observed radio emission exceeding that expected from SF (Ark 347), in which case we may assume the excess arises from the AGN; two examples in which the extended radio emission matches that predicted for pure star formation (IC 2637 and NGC 3516); and one case for which the predicted flux density falls between the total observed flux density and that of the extended emission, in which we can assume that there is additional star formation within the unresolved core, which was removed with the core subtraction (MCG+06-16-028). The next section examines how well the canonical FIR-radio relation predicts this extended emission for our entire sample.

2.5.2 The FIR-Radio Correlation for BAT AGN

Our high resolution maps allow us to spatially decompose the emission into circumnuclear extended structure and an AGN nuclear component, which we can then compare to the star formation flux density expected from the canonical and

oft-used FIR-radio correlation for normal galaxies from Condon [1992]. This allows us to determine whether star formation in the immediate environment of an active nucleus differs substantially from that in the wider host.

As described in Section 2.3, in order to fully capture the extended emission we subtract the core flux density measured in the 1″ image from the total 6″ flux density. This enables us to capture low surface-brightness emission that may not have been apparent in our higher resolution maps. It is this extended flux density, $S_{\rm ext} = S_{6''} - S_{\rm core}$, that we test against the radio flux density expected from SF via the Condon [1992] relation, using the FIR SF component calculated with our SED modelling (see Section 2.5.1). The values are given in Table 2.1.

Figure 2.5 plots the observed radio flux density compared to that predicted from star formation both before (left) and after (right) removal of the central core source. If we consider the entire flux density in the 6″ image, the radio flux density is systematically higher than that predicted from the star-formation component of the FIR SED. The BAT AGN therefore lie above the FIR-radio correlation when the total 22 GHz radio flux density is included. This is a similar conclusion to that reached by Zakamska et al. [2016], who found that radio-quiet quasars and star-forming galaxies fall on two distinct FIR-radio relations, with the quasars having substantially higher radio fluxes. Older studies like Sopp & Alexander [1991] found that radio-quiet Seyferts tend to lie on the same FIR-radio luminosity relation as inactive late-type galaxies, albeit in much lower resolution observations. Rosario et al. [2013] also found that radio-quiet Seyferts occupied a similar mid-IR/radio phase space as normal star forming galaxies. However, all of these samples were

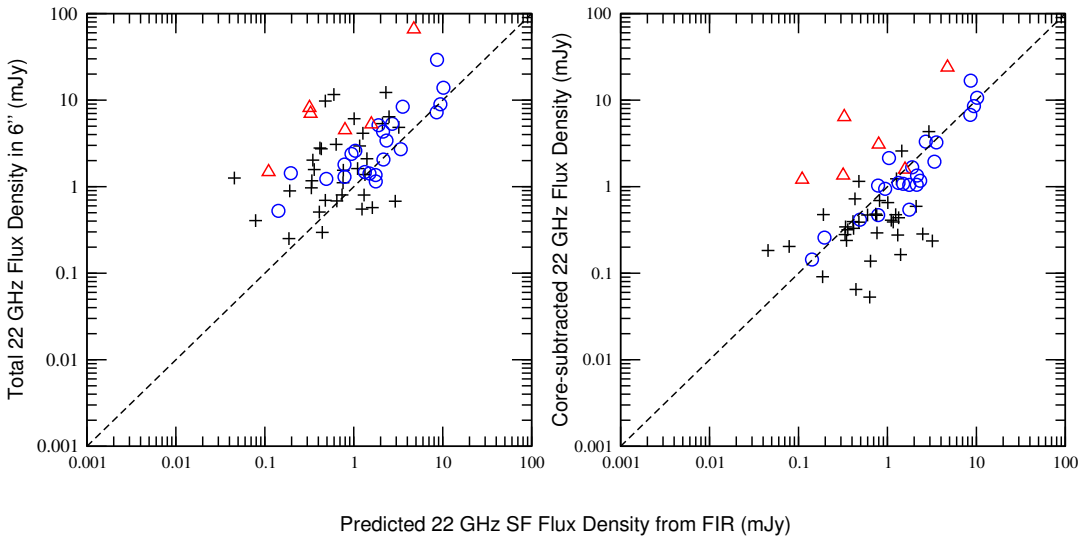

Figure 2.5: The observed 22 GHz flux density versus the predicted flux density from star formation based on our SED fitting (Section 2.5.1) for the full 6″ taper (left) and for the 6″ taper with the unresolved 1″ core flux density removed (right). The dashed line is 1-to-1. Symbols correspond to jet-like sources (red triangles), extended sources (blue circles), and compact sources (black plusses).

optically-selected and may suffer from biases not present in our hard X-ray selected sample. Wong et al. [2016] found that their sample of BAT AGN lie on the FIR-radio correlation; however, they used the total 60μm luminosity from *IRAS*, rather than decomposing the full FIR SED into an AGN and SF component, in order to directly compare to the 1.4 GHz vs. 60μm luminosity relation from Yun et al. [2001]. Had they removed any AGN contribution to their 60μm luminosities, the radio flux densities observed would have been above what was expected from the FIR-radio correlation, consistent with our result.

The right panel of Figure 2.5 demonstrates the effect of removing the core radio component. The sources behave differently based on morphology. Most of the jets, as expected, remain above the expected emission from star formation. The core-dominated sources fall both above and below, but mainly below. Objects that have higher flux densities than predicted can be attributed to radio jet/outflow emission, which is perhaps not surprising since these are core-dominated sources. Those with less emission than predicted can be attributed to over-subtraction of star formation, since some of the core emission is likely due to star formation. Alonso-Herrero et al. [2016] showed recently that a number of Seyferts harbor star formation within an unresolved $\sim$0.3″ point source in mid-IR imaging, so it is likely that many of our radio cores contain some star formation.

Finally, one can see that the majority of objects with extended star formation morphology lie strikingly near the predicted value from the infrared star formation component. This information is also presented as a histogram in Figure 2.6, for easier visualization. The blue sample in the histogram (the objects with extended

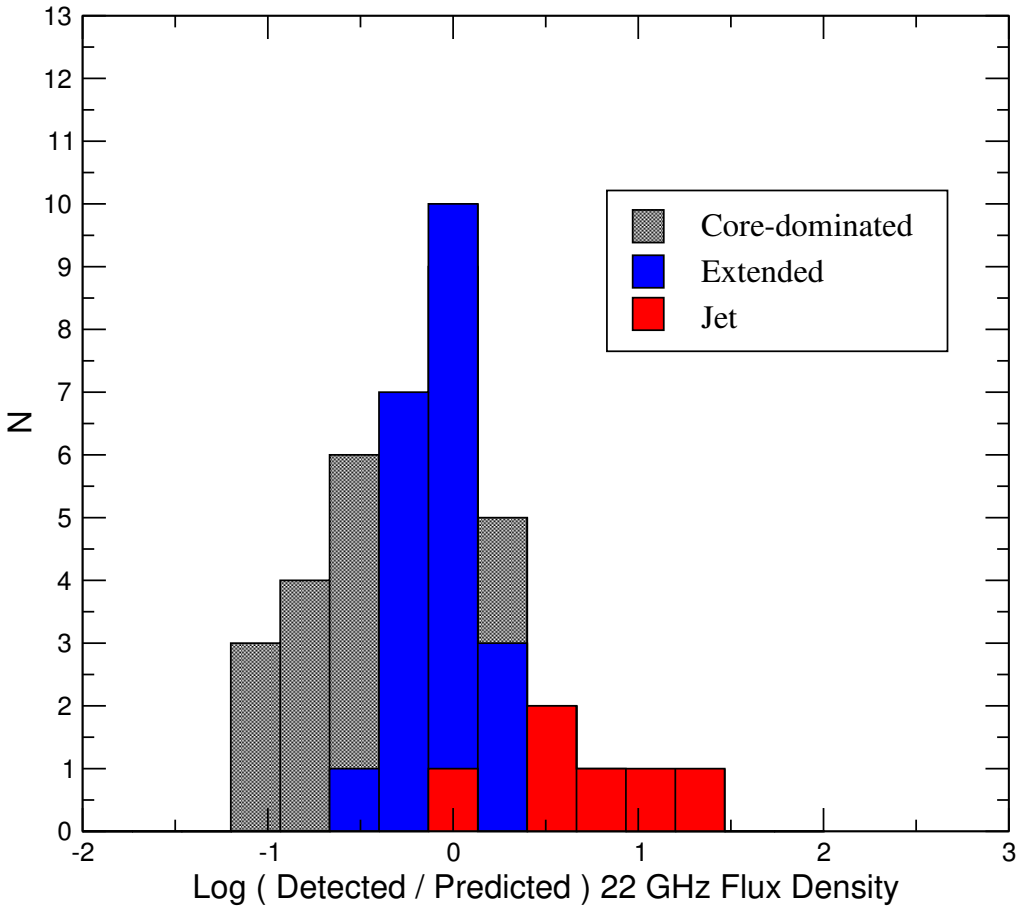

Figure 2.6: Histogram showing distribution of values of the ratio of predicted SF radio flux density from SED fitting to measured radio flux density in extended emission for various source morphologies. Objects near the center point are those for which the predicted value was closest to what was measured.

morphology) cluster around a ratio of detected vs. predicted flux density of unity. We therefore conclude that once the unresolved AGN contribution to the 22 GHz and FIR flux is removed, the star formation within 75-1000 pc of the nucleus adheres to the predictions of the canonical FIR-radio relation for our sample of radio-quiet, X-ray selected AGN. Our conclusion is consistent with the results of Baum et al. [1993], but inconsistent with the result of the subtraction of $\sim 0.1''$ cores by Roy et al. [1998], who found that the core removal did not improve the relation. However, inspection of their Figure 1 shows that while the scatter in the FIR-radio correlation did not improve after core subtraction, the sources do settle more evenly along the line, similar to our results. Therefore, although the radiation fields, star formation histories, or other factors may be different in the central few hundred parsecs than in the widespread galaxy, it does not significantly affect the physics which gives rise to the FIR-radio relation, and the infrared and radio properties of circumnuclear star formation in AGN is not manifestly different than in star forming galaxies.

Our results show that the FIR-radio relation applies in AGN, including their inner regions. They also confirm that the star formation component can be reliably decomposed and measured from the FIR SED. However, radio emission should not be used in high-redshift radio-quiet AGN to estimate the star formation rate, since spatial resolution will be inadequate to separate emission due to star formation and the AGN.

2.6 The Origin of Radio Emission in Radio-Quiet AGN

2.6.1 The L_X/L_R Correlation

Once it was established that even radio-quiet AGN tend to have radio cores, the origin of this core emission became a matter of debate. One early school of thought was that all of the radio emission in radio-quiet cores came from the same sort of relativistic jets that power the large, striking plumes of synchrotron emission seen in the Fanaroff-Riley classes [Fanaroff & Riley, 1974]. However, if all black holes are capable of launching synchrotron jets, and the emission from radio quiet AGN results simply from small, weak versions of such jets, one expects that radio loudness would be a smooth continuum across large AGN samples. The existence of such a smooth distribution was in doubt, since early studies concluded that the AGN radio-loudness distribution was bimodal [Strittmatter et al., 1980, Kellermann et al., 1989]. More recent work, however, has shown these claims to be incorrect [e.g., Condon et al., 2013]. Amongst luminous quasars, deep radio surveys have suggested a smooth distribution [White et al., 2000, Cirasuolo et al., 2003] and Brinkmann et al. [2000] saw no evidence for a bimodal luminosity distribution in the cross-matched ROSAT-FIRST catalog. Finally, Ballo et al. [2012] and Bonchi et al. [2013] found no evidence for a bimodal distribution in large samples of hard X-ray selected AGN of various Seyfert type. Although not bimodal, the radio luminosity distribution can be explained by the superposition of two populations, powered by different phenomena. Kimball et al. [2011] and Condon et al. [2013] have shown that

the radio-faint population may originate from star formation in the radio-quiet QSO host, an idea also put forward by Sopp & Alexander [1991] and Padovani [2011]. Padovani et al. [2015] found two very distinct populations of radio-quiet and radio-loud AGN in the *Chandra Deep Field*-South VLA sample, described by differing characteristic luminosity functions and Eddington ratios. Padovani et al. [2015] also showed that star forming galaxies begin to dominate the faint radio sky at about 0.1 mJy, which is the same value at which radio-quiet AGN begin to outnumber radio-loud AGN.

However, Zakamska et al. [2016] found that star formation alone was insufficient to explain the core radio emission in their sample of radio-quiet quasars. Our data allow us to isolate the core emission, having directly measured and removed the emission from extended star formation. This enables us to study the correlation of the nuclear radio luminosity with properties such as black hole mass and accretion rate and how they might constrain the physical origin of radio-quiet emission.

There are many reasons to expect a correlation between the X-ray and radio properties of an accreting compact source: the X-ray emission in radio-loud AGN could be interpreted as Compton up-scattered radio synchrotron photons; there are theoretical models postulating a fundamental connection between accretion flows and jet formation; accretion onto compact objects involves both hot accretion flows manifesting in synchrotron radiation of relativistic electrons as well as the launch of jets or outflows emitting synchrotron emission in the radio band; and so on. Indeed, an approximately linear correlation between X-ray and radio luminosity has been observed for many years, over a wide range of AGN bolometric luminosities [Canosa

et al., 1999, Brinkmann et al., 2000, Salvato et al., 2004, Panessa et al., 2007, Ballo et al., 2012]. Laor & Behar [2008] found that the Güdel-Benz relation for coronally active stars [$L_{\rm R}/L_{\rm X} \sim 10^{-5}$, Güdel & Benz, 1993] also held for ultra-luminous X-ray sources (ULXs), Seyfert nuclei and radio-quiet quasars, and suggested that therefore the origin of the $L_{\rm R}/L_{\rm X}$ relation is likely coronal. Further, Behar et al. [2015] found that the 95 GHz emission in a sample of eight radio-quiet AGN followed a $L_{\rm R}/L_{\rm X} \sim 10^{-4}$ relation, but that accounting for X-ray absorption could bring their sample into alignment with the coronal 10^{-5} value. Radio-loud AGN lie substantially above the relation, with $L_{\rm R}/L_{\rm X} \sim 1$, implying different physical origins [e.g., Behar et al., 2015, Balmaverde et al., 2006].

We first explore the correlation between the radio and X-ray luminosities. The 14-195 keV luminosities are taken from the *Swift*-BAT catalog. The radio luminosities are given as νL_{ν}, for consistency with previous studies [e.g., Laor & Behar, 2008]. Figure 2.7 shows the correlations between $L_{\rm X,14-195\ keV}$ and $L_{R,22\ \rm GHz}$ for the full 6″ integrated emission (i.e., including the extended star formation; left panel), the compact core only (middle panel), and the integrated 6″ emission minus that predicted from star formation by the infrared SED fitting (right panel). Regarding those luminosities given in the right panel, since we have shown that the infrared decomposition correctly predicts the radio emission from star formation, the difference between the total luminosity and the prediction for star formation must be attributable to the AGN. The Spearman rank correlation coefficients (ρ) and the slopes of the regression lines (μ) are also given. We note that the correlation coefficient for all three panels is very close to that found by Laor & Behar

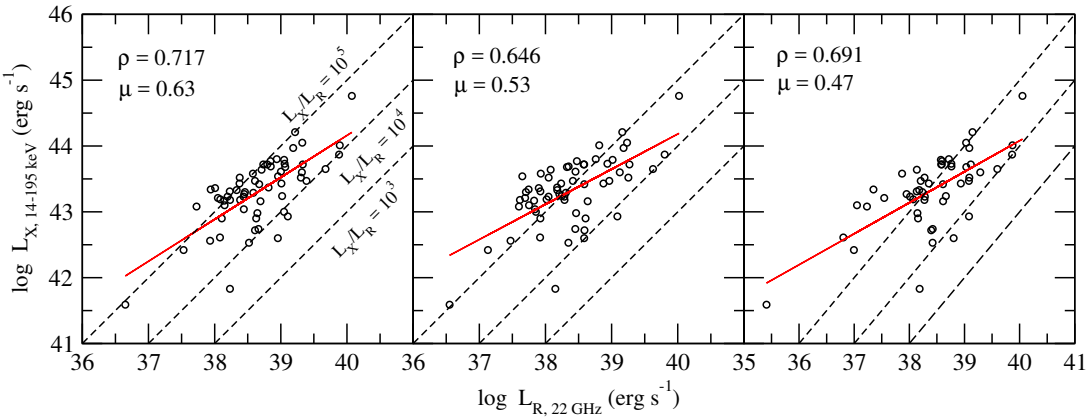

Figure 2.7: Hard X-ray versus 22 GHz luminosities for the total emission in 6″(left panel), the compact core emission density only (middle panel), and the 6″total emission minus that predicted from star formation from the infrared SED fits (right panel). The red lines show the best linear fit to the data. Dashed lines show the $L_X/L_R = 10^5$, 10^4, and 10^3, for comparison with previous studies (see text). The slope of each best-fit line (μ) and the Spearman rank correlation coefficient (ρ) are shown in each panel. For our sample sizes, the 1% probability of a chance relationship corresponds to $\rho \sim 0.3$, which is comfortably exceeded in each case.

[2008] for radio-quiet quasars ($\rho = 0.71$, see their Figure 2, top panel). The Spearman correlation coefficients all comfortably exceed the 1% probability chance value ($\rho_{0.01} \sim 0.35$).

Having established the correlations, we can compare the luminosity ratios to those predicted by various models. Our sources cluster between the $L_{\rm X}/L_{\rm R} \sim 10^5$ and 10^4 lines for the full 6″ emission, and around the $L_{\rm X}/L_{\rm R} \sim 10^5$ line for the core luminosity and the total minus the prediction for star formation. This is consistent with the coronal relationship found by Laor & Behar [2008] and Behar et

al. [2015]. None of the sources, even those with miniature jets (those in Figure 2.2) are anywhere near $L_{\rm X}/L_{\rm R} \sim 1$, despite a significant radio component coming from the jets. This may be because these jets are not scaled-down versions of the large, collimated relativistic radio jets studied in radio-loud samples, but are instead AGN-driven outflows with radio emission from either shocks or magnetic reconnection in a wind [Miller et al., 2006, Fukumura et al., 2010]. It should also be noted that the slopes of the best-fit relations are not significantly different in the panels showing the entire 6″ emission than in the core measurements. We therefore conclude that the $L_{\rm X}/L_{\rm R}$ relationship does not successfully distinguish between AGN-driven outflows (not including well-collimated relativistic jets) and star formation when interpreting radio emission in radio-quiet AGN.

2.6.2 The Fundamental Plane of Black Hole Activity

A scattered correlation between the radio luminosity, the X-ray luminosity, and the black hole mass in accreting systems, dubbed the "fundamental plane of black hole activity," has also been seen in many studies [Merloni et al., 2003, Falcke et al., 2004, Gültekin et al., 2009]. It takes the following form:

$$\log\, L_R = \xi_{\rm RX}\, \log\, L_X + \xi_{\rm RM}\, \log\, M + b_{\rm R} \tag{2.2}$$

Merloni et al. [2003] found values of $\xi_{\rm RX} = 0.60 \pm 0.11$ and $\xi_{\rm RM} = 0.78^{+0.11}_{-0.09}$ for the coefficients using a multivariate regression analysis, with a dispersion $\sigma_{\rm R} = 0.88$. They go on to use these measured values to constrain the physics of the

accretion flow, following a scale-invariant disk-jet coupling model, and conclude that the observations are most consistent with radiatively inefficient accretion flows, such as ADAFs, as the source of the X-ray emission in objects where $L_{bol}/L_{Edd} \sim$ a few percent. This scale-invariant model assumes that all of the accretion disk physics can be reduced to a single observable quantity: the radio spectral index. Merloni et al. [2003] provide an excellent summary of this analysis in their Section 5, while the full treatment can be found in Heinz & Sunyaev [2003]. Of course, such interpretations are based on the assumption that the radio emission comes from a scaled-down jet, which is difficult to reconcile with both the fact that AGN seem to follow the Güdel-Benz relation and our own discovery that only a small fraction of BAT AGN have jet morphology at high resolution. This is corroborated by studies in which the core emission in the small number of radio-quiet quasars with VLBI imaging remains unresolved even at milliarcsecond resolutions [e.g., Ulvestad et al., 2005]; however, there are not currently any similar VLBI studies of large AGN samples in our luminosity range. Merloni et al. [2003] used 5 GHz measurements from a broad literature sample, while our sample is at 22 GHz, as well as using 2-10 keV X-ray luminosities as opposed to our 14-195 keV BAT luminosities, so direct comparison of the observed coefficients is not appropriate. However, we here perform a parallel analysis to theirs, and propose that our ultra-hard X-ray luminosities may provide a more pure estimate of the true X-ray power of the AGN cores than the 2-10 keV emission, and may perhaps be more appropriate for fundamental plane predictions.

The matter of measuring black hole masses in AGN is tricky: $M_{BH} - \sigma_*$ measurements are notoriously unreliable [e.g., Dasyra et al., 2007], while dynamical

methods are impossible for AGN at our sample's distance. In order to minimize confusion, we have decided to use only the most reliable methods of M_{BH} measurement available. In order of reliability, these are: water maser emission, reverberation mapping, and the width of the broad Balmer emission lines. Two of our objects have water maser mass measurements: NGC 1194 [Greene et al., 2014] and NGC 4388 [Greene et al., 2010]. Nine of our AGN have reverberation estimates in the AGN Black Hole Mass Database [Bentz et al., 2015]. Measurements based on the doppler-broadening of the Balmer emission lines are less reliable, being subject to inclination modeling effects [Collin et al., 2006, Peterson, 2014]. However, we are including these measurements for the five of our Type 1 AGN with values in the literature to maximize sample size. The masses used for each object and the references from which we took the measurements are given in Table 2.2, along with the other parameters used to calculate the predicted fluxes. We have used these masses, our 22 GHz core luminosities and our BAT X-ray luminosities in Equation 2 to calculate the predicted radio luminosity for the scale-invariant jet model of Heinz & Sunyaev [2003]. The result is shown in Figure 2.8. Our observed 22 GHz core luminosities lie on a relation with a slope roughly consistent to that predicted by the fundamental plane at 5 GHz, but are systematically below the predictions. If the 22 GHz luminosities are systematically fainter than at 5 GHz, it is possible that the objects would shift upwards onto the relation. However, Merloni et al. [2003] point out that the scatter in the fundamental plane is likely to be explained by inherent scatter in the radio spectral indices α, so we do not attempt to scale our 22 GHz measurements to 5 GHz as we do not have spectral index information for the full

Table 2.2: Fundamental Plane Parameters

Name	Log M_{BH}	M_{BH} source	Log $L_{14-195keV}$ (erg s^{-1})	Log Predicted L_{5GHz} (erg s^{-1})
CGCG 229-015	6.91	RM[1]	43.31	38.10
IC 2637	7.00	Hα[2]	43.47	38.26
Mrk 279	7.44	RM[3]	43.97	38.90
Mrk 590	7.57	RM[3]	43.43	38.68
Mrk 739E	7.05	Hβ[4]	43.37	38.24
Mrk 766	6.82	RM[5]	42.9	37.78
Mrk 79	7.61	RM[3]	43.72	38.89
Mrk 817	7.59	RM[6]	43.79	38.91
Mrk 926	8.05	Hβ[7]	44.76	39.85
Mrk 975	7.23	Hβ[8]	44.05	38.78
NGC 1194	6.50	maser[9]	43.19	37.70
NGC 3516	7.40	RM[10]	43.33	38.48
NGC 4388	6.93	maser[11]	43.64	38.31
NGC 5273	6.66	RM[12]	41.59	36.87
NGC 5548	7.72	RM[3]	43.69	38.95
UGC 03478	5.90	Hβ[8]	42.61	36.89

Quantities necessary for and predicted by the fundamental plane of black hole activity as described by Merloni et al. [2003]. Sources of the black hole mass measurements are: [1]Barth et al. [2011a], [2]Greene et al. [2005], [3]Peterson et al. [2004], [4]Koss et al. [2011a], [5]Bentz et al. [2010], [6]Peterson et al. [1998], [7]Kollatschny & Zetzl [2010], [8]Botte et al. [2004], [9]Greene et al. [2014], [10]Denney et al. [2010], [11]Greene et al. [2010], [12]Bentz et al. [2014]

sample. The fact that our objects follow a similar relation to the fundamental plane relation is consistent with the recent result at 1.4 GHz from Wong et al. [2016]. In short, the 22 GHz core luminosities of the small subset of our objects with black hole mass measurements are systematically below, but conform to a similar relation, to those predicted by the scale-invariant jet model of Heinz & Sunyaev [2003], but are also broadly consistent with the coronal model supported by Laor & Behar [2008].

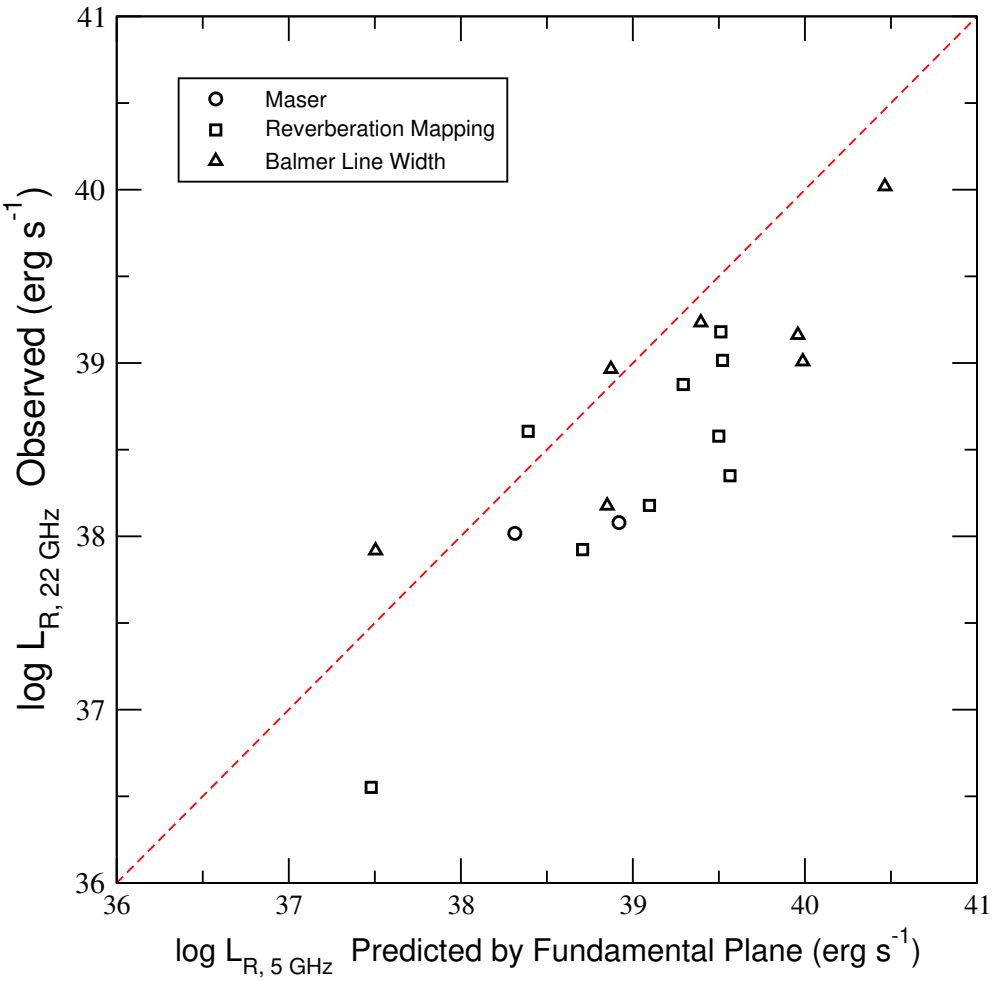

Figure 2.8: Plot of the core radio luminosities observed in our sample versus those predicted by the fundamental plane of black hole activity, with symbols differentiating the black hole mass measurement method used. The red dashed line indicates a 1-to-1 correspondence.

2.7 The Main Sequence of Star Formation and Feedback

There is a well-studied linear relationship between the total stellar mass of normal star-forming galaxies and their star formation rates (SFRs), which holds both locally and at moderate redshifts [e.g., Brinchmann et al., 2004, Salim et al., 2007, Rodighiero et al., 2010], and maybe even at high redshifts [e.g., Heinis et al., 2014, Pannella et al., 2015]. Since AGN host galaxies are well-known to lie in the otherwise sparsley-populated region between the blue, star forming sequence and the "red and dead" ellipticals on color-mass plots [e.g., Nandra et al., 2007, Silverman et al., 2008, Schawinski et al., 2009a], it was long thought that AGN host galaxies would fall below this "main sequence of star formation," since they should be in the process of heating and evacuating their molecular gas. Many of the first main sequence (MS) studies to include AGN did not find this, however; instead, AGN were found to lie mainly on the MS [Mullaney et al., 2012, Rosario et al., 2013]. Such a finding supports the idea of co-evolution of the host galaxy and the AGN, rather than ongoing interaction. Other studies have found that AGN hosts do indeed fall below the main sequence [Salim et al., 2007, Ellison et al., 2016], and that their loci on the SFR-M_* diagram are nearly perpendicular to the main sequence [Leslie et al., 2016]. Shimizu et al. [2015] found the same result for the BAT AGN: that they lie systematically below the star formation main sequence, and interpret this as evidence that AGN feedback reduces the amount of cold gas available for star formation and reduces the SFR of the entire galaxy.

2.7.1 Overview of Stellar Mass and SFR Measurement

Shimizu et al. [2015] compared the BAT AGN to the star formation main sequence as calculated from the *Herschel* Reference Survey [HRS; Boselli et al., 2010], a complete sample of ∼300 galaxies with a wide variety of morphological types and with photometry matching that of the BAT sample, and the *Herschel* Stripe 82 survey [HerS; Viero et al., 2014], which includes objects with higher stellar masses more consistent with the BAT sample.

The stellar masses (M_*) for the galaxies were calculated using the formula

$$\log(M_*/L_i) = -0.963 + 1.032(g - i) \tag{2.3}$$

from Zibetti et al. [2009]. This was the same equation used to calculate the stellar mass from the *Herschel* Reference Survey (HRS) by Cortese et al. [2012]. The $g-i$ color was calculated using the Koss et al. [2011b] photometry. This information was available for 41 of our sources.

The SFRs were calculated by fitting the *Herschel* SEDs with the Casey et al. [2012] model (see Section 2.5.1). Once the star formation contribution to the IR emission is isolated, the SFR is calculated using the following relation from Murphy et al. [2011]:

$$\mathrm{SFR_{IR}} = \frac{L_{\mathrm{IR}}[\mathrm{erg\ s^{-1}}]}{2.57 \times 10^{43}}, \tag{2.4}$$

where L_{IR} is the total infrared luminosity from 8-1000μm. In most of our sample, the FIR emission is unresolved by *Herschel*'s 6″ imaging. In our redshift

range, this scale corresponds to $\sim 0.5 - 6$ kpc. Our *Herschel* observations were sensitive to emission beyond this scale, and when such emission was observed it was included in the global SFR calculation. If there was significant extended emission in the host galaxies that was of insufficient surface brightness to be observed, our SFRs would be underestimated. To check whether such emission exists, we located several of our sources for which the *Herschel* archive had deeper observations, and then compared the radial profile from our observation against the archival one. There was no significant difference in any of the sources we compared, indicating that we are unlikely to be missing low surface brightness extended star formation in a majority of our sources. The stellar masses and SFRs of our sample used in this analysis are given in Table 2.3.

2.7.2 Radio Morphologies and the Main Sequence

We can now add our morphological information to the plot in Shimizu et al. [2015], since our sample was drawn from theirs. The result is shown in Figure 2.9. With one exception (Mrk 477), all jet-dominated and core-dominated sources are either within or well below the main sequence, while objects with nuclear star formation evident in our images reside on the main sequence.

Of the jet-like morphologies for which stellar masses are available, 4/4 objects fall more than 1σ below the main sequence, as well as 13/22 objects with core-dominated morphology, compared to only 3/15 objects with extended radio morphologies. All 9 sources more than 2σ below the main sequence are jet-like or

Table 2.3: Measured Star Formation Properties

Name	Log M_* $M_\odot$	Log SFR $M_\odot$ yr^{-1}
2MASX J0353+3714	9.89	0.225
2MASX J0444+2813	10.83	0.067
2MASX J1200+0648	10.93	0.677
2MFGC 02280	10.49	0.340
ARK 347	10.51	-0.083
CGCG 122-055	10.13	0.037
CGCG 420-015	10.82	0.345
IC 0486	10.75	0.629
IC 2461	9.47	-0.496
MCG +04-48-002	10.36	1.048
Mrk 1210	9.99	-0.026
Mrk 18	9.73	-0.049
Mrk 198	10.25	0.463
Mrk 279	10.77	0.581
Mrk 477	9.70	0.919
Mrk 590	11.06	0.564
Mrk 739E	10.65	1.024
Mrk 766	10.09	0.488
Mrk 79	10.79	0.600
Mrk 817	10.56	0.935
Mrk 926	11.20	0.862
NGC 1194	10.66	-0.686
NGC 2110	11.07	0.292
NGC 235A	10.71	0.820
NGC 2992	10.48	0.478
NGC 3081	10.45	-0.190
NGC 3516	10.83	-0.145
NGC 3786	10.23	0.083
NGC 4388	10.02	0.046
NGC 513	10.62	0.858
NGC 5231	10.71	0.457
NGC 5273	9.82	-1.229
NGC 5548	10.62	0.245
NGC 7679	10.16	1.174
NGC 985	10.89	1.042
UGC 03601	10.19	-0.099
UGC 07064	10.69	0.892
UGC 08327	10.80	0.951
UGC 11185	10.72	0.559
UGC 12282	11.37	0.544
UGC 12741	10.24	0.068

Total stellar masses and star formation rates measured as described in Section 2.7.1.

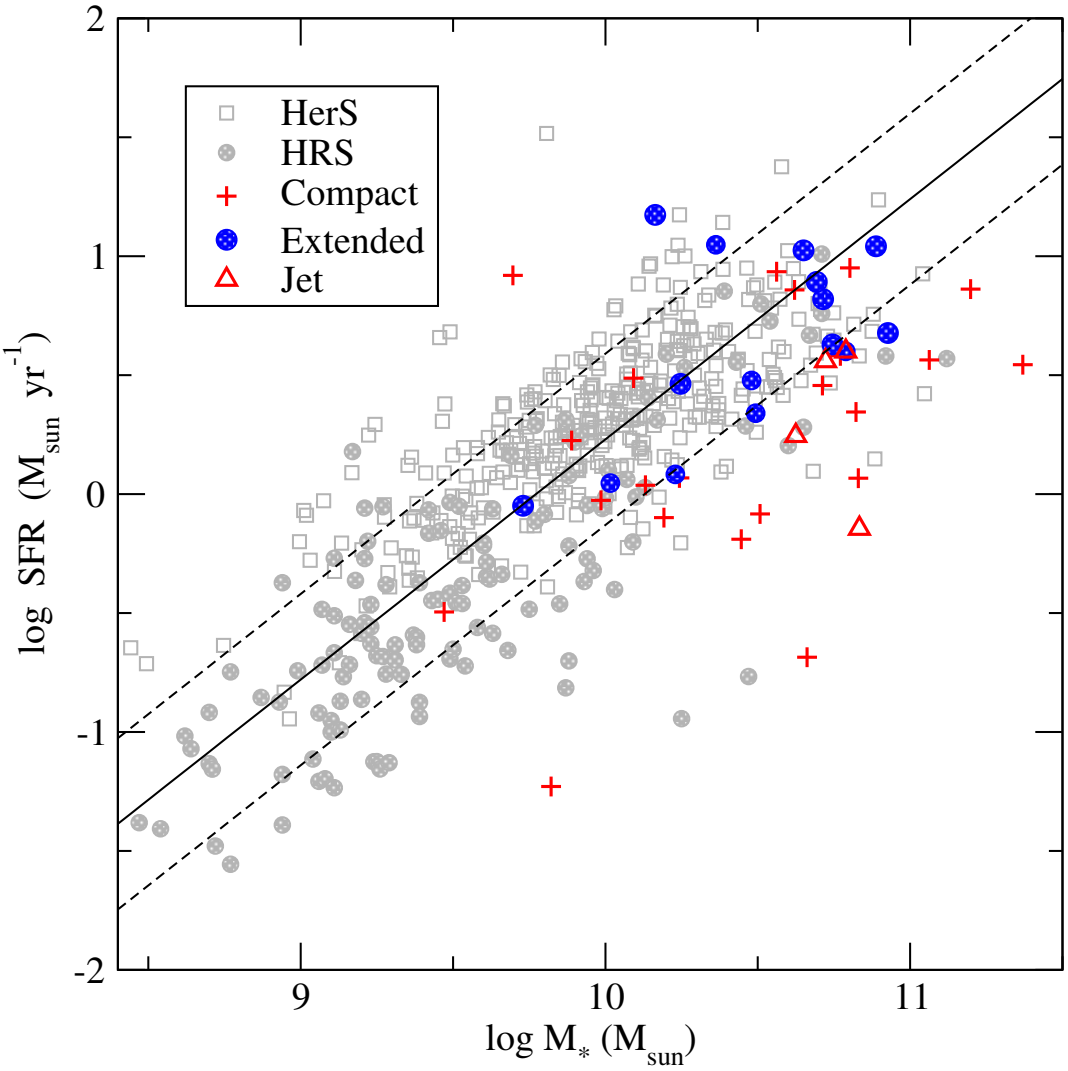

Figure 2.9: The relation between stellar mass and star formation rate for the *Herschel* reference survey (grey circles), *Herschel* Stripe 82 survey (grey squares) and BAT AGN with compact core-dominated (red plusses), extended (blue circles), and jet-like (red triangles) 22 GHz morphology. The solid line represents the best fit to the star formation main sequence derived in S15, and the dashed lines are the 1σ scatter.

core-dominated. This picture is somewhat complicated by the fact that NGC 4388 and NGC 2992, while they have extended non-jetlike morphology, are certainly dominated by AGN-driven outflows (see Section 2.4.2). These two objects lie within the main sequence on the plot.

Studies on the host galaxies of X-ray selected AGN, and indeed for the *Swift*-BAT AGN themselves, often find that they lie in the so-called "green valley", morphologically between the blue, star forming galaxy sequence and the "red dead" ellipticals [e.g., Nandra et al., 2007, Schawinski et al., 2009b]. In Shimizu et al. [2015], this conclusion was borne out: the objects lie below the main sequence of star formation, but not as far below as red ellipticals. The interpretation has often been that these galaxies are in the process of transitioning between the two regions through ongoing star formation quenching. Our results suggest that when an AGN core or a jet dominates the arcsecond-scale radio morphology, the global host star formation tends to lie below the star forming main sequence. We have proposed a large VLA follow-up program to image BAT AGN chosen explicitly to lie below the main sequence to confirm this result.

2.8 Conclusions

We have imaged 62 radio-quiet ultra-hard X-ray selected AGN using the VLA, resulting in 22 GHz maps with 1″ spatial resolution. The results and implications are described here.

1. We find that the extended radio emission has a diverse range of morpholo-

gies, including circumnuclear star formation rings, amorphous patchy star formation, and miniature radio jets or outflows. It is therefore not appropriate to assume that all radio emission in lower-resolution imaging surveys of radio-quiet AGN is produced by small synchrotron jets.

2. After decomposing the FIR SED into AGN and SF components, we have compared the 22 GHz flux density of the spatially resolved star formation to that predicted by the FIR-radio correlation, and found that it matches very closely. We conclude that the FIR-radio correlation holds in the circumnuclear AGN environment, but that care must be taken to remove the AGN contamination *from both the FIR and radio emission* before it is applied. Consequently, radio emission in radio-quiet AGN should not be used to calculate star formation rates at high redshifts, when spatial decomposition is not possible.

3. We have compared our isolated core radio luminosities to the BAT X-ray luminosities and found a strong correlation, as have previous studies. The correlation we find is consistent with a coronal origin for the radio emission in radio-quiet AGN. We have also found that the $L_{\rm R}/L_{\rm X}$ relation for our sample does not change significantly whether we are measuring the total 22 GHz radio luminosity, or only the central compact emission. The fact that $L_{\rm R}/L_{\rm X}$ does not differ wildly in our sample between jet-like morphologies (attributed to non-relativistic AGN outflows) and star formation indicates that using the ratio to distinguish between various mechanisms of radio emission in radio-quiet AGN is inappropriate, unless one is trying to identify strong relativistic jets. We have also predicted the expected radio luminosities of our sources using the fundamental plane of black hole activity, and found that our sample

is consistent with the scale-invariant jet model used in constructing the fundamental plane. The jet model has numerous drawbacks, including milliarcsecond imaging failing to resolve jets as well as the consistency of L_X/L_R all the way down to galactic black holes. Nevertheless, the small number of BAT AGN for which we have reliable $M_{\rm BH}$ measurements conform to the fundamental plane predictions.

4. The parent sample of our objects was found by Shimizu et al. [2015] to fall below the main sequence of star formation; that is, to have lower global star formation rates than normal galaxies at a given stellar mass. When we enhanced this study with our high-resolution radio morphological information, we found that the objects objects with extended radio emission tend to lie on the main sequence, while those below the main sequence exhibit compact or jet-like radio morphologies. This is the first direct connection between radio morphology and the location of AGN with respect to the main sequence of star formation, and may be evidence of ongoing star formation quenching.

Acknowledgements

We acknowledge Peter Teuben and Kartik Sheth for assistance with CASA data reductions, as well as Heidi and Drew Medlin for their prompt and useful assistance in VLA observations scheduling. We also acknowledge Sylvain Veilleux and Ehud Behar for many helpful conversations. KLS is grateful for support from the National Radio Astronomy Observatory (NRAO). The NRAO is a facility of the

National Science Foundation operated under cooperative agreement by Associated Universities, Inc.

Chapter 3: KSwAGS: A *Swift* X-ray and UV Survey of the *Kepler* Field

3.1 Introduction

The *Kepler* mission was designed to detect exoplanets in the habitable zone by searching for repeating transits in the light curves of over 150,000 sunlike stars. The exceptional photometric and temporal precision, high duty cycle and rapid, continuous sampling required for this task make *Kepler* a unique asset for the study of various other astrophysical targets in its 100 square-degree field of view (FOV). To detect exoplanets with up to year-long orbital timescales, *Kepler* remained continuously pointed at a region of the sky in the constellation Cygnus, chosen for its high density of observable dwarf stars. During its prime mission, *Kepler* collected hundreds of thousands of light curves for sources over baselines of a few months to 4.25 years by telemetering "postage stamps" of pixels around chosen stars and sampling with 30-minute cadence. In addition to high precision light curves, *Kepler* also produces Full Frame Images (FFIs), 29.4-minute exposures of the entire FOV, approximately once per month. The *Kepler* Science Center maintains that the full field contains $\sim$10 million stars above the confusion limit of 20-21 mag, and

the FFIs can provide photometry on monthly cadences for all objects in the *Kepler* FOV, regardless of whether high-cadence light curves were collected. This rich data set includes previously unidentified variable astrophysical sources over an impressive range of distance scales, both within the Galaxy and throughout the larger universe. Sources within the Milky Way include RR Lyrae stars [Guggenberger, 2012], rapidly oscillating peculiar A (roAp) stars [Balona et al., 2013], and cataclysmic variables (CVs) [Scaringi et al., 2013].

Optically variable extragalactic sources such as Seyfert 1 galaxies [Mushotzky et al., 2011] and BL Lac objects [Edelson et al., 2013] are tantalizing candidates, since the accretion physics in active galactic nuclei (AGN) is poorly understood. The size scale of the accretion disk is approximately $\leq$ 0.01 parsecs, or $\sim$1 milliarcsec for even the nearest active galaxies. Such a measurement is still well below resolvable scales for any optical observatories. Variability studies are then the only direct probe of conditions within the disk itself, and consequently of the process of accretion. Theory predicts model-dependent light curve characteristics; for example, Reynolds & Miller [2009] predicted clear g-mode oscillations and characteristic frequencies in the power spectrum that correspond to local acoustic waves. One also expects that the characteristic timescales of the disk (i.e., the thermal, viscous, and dynamical timescales) would be evident in light curves with sufficiently rapid and regular sampling. *Kepler* provides the AGN community with its first opportunity to measure such effects in the optical.

Kepler's bounty of unprecedented high-precision light curves has resulted in its FOV being one of the best-studied regions of the sky. Objects in the KIC (*Kepler*

Input Catalog) overlap with the 2-Micron All-Sky Survey [2MASS; Skrutskie et al., 2006], the Wide-field Infrared Survey Explorer [WISE; Wright et al., 2010], and the Galaxy Evolution Explorer survey [GALEX; Martin et al., 2003]. Additionally, Everett et al. [2012] conducted an optical photometric survey of the field in the UBV bands. An X-ray survey of the Kepler field is therefore prudent, providing an important and unique resource for locating interesting variable objects in this field.

X-ray selection is an effective way to curate a sample of astrophysically interesting variable stars and extragalactic sources. To capitalize on the wealth of data for the objects in the *Kepler* field, both photometric and archival, we have conducted the *Kepler-Swift* Active Galaxies and Stars survey (KSwAGS), a *Swift* X-ray telescope (XRT) survey of four modules of the *Kepler* field that is approximately ten times deeper than the ROSAT All-Sky Survey [RASS; Voges et al., 1999]. We chose these four modules to lie along a line approximately perpendicular to the galactic plane, sampling a range of galactic latitudes. Additionally, the co-aligned *Swift* UV/Optical Telescope (UVOT) provides concurrent UV coverage for each KSwAGS pointing. We present here the first KSwAGS catalog of X-ray sources in the original *Kepler* FOV, their UVOT and archival data, and an introduction to the KSwAGS series of temporal analysis papers. This first phase of the KSwAGS survey detected 93 unique X-ray sources. This includes a number of known stellar variables and two previously identified AGN. For newly discovered sources, we present the best determination of the nature of the object via optical spectra, X-ray to optical flux ratios (f_X/f_V), the shapes of the broadband spectral energy distribution (SEDs), and, where possible, inspection of the optical light curves. Since the *Kepler* FOV

was chosen explicitly to be typical of the Milky Way galaxy, results should be widely relevant and offer a typical density of exotic variable sources near the galactic plane. This paper serves as an introduction to the survey, which is currently ongoing in the new *Kepler* (known as K2) ecliptic plane fields. The time variability physics and temporal analyses will be presented in the following chapter, focused separately on the stellar sources and the AGN.

This paper is organized as follows: in Section 3.2, we describe our X-ray and UV survey and the identification of the optical counterparts. Section 3.3 explains the various methods used to classify the sources as either stellar or extragalactic, and to categorize the sources based on their optical spectra or archival information. In Section 3.4, we provide samples of the light curves and analysis of a stellar source and an AGN, to exemplify the content of the follow-up papers dedicated to each of these samples. Section 3.5 describes our ongoing survey in the new ecliptic plane K2 fields, and the final section summarizes the products of the survey and future directions.

3.2 Survey Field and Source Detection

KSwAGS was conducted with the *Swift* X-ray Telescope (XRT), which operates in the 0.2 - 10 keV range with a sensitivity of 2×10^{-14} erg cm^{-2} s^{-1} in 10^4 seconds. The XRT field of view (FOV) is 23.6×23.6 arcmin [Burrows et al., 2005]. The co-aligned UV/Optical Telescope (UVOT) is sensitive to the 170-650 nm range and has a sensitivity of $B = 22.3$ in white light in 1000 seconds and a FOV of 17×17

arcmin [Roming et al., 2005]. The UVOT has six broad-band optical and UV filters; the KSwAGS survey uses the the near-UV *uvm2* filter (λ_c = 2246 Å), since the *Kepler* FOV is already well-studied in the optical. Additionally, the UVOT NUV filters suffer from a phenomenon known as "red leak," in which the NUV flux is artificially inflated by the counting of optical photons due to red tails in the filters' transmission curves. The *uvm2* filter has the smallest amount of red leak of the three NUV filters [Breeveld et al., 2011].

The entire *Kepler* FOV consists of 21 modules. KSwAGS covers four of these modules, outlined in red in Figure 3.1, and subtends ∼6 square degrees. The modules are roughly perpendicular to the galactic plane, decreasing in galactic latitude from Region 1 to Region 4. Each of the four modules is covered in 56 total pointings, indexed from 00 to 55, with each pointing lasting approximately 2 kiloseconds. Figure 3.2 shows the locations of the XRT and UVOT pointings on the sky; note the smaller UVOT field of view.

For source detection, the XRT raw images and exposure maps were analyzed using `XIMAGE`. The background was optimized and the sources were located using the task `detect` with a S/N $\geq$ 3, making use of the `bright` qualifier. The `bright` flag creates a weighted mean of each excess and optimizes the point-spread function (PSF), preventing the detection algorithm from erroneously interpreting one large source as several smaller "detections"; however, note that if two *real* sources were within the optimized PSF, our method would report only one source.

After removing duplicate sources from pointing overlaps and eliminating detections of extended emission from single sources, we have detected 93 total X-

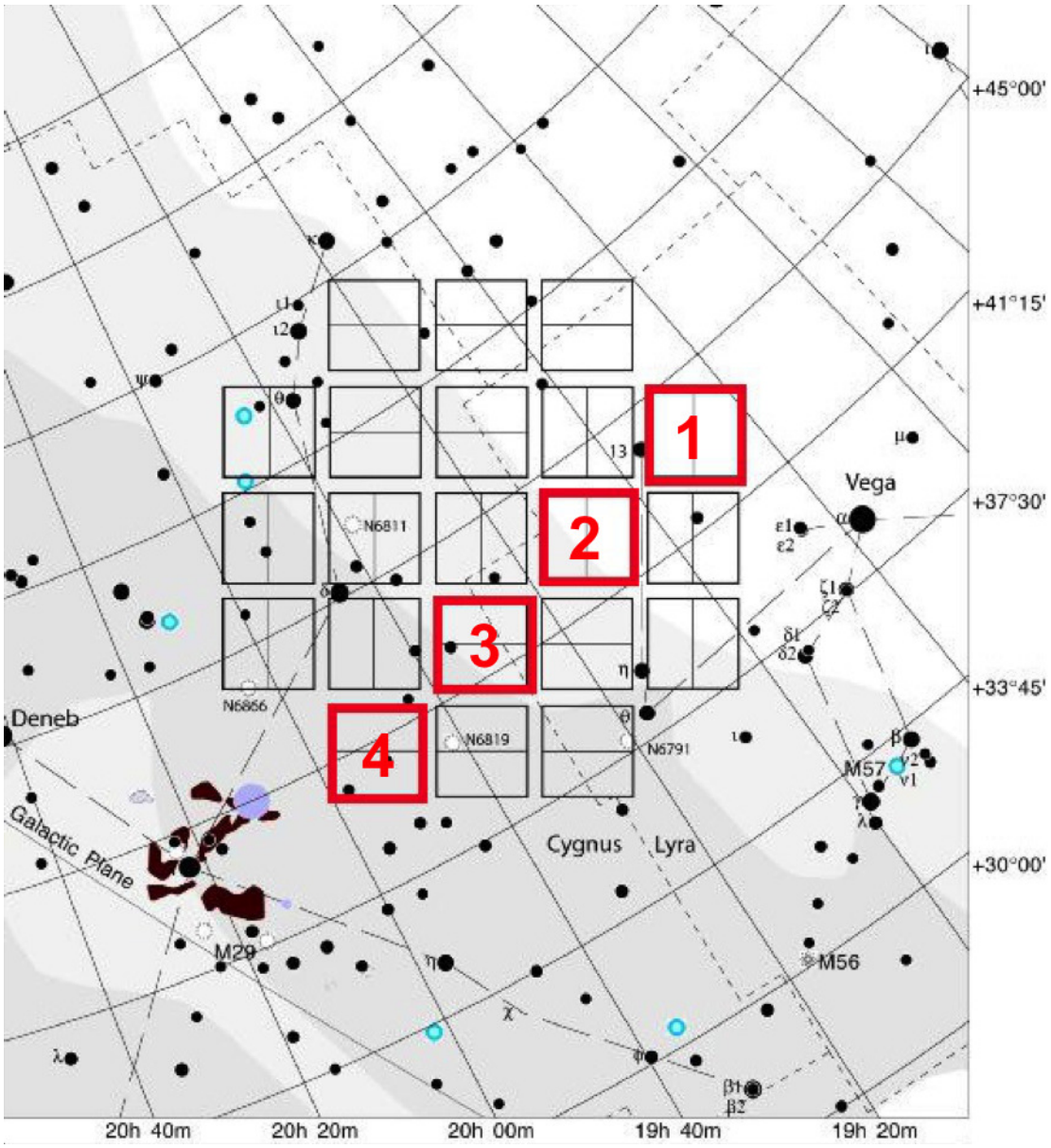

Figure 3.1: Map of the *Kepler* FOV, with the *Swift*-surveyed modules outlined in red. Region 1 is the upper right module, with the regions increasing in number toward the galactic plane (bottom left).

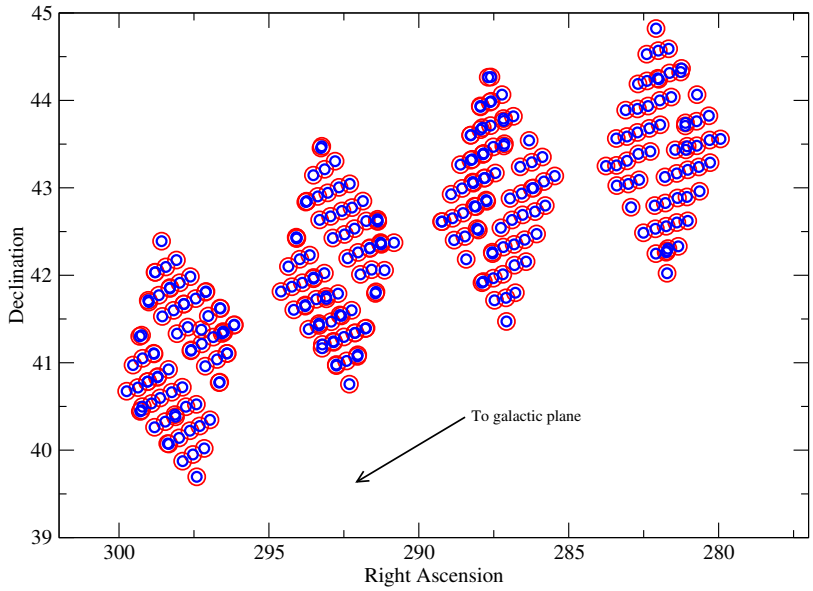

Figure 3.2: Arrangement of our XRT pointings (red) and UVOT pointings (blue). The UVOT FOV is approximately half the size of the XRT FOV. Overlapping circles occur when multiple pointings were required to obtain the full 2ks observation. The right ascension axis is inverted for easier comparison to Figure 3.1. Note that the shape of the UVOT FOV is actually roughly square, but is oriented at various angles within the larger XRT FOV. We use circles here to illustrate the approximate difference in UV/X-ray coverage.

ray sources with S/N $\geq$ 3, which corresponds to approximately 12 total counts or 0.006 cts s^{-1} within our narrow range of exposure times and background estimates. Table 3.1 lists these detections, as well each source's XRT count rate and exposure time. In this table, we assign each source an identifying number (KSw #) based on increasing right ascension. We will use this ID number to refer to the sources throughout the paper and in subsequent tables.

Table 3.1: *Swift* XRT and UVOT Sources in the *Kepler* FOV

Src	RA (X-ray)	Dec (X-ray)	Region	Pointing	Ct Rate	Exp Time (s)	S/N	RA (UV)	Dec (UV)	UVOT Flux (mJy)	Notes
1	280.9950	43.4720	1	12	0.0105	1829.18	3.839	280.9955	43.4743	8.075	
2	281.0685	43.6865	1	13	0.00691	1770.9	3.103	281.0698	43.686	0.004	
3	281.1287	43.2791	1	11	0.00803	1617.21	3.105	281.1273	43.2803	0.041	
4	281.2845	42.6883	1	16	0.00793	1722.52	3.146	281.2855	42.688	0.013	
5	281.5498	42.6175	1	16	0.0187	1720.15	4.963	281.5518	42.6183	0.007	
6	281.7771	43.6767	1	28	0.0168	1674.88	4.207				No UVOT data
7	281.8198	42.3348	1	24	0.011	1601.88	3.756	281.8209	42.3336	0.018	
8	282.1510	44.8243	1	32	0.0129	1668.11	4.184	282.1502	44.8241	0.024	
9	282.1965	42.7612	1	35	0.228	1589.43	18.11	282.1963	42.7609	0.031	
10	282.2645	43.7389	1	37	0.0125	1666.28	3.998				No UVOT data
11	282.3341	43.7350	1	37	0.0137	1888.35	4.43				No UVOT data
12	282.3970	43.7171	1	37	0.00752	1920.81	3.25				No UVOT data
13	282.6576	43.4456	1	43	0.0344	1940.96	7.538	282.6572	43.4447	0.390	
14	282.7376	42.9820	1	42	0.0205	1702.46	5.138	282.737	42.9819	1.130	
15	283.1236	43.6753	1	50	0.00853	1873.03	3.381	283.1242	43.6752	0.044	
16	283.4132	43.1623	1	52	0.00747	1933.13	3.158				Out of FOV
17	283.4805	43.4608	1	53	0.0121	1427.32	3.08				Out of FOV
18	283.5507	43.2023	1	53	0.0094	1702.04	3.388	283.5496	43.2029	0.071	
19	286.3436	43.4668	2	8	0.0104	1440.55	3.024	286.3436	43.4675	0.115	
20	286.3582	42.4609	2	10	0.257	1096.97	15.7	286.3581	42.4611	0.451	
21	286.5829	42.5433	2	11	0.0112	1767.65	3.69				Out of FOV
22	286.8068	41.5243	2	20	0.0796	1274.54	8.031				Out of FOV
23	286.8176	44.0189	2	16	0.122	1573.93	11.24				Out of FOV
24	287.0422	43.7961	2	24	0.0106	1863.42	3.92	287.0419	43.7962	0.009	
25	287.1229	42.3448	2	25	0.0118	1611.42	3.761	287.1238	42.344	0.123	
26	287.2791	44.1560	2	26	0.00793	1714.99	3.133				No UV CP
27	287.2975	41.5352	2	20	0.0184	1598.75	4.455				Out of FOV
28	287.7060	42.9274	2	36	0.0121	3357.91	5.152	287.7059	42.9268	3.410	
29	287.7355	43.5900	2	40	0.00531	3473.52	3.79	287.7359	43.5907	0.044	
30	287.8162	44.1634	2	35	0.00492	3035.28	3.361				Out of FOV
31	287.8831	42.8539	2	36	0.00565	2787.61	3.06	287.8829	42.856	0.008	
32	287.9496	42.0781	2	39	0.00375	3131.29	2.998				Out of FOV
33	287.9973	41.8501	2	39	0.0078	3349.98	4.565	287.9983	41.8504	0.020	
34	288.0440	43.1298	2	44	0.00906	2662.11	4.21	288.0438	43.1288	0.054	
35	288.2545	42.2036	2	47	0.0119	1629.74	3.688	288.2551	42.2034	0.120	
36	288.3293	42.4670	2	42	0.0303	423.119	3.138				Out of FOV
37	288.5651	42.0827	2	47	0.0344	1629.74	6.477				Out of FOV
38	288.5717	42.6082	2	49	0.0248	1649.34	5.6	288.5718	42.6089	0.046	
39	288.6929	42.3920	2	52	0.0134	1709.98	4.119	288.6932	42.3918	0.080	

Table 3.1 – continued from previous page

Src	RA (X-ray)	Dec (X-ray)	Region	Pointing	Ct Rate	Exp Time (s)	S/N	RA (UV)	Dec (UV)	UVOT Flux (mJy)	Notes
40	288.7612	43.3231	2	51	0.0155	1714.79	4.496	288.7613	43.323	0.060	
41	291.1622	42.7210	3	3	0.00728	1767.81	3.078				Out of FOV
42	291.3922	41.7268	3	4	0.0108	1711.13	3.846	291.392	41.7271	0.012	
43	291.5486	42.7656	3	3	0.0148	1379.1	3.989				Out of FOV
44	291.6264	41.5510	3	8	0.0841	1115.95	9.203				Out of FOV
45	291.6717	42.1556	3	6	0.00688	1751.02	3.12				Out of FOV
46	292.0210	42.0779	3	10	0.0066	1867.94	3.01				No UV CP
47	292.1626	41.7436	3	16	0.0101	1878.94	3.611				Out of FOV
48	292.1953	42.7736	3	15	0.00715	1836.44	3.109	292.1957	42.7734	0.009	
49	292.2361	43.0941	3	17	0.0261	1824.52	6.291	292.235	43.0936	0.204	
50	292.3142	42.6770	3	15	0.0116	1893.66	3.99	292.313	42.6764	0.027	
51	292.4233	41.2553	3	22	0.00643	1997.72	3.101				No UV CP
52	292.5009	42.2127	3	19	0.00669	1852.89	2.999	292.502	42.2138	0.165	
53	292.6304	42.8299	3	23	0.0148	1948.25	4.669	292.6299	42.8293	0.293	
54	292.6719	43.0381	3	25	0.00965	2027.3	3.918				Out of FOV
55	292.8015	43.2247	3	28	0.0331	1885.49	6.909	292.8021	43.2243	0.465	
56	293.0162	41.0456	3	37	0.0176	1095.07	4.012				Out of FOV
57	293.1699	42.8071	3	33	0.0136	1785.2	4.055	293.1702	42.8074	0.048	
58	293.1876	41.0621	3	37	0.00863	1573.6	3.3				No UV CP
59	293.2583	41.6922	3	42	0.00461	3048.38	3.052	293.2581	41.6923	0.016	
60	293.3043	43.1656	3	43	0.0141	1565.68	3.917	293.3041	43.1653	0.009	
61	293.4492	41.1218	3	37	0.0141	1433.14	4.118				Out of FOV
62	293.5059	41.3211	3	46	0.0248	2363.78	6.557	293.5067	41.3207	0.006	
63	293.6725	42.4138	3	45	0.0213	1475.13	4.429				Out of FOV
64	293.8478	41.2915	3	46	0.00992	2484.73	4.114				Out of FOV
65	293.9017	42.8962	3	47	0.0111	2231.23	4.395	293.9013	42.896	0.040	
66	293.9578	42.3660	3	51	0.00478	2707.55	3.142	293.9579	42.366	0.092	
67	294.0024	41.9892	3	49	0.00803	2040.93	3.407	294.0035	41.9896	0.015	
68	294.1042	42.4103	3	51	0.0115	2672.43	4.812	294.1045	42.4106	0.039	
69	294.1987	41.7921	3	53	0.00566	2544.91	3.224	294.2041	41.791	0.445	
70	294.3325	41.6892	3	53	0.00658	2544.91	3.11	294.3319	41.6852	2.700	
71	294.3559	41.7774	3	53	0.0204	2544.91	6.22	294.3562	41.7774	0.098	
72	294.4295	41.7054	3	55	0.00585	3116.57	3.366	294.43	41.7055	0.015	
73	296.4893	41.7504	4	3	0.0104	1948.69	4.04				Out of FOV
74	296.5844	40.7630	4	4	0.0102	2099.18	4.029				No UV CP
75	296.8341	40.9947	4	5	0.00906	1913.95	3.571	296.8311	40.9946	91.958	
76	296.9863	41.5419	4	8	0.0118	1781.26	3.856	296.9858	41.541	0.020	
77	297.0958	41.3399	4	6	0.0162	1883.6	4.416				Out of FOV
78	297.1825	39.9171	4	11	0.0132	1977.29	4.41	297.1835	39.9169	108.980	
79	297.3499	41.5886	4	17	0.0959	1822.85	11.45	297.3492	41.5892	0.021	

Table 3.1 – continued from previous page

Src	RA (X-ray)	Dec (X-ray)	Region	Pointing	Ct Rate	Exp Time (s)	S/N	RA (UV)	Dec (UV)	UVOT Flux (mJy)	Notes
80	297.3761	41.6051	4	17	0.00916	1871.98	3.457	297.3765	41.6054	0.009	
81	297.3857	39.6107	4	15	0.00652	1896.59	3.008	297.3849	39.6103	0.264	
82	297.5560	42.1157	4	20	0.012	1641.57	3.661				Out of FOV
83	297.7414	40.9773	4	19	0.0117	2939.39	5.362				Out of FOV
84	297.8264	41.3590	4	29	0.0259	1515.32	5.037				Out of FOV
85	297.8535	40.7351	4	26	0.00933	1792.64	3.514	297.8532	40.7355	21.210	
86	297.9148	40.1621	4	28	0.00922	1731.57	3.493				No UV CP
87	297.9698	41.6411	4	32	0.00926	1558.74	3.061				Out of FOV
88	298.4782	40.8922	4	43	0.00871	1525.06	3.182				Out of FOV
89	298.6474	41.4640	4	39	0.00835	1703.89	3.221	298.647	41.4643	2.831	
90	298.7180	41.9749	4	44	0.00662	1817.06	3.02				No UV CP
91	298.7625	40.9228	4	43	0.013	1710.56	4.163	298.7625	40.9219	0.311	
92	298.9334	41.9845	4	44	0.0301	1817.79	6.659				No UV CP
93	299.8686	40.7339	4	55	0.607	1634.21	28.82				No UV CP

On the *Swift* spacecraft, the XRT and UVOT are co-aligned to allow for simultaneous multiwavelength follow-up of GRBs detected onboard. To identify the counterpart in the simultaneous UVOT images, we overplotted a contour map of each XRT source onto the co-aligned UVOT image, and selected the counterpart visually. Once a counterpart is selected, we use the FTOOL `uvotsource` to obtain the UV source's position and flux density. This information is also given in Table 3.1. The UVOT FOV is approximately half the size of the XRT FOV, so some of our sources do not have UVOT counterparts listed because the XRT source was beyond the edge of the UVOT image. Note, however, that the overlap of our *Swift* pointings (see Figure 3.2) mitigates this problem to some degree, and so $\sim 65\%$ of our XRT sources have measurable UVOT counterparts.

Once all detectable UVOT counterparts had been identified, we looked up their optical counterparts in the *Kepler* Input Catalog (KIC). For our typical S/N ratio, the XRT can typically localize a source position to $3.5''$ with 90% confidence. Much of this uncertainty is due to the star-tracker attitude solution onboard the spacecraft [Goad et al., 2007]. Positional uncertainty can be reduced when a UVOT sky image is present. With a PSF of $2.5''$ for each filter and a pixel scale of $\sim 0.5''$, an uncorrected UVOT position is typically accurate to within $1''$ [Roming et al., 2005]. When stars in the UVOT field of view can be matched to the USNOB1 catalog, the aspect correction can result in UVOT positions that are accurate to within $0.5''$. Therefore, if the object has a UVOT counterpart, we use this position to query the KIC. An X-ray source might not be detected as UVOT source if it suffers from heavy extinction either from dust in the Milky Way or, in the case

of AGN, from innate host galaxy dust. This is certainly the case for KSw 93, Cygnus A, which is a very bright X-ray source but is also a Type 2 AGN. However, the majority of our sources without UVOT counterparts result from the relative FOV sizes between the XRT and the UVOT. Table 3.2 denotes which of these was the case. In the absence of a UVOT source, we query using the X-ray coordinates. The set of coordinates that was used to query the KIC is given for each source in Table 3.2. In 16 cases, an object had more than one possible KIC counterpart within 5″; the KSwAGS source number of each of these targets is indicated by an asterisk in Table 3.2. We have done a case-by-case analysis for each of these to determine which counterpart is the most likely. In the cases of KSw 2, 20, 35, 39, 55, 82, and 93, we have spectroscopically confirmed the listed KIC counterpart as an AGN (see Section 3.3.1). Since AGN are ubiquitously X-ray sources, we can be confident that this is the correct identification. In the case of KSw 85, the listed KIC counterpart is a known ROSAT source and active star, and KSw 35 is a spectroscopically-confirmed white dwarf. The remaining cases (KSw 19, 26, 37, 41, 45, 50, 72, and 77) are less certain; we determined the most likely KIC counterpart for these objects by overlaying UVOT and XRT contours on STSci-DSS III images and choosing the optical source most congruent with the available contour sets. Once determined, the KIC counterpart can then be used to obtain the flux ratio f_X/f_V (Section 3.3.2), magnitudes from various sky surveys in other wavebands to construct broadband spectral energy distributions (SEDs) (Section 3.3.3), and most importantly, all quarters of *Kepler* time series data for the source (Section 3.4).

Table 3.2: Broadband fluxes and properties of *Swift* sources

Src	KIC ID	Kep Mag	GALEX FUV	GALEX NUV	U	B	V	J	H	K	log f_X/f_V	Light Curve?	Query Coords	Angular Sep. (")	ID
1	7730305	9.32			180.96	414.91		735.34	572.66	389.7		Y	UV	2.58	Binary Star
2*	7868547	18.94										Y	UV	0.96	
3	7582708	19.18	0.019	0.021								Y	UV	0.3	
4	7091410	20.4				0.04	0.05				0.4		UV	0.6	
6	7869590	10.87	0.008	0.129	6.46	39.26	98.81	385.56	422.57	319.99	-2.61	Y	X	2.94	δ Cepheid[1,2]
7	6837514	19.67											UV	0.6	
8	8669504	18.95	0.007	0.011		0.02	0.04	0.24	0.33	0.32	0.7		UV	1.14	
9	7175757	18.13		0.036	0.07	0.08	0.1				1.54	Y	UV	0.3	BL Lac[3,4]
12	7939256	18.37	0.021	0.037	0.1	0.11	0.12				-0.02		X	3.6	
13	7732964	10.95			18.59	61.26	115.14	238.17	228.61	173.27	-2.36	Y	UV	1.8	Variable[2]
14*	7339343	11.52			18.72	49.02		116.65	94.08	64.14		Y	UV	1.44	Puls. Var[5]
15	7871931	18.86	0.016	0.035	0.06	0.07	0.07				0.22		UV	0.66	
16	7505473	16.22		2.669		146	573.86	30.99	33.42	29.07	-0.72	Y	X	4.92	
18	7587184	18.81		0.013	0.04			0.23	0.38	0.66			UV	0.6	
19	7739728	12.5		0.139	4.48	14.4	27.29	63.46	64.49	46.9	-2.26	Y	UV	0.24	Variable[2]
20*	6932990	11.13						4.22	5.9	0.32		Y	UV	0.3	Zw 229 (Sy1)[6,7]
22	6190679	9.03			41.27	225.71		1934.14	2035.64	1542.87		Y	X	0.78	K Star[8]
23	8153411	12.64			4.04	3.46	3.13	0.72	0.74	0.56	-0.25	Y	X	0.78	MV Lyr[9]
24	7948154	14.14			0.83	3.5	7.58	25.88	28.44	20.91	-1.69		UV	0.36	
25	6849023	18.32	0.041	0.104	0.13	0.18	0.2	0.23	0.36	0.51	-0.06		UV	0.54	
26*	8222218	20.27											X	1.56	
27	6191857	16.52			0.17	0.27	0.47	2.13	2.68	3.34	-0.25		X	0.96	
28	7350496	9.326	0.042	4.014	136.27			875.97	733.67	507.61		Y	UV	1.2	G Star
29	7811562	18.86			0.03	0.05	0.06				0.13		UV	0.3	
30	8223265	19.13			0.04	0.05	0.05				0.16		X	2.28	
31	7270227	16.43			0.23	0.52	0.85	1.22	1.2	0.79	-1.01		UV	0.78	
32	6594085	18.47				0.05	0.05						X	4.38	
33	6431946	19.36											UV	0.12	
34	7516296	18.73	0.015		0.05	0.05	0.07				0.31		UV	0.24	
35*	6766476	17.98			0.13	0.14	0.17						UV	0.12	
37*	6595746	19.48						0.83	1.01	1.45			X	1.74	
38	7107762	13			3.84	10.44	18.33	36.79	35.08	25.12	-1.71	Y	UV	0.54	
39*	6853073	18.27			0.12	0.16	0.18	0.23	0.32	0.69	0.04		UV	0.18	
40	7674095	18.09			0.07	0.06	0.06				0.56		UV	0.3	
41*	7198225	18.89					0.05				0.38		X	2.76	
42	6362752	19.02					0.03				0.66		UV	0.42	
43	7199582	19.52				0.04	0.04				0.69		X	4.08	
45*	6691018												X	2.28	

Table 3.2 – continued from previous page

Src	KIC ID	Kep Mag	GALEX FUV	GALEX NUV	U	B	V	J	H	K	log f_X/f_V	Light Curve?	Query Coords	Angular Sep. (")	ID
46	6606776	19.11											X	3.72	
47	6365080	11.45			29.81	63.79	92.73	112.64	94.08	66.55	-2.8	Y	X	1.8	Rot. Var.[5]
48	7201595	18.46		0.004									UV	0.6	
49	7446357	15.8			0.7	0.47	0.44	0.57	0.44	0.46	-0.06	Y	UV	0.72	V1504 Cyg[10]
50*	7119467	18.44											UV	2.46	
52	6779613	12.62	0.003	0.238	5.91	15.57	26.55	46.83	42.73	30.22	-2.44	Y	UV	0.24	γ Doradus[5]
53	7284688	11.23	0.007	0.395	14.97	41	70.28	121.25	109.22	76.48	-2.51	Y	UV	0.36	Ecl. Binary[5,8,11,12]
54	7447756	7.27			53.46			16191.55	24791.34	24050.85			X	1.5	M Star
55*	7610713	16.74						1.01	1.3	1.94		Y	UV	0.72	
56	5794742	17.65	0.027	0.051	0.11	0.12	0.23	1.04	1.56	1.76	0.05		X	1.68	
57	7286410	13.05			2.17	8.32	16.98	48.09	51.37	37.29	-1.93	Y	UV	0.06	Variable[5,8,13]
59	6289488	18.4											UV	0.6	
60	7532798	19.46			0.05	0.07	0.09				0.38		UV	1.98	
61	5881515	19.09											X	1.44	
62*	6047927	18.67						0.17	0.41	0.56			UV	1.38	
64	5966921	14.49			0.13	0.83	2.44	23.49	28.89	22.32	-1.23	Y	X	4.02	
65	7288925	19.06			0.07	0.09	0.1				0.21		UV	0.6	
66	6870455	7.66			36.44			11420.58	18702.51	14870.67			UV	0.48	K Star
67	6529378	13.82			1.07	4.7	10.93	38.7	42.73	32.5	-1.97	Y	UV	0.66	
68	6956279	19.12			0.04	0.05	0.06				0.49		UV	0.18	
69	6371741	14.5			2.13			4.29	2.85	1.95		Y	UV	0.66	
70	6293269	18.13				0	84.65	33.15	38.15	30.72	0.05		X	1.08	
71	6372268	11.44			6.15	27.67	63.16	229.56	260.56	189.12	-2.33	Y	UV	0.72	
72*	6372529	19.05											UV	0.54	
73	6380580	11.38			24.77	57.86	93.59	133.32	115.96	80.6	-2.79	Y	X	1.08	γ Doradus[5]
75	5724440	7.874						1808.37	1259.8	847.09		Y	UV	3.72	δ Scuti[14,15]
76	6224104	15.16			0.66	1.67	2.7	4.07	3.43	2.43	-1.2		UV	0.18	
77*	6062112	19.74											X	2.46	
78	4857678	7.01						5139.12	3759.24	2572.35		Y	UV	0.96	F Star[15]
79	6225816	10.34						671.26	709.09	538.93		Y	UV	2.76	Rot. Var.[5]
80	6305971	19.47					0.05				0.4		UV	0.36	
81	4585976	12.23			9.03	23.5	39.45	65.24	52.42	37.77	-2.62	Y	UV	0.036	γ Doradus[5]
82*	6714686	16.01						0.68	0.9	1.06			X	1.38	
83	5728924	18.16			0.06	0.06	0.09	0.5	0.82	1.26	0.27		X	4.32	
84	6065241	14.69			0.19	1.11	3.74	43.9	49.97	38.76	-1		X	1.68	
85*	5557932	8.14						2321.07	1901.52	1329.02		Y	UV	0.48	G Star
88	5646749	17.01				0.13	0.26	0.58	0.7	0.39	-0.31		X	0.36	
89	6150124	7.25						8695.38	8431.41	6085.98		Y	UV	0.6	G Star
91	5733906	11.83			11.55	32.96	56.18	106.39	100.9	73.71	-2.47	Y	UV	0.66	Puls. Var[16]
92	6550385	17.77			274.15	661.84	74.34	0.35	0.59	0.12	0.77		X	1.38	

Table 3.2 – continued from previous page

Src	KIC ID	Kep Mag	GALEX FUV	GALEX NUV	U	B	V	J	H	K	log f_X/f_V	Light Curve?	Query Coords	Angular Sep. (")	ID
93*	5568067	11.59						2.19	3.23	3.24		Y	X	1.26	Cyg A[17]

The nearest KIC counterparts to the X-ray / UV sources, out to a maximum separation of 5″, and their corresponding *Kepler* magnitudes and fluxes in the FUV and NUV (from *GALEX*), the optical *UBV* bands (from the Everett et al. [2012] survey) and the infrared (from 2MASS). All fluxes are shown in mJy. Also given are the f_X/f_V ratios plotted in Figure 3.5, whether an archived light curve is available in the KIC, whether the X-ray or UV coordinates were used to query the KIC, the angular separation between the query coordinates and the KIC source, and any identifications of the objects in NED or SIMBAD. The references for the IDs are as follows: [1]Schmidt et al. [2011], [2]Pigulski et al. [2009], [3]Kapanadze [2013], [4]Massaro et al [2009], [5]Debosscher et al. [2011], [6]Mushotzky et al. [2011], [7]Carini & Ryle [2012], [8]Gaulme et al. [2013], [9]Scaringi et al. [2012], [10]Cannizzo et al. [2012], [11]Coughlin et al. [2011], [12]Prša et al. [2011], [13]Slawson et al. [2011], [14]Catanzaro et al. [2011], [15]Uytterhoeven et al. [2011], [16]Balona [2012], [17]Baade & Minkowski [1954].

Of all 93 sources, 23 were already identified in the literature. We obtained optical spectra for an additional 30 sources on the 200-inch Hale telescope at Palomar Observatory during August 26-28 2014. These spectra were obtained using the double beam spectrograph (DBSP) with a slit width of 1″, equipped with the D-55 dichroic filter to split light between the blue and red arms. The blue arm used a 1200 mm^{-1} grating with R∼7700 and covered 1500 Å. The red arm used a 1200 mm^{-1} grating with R∼10,000 and covered 670 Å. We observed at least two spectrophotometric stars each night and arc lamp exposures were obtained before each source exposure at the source location. Red spectra were wavelength calibrated with a HeNeAr lamp and blue spectra with a FeAr lamp. While one night was clear and provided stable seeing at $\sim 1''$, our seeing deteriorated on the second night, restricting our observations to targets with optical magnitudes $M_V \leq 17$. Data reduction was done using IRAF two- and one-dimensional routines for spectroscopic data and produced a final one-dimensional spectrum for each observation. Optical spectra are further discussed in Section 3.3.1.

3.3 Characteristics of Sources

All sources are summarized in Table 3.2, which contains their most likely KIC counterparts; all available fluxes from GALEX, the Everett et al. [2012] *UBV* survey, and 2MASS; the X-ray to optical flux ratios; and whether or not the object has an archived *Kepler* light curve. We also provide any previous identifications of the sources in the literature or from the online databases of SIMBAD and NED.

KSwAGS has provided new X-ray and UV data for a highly diverse mix of stellar sources, including rapid rotators, pulsating variables, eclipsing binaries, and γ Doradus, δ Scuti, and δ Cepheid type stars. We have also detected the known Seyfert 1 AGN Zw 229-15, a catalogued BL Lacertae object, and the radio galaxy Cygnus A. From the literature identifications and our optical spectra, we know with certainty the optical counterparts of 53 sources total (57%). For 9 additional sources, we can confidently assess whether the counterpart is stellar or extragalactic using a combination of apparent magnitude (e.g., an object with $V \sim 8$ is too bright to be an AGN), f_X/f_V, $U-B$ color (e.g., a $V \sim 20$ source with a very high f_X/f_V is most likely to be an AGN), or broadband SED shape.

We expected that the relative fraction of stellar and extragalactic sources in a survey region would depend on the galactic latitude of the region. Figure 3.3 shows the distribution in our four observing modules of the 62 sources for which we can confidently state a stellar or extragalactic origin. As the modules approach the galactic plane, the number of stellar sources outpaces the number of extragalactic sources, as expected. The diverse methods of classifying these sources prevents a robust analysis of the error; we display the trend only to illustrate the survey contents.

Below we outline the various methods used to classify the survey sources as either stellar or as AGN. Briefly: optical spectra are the most certain form of classification, but we do not have spectra for all KSwAGS targets. The X-ray to optical flux ratio offers a fairly stringent characterization at its extreme ends, but is degenerate at intermediate values. Broadband spectral energy distributions (SEDs)

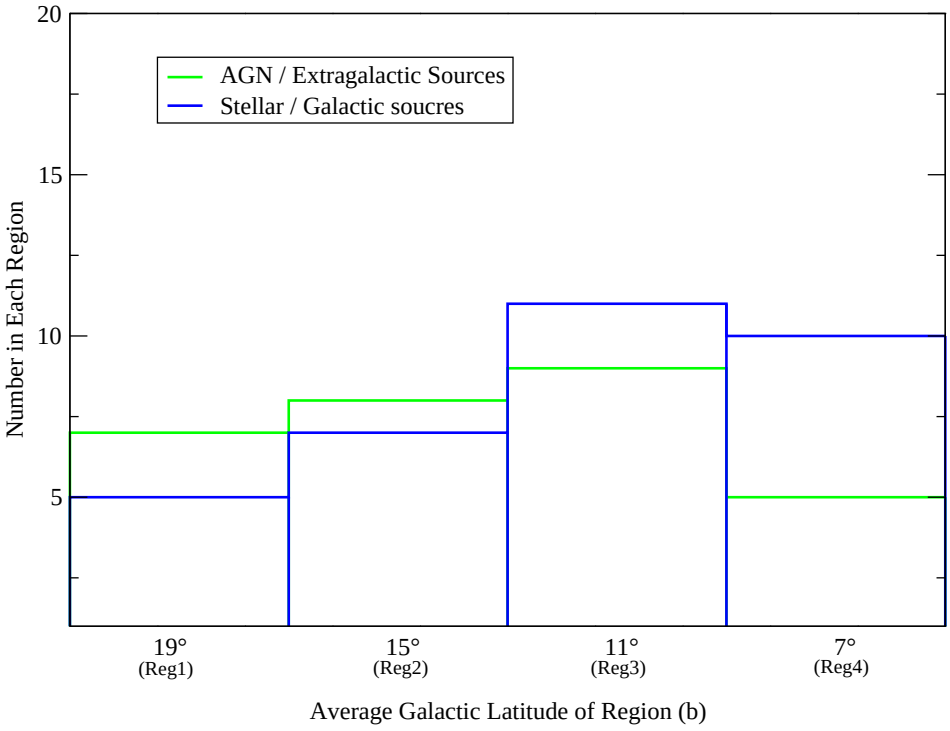

Figure 3.3: Distribution of source types by average galactic latitude of each of our 4 regions. As shown in Figure 3.1. Region numbers increase as they approach the galactic plane; Region 1 is furthest from the galactic plane with $b \sim 19°$, while Region 4 is the closest with $b \sim 7°$. Stellar sources begin to outnumber extragalactic sources closer to the plane, as expected. The plot includes the 62 sources classified by spectra, light curve behavior, or a combination of f_X/f_V ratio, $U-B$ color, and apparent magnitude. Sources with unknown or uncertain classifications are not included in the plot.

can be constructed for sources with adequate archival data in surveys at multiple wavelengths; the SED shape is recognizably different between stars and AGN and can be used to classify some sources. Finally, in the event that a source has very little archival data or an intermediate flux ratio value but does have a *Kepler* light curve, one can use the temporal behavior to rule out an AGN in cases where the variability is strongly periodic.

3.3.1 Optical Spectra

We obtained simultaneous blue and red optical spectra for 31 sources in our sample with the double beam spectrograph (DBSP) on the 200-inch Hale telescope at Palomar Observatory. As described above, poor seeing on one of our nights restricted our observations to targets with $M_V \leq 17$, reducing the number of faint targets and disproportionately removing AGN from the observable sample; thus, most of our spectroscopic targets are stellar in nature. In all, the Palomar spectra identified 21 stellar sources and 10 AGN. Figure 3.4 shows typical example spectra of three sources: a chromospherically active star, which are quite common in our sample; a type 1 AGN; and a normal A-type star. It is probable that the A star has a white dwarf companion that is producing the observed X-ray emission; alternatively, there may be confusion with a background X-ray source. Below we discuss the spectral properties of the AGN and stellar sources.

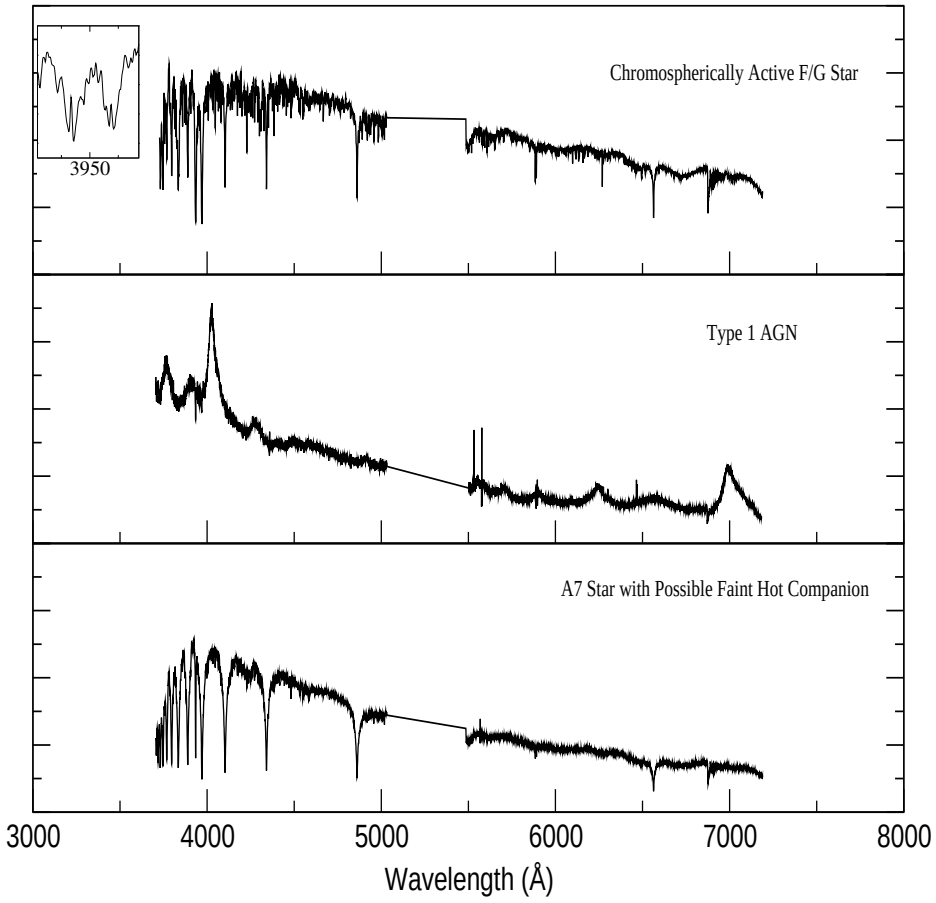

Figure 3.4: Optical spectra from the 200-inch Hale telescope at Palomar observatory, for three representative KSwAGS objects. In order from top panel to bottom, they are KSw 19, KSw 55, and KSw 69. The inset in the top panel is an expanded view of the Ca H and K lines (λ3969Å and λ3933Å), exhibiting the bright emission cores typical of chromospherically active stars.

3.3.1.1 AGN Spectra and Measured Parameters

There are ten AGN among our Palomar spectra. Nine of them were type 1 (e.g., exhibit broad emission lines with $\mathrm{FWHM}_{H_\beta} \geq 1000$ km/s), while one target, KSw 82, is a likely BL Lac object, exhibiting the typical flat, featureless continuum in multiple deep (∼3200s) exposures. Newly confirmed AGN include KSw 2, 3, 25, 27, 39, 40, 55, 68, 82 and 92. They join the three previously known AGN in our sample: the BL Lac object BZB J1848+4245 (KSw 9), the type 1 AGN Zw 229-15 (KSw 20), and the radio galaxy Cygnus A (KSw 93). Their spectral types and redshifts are given in Table 3.3. Our spectral analysis indicates that the KSwAGS AGN encompass a wide range of black hole masses ($7.3 \leq \log \mathrm{M_{BH}} \leq 9.4$), redshifts ($0.03 \leq z \leq 1.5$), and Eddington ratios ($0.003 \leq \lambda_{Edd} \leq 0.45$).

It has long been theorized that the characteristic optical variability timescale in the accretion disk of an AGN should correlate with the mass of the supermassive black hole. This relationship has already been demonstrated in the X-ray, where a break frequency in the power spectrum has been detected. The timescale associated with the break is assumed to correspond to the physical size of the accretion disk [Uttley et al., 2002] and has been found to correlate with the black hole mass [McHardy et al., 2004]. For further discussion, see Section 3.4.1. Recently, our group published the discovery of the first optical break frequency discovered in an AGN, using the *Kepler* light curve of Zw 229-15 [Edelson et al., 2014].

With this in mind, we calculate the redshift and black hole masses of our spectroscopically-confirmed AGN and present the values in Table 3.3. We calculated

Table 3.3: Parameters of Spectroscopic AGN

KSw Num.	Type	z	Log M_{BH}	λ_{Edd}
2	Sy 1	1.506	8.53	1.474
3	Sy 1	1.177	8.404	0.452
9 (BZB J1848+4245)	BL Lac			
20 (Zw 229-15)	Sy 1	0.0266	7.29	0.038
25	Sy 1	0.609	8.898	0.042
27	Sy 1	0.056		
39	Sy 1	0.533	8.382	0.113
40	Sy 1	0.38	8.111	0.109
55	Sy 1	0.437	8.783	0.069
68	Sy 1	0.36	8.553	0.026
82	BL Lac?			
92	Sy 1	0.182	8.473	0.017
93 (Cyg A)	Radio Galaxy	0.056	9.398	0.003

Spectroscopic type, redshifts, black hole masses and Eddington ratios of spectroscopically-confirmed AGN. Redshifts and black hole masses are not measurable for BL Lacs due to the lack of optical lines. Values of M_{BH} were obtained using the FWHM of the Mg II λ2799 Å or the Hβ line for high and low redshifts, respectively. Unfortunately, the redshift in source 27 was such that Hβ fell in the dichroic break and was too low for measurement of Mg II. Values of redshift and black hole mass for KSw 93, which is Cygnus A, were obtained from Tadhunter et al. [2003]. See Section 3.3.1.1 for details on how values were obtained.

the black hole masses using the formulae from Wang et al. [2009]; in the 7 objects that are low-redshift enough for the spectrum to contain Hβ, we use the relation:

$$\log\left(\frac{\mathrm{M_{BH}}}{10^6\ \mathrm{M_\odot}}\right) = (1.39 \pm 0.14) + 0.5\ \log\left(\frac{\mathrm{L_{5100}}}{10^{44}\ \mathrm{erg\ s^{-1}}}\right) + (1.09 \pm 0.23)\ \log\left[\frac{\mathrm{FWHM(H\beta)}}{1000\ \mathrm{km\ s^{-1}}}\right]. \quad (3.1)$$

For our three AGN with $z > 0.6$, the Hβ line is outside the clean region of the optical observing window, so we use the lower-wavelength Mg II λ2799 Å line for BH mass estimation with the following relation:

$$\log\left(\frac{\mathrm{M_{BH}}}{10^6\ \mathrm{M_\odot}}\right) = (1.13 \pm 0.27) + 0.5\ \log\left(\frac{\mathrm{L_{3000}}}{10^{44}\ \mathrm{erg\ s^{-1}}}\right) + (1.51 \pm 0.49)\ \log\left[\frac{\mathrm{FWHM(MgII)}}{1000\ \mathrm{km\ s^{-1}}}\right], \quad (3.2)$$

where L_{3000} and L_{5100} are the continuum luminosities at 3000 Å and 5100 Å, respectively. The Eddington ratio $\lambda_{Edd} = L_{Edd}/L_{bol}$ is a measure of the observed luminosity compared to the theoretical luminosity output of the maximal spherical accretion rate (known as the Eddington luminosity). With the masses in hand, we may calculate the Eddington luminosity for each of the sources via $L_{Edd} = 1.38 \times 10^{38}\ (M_{BH}/M_\odot)$ erg s^{-1}. The bolometric luminosity is estimated from the $0.2-10$ keV X-ray luminosity using the bolometric correction factor of $\sim$15 given by Vasudevan & Fabian [2007]; while this correction is widely used, there is significant empirical scatter in this relation, so the Eddington ratios given in Table 3.3 should be assumed with caution until detailed SED modeling is performed. The AGN

types, redshifts, black hole masses and Eddington ratios are given for our confirmed AGN in Table 3.3. In the next chapter, we will determine whether these AGN properties correlate with variability characteristics such as amplitude and characteristic frequency. A sample of the ongoing temporal analysis is given in Section 3.4.

3.3.1.2 Stellar Spectra

The Palomar spectra of the KSwAGS survey stars fall into roughly three groups. The first is comprised of typical M-dwarf spectra with strong Ca HK emission lines. M dwarfs with strong chromospheric activity are known to be X-ray sources, with high activity levels generally attributed to rapid rotation. Such rotation can indicate that the M dwarf is young and retains some innate formation spin, or that the star is in a binary with spin-orbit coupling [Lépine & Gaidos, 2011]. There is also a population of normal main-sequence spectra, which are not indicative of X-ray activity. In these cases, it is possible that there is a dim white dwarf companion contributing the X-ray flux that is too faint to affect the optical spectrum. Finally, there is a large population of G through K stars that exhibit broad and complex emission structures in their H alpha lines and the Ca HK lines (see top panel of Figure 3.4). The effective surface temperatures and surface gravities from the KIC for the stellar sources are given in Table 3.4; also given are the spectral types gathered from the Palomar spectra. The spectral type can be inferred from the effective temperature even for those objects without Palomar spectra; however, note that the KIC temperatures are derived from *griz* photometry and may be

$\sim 100 - 200$ K too low in many cases [Pinsonneault et al., 2012].

3.3.2 X-ray to Optical Ratios

When an X-ray source has a UV/optical counterpart, the calculation of the X-ray to optical flux ratio can provide source classification information. As noted in Maccacaro et al. [1988] for the Einstein Extended Medium Sensitivity Survey [EMSS; Gioia et al., 1990] sources, the X-ray to optical flux ratio is a powerful tool in optical identification of X-ray sources. In general, all classes of AGN, including BL Lac objects, Seyfert galaxies and QSOs, have by far the highest f_X/f_V ratios, followed by stellar accreting binaries. Coronal stellar sources such as dMe stars typically have the lowest ratios. Krautter et al. [1999] measured f_X/f_V average values across a range of objects for a representative region of the RASS. Their average ratio values are $log[f_X/f_V] = -2.46 \pm 1.27$ for stellar sources and $log[f_X/f_V] = +0.41 \pm 0.65$ for AGN.

The optical counterparts for KSwAGS sources are drawn from the KIC (for details on counterpart identification, see Section 4.2). We draw our V magnitudes used in constructing these ratios from the Everett et al. [2012] UBV optical survey of the *Kepler* FOV; the fluxes in these bands for objects covered by the UBV survey are provided in Table 3.2.

Typical X-ray detections have too few counts per energy bin to model the X-ray spectrum; therefore, in order to obtain the X-ray flux from the XRT count rates, one must assume a photon index that fits the general continuum shape of the

Table 3.4: Parameters of Spectroscopic Stars

KSw Num.	T_{eff} (K)	Log g	Spectral Type
1	5953	4.297	F
6	4478	2.64	
13			G
14	5607	4.307	G
16			G
19	4817	4.093	K
22	4551	1.941	
23	8973	4.001	
24	4590	2.485	
28	5453	3.744	G
35			F
38	4967	4.376	K
47	5899	4.232	F
49	9046	4.014	
52	5513	3.7	
53			
54			M
57	4667	3.317	K
64	3831	4.291	M
66			M
67			
69	8742	3.929	A
71			K
73	5570	3.906	
75	7292	3.566	
76	6165	4.282	F
78			F
79			
81	5641	3.902	
84			M
85	5617	4.21	G
89			G
91	5241	3.688	K

Effective surface temperature, surface gravities, and spectral types indicated by the Palomar spectra for the 33 confirmed stellar KSwAGS sources. The temperatures and gravities are from the *Kepler* Input Catalog (KIC), while the spectral types are given only for those objects with Palomar spectra.

underlying spectrum. Since we do not know the source type, we instead use PIMMS [Mukai, 1993] to calculate the flux of each object using a range of feasible photon indices, from $\Gamma = 1$ to 2.5. This range encompasses typical values of Γ for all object types, from active stellar sources to AGN. Heinke et al. [2008] found that magnetic and nonmagnetic CVs from the ASCA X-ray survey have average photon indices of $\Gamma = 1.22 \pm 0.33$ and 1.97 ± 0.20, respectively. Values of Γ for AGN have been measured for many samples and range from $\Gamma \sim 1.5 - 2.5$ [e.g. Nandra & Pounds, 1994, Page et al., 2005]. In all PIMMS count-to-flux conversions, we use the galactic column density at the source position cataloged by Kalberla et al. [2005]. We do not find that the choice of photon index changes the value of f_X/f_V significantly.

In Figure 3.5, we show the f_X/f_V ratio of all survey sources that have an optical counterpart in the KIC within 5 arcseconds of the UVOT position (or the XRT position, if the object was outside the UVOT FOV or had no UVOT counterpart). For objects without V magnitudes in the KIC, we use the *Kepler* magnitude (given in Table 3.2 as "kepmag") as a very rough proxy. The *Kepler* magnitude is a generic optical magnitude calculated using various available optical measurements for any given object in the FOV; its detailed determination can be found in Brown et al. [2011]. Denoted in the figure are the average values for extragalactic and galactic sources from Krautter et al. [1999]. The KSwAGS survey conforms to these typical ratio values: the average value for all confirmed stellar objects in our survey for which optical data was available is $log[f_X/f_V] = -2.09 \pm 0.27$; for confirmed AGN, the value is $log[f_X/f_V] = +0.44 \pm 0.81$. The calculated values of the ratio for each object are given in Table 3.2. Figure 3.5 shows that the full distribution of KSwAGS

sources cluster around the AGN and stellar average values, but have a significant spread. Indeed, as Krautter et al. [1999] points out, there is overlap between the two types of objects. In particular, white dwarfs and cataclysmic binaries show very high f_X/f_V ratios for stellar sources, reaching into the lower tail of the AGN range. Therefore, in absence of a spectrum, a low or high f_X/f_V value will at least offer a reliable classification of whether an X-ray source is stellar or extragalactic. Intermediate values of f_X/f_V are not reliable classifiers, as there is significant overlap between source types for middling ratios.

3.3.3 SEDs

Using the multiple photometric data points provided from the 2MASS, GALEX, and UBV Everett et al. [2012] surveys, along with our UVOT and XRT data, we can construct broadband spectral energy distributions (SEDs) for our sample across a wide wavelength range from infrared through X-ray. The archival surveys utilize varying magnitude systems, so in order to construct the SED, we converted these various systems to the consistent unit of millijanksies (mJy). The following discussion outlines this conversion process for each different survey. The final mJy fluxes are given in Table 3.2.

3.3.3.1 GALEX Magnitudes

The GALEX satellite surveyed the sky in the FUV and NUV bands, with effective wavelengths of 1538.6 Å and 2315.7 Å, respectively. GALEX data releases

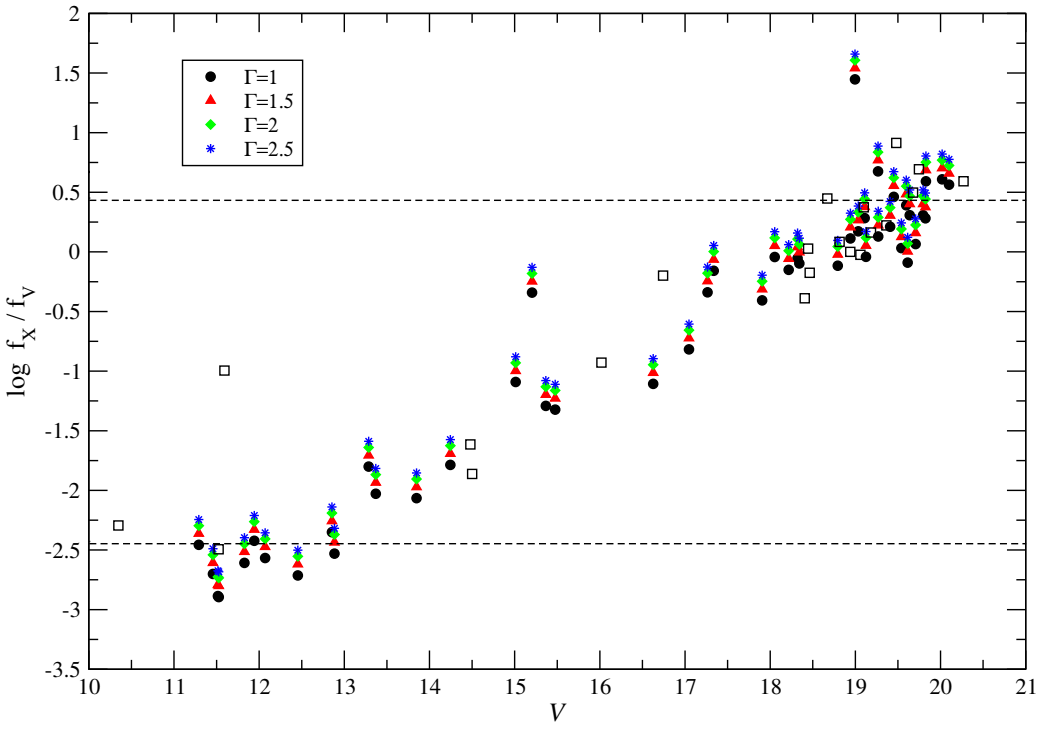

Figure 3.5: X-ray and optical flux ratios for all sources in the sample with a V magnitude given by the Everett et al. [2012] survey. Lines indicate the average value of this ratio for all stellar objects, $\langle log[f_X/f_V]\rangle = -2.46 \pm 1.27$, and for all AGN types, $\langle log[f_X/f_V]\rangle = 0.41 \pm 0.65$, as given in Krautter et al. [1999]. The X-ray fluxes were estimated using a variety of values for the photon index (Γ), shown in the legend. Black squares indicate objects for which no V magnitude is available, and so the Kepler magnitude was used as a rough proxy. These values should be considered very approximate.

GR6 and GR7 included increased coverage of the *Kepler* FOV, resulting in the KIC-GALEX crossmatched survey. There are two possible search mechanisms for the crossmatched survey. As defined by GALEX, they are 1) the "accurate" search method, which only returns a counterpart that is within 2.5″ of the query coordinates and is unique (i.e., there are no other matches to either the KIC or GALEX source within this separation), and 2) the "complete" search method, which returns all counterparts within 5″ of the query coordinates. In order to reduce spurious information in our survey, we have provided GALEX magnitudes only when our KIC coordinates have a GALEX counterpart using the "accurate" method.

The survey uses the AB magnitude system [Oke & Gunn, 1983]. The zero points of the GALEX magnitudes for the two bands were calculated by Morrissey et al. [2007] to be 18.82 (FUV) and 20.08 (NUV). Additionally, one count per second in GALEX corresponds to reference fluxes of 1.40×10^{-15} and 2.06×10^{-16} erg cm^{-2} s^{-1}Å^{-1} in the FUV and NUV, respectively. Conversion of the given magnitudes to fluxes in erg cm^{-2} s^{-1}Å^{-1} is thus achieved using the following formulae:

$$f_{FUV} = 1.40 \times 10^{-15} \cdot 10^{\frac{m_{AB,FUV} - 18.82}{-2.5}} \tag{3.3}$$

$$f_{NUV} = 2.06 \times 10^{-16} \cdot 10^{\frac{m_{AB,NUV} - 20.08}{-2.5}} \tag{3.4}$$

Conversion to frequency units is then simply achieved by multiplying each flux by λ^2/c, where λ is the peak wavelength of the band, and can then be directly converted to mJy.

3.3.3.2 UBV and 2MASS Magnitudes

The conversion to flux density is simpler for the UBV and 2MASS magnitudes, as their flux density zero points are known and tabulated in the proper units for our purposes. In this case, the flux in Jy for any band A is calculated using:

$$f_A = f_{A,0} \cdot 10^{\frac{m_A}{-2.5}} \tag{3.5}$$

Aiming to facilitate optical source selection of interesting targets in the *Kepler* field, Everett et al. [2012] completed a UBV photometric survey of the field with the NOAO Mosaic-1.1 Wide Field Imager and the WIYN 0.9 m telescope on Kitt Peak. The magnitudes are in the traditional Vega-based Johnson system, and can be converted easily to fluxes using the standard tabulated fluxes at zero magnitude of the U, B, and V bands of 1823, 4130, and 3781 Jy.

The absolute calibration of the 2MASS survey was performed by Cohen et al. [2003]. The fluxes at zero magnitude for the JHK filters are 1594, 1024, and 666.8 Jy, respectively.

With all given magnitudes converted to consistent flux units, we constructed the broadband SEDs for objects that have data in at least three wavebands. Plotted in Figure 3.6 are the SEDs of five representative objects from different regions of the f_X/f_V plot; three stellar objects and two AGN. This analysis is only informative for objects with data in 2MASS, the Everett et al. [2012] UBV survey, and/or GALEX, so we have displayed the SEDs for objects of each type with the most available data points. Note that AGN will necessarily have fewer detections in the ancillary surveys,

since they are relatively much fainter on average than stellar sources in the optical and UV. Only two of the sources have GALEX data. The GALEX NUV filter overlaps with the UVOT M2 filter; however, because the observations are widely disparate in time, discrepancies in the flux values might indicate time variability. Additionally, since the 2MASS and UBV measurements are also disparate in time, SED fitting is not appropriate.

Nonetheless, one can clearly see that the AGN-type SEDs are flatter than the stellar SEDs at lower frequencies, and differ characteristically enough to allow for reliable source classification.

3.4 Sample Light Curves

The driving motivation behind this survey is the unprecedented photometric precision of *Kepler* and its application to astrophysical sources beyond exoplanet detection. Over its ∼4 year operational lifetime, *Kepler* routinely monitored over 150,000 stars, the overwhelming majority of which show no evidence of transiting exoplanets due to simple geometry. The unmatched photometric quality of the dataset will result in the *Kepler* targets being the best monitored astrophysical sources ever, and ancillary data will help insure they are also the best understood. There are many types of X-ray bright, optically variable sources both within and beyond the Galaxy. The MAST Kepler Data Search tool allows the user to input coordinates, object names, or KIC ID numbers and obtain all available quarterly light curves for any object. All *Kepler* data is now public, so if an object has been

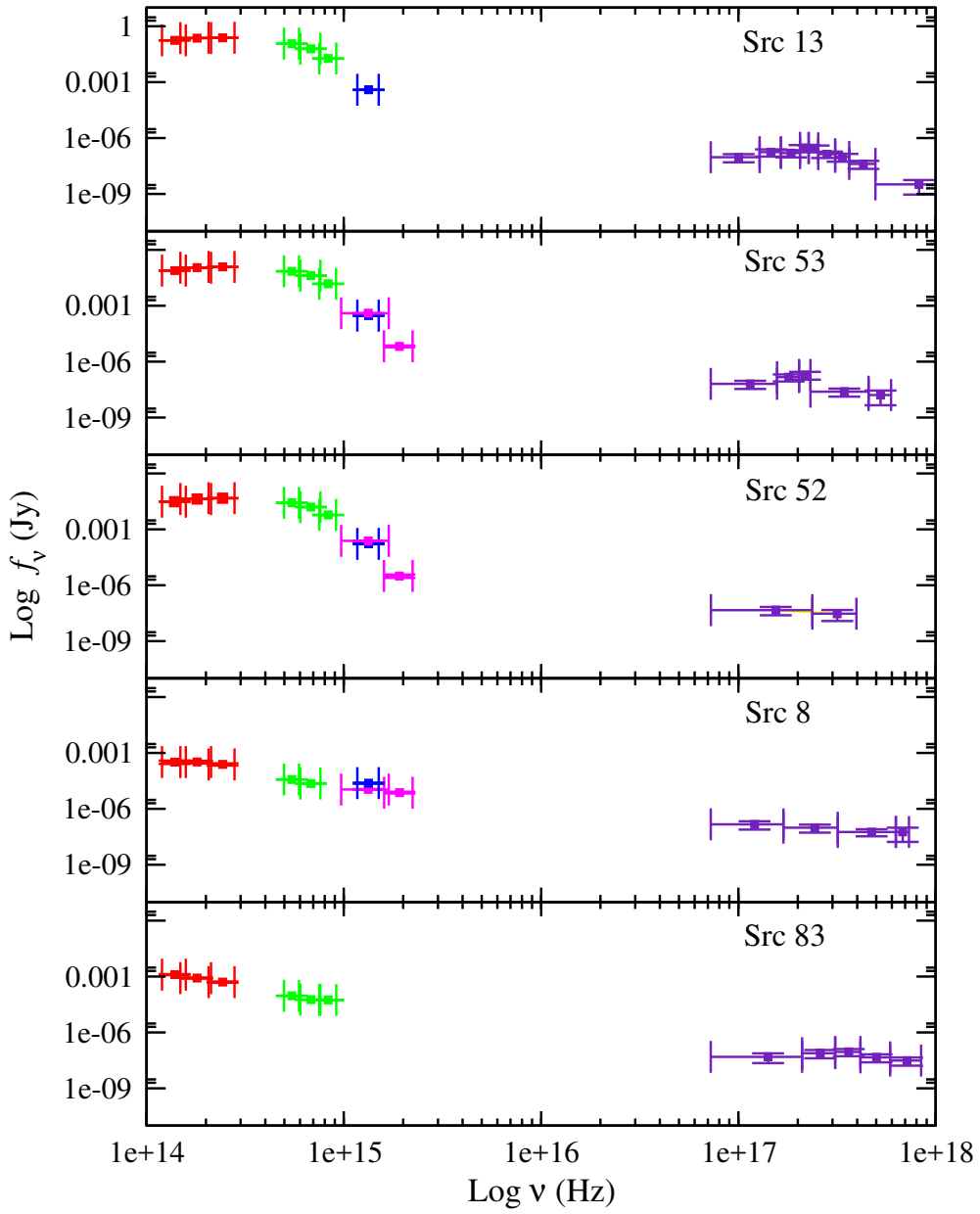

Figure 3.6: Broadband SEDs for three stellar objects (top three panels) and two AGN (bottom two panels). Red points are the 2MASS JHK colors, green points are UBV fluxes calculated from the Everett et al. [2012] survey, blue points are UVOT M2 filter fluxes, magenta points are GALEX FUV and NUV fluxes, and purple points are XRT fluxes from this survey. The objects were selected as stellar or AGN based on their log f_X/f_V values (i.e., their position on Figure 3.5).

observed, in general one can download and analyze the light curves.

To demonstrate the temporal analyses to be carried out on the survey products, we have selected one representative object from each class (stellar and AGN). The following sections constitute a sample of results to be presented in upcoming papers focusing on the spectral and time-series analysis of each source type.

3.4.1 AGN: Timing Overview

The discovery of AGN in the *Kepler* FOV was the original primary motivation for this survey. Although a few AGN were known to be in the field, a lack of overlap with large spectroscopic surveys like SDSS prevented the curation of a sizable sample. Additionally, the known AGN in the field were typically selected by techniques known to bias the final sample. X-ray detection is the least-biased AGN selection method, as it is immune to all but the most intense dust obscuration and to the effect of dilution of the optical or infrared colors by host galaxy starlight [Mushotzky, 2004]. Our survey is approximately ten times deeper than the ROSAT All-Sky Survey (RASS), which included only a handful of confirmed AGN in this region of the sky.

The optical emission in an AGN is believed to originate in an accretion disk. The variability of this emission then implies stochastic processes within the disk. There are several candidate processes that theoretically give rise to rapid optical variability, including reprocessing of the variations of the central X-ray source, the

orbital dynamics of the gas in the disk itself, spatial viscosity variations, and turbulent thermal processes. A clear understanding of the relationship of AGN parameters to overall variability requires a self-consistent, complete theory of accretion disks including radiative physics; this does not yet exist and there are many hurdles left for such simulations. The approach has therefore been largely empirical, involving observed correlations like the McHardy et al. [2004] study showing a relationship between the characteristic timescale of X-ray variability and black hole mass spanning many orders of magnitude, from stellar-mass black hole systems like Cygnus X-1 to Type 1 Seyfert galaxies. Such observations remain unexplained, but seem to be robust for the 2-10 keV band [e.g., González-Martín & Vaughan, 2012, Ludlam et al., 2015]. Additional approaches have involved mathematical modeling of observed variability as a damped random walk model [MacLeod et al., 2010] and propagating fluctuations that produce flicker noise [Lyubarskii, 1997].

The *Kepler* data are superior to all previous AGN light curves ever obtained, in both photometric precision and continuous sampling frequency. The proper analysis techniques to analyze these light curves must be carefully constructed to mitigate the systematic errors known to be present in the *Kepler* data, such as the Moiré pattern drift noise [Kolodziejczak et al., 2010] and the inter-quarter discontinuities introduced by spacecraft rolls.

Orbital timescales for typical AGN black hole masses ($10^6 - 10^9 M_\odot$) span a few days to months; timescales which we can probe using the *Kepler* light curves. Edelson et al. [2014] reported the first detection of an optical timescale break, detected at $\sim$ 5 days, for one of our X-ray detected previously-known AGN (Zw 229-15).

A small number of our confirmed AGN have continuous *Kepler* monitoring (see Table 3.2, columns with "Y"). Our original intent was to propose for *Kepler* to monitor all KSwAGS X-ray sources as soon as we had confirmed them; however, only four of the newly discovered sources were being monitored at the time of the failure of the second reaction wheel that put an end to the original *Kepler* mission. For those objects without archived light curves, we are able to construct coarsely sampled light curves with 30-day cadence for the entirety of the 4 year mission using the full-frame images (FFIs): snapshots of the entire FOV downloaded each month to verify pointing calibrations. We have written a customized pipeline to handle the FFI data cubes and produce a light curve for any source that was on silicon, whether or not it was included in the Kepler Input Catalog (KIC). Figure 3.7 demonstrates that our FFI method faithfully tracks the variability in the archived light curve for KSw 9 (KIC 7175757; BZB J1848+4245). The displayed data is typical of the AGN light curves in our sample: aperiodic and stochastic, with both short- and long-term variability and with higher amplitudes at longer timescales.

In the next chapter, we explore in detail the variability of the AGN in our sample, using our custom pipelines for both the FFIs and the archived data. It will also include all of the spectra and measurable X-ray properties of our confirmed AGN. We plan to use a variety of time series analysis techniques to search for characteristic timescales and correlations of variability properties with the measured parameters.

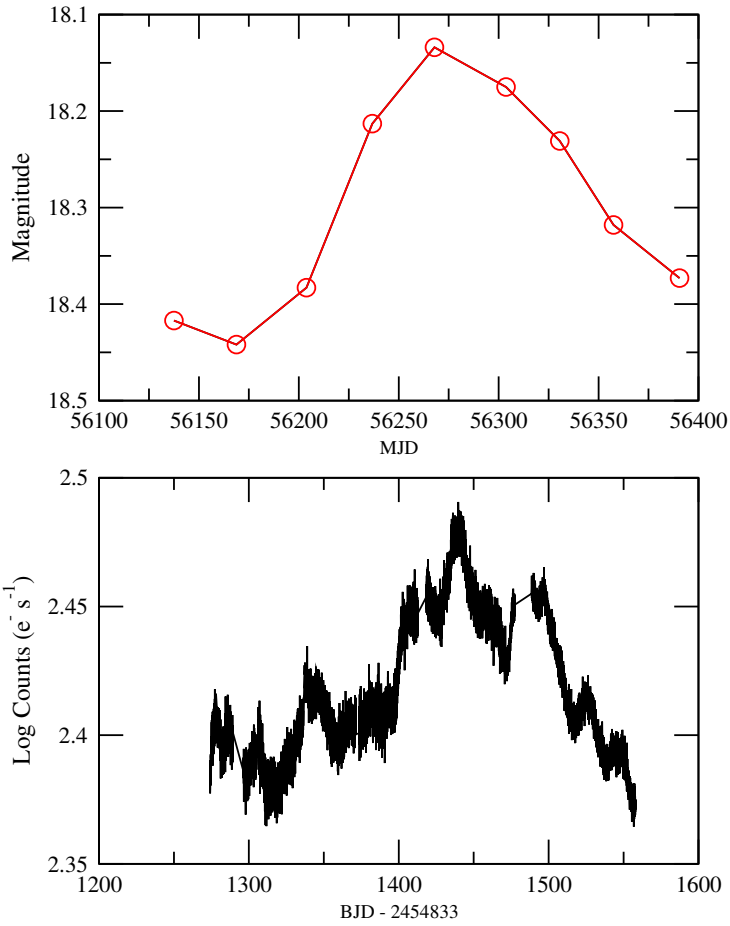

Figure 3.7: The full-frame image (FFI) light curve with 30-day sampling (top panel) and the standard *Kepler* light curve with 30-minute sampling (bottom panel) for KSw 9 (KIC 7175757), a BL Lac type AGN. The bottom panel's flux units have been put into a log scale for consistency with the magnitude units in the top panel. Both light curves are the output of our custom pipeline. While the FFI light curve involves different extraction apertures and procedures, as well as entirely different source images, the behavior of the variability is faithfully tracked.

3.4.2 Stars: Timing Overview

As described in Section 3.3.1.2, the Palomar spectra of the KSwAGS survey stars fall into roughly three groups: M dwarfs with strong line emission, normal main sequence spectra, and G through K stars with broad and complex emission structures in their H alpha lines and the Ca H and K lines. Their $v\sin i$ measurements cluster around roughly 100 km/sec, implying that, as a group, they are rapid rotators. Rapid rotation and X-ray luminosity are strongly correlated, and such stars are concentrated in two basic stellar populations: young stars, which have not had time to lose their angular momentum, and binary stars, where tidal transfer of orbital momentum maintains the rotational angular momentum.

Preliminary investigation of the 27 *Kepler* light curves of KSwAGS stellar sources supports this. Fourier analysis of these sources detects highly significant periods in 22 of the 27 objects. Twenty have periods of 10 days or less, and nine of these have periods less than one day. Most show evidence of slow period and amplitude evolution over multiple *Kepler* quarters. Figure 3.8 shows the light curves and dynamic power spectra over two years for KSw 47 (KIC 6365080). In this example, we note the complex interplay between two fundamental periods at ∼2.8 days and ∼0.64 days, with constant frequencies but dramatically varying amplitudes. McQuillan et al. [2014] include this object in their large sample of rotationally variable stars in the *Kepler* field, and attribute the longer period to rotation; however, they only exclude pulsating stars by making a simple cut in effective temperature, and have likely not excluded all pulsators. The effective temperature in the KIC is given

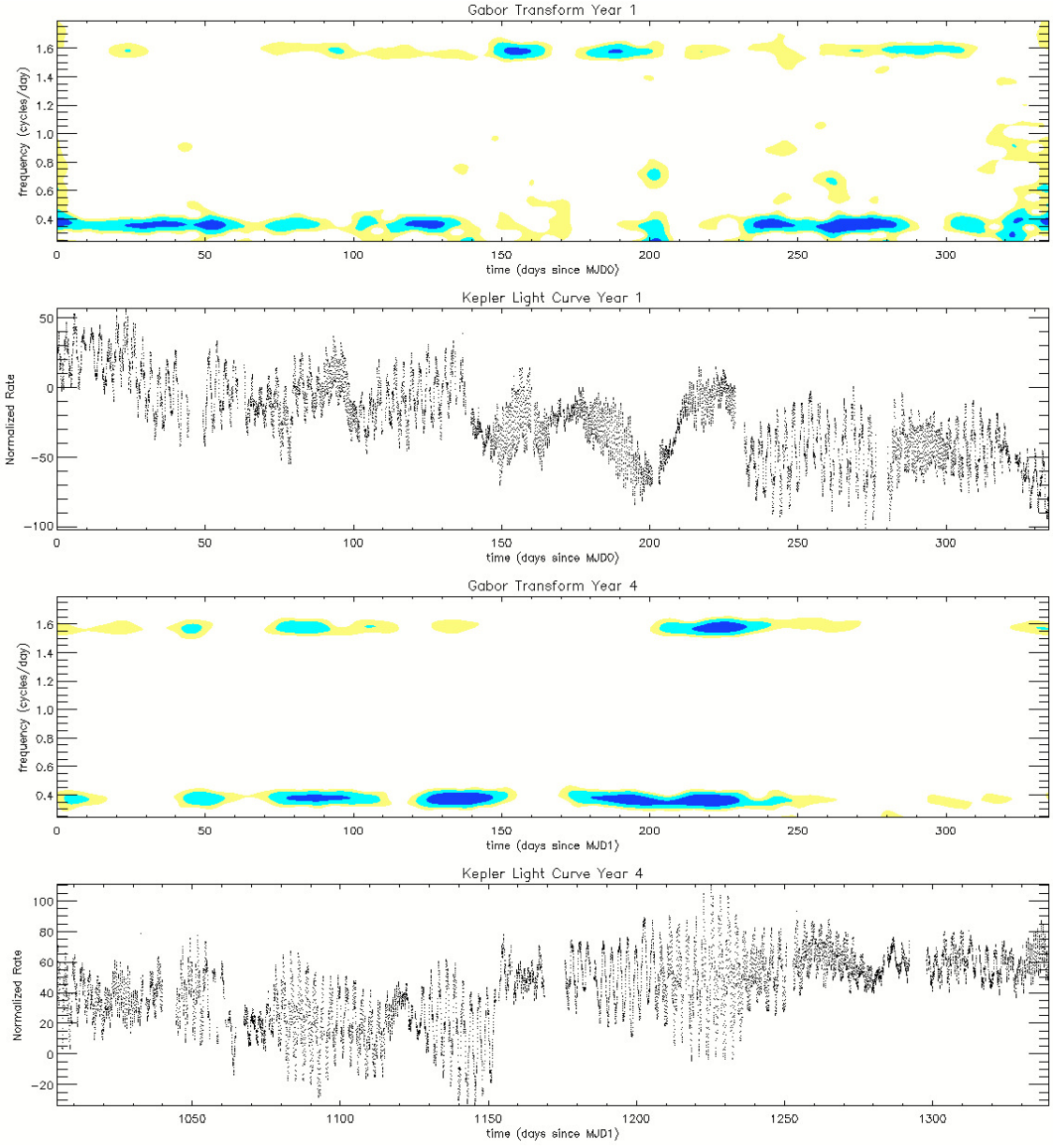

Figure 3.8: Light curves and dynamical power spectra (also known as Gabor transforms) for the first and fourth years of continuous *Kepler* monitoring of the variable star KSw 47 (KIC 6365080). There are two dominant periods with constant frequency but varying amplitude. Such light curves appear frequently in our sample of X-ray bright, *Kepler*-monitored stars.

as $T_{eff} = 5900$ K from *griz* photometry; however, our Palomar spectrum suggests an F type star. This is not necessarily unusual: the KIC temperatures may be $\sim 100 - 200$K too cool, as reported by Pinsonneault et al. [2012]. If the shorter period is indeed due to pulsation, then the frequency and stellar type suggest the object is an RR Lyrae star, which typically have periods of $0.2 - 1$ days. Such complex, multi-periodic light curves are typical for a number of KSwAGS targets. Further investigation of *Kepler* photometry will allow us to track the growth, migration, and decay of starspots, differential rotation, activity cycles, and flaring on a wide variety of single and binary stars, offering a unique opportunity to measure magnetic activity cycles for a large sample of late-type stars, which could provide important constraints for developing better stellar dynamo models and a clearer understanding of how they function. The timing properties of the KSwAGS stellar sources will be fully investigated in an upcoming paper in this series.

3.5 Continuation in the K2 Fields

Since the second reaction wheel failure and the resulting loss of pointing stability in the original FOV, the *Kepler* mission has been modified and repurposed as "K2". The new mission utilizes solar radiation pressure and the remaining two wheels to maintain pointing for approximately 3 months at a time, in fields aligned along the ecliptic plane [Howell et al., 2014]. The new incarnation has been proven to produce photometric precision on par with that of the nominal mission, according to the K2 photometry status report conducted after the redesign in December 2013.

We have surveyed K2 Field 4 with *Swift* using the same array of pointings as our original survey described in this paper. We supplemented our successful K2 monitoring proposal with sources from various additional X-ray missions including *ROSAT*, *Chandra*, and XMM-*Newton*, as well as from the Million Quasar Catalog ("Milliquas")[1]. Additionally, we have submitted the pointing coordinates for K2 Fields 8 and 10 to *Swift*; the survey in those fields will begin presently. We expect to continue to publish future versions of the KSwAGS survey as we increase our sample in the new fields; additionally, all future KSwAGS sources will have 30-minute cadence light curves for the full 3 month duration of each field pointing. The K2 campaign covers a wide range of galactic latitudes; the field we have surveyed so far, Field 4, is in the constellation Taurus at an approximate galactic latitude of $b \sim 15°$. We have communicated with the *Kepler* and K2 Guest Observer (GO) offices to add our X-ray and UV survey products to the KIC and the EPIC (Ecliptic Plane Input Catalog), so that the wider astronomical community can access these data for their own analyses.

3.6 Summary

This paper has introduced and described the KSwAGS survey, a *Swift* XRT and UVOT survey of four modules of the *Kepler* FOV. The survey discovered 93 total X-ray sources with S/N$\geq$3, with exposure times of $\sim$2000 seconds per pointing. Of these, 60 have counterparts that were observed simultaneously with UVOT

[1]Milliquas is unpublished but can be accessed at http://quasars.org/milliquas.htm or via the NASA HEASARC at http://heasarc.gsfc.nasa.gov/W3Browse/all/milliquas.html.

(the remaining 33 were not in the corresponding UVOT images of any of our XRT pointings, due to the smaller FOV of the UVOT telescope). The aim of the survey was to obtain X-ray sources that are likely to have optical counterparts with variability of astrophysical interest, especially AGN. The survey also produced a large number of stellar sources, both new and previously known in the literature. In most cases, the KSwAGS survey provides the first X-ray and UV observations for these objects.

Twenty-three of the source counterparts had optical classifications in the literature. We obtained optical spectra at Palomar for an additional 30 sources. Of these 53 total sources with certain identification, 13 are AGN and 40 are stars. In the absence of spectra, we demonstrate that most of the survey sources can be categorized as either stellar or extragalactic using the flux ratio f_X/f_V or broadband SED shape.

As a sample of the future analysis to be carried out on the KSwAGS sources, we have shown example light curves and dynamical power spectra of a typical star from our survey, and both types of light curves (FFI and standard *Kepler*) for an AGN.

The KSwAGS survey has identified numerous new X-ray sources in the original *Kepler* field which can be followed up either using archived light curves from the KIC database, or by constructing 30-day cadence light curves using the FFIs, which can be done for any source in the survey regardless of whether it was monitored by *Kepler*. This opens up a new phase space of X-ray and UV bright targets with high-quality optical time sampling. The survey is currently continuing in Fields 4, 8

and 10 of the K2 mission, the new extension of *Kepler* to the ecliptic plane, and will continue to yield a rich crop of X-ray bright, optically variable targets for monitoring with the most exquisite photometer of our time.

Acknowledgements

We would like to thank the referee for a helpful report which improved the manuscript. We acknowledge Trisha Doyle for her assistance during the Palomar observing run. We also acknowledge the extremely helpful and accommodating staff at Palomar Observatory. The GALEX data for many of our KSwAGS sources was obtained thanks to A. Brown's GALEX GO programs GI4-056 and GI5-055, a UV survey specifically designed to locate active stars in the *Kepler* field. This publication makes use of data products from the Wide-field Infrared Survey Explorer, which is a joint project of the University of California, Los Angeles, and the Jet Propulsion Laboratory/California Institute of Technology, funded by the National Aeronautics and Space Administration. KLS is grateful for support from the NASA Earth and Space Sciences Fellowship (NESSF), which enabled the majority of this work.

Chapter 4: *Kepler* Timing of Active Galactic Nuclei

4.1 Introduction

Active galactic nuclei (AGN) are the most luminous non-transient objects in the universe, powered by accretion onto a central supermassive black hole. The fueling required to ignite the AGN phase can be caused by gravitational tidal torques in major mergers or by secular processes. Simulations of this fueling are well understood on kiloparsec scales; however, the situation becomes obscure on the small scales where the accretion is actually taking place. The accretion disk of an AGN is too small to be directly imaged, on the order of 10^{-2} parsecs from simple theoretical considerations, and has been constrained to be smaller than this in some AGN through microlensing observations [Rauch & Blandford, 1991]. Fortunately, we can take advantage of one ubiquitous property of AGN accretion disks: variability.

The optical continuum light in AGN is primarily supplied by the accreting matter itself, frequently assumed to be thermal emission from the standard geometrically-thin Shakura & Sunyaev [1973] disk. Although the disk geometry may vary from object to object based on, for example, accretion rate, the optical variability must come from highly nuclear regions based on the relatively fast timescales on which it is observed, on order hours to days to months [e.g., Pica &

Smith, 1983]. It has long been hoped that the study of this variability would offer a window into the central engine physics, but this result has proved elusive.

Theoretically, several models have been proposed to explain the observed optical variability. These include magnetohydrodynamic (MHD) turbulence driven by the magneto-rotational instability [MRI, Balbus & Hawley, 1991, Reynolds & Miller, 2009], Poissonian flares [Cid Fernandes et al., 2000], microlensing [Hawkins, 1993], starburst activity in the host [Aretxaga et al., 1997], and a damped random walk of thermal flux within the disk [Kelly et al., 2013, Zu et al., 2013]. Observational studies of optical variability in AGN have mostly been obtained by using long, dedicated ground-based monitoring campaigns with the typical goal of black hole mass estimation via reverberation mapping [e.g., the Lick AGN Monitoring Project or LAMP, Barth et al., 2011b]. There have also been reconstructions of quasar light curves from multi-epoch archival data, such as those obtained from the SDSS Stripe 82 survey by MacLeod et al. [2010] and from Pan-STARRS by Simm et al. [2015], as well as studies of ensemble AGN variability [Wold et al., 2007] and many others.

Very rich studies of AGN variability have been conducted in the X-ray band, with a number of important results. Characteristic timescales and candidate quasi-periodic oscillations have been detected in the power spectral density functions (PSDs) of X-ray AGN light curves [Papadakis & Lawrence, 1993, 1995, Uttley et al., 2002, Markowitz et al., 2003, Vaughan & Fabian, 2003, Uttley & McHardy, 2005, González-Martín & Vaughan, 2012]. These characteristic timescales, defined as the point at which the PSD "breaks," or flattens, towards low frequencies, have been found to correlate with the black hole mass in AGN [McHardy et al., 2004]. Recent

work by Scaringi et al. [2015] has shown that across a wide range of accreting objects including AGN, the break frequency scales most closely with the radius of the accretor (in the case of black holes, the innermost stable circular orbit).

Ground-based optical AGN timing has struggled to make the same progress as X-ray variability studies perhaps owing both to poorer photometric sensitivity from the ground and long, irregular gaps in sampling which hampered traditional PSD-analysis approaches. Unfortunately, the X-ray emission in AGN is still far more mysterious than the optical emission. The geometry and location of the X-ray emitter and whether it is a corona, the base of a jet, or some other source is still under contention. It would therefore be desirable to have optical light curves with many of the same properties (e.g., continuous sampling and high photometric precision) as X-ray light curves. This has been finally achieved with the *Kepler* space telescope.

The *Kepler* mission was launched to detect exoplanets in the habitable zone by searching for repeating transits in stellar light curves. In order to detect such transits for planets with orbital periods $\geq$1 year, *Kepler* remained continuously pointed at a region of the sky in the constellations Cygnus and Lyra, chosen for its high density of observable dwarf stars. The *Kepler* mission was broken into 17 individual quarters of data, covering 4.25 years in total, with 30-minute sampling across the full baseline for $\sim 160,000$ exoplanet search target stars and across various partial baselines for Guest Observer proposed targets. Initially, only two AGN were known to exist in the *Kepler* field of view (FOV). Using the infrared photometric selection technique of Edelson & Malkan [2012] and X-ray selection from the *Kepler-Swift* Active Galaxies

and Stars survey [Smith et al., 2015], we have discovered dozens of new AGN in this field with a wide range of accretion rates and black hole masses as measured from single-epoch optical spectra.

Some work has been done on these AGN in recent years. Mushotzky et al. [2011] and Kasliwal et al. [2015] have found that *Kepler* PSD slopes are too steep to be consistent with the predictions of the damped random walk model, and Carini & Ryle [2012] and Edelson et al. [2014] both reported optical characteristic timescales in the *Kepler*-monitored AGN Zw 229-015. We present here a comprehensive analysis of this sample of *Kepler*-monitored AGN, with light curves extracted from a custom AGN-optimized pipeline and Fourier-derived PSD results. We examine the data for correlations with various physical parameters, similarities with X-ray observations, and characteristic timescales. We also present two interesting individual objects, a candidate optical quasi-periodic oscillation and an unusual flare. These data explore a new realm of variability not observable from the ground.

4.2 Selection and Data Reduction

4.2.1 Sample Selection

The majority of our objects were selected using the infrared photometric algorithm developed by Edelson & Malkan [2012]. Their statistic, S_I, is based on photometric fluxes from the 2-Micron All-Sky Survey [2MASS; Skrutskie et al., 2006] and the Wide-field Infrared Survey Explorer [WISE; Wright et al., 2010]. The distribution of S_I among ~ 5000 sources with 2MASS/WISE photometry and

SDSS spectra is bimodal, showing separation surrounding the value of S_I=0.888. Selection below this value indicates a high likelihood of the object being a Type 1 AGN, quasar, or blazar. There is still some small chance that the object is stellar, and so optical spectra are required for positive identification (see next section). In the end, 41 objects met the infrared and spectroscopic criteria for AGN classification. The length of the light curves varies from target to target, depending on when *Kepler* began monitoring each one. Some light curves span a single year, and some span up to four years. We have imposed several criteria for rejection: 1) any quarter falls on Module 3, which failed early in the mission, resulting in quarter-long gaps in the light curve, 2) an overly-crowded field near the target that would unavoidably include stars in the extraction aperture (see Section 4.3.1), and 3) unacceptable levels of rolling band noise in the extraction region. The latter two are further described in Section 4.3.

Three objects were hard X-ray selected in the *Swift*-XRT survey by Smith et al. [2015], which covered four modules of the *Kepler* field and continues currently in the K2 fields. The survey detected approximately 30 new AGN confirmed with optical spectral follow-up, but only four were requested for monitoring before the failure of *Kepler*'s third reaction wheel in 2013. Two of these, Zw 229-15 and KIC 7610713, overlap with the previous infrared-selected sample. The other two X-ray selected targets are the BL Lac object BZB J1848+4245 (KIC 7175757) and the radio galaxy Cygnus A, which is excluded from this analysis because it is a Seyfert 2.

The final sample consists of 21 spectroscopically-confirmed AGN, listed in Table 4.1.

Table 4.1: The *Kepler* AGN

KIC #	RA	DEC	z	Kep. Mag.	log M_{BH} $M_\odot$	log L_{Bol} erg s^{-1}	Edd. Ratio	PSD Slope	τ_{char} days	Q
10841941	18 45 59.578	+48 16 47.57	0.152	17.30		44.95		-2.1		7
10645722	18 47 22.340	+47 56 16.13	0.068	15.69	7.73	44.18	0.023	-2.4		8
7175757	18 48 47.117	+42 45 39.54		18.13				-2.5		4
2694186	19 04 58.674	+37 55 41.09	0.089	13.46	7.66	44.71	0.089	-2.5		10
6932990	19 05 25.969	+42 27 40.07	0.025	11.13	6.91	44.11	0.125	-3.4	16.0	14
2837332	19 10 02.496	+38 00 09.47	0.130	17.62	7.52	44.23	0.040	-2.5		6
9145961	19 11 32.813	+45 34 51.35	0.546	17.11	8.59	45.78	0.124	-1.7		4
12401487	19 11 43.365	+51 17 56.94	0.067	19.42	7.8	44.32	0.026	-2.8	35.7	4
5781475	19 15 09.127	+41 02 39.08	0.222	17.62				-2.2		4
8946433	19 17 34.883	+45 13 37.57	0.078	14.29	7.58	44.77	0.124	-2.4		4
11606854	19 18 45.617	+49 37 55.06	0.918	17.75		46.94		-2.0		12
12010193	19 19 21.644	+50 26 46.25	0.067	16.82		44.80		-2.7	46.2	4
9215110	19 22 11.234	+45 38 06.16	0.115	15.63	7.3	44.14	0.055	-3.0	9.6	8
7523720	19 22 19.963	+43 11 29.76	0.132	17.63	7.37	44.40	0.085	-2.3		4
12158940	19 25 02.181	+50 43 13.95	0.067	14.85	8.04	44.25	0.013	-3.3	31.6	12
12208602	19 26 06.318	+50 52 57.14	1.090	18.45	8.94	46.13	0.123	-1.9		12
9650712	19 29 50.490	+46 22 23.59	0.128	16.64	8.17	45.62	0.226	-2.9	53.0	12
10798894	19 30 10.409	+48 08 25.69	0.091	18.23	7.38	44.36	0.076	-2.4		3
7610713	19 31 12.566	+43 13 27.62	0.439	16.74	8.49	45.74	0.140	-2.5		8
3347632	19 31 15.485	+38 28 17.29	0.158	17.65	7.43	44.66	0.135	-2.4		7
11413175	19 46 05.549	+49 15 03.89	0.161	17.07	7.9	45.01	0.101	-2.8		3

The physical properties of the *Kepler* AGN, sorted by right ascension. The Kep. Mag. is the generic optical "Kepler magnitude" used in the KIC and calculated in Brown et al. [2011]. The final column (**Q**) denotes the number of quarters for which long-cadence *Kepler* monitoring is available.

The original *Kepler* mission spanned ∼4 years, broken up into 17 individual quarters, and ended prematurely when the spacecraft's third reaction wheel failed. Each quarter lasts approximately 90 days; exceptions are the initial Quarter 0 (ten days), Quarter 1 (one month) and the final Quarter 17 (32 days). Between quarters, the spacecraft rotated to preserve the sunward pointing of the solar panels. This resulted in a flux discontinuity across quarters due to the sources landing on different parts of the CCD, presumably with different quantum efficiencies. The *Kepler* detector is divided into 21 modules, each of which has four output channels. Module 3 failed during Quarter 4; thus, any source in that position in the FOV will have quarter-long gaps every three spacecraft rotations. We have excluded all targets that suffered from this, as the principal advantage of *Kepler* is the remarkably even and consistent cadence, which is the basis for our Fourier analysis techniques. Our shortest light curve lasts 3 quarters. Each light curve length is given in Table 4.1.

4.2.2 Optical Spectra and Physical Parameters

In order to positively identify IR or X-ray selected sources as AGN, optical spectroscopy is required. We obtained spectra for all targets across four observing runs: August 2011 and June 2012 using the KAST double spectrograph on the Shane 3-m telescope at Lick Observatory, August 2014 at Palomar Observatory using the double-beam spectrograph, and June 2015 using the DeVeny spectrograph on the Discovery Channel Telescope at Lowell Observatory. We only requested *Kepler* monitoring for confirmed Type 1 AGN, as these are the most likely to exhibit

optical variability. Type 2 AGN suffer from dust obscuration, and have an optical continuum contributed mostly by non-varying galaxy starlight rather than the accretion disk.

Although the spectrographs used had a variety of resolving powers, all were sufficient to measure with confidence the FWHM of the Hβ or Mg II lines. These lines are frequently-used single-epoch tracers of the supermassive black hole mass, $M_{\rm BH}$, which we calculate using the calibrated formulae from Wang et al. [2009] (see their Equations 10 and 11).

The calculation of Eddington ratio requires a proxy for the bolometric luminosity. Although X-ray luminosity is the most reliable, not all objects in our sample have archival X-ray fluxes. For consistency, we therefore use the luminosity at 5100Å and the updated bolometric luminosity corrections by Runnoe et al. [2012].

The parameters calculated from our optical spectra for the full sample are given in Table 4.1.

4.3 Data Reduction of *Kepler* Light Curves

We recognized early in our analysis that the fully-processed archival *Kepler* light curves were unsuitable for AGN science. The mission's original science goal was to find periodic signals in point sources. This is fundamentally different from the signal of interest in AGN science: the variability is stochastic, and the AGN resides in an extended host galaxy (although luminous quasars are typically point sources that outshine their host, most of our sample and most AGN in general are

of the less luminous Sy1 type). Using *Kepler* light curves for AGN analysis requires a number of steps that we have cultivated after several optimization tests. The general outline of the steps described in this section is as follows: 1) modifying the apertures for photometric light curve extraction, 2) assessing and removing objects badly affected by rolling band noise, 3) carefully removing long-term systematics due to spacecraft effects, 4) stitching across observing quarters and interpolation over gaps, and 5) removing spurious behavior during thermal recovery periods.

4.3.1 Customized Extraction Apertures

Kepler extracts its light curves using aperture photometry from a postage-stamp image of the sky surrounding the target, called a Target Pixel File (TPF). Originally designed for stellar extractions, the default apertures are nearly always too small for AGN science because the host galaxies extend beyond the mask. This causes artificial rising and falling of the light curve as the aperture encompasses more or less of the source due to spacecraft drift effects. Thus, the first step in adapting the light curves for AGN is to create larger custom extraction apertures. This can be achieved with the tools `kepmask`, which allows the user to select pixels by hand to add to the extraction aperture, and `kepextract`, which compiles the light curve including the selected pixels, from the PyKe software package [Still & Barclay, 2012]. Some locations on the detector are more subject to drift effects than others, so this and host galaxy shape/size, as well as crowdedness of the field, requires an individual approach to creating the extraction mask. An ideal mask is

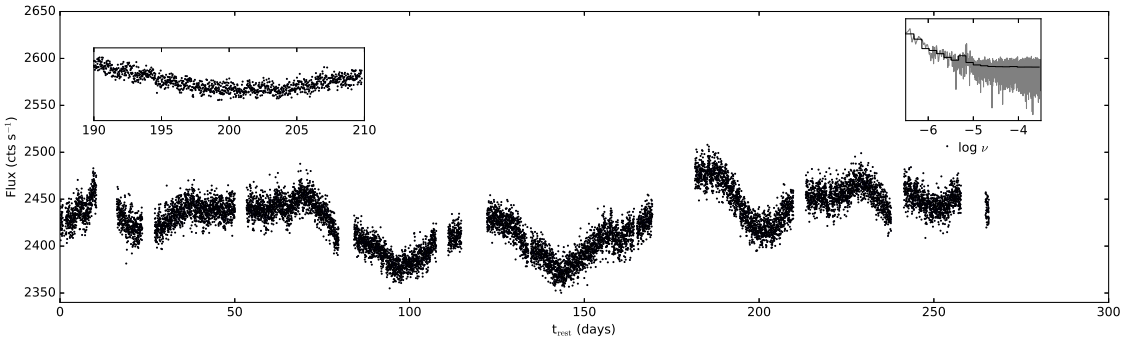

Figure 4.1: Light curve of spectroscopic AGN KIC 11614932, an object with stellar contamination within the extraction aperture. An affected excerpt of the light curve (left) and the power spectrum of the full light curve with the periodic signal visible (right) are shown as insets.

as small as possible to minimize background noise in the light curve, while large enough to fully encompass the galaxy drift throughout the entire duration of the quarter. In order to determine the optimal aperture, we made movies of every 10 frames in each TPF to assess the maximal extent of the drift. The aperture for each source is large enough for a 1-pixel buffer zone around this maximal drift extent. Several objects were necessarily excluded if this optimal aperture happened to include another object in the field. Some examples of these apertures for the previously-studied AGN Zw 229-015 can be seen in Edelson et al. [2014]. For a given object, we used the same aperture shape (i.e., the dimensions and number of total pixels) for every quarter.

As a cautionary tale, we show the case of our spectroscopically-confirmed AGN KIC 11614932. Figure 4.1 shows the full light curve, which exhibits the stochastic variability expected for an AGN. However, at approximately 160 days, a strong

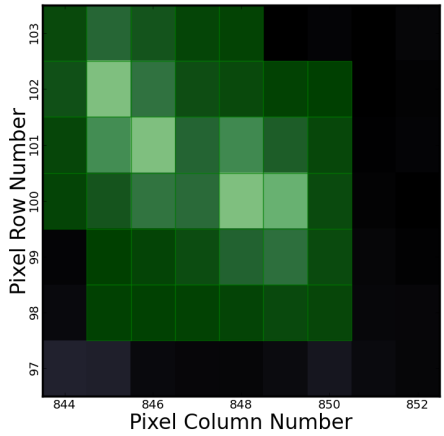

Figure 4.2: The *Kepler* view of the region around KIC 11614932 (shown in the `kepmask` user interface), which clearly includes a nearby contaminating star, with the only aperture possible following our extraction requirements shown in green. This object was rejected from the sample.

stellar variability signature becomes apparent. The $\sim$ 1.6 day periodicity of this star can also be seen in the PSD (inset in the figure). The star in question was close enough to the extended AGN host galaxy that it was impossible to remove from the mask while still encompassing the drift effects. Only partially encompassing the star will also result in drift effects. The only possible aperture is shown in Figure 4.2. Our recommendation is to always compare one's extraction aperture with the highest-available resolution images of the sky in the vicinity of the object to ensure that such contamination is unlikely.

4.3.2 Rolling Band Noise

Electronic crosstalk between the science CCDs and the fine guidance sensor clocks produces an interference pattern known as rolling band noise or "Moire

pattern noise," which moves across the detector [Kolodziejczak et al., 2010]. The Dynablack algorithm module in the *Kepler* pipeline [Van Cleve & Caldwell, 2016] assesses the level at which this pattern affects any given pixel. All TPFs from Data Release 25 (the most current at the time of this writing) include a column (RB_LEVEL) with this information, given as a severity level in units of detection threshold calibrated to 20 ppm for a typical 12th magnitude star (see Section A.1.1 in the data release notes for DR25). We have made plots of this severity level versus observing cadence for each object, and reject any object where the RB_LEVEL severely affects a quarter. The detection threshold in our targets is considerably higher than for a 12th magnitude star, but the rolling band level rarely exceeds 2.0 in the majority of objects. We show three example cases in Figure 4.3. In cases such as KIC 10663134, the object was rejected due to serious rolling band contamination; the effect of the rolling band on the light curve is shown in Figure 4.4. Occasionally, the pattern is flagged to affect one to five individual 30-minute cadences, but immediately returns to undetectable levels. This can be seen in KIC 3347632. In these cases, we simply ignore the *Kepler* flux for those cadences and linearly interpolate over them.

4.3.3 Long-term Systematics

Large extraction masks still do not fully remove the spacecraft systematics. In particular, there are long-term trends in the data which are well known, especially differential velocity aberration (DVA). For the long-timescale drifting, corrections

Figure 4.3: Rolling Band Severity Levels for Representative Cases

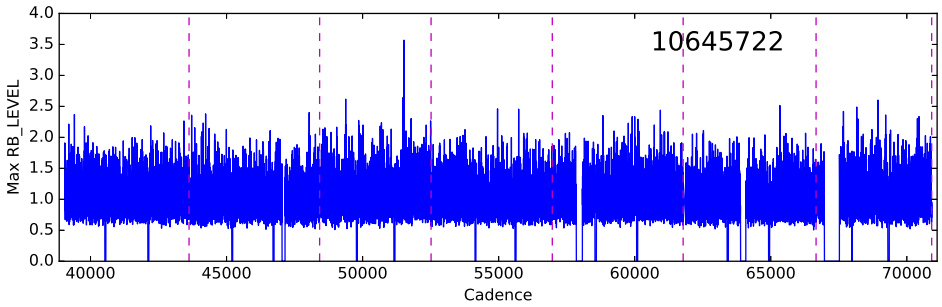

(a) A typical object from the sample in which the rolling band severity level does not significantly exceed 2. Pink dashed lines denote quarter boundaries.

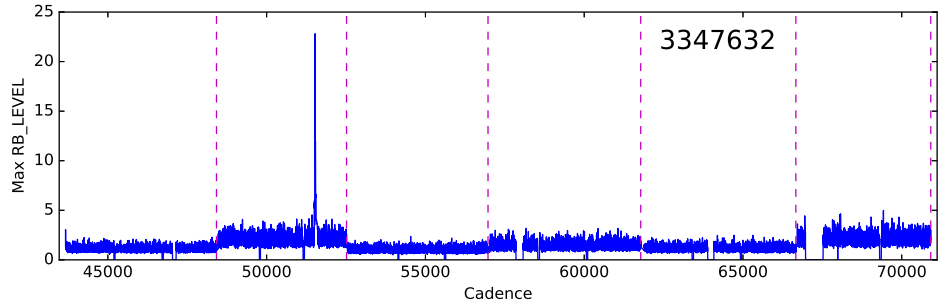

(b) An object in which the rolling band severity level spikes for a single cadence or a few subsequent cadences. In these cases, the fluxes are ignored and interpolated over. Pink dashed lines denote quarter boundaries.

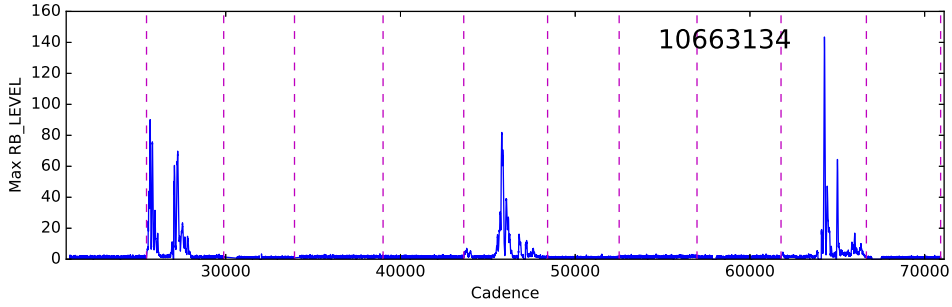

(c) An object which was rejected due to significant and persistent rolling band contamination. Pink dashed lines denote quarter boundaries

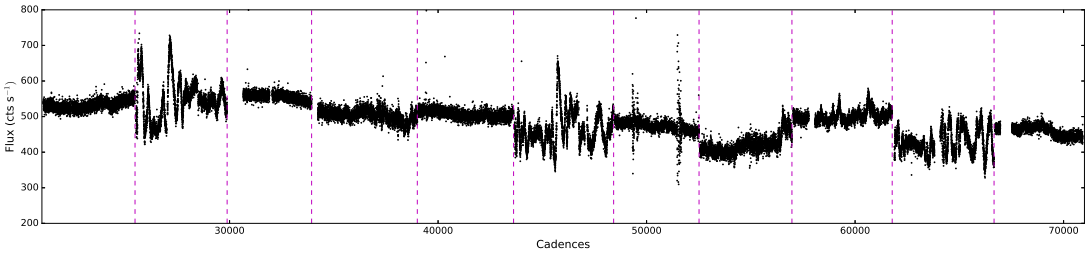

Figure 4.4: Light curve of KIC 10663134, an object badly affected by rolling band noise as shown in Figure 4.3.

can be obtained using the cotrending basis vectors (CBVs). A full description of their application can be found in the *Kepler* Data Characteristics Handbook. In short, although stars can vary, their variability should not be correlated with each other. The *Kepler* software keeps track of a series of sixteen orthonormal functions that represent correlated features from a reference ensemble of stellar light curves. One can remove systematic trends by fitting these CBVs to a given light curve. The over-application of these vectors can easily result in over-fitting of the light curve, especially in AGN, whose intrinsic variability mimics these trends. The ideal choice of number of applicable CBVs is therefore an optimization process between removing long-timescale systematics and overfitting genuine physical signal, a difficult balance to strike in stochastically varying sources.

The Data Characteristics Handbook points out that typically, eight CBVs is ideal for removing instrumental trends from stellar targets, flattening them enough to enable transit searches. Eight CBVs always over-fit AGN in our trials, as spacecraft systematic features coincidentally overlapped with intrinsic behavior. We could see this by examining the CBVs themselves and nearby stars, noting that the de-

gree to which a given CBV trend was actually present in the data was quite weak compared to the weight given to it in fitting a coincidentally-varying segment of an AGN light curve. In order to assess the optimal number of CBVs for fitting AGN light curves, we have incrementally increased the number from 1 to 8 while tabulating these effects. We have conservatively determined that two CBVs is the optimal number for correcting our large-aperture extracted light curves. After this point, legitimate variability begins to be mitigated by overfitting. In the interest of reproducibility and consistency, we apply the same number of CBVs to each light curve. To illustrate the degree to which systematics likely still remain in the light curves, we apply two CBVs to three stars chosen from different locations on the *Kepler* detectors. These stars were not selected by any of the numerous stellar variability surveys of the *Kepler* field and are likely to be intrinsically quiet. We extracted their light curves across various sets of quarters in the same manner as our AGN (although this is not strictly necessary, since these stars are point sources without the extended emission that necessitates the approach in AGN), and applied the first two CBVs to each one using the PyKe task `kepcotrend`. Figure 4.5 shows the results. Long-timescale systematic trends are clearly removed, leaving the light curves mostly flat. Although some artificial variability surely remains, we have eliminated the trends most likely to affect our power spectral density analysis while preserving as much intrinsic AGN variability as possible.

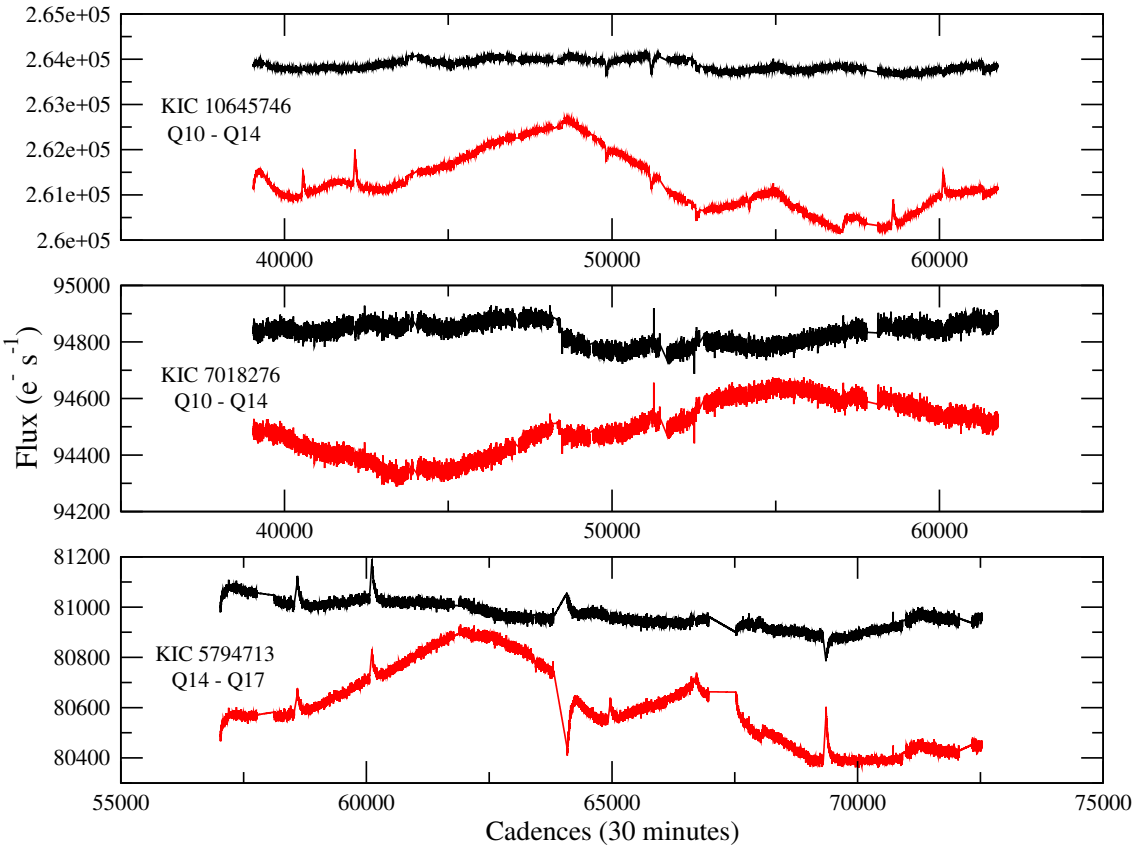

Figure 4.5: Light curves of three quiet stars before (red) and after (black) the application, fitting, and removal of the first two cotrending basis vectors.

4.3.4 Interquarter Stitching and Interpolation

The next obstacle is the inter-quarter discontinuities introduced by spacecraft roll. We have chosen to additively scale the light curves based on the average fluxes of the ten cadences before and after the discontinuity (from the light curves with the previously described extraction and CBV corrections already applied). Multiplicative scaling frequently resulted in artificial inflation of flare-type features, and so we consider it less physically valid.

Finally, there are various data flags which were tabulated by *Kepler* as the data collection proceeded, including those for attitude tweaks, reaction wheel zero crossings, intervals where the spacecraft briefly paused to transmit data to Earth, cosmic ray detections within the extraction aperture, etc. (see Table 2-3 in the *Kepler* Archive Manual). We have excluded cadences with any of these data flags. In most cases, these exclusions consist of a single cadence, or 2-3 cadences grouped together. We have linearly interpolated over these gaps. In some cases, especially when the spacecraft is in Earth-point for data transmission, as many as $\sim$600 sequential cadences (12.5 days) can be flagged. To maintain the even sampling required for our method, we have also linearly interpolated over these gaps, inserting a point where each cadence would be (every 29.4 minutes). We have also interpolated over the gaps in between quarterly rolls (typically about 1 day). One might naturally wonder whether this interpolation method would affect the measured power spectral slopes or other properties. By interpolating linearly, we are not introducing any additional spectral power at a particular frequency, especially because the gaps are

irregular and brief. We have performed both simple linear interpolation, as well as linear interpolation based on the LOWESS method of smoothing the existing data points and making calculations based on local values [Cleveland, 1979]. The power spectral density slopes are nearly identical (to the 0.01 level) for both methods. In no case do the interpolated points consist of more than 10% of the total light curve. Interpolated fluxes are used only in the power spectrum Fourier analysis, and are of course excluded from estimates of the light curve variance, rms-flux relation analysis, and flux distribution histograms.

4.3.5 Thermal Recovery Periods

After the monthly data downlinks which require the spacecraft to change position for transmission to Earth, the photometer experiences thermal gradients. These result in focus changes, which eventually settle around 2 to 3 days after the downlink. The result is a transient-like flare or dip in the light curve. This period of focus settling is referred to as "thermal recovery." These cadences are not flagged by the *Kepler* pipeline, but the Earth-pointed downlinks are. In order to prevent these downlinks from affecting our analysis, we automatically replace the 150 cadences ($\sim$3 days) following an Earth-point flag with linearly interpolated data. The thermal recoveries can profoundly affect the power spectra, especially in high S/N light curves.

As an example, in Figure 4.6 and Figure 4.7 we show the result of flagging and removing the thermal recovery periods from the light curve of KIC 9650712. There

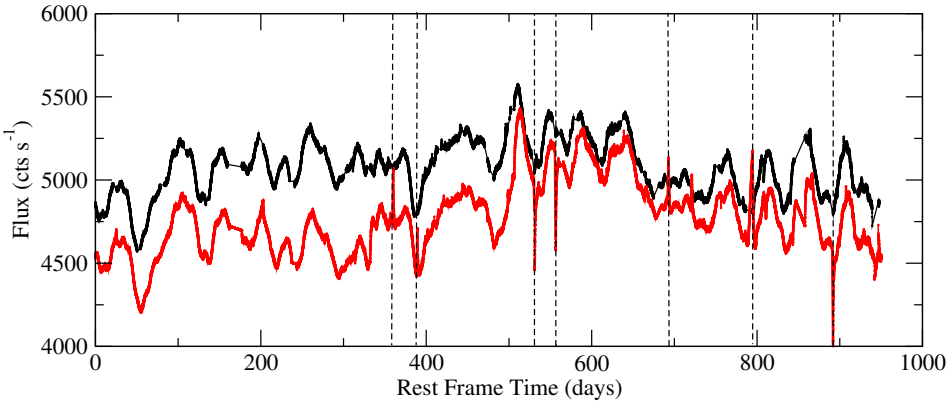

Figure 4.6: Light curve of KIC 9650712 before (red) and after (black) the correction of thermal recovery periods. The occurrences of some significant thermal events are shown by dotted lines.

is no other difference between the reduction methods of the light curves displayed in the graphs. The power spectrum (Figure 4.7) is clearly affected, displaying a spurious characteristic timescale when generated by the uncorrected light curve.

4.4 Light Curves

The final reduced light curves of the sample are given in Appendix A. In the first set of figures, the axes are scaled differently for each object so that interesting features can be seen, and time axes have been corrected to the galaxy's rest frame using the spectroscopic redshift. The only exception is KIC 7175757, which is classified as a blazar and has no spectroscopic features. Since a redshift could not be determined for this object, the light curve is shown in the observed frame.

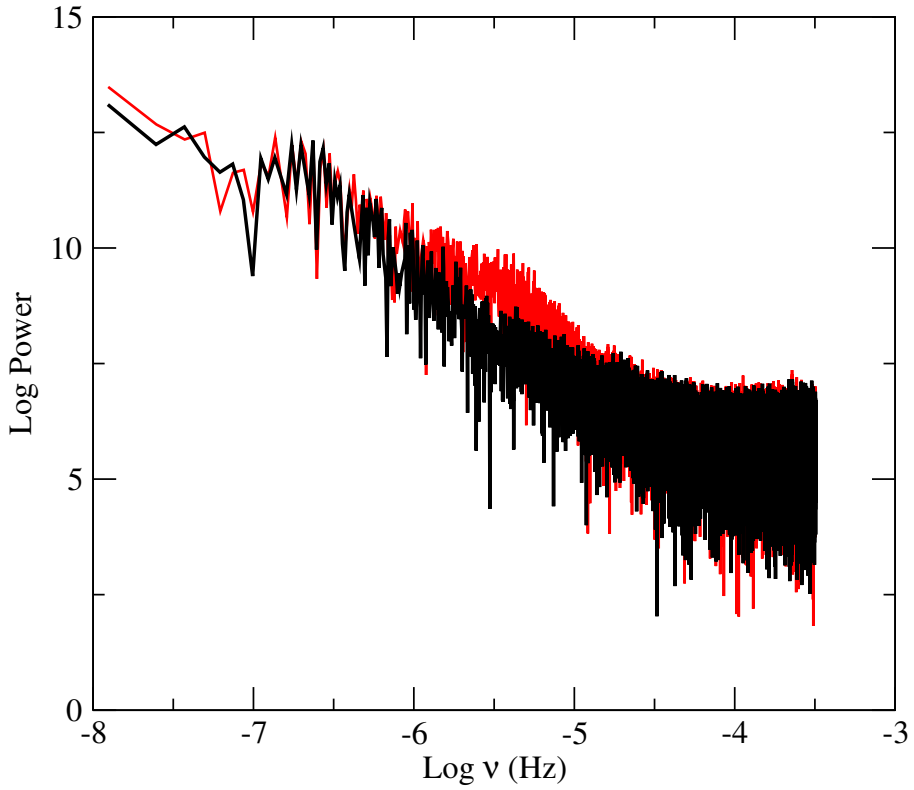

Figure 4.7: Power spectrum of KIC 9650712 before (red) and after (black) the correction of thermal recovery periods, generated from the light curves shown in Figure 4.6.

In order to better highlight the differences in behavior and monitoring baseline, the second figure in Appendix A shows the same light curves, but on identical flux and time-baseline axes. The y-axis range is chosen to be 30% of the mean flux (15% in either direction). It is immediately obvious that most of the apparently-dramatic behavior in the light curves is well below the 10% variability level, often occurring at approximately the 0.1-5% level. Such variability would be very difficult to detect in ground-based variability surveys with current instruments. This is an important point: many AGN which are currently classified as non-variable are probably quite variable at these levels. All of the 21 spectroscopically-confirmed Sy 1 AGN in our sample exhibited some degree of variability. There are some cases, however, in which a shorter monitoring interval would have resulted in an object seeming non-variable. Take, for instance the case of KIC 12208602: except for the discrete event that begins at approximately 220 days in the rest frame, the light curve is statistically flat. This work exemplifies the importance of high-cadence, high-sensitivity, long-baseline monitoring for the classification of AGN as variable or otherwise based on optical light curves. We should refrain, for example, from drawing conclusions about obscuration and the unified model that rely on variability classifications from ground-based light curves

4.5 Power Spectra

The shapes of the power spectral density functions (PSDs) are the product that is most immediately comparable to theoretical expectations. This function

shows the relative power in the variability as a function of temporal frequency. The variability of AGN is a red noise process, meaning that successive samples are correlated in time. The power spectra of such processes are well described by a power law, where the spectral density S varies with the temporal frequency as $S \propto f^{\alpha}$. Our investigation of the power spectral density functions (PSDs) has two main goals. The first is to determine whether any of our objects shows evidence for a characteristic variability timescale, which manifests as a "break" in the power law, causing the PSD to be best fit by a steep power law at high frequencies and a shallower power law at low frequencies (e.g., a piecewise linear function in log-log space). The position of such a break, $\nu_{\rm char}$, and its corresponding timescale, $t_{\rm char}$ could conceivably be connected to a series of relevant physical timescales in the disk (e.g., the viscous, dynamical, and thermal timescales). Additionally, the MHD model of Reynolds & Miller [2009] predicts characteristic frequencies in the power spectrum that correspond to local acoustic waves. Break timescales have been reported in a few *Kepler* AGN, with inconsistencies in the only object studied by multiple authors: Carini & Ryle [2012] found that Zw 229-015 could be modeled as a break either at ∼95 or ∼43 days, while Edelson et al. [2014] reported an optical break timescale of ∼5 days.

The second goal is to measure the slope of the high-frequency portion of the PSD. The high-frequency slopes of optical PSDs have been found by many to be $\alpha \sim -2$ [e.g., Czerny et al., 2003, Koslowski et al., 2010, Zu et al., 2013]. This value is appealing, because it is the same as the high-frequency slope observed in the X-ray literature and it is consistent with the very popular "damped random walk"

model for AGN variability proposed by Kelly, Bechtold & Siemiginowska [2009]. However, earlier work using *Kepler* has been in disagreement with ground-based studies. Mushotzky et al. [2011] published early results for four *Kepler*-monitored AGN, and found that their PSD slopes were inconsistent with predictions from the damped random walk model. The slopes reported varied from $\alpha = -2.6$ to -3.3. This is considerably steeper than previous optical PSD measurements. This conclusion was also reached by Kasliwal et al. [2015], who found that the damped random walk model was insufficient to capture the range of *Kepler* AGN behavior.

To create our power spectra, we use the light curves produced as described in Section 4.3, including interpolation to enable Fourier methods. We then fit the entire light curve with a line, and remove this linear trend. This will remove the lowest-frequency component of the power spectrum. Although any linear rise or fall across the full baseline might indeed be real, we must use consistent methodology to study the variability in the same time regime for all objects. By removing this trend, all of the PSDs are now on equal footing for studying variability on timescales of 1 to 100s of days. The mean of these flattened light curves is subtracted, and a simple discrete Fourier transform is performed. We have normalized the light curves by a constant $A^2_{\rm rms} = 2\Delta T_{\rm samp}/\bar{x}^2 N$, where $\Delta T_{\rm samp}$ is the sampling interval, $\bar{x}$ is the mean count rate in cts s^{-1}, and N is the total number of data points. This normalization was defined by Van der Klis [1997] and is cited by Vaughan & Fabian [2003] as particularly useful for AGN, since the integrated periodogram yields the fractional variance of the light curve. In this scheme, the expected Poisson noise is given by Equation A2 in Vaughan & Fabian [2003], with the mean background count

rate estimated from several background pixels nearby the source. We also resample the power spectra into 25 frequency bins, for fitting purposes. The resulting PSDs are shown in Appendix B, along with the best-fitting power law models that we describe next.

In order to determine the best-fitting high-frequency slope and the significance of any characteristic break frequencies, we employ the Monte Carlo method described in detail by Uttley et al. [2002]. Such methodology is necessary for measuring goodness-of-fit of various power law models, because it allows for an estimate of the error bars on the observed PSDs. We describe it briefly here.

First, we use the Timmer & König [1995] method to simulate a very long light curve with a given PSD slope. This light curve is made long enough that 500 light curves of the same length as the actual observations can be drawn from it without overlap, and with three-times finer resolution than the observed light curves. This mitigates the effects of both red noise leak and aliasing (see the discussion in Uttley et al. 2002). We rebin the simulated light curve to have the observed sampling (i.e., the bins have three measurements each). We then introduce gaps with the same location and duration as those in the observed light curve to each of the 500 simulacra, and treat them precisely as we treated the observed light curves, with the same flattening and interpolation techniques. This new simulated set is used to create 500 power spectra. The rms spread of the simulated power spectra about the mean determine the "error bars" on the observed power spectra. We can then fit the data to the model, and calculate a χ^2 value. We do not fit any data that is beyond the cutoff where Poisson noise takes over in the light curve, shown by the dashed lines

in the figures in Appendix B. Importantly, the χ^2 value obtained from this fit cannot be compared to the standard χ^2 distribution. To create a comparable distribution, we measure each of the 500 simulated power spectra against the model and create a sorted distribution of their χ^2 values. The goodness-of-fit of the observed power spectrum to the model is then measured by calculating the percentile value above which the observed χ^2 exceeds the simulated distribution. This percentage is the confidence with which we can reject the model.

We do this for each object separately (so that each distribution of simulated power spectra have the same gaps and sampling as the observations), for PSD slopes of $-1.5 \leq \alpha \leq -3.5$, in steps of 0.1. The slope that can be rejected with the least confidence is the slope we consider to be the best fit for each object. These slopes are given in Table 4.1, and are shown as a histogram in Figure 4.8. Most of our slopes agree with previous results in that they are steeper than $\alpha = -2$, with some slopes steeper than -3 [Mushotzky et al., 2011, Kasliwal et al., 2015]. Some objects have slopes consistent with -2. Our two radio-loud objects, KIC 12208602 and KIC 11606854, are well-fit by $\alpha = -1.9$ and -2.0 respectively. These relatively shallow slopes are the same as those measured for these objects by Wehrle et al. [2013].

If all of the models in the set of α values can be rejected with more than 75% confidence, we examine the PSD for flattening at low frequencies by testing whether or not a reduction in χ^2 occurs with a broken power law model. If the broken model is a better fit, we calculate the turnover frequency by fitting the high-frequency data with the best-fitting slope, and iterating a model with break frequencies in the

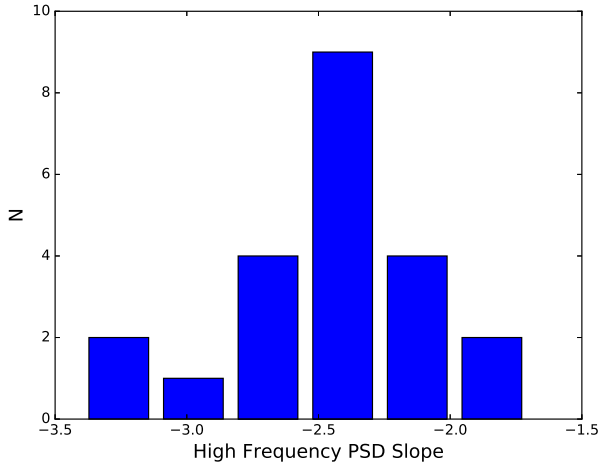

Figure 4.8: Histograms of the best-fitting high-frequency PSD slopes as measured by the simulations described in Section 4.5.

range of $-5.5 < \log \nu < -7.0$ in steps of 0.1. The break frequency resulting in the best reduced χ^2 value is given in Table 4.1. Of the 21 objects in the sample, 6 demonstrate significant low-frequency flattening in which a broken power-law model represents a reduction in χ^2. The χ^2 values are given in Table 4.2 and their PSDs are shown in Figure 4.9. Another object, KIC 9650712, is poorly fit by all of our values of α, and is better fit by a broken power law with $t_{\rm char} \sim 53$ days. However, it can also be well-modeled as a single power law with the addition of a quasi-periodic component. For this reason we use a different symbol for this break timescale in plots, so that readers may ignore it in this context. The possibility that this is a detection of an optical quasi-periodic oscillation (QPO) is discussed in Section 4.6.3. We also point out that unfortunately, the Hβ line in KIC 12010193 is too weak and noisy to permit a reliable black hole mass measurement, and so it is omitted from

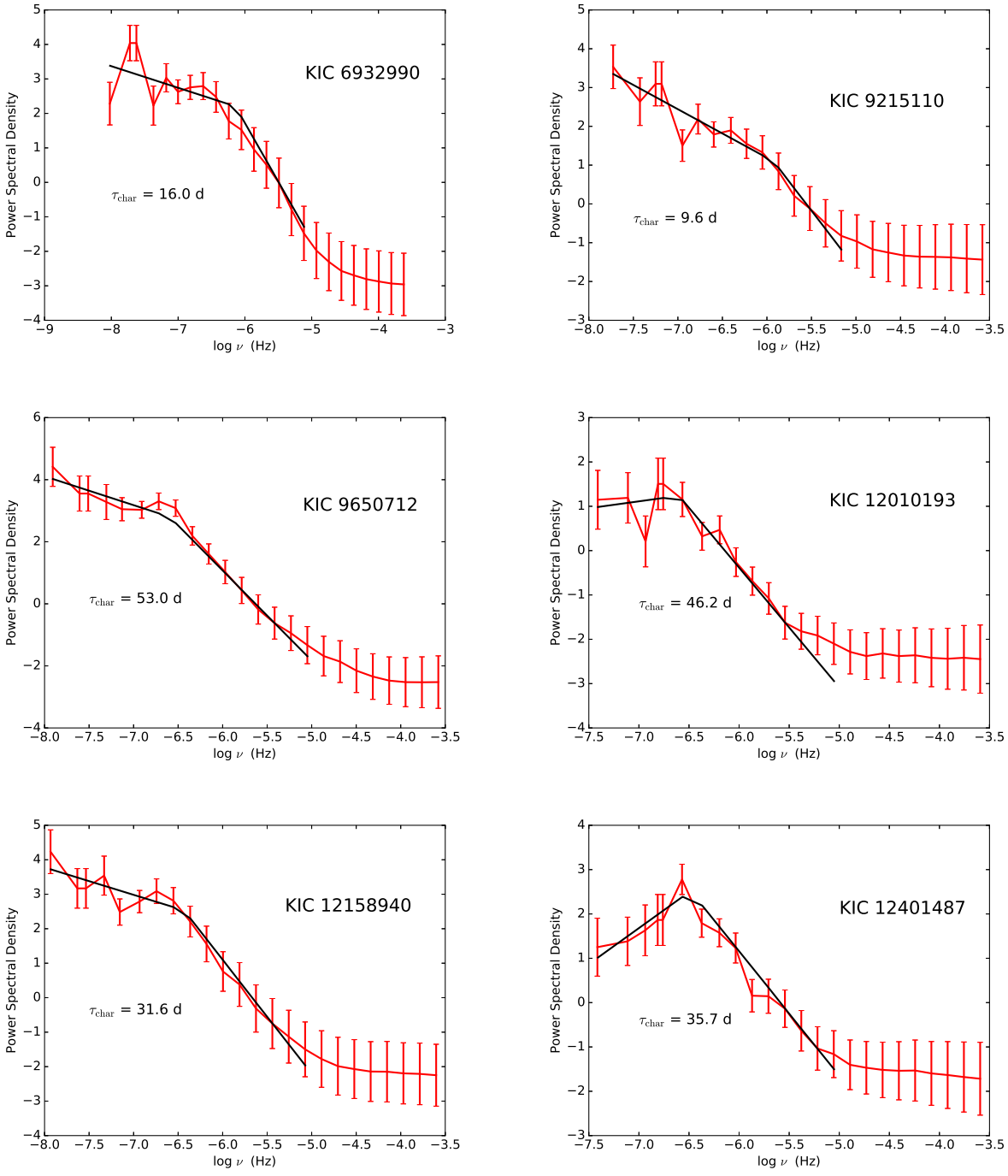

Figure 4.9: Power spectra of the six AGN which require a broken power-law model for an acceptable fit. Error bars are derived from the Monte Carlo method of Uttley et al. [2002]. The best-fitting break timescale is shown in each plot. See Section 4.5 for details concerning the fitting.

Table 4.2: χ^2 in Broken Power-Law AGN

KIC #	χ^2 Single	χ^2 Broken	Red. χ^2 Single	Red. χ^2 Broken
6932990	76.05	13.44	6.91	1.22
12401487	46.9	7.0	4.69	0.70
12010193	18.18	10.9	1.81	1.09
9215110	51.12	7.15	5.11	0.71
12158940	35.46	73.4	3.22	0.56
9650712	37.87	7.46	3.44	0.67

Values of χ^2 and reduced χ^2 for the objects with candidate characteristic timescales.

the plots of variability versus physical parameters in Section 4.6.2.2.

4.6 Results

The goal of this project and future analyses is twofold: to determine whether any AGN physical parameters, or combination thereof, correlates with variability statistics in such a way as to clarify the physical mechanism of accretion and enable large-scale measurements of AGN parameters in future surveys, and to determine the extent to which the optical and X-ray variability is interrelated. We can attain the first goal using the parameters measured by our optical spectra, and checking for correlations across a comprehensive set of variability metrics and PSD properties based on the existing literature. We can attain the second goal by comparing the *Kepler* timing behavior to well-known properties of X-ray variability in AGN; if the optical light curves exhibit similar properties, albeit on slower timescales, we can assume that a large fraction of the optical variability is the result of reprocessing.

Before discussing our results, we would like to emphasize that the *Kepler* light curves are probing an entirely new regime of variability, on timescales of hours with year-long baselines, and with ∼few percent amplitudes that would often be

undetectable from the ground. These results should be viewed as the properties of this new regime, not as contradictions or confirmations of ground-based optical timing studies.

4.6.1 RMS-Flux Relationships and Flux Distribution Histograms

The traditional model for AGN accretion disks is the standard optically thin, radiatively thick α-disk [Shakura & Sunyaev, 1973]. Although broadly consistent with spectral observations, this model is challenged by the fact that it should be thermally and viscously unstable, especially in the radiation-dominated inner regions where accretion is taking place. As Kelly, Bechtold & Siemiginowska [2009] point out, variability is a natural probe of temperature fluctuations within the disk since they lead to an understanding of the stress-pressure coupling, and can provide a powerful test of the traditional α-disk model.

Numerous theoretical models which deviate from or complicate the α-disk have been proposed to explain the observed variability. The most intuitive explanation is fluctuations in the global mass accretion rate: radiation output increases and decreases as more or less matter is converted into energy. This model has enjoyed broad consistency with some observations of luminous quasars [Gu & Li, 2013], but struggles to explain the short timescales of the variability: as matter is added to the disk, the rate at which this increases the total optical radiative output is approximately the viscous time. For typical black hole masses, this can be hundreds of years, while variability is seen on timescales of days and hours. A more favored

idea is that the rapid optical variability is powered by reprocessing of fast variations in the X-ray and far-UV light very close to the black hole, which can happen on the requisite timescales.

In the traditional model, α is a constant that embodies one prescription of the stress-pressure coupling which governs the outward transport of angular momentum and, thereby, the inward transport of material for accretion. More realistic prescriptions allow α to vary throughout the disk. These inhomogeneities can be generated by various instabilities, especially the magneto-rotational instability [MRI; Balbus & Hawley, 1991]. Local fluctuations then propagate inwards with the accreting material.

Steady advances in the resolution and power of magnetohydrodynamic simulations have suggested several observable consequences of the propagating fluctuations model. One testable prediction is that histograms of the fluxes observed in a light curve will be log-normal, rather than gaussian. This has been seen in X-ray light curves of galactic black holes [e.g., Uttley & McHardy, 2005], but not optical. They also predict that the rms varability of a given segment of the light curve will linearly correlate with the mean flux of that segment. This has also been seen in X-ray AGN variability studies, as well as X-ray light curves of stellar mass black holes and accreting neutron stars [Uttley & McHardy, 2001, 2005], but has not been sought after in optical AGN light curves. If indeed the fluctuations originate further out in the disk where optical emission dominates, and then move inward to cause the observed X-ray variability, we should see these traits in optical AGN time series. Understanding the origin and interaction of the X-ray and optical emitting regions

will enable tight constraints on important theoretical questions in AGN physics, especially on shape and location of the X-ray corona.

We have rebinned each light curve into 2-day bins to overcome noise fluctuations, and then cut each light curve into 50-day segments. For each segment, we calculate the mean flux and the standard deviation of the flux values. None of our objects exhibits any correlation between these two quantities. A typical plot is shown in Figure 4.10. This is in stark contrast to X-ray light curves of AGN, which show remarkably tight linear correlations between flux and variability [e.g., Edelson et al., 2002, Vaughan et al., 2003, McHardy et al., 2004] that are also seen in stellar-mass black holes [Uttley & McHardy, 2001]. X-ray light curves typically probe much shorter timescales (on the order of seconds to minutes for AGN) than optical light curves, so this result may indicate that the origin of the variability on day to year timescales is not simply reprocessing of faster variability in the X-ray emitting region.

We have also created histograms of the fluxes in each light curve (without interpolation). These have a wide variety of shapes in our sample and are shown in Appendix C. Some are well-fit by log-normal distributions, as predicted by the propagating fluctuations model and frequently seen in X-ray AGN variability studies, but most are best represented by other shapes. Perhaps the most intriguing are those that are best-fit by a bimodal distribution of two gaussians. The light curves of these objects in Appendix A are marked by red dotted lines that denote the peak values of each gaussian component. Most of the time, the bimodal behavior is due to the AGN seeming to transition to a lower flux state, and then return to the orig-

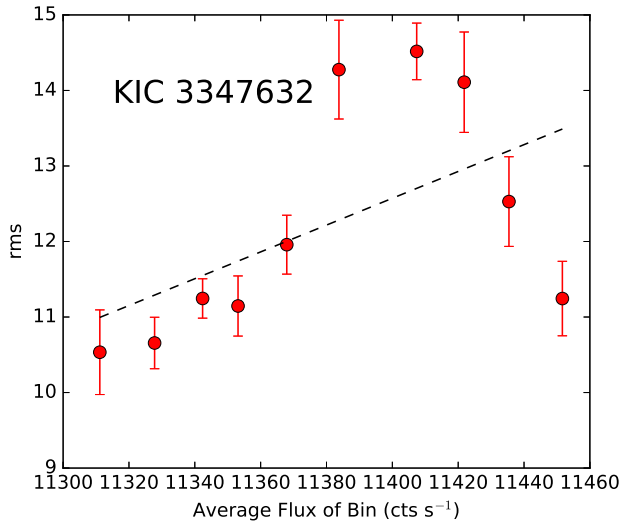

Figure 4.10: Typical rms-flux relation plot showing no correlation between the two quantities.

inal state several hundred days later, as exemplified in KIC 3347632, KIC 9145961, KIC 9215110, and KIC 10841941. The fact that the light curve tends to return to the the same average original flux could indicate preferred accretion states; however, the fact that the variability properties do not seem to change when the object is in a low or high state is perhaps contrary to expectations for state transitions. Another possible explanation is the passing by of obscuring material. One can imagine a cloud of gas and dust passing in front of an unobscured varying continuum source, dimming the source without affecting the observed variability. When the cloud had passed, the average flux would return to the original state, as we see in these cases.

One might expect that objects with high X-ray/optical flux ratios would be more likely to experience significant reprocessing and therefore more likely to show the same properties as X-ray light curves. Of our 21 objects, 17 have archival X-ray

information in the Second ROSAT All-Sky Survey [Boller et al., 2016] or XMM Slew Survey [Saxton et al., 2008]. We converted the X-ray count rates to fluxes assuming a power law with $\Gamma = 1.8$ as the X-ray spectral slope and galactic column densities from Kalberla et al. [2005]. For optical fluxes, we use the same 5100Å or 3000Å flux that was measured for bolometric luminosity calculations in Section 4.2.2. In the case of XMM data, we use only the flux in Band 6, 0.2-2 keV, which is the closest XMM band to ROSAT (0.1-2.4 keV). Although these are approximate measures, especially since they are disparate in time from the optical spectra, we require only a qualitative handle on the degree to which the X-ray flux may influence the optical behavior. The values range between $F_X/F_O = 0.03$ to 4.21, with a mean of 0.08. None of these is particularly high. As stated before, there is no variability-flux relationship even for the highest F_X/F_O objects. We also do not see any tendency for higher F_X/F_O objects to be more often well-fit by lognormal distributions.

4.6.2 Variability Properties and Physical Parameters

4.6.2.1 A Brief Summary of Past Results

Next, we test for possible correlations of various properties of the optical variability with the physical parameters of the AGN: black hole mass ($M_{\rm BH}$), bolometric luminosity ($L_{\rm bol}$), and Eddington ratio ($L/L_{\rm Edd}$). We have measured these properties from the optical spectra as described in Section 4.2.2. Correlations would offer physical insight into the geometry and causal relationships within the central engine and potentially enable measurements of vast samples of black hole masses and ac-

cretion rates from easily-observed variability statistics. If this can be accomplished, upcoming large timing surveys like LSST would have unprecedented insights into the cosmological buildup of black holes in the universe, with implications for galaxy evolution and the growth of structure.

The literature on this subject is varied and often contradictory. This arises from two principal points. First, any given study must choose how to quantify the "variableness" of a light curve. Many authors invent their own measures of variability; for example, Wold et al. [2007] use the standard deviation, mean, median and maximum of the distribution of values of $\Delta m_{ij} = m_i - m_j$, the difference in magnitude of subsequent photometric measurements. Kelly et al. [2013] use the square of a parameter of the Ornstein-Uhlenbeck process that describes the strength of the driving noise, ς^2, which controls the amplitude of variability on timescales much shorter than the characteristic time. There are other such examples, and most of them indeed capture the "strength" of variability across sources, but at the cost of complicating comparisons between different works. The second sticking point in the literature is the great variety of sources of light curves, with significant differences in sampling rate and uniformity, photometric accuracy, and the properties of the AGN sample. The relatively small literature ranges from studies of 13 Sy1 galaxies from AGN Watch [Collier & Peterson, 2001] to ensemble studies of tens of thousands of quasars from the Palomar-QUEST survey [Bauer et al., 2009]. Depending on the properties of the light curves, authors choose to use structure functions, power spectra, or autocorrelation analyses. In addition to the different analysis techniques, the intrinsic variability properties of relatively low-luminosity Seyferts may be quite

different from luminous quasars, and there is even evidence that radio loudness might be correlated with variability [most recently, by Rakshit & Stalin, 2017] - and so, the selection effects that plague the rest of AGN literature are also at work here.

Space-based light curves like those from *Kepler*, K2, and TESS have the potential to address some of these problems, in that their sampling rate, uniformity, and photometric precision is far better than ground-based surveys. Such light curves can be downsampled to resemble any ground-based survey, and the timing results from a given study could be compared to the "true" behavior (the space-based measurements being, presumably, as close as we can get).

The *Kepler* sample of AGN is small, due to the unexpectedly short lifetime of the spacecraft preventing our obtaining long-baseline light curves of a much larger sample (see Section 4.2). Because of this, we cannot bin by physical parameter, which is a strong limitation since the variable behavior in any given light curve will likely dilute any correlations with physical origins.

There are a few conclusions that seem to be reasonably consistent across the optical variability literature so far. First, variability has been seen to correlate with redshift and hence anticorrelate with rest wavelength, which is best understood as the tendency of UV light to be more variable than optical [e.g., Cristiani et al., 1997]. An anticorrelation between luminosity and variability was first discovered by Angione & Smith [1972], and has been confirmed many times since. This relationship was seen by Hook et al. [1994] in a sample of 300 optically-selected quasars, by Cristiani et al. [1997] in a sample of 149 optically-selected QSOs, by Giveon et al.

[1999] in a sample of 42 Palomar-Green quasars, by Kelly et al. [2013] in a sample of 39 AGN, by Simm et al. [2016] in 90 X-ray selected AGN across a broad redshift range, in ensemble studies of thousands of quasars binned by luminosity and black hole mass [Bauer et al., 2009, Wilhite et al., 2008, Zuo et al., 2012], and all the way into the most recent studies of Seyferts in the Catalina survey [Rakshit & Stalin, 2017]. In contrast, Wold et al. [2007] do not see any trend between variability and luminosity in a matched sample between the Quasar Equatorial Survey Team Phase 1 (QUEST1) survey and the SDSS; however, they believe this may be due to the strong trend between redshift and luminosity in their data.

While the relationship with luminosity seems fairly well established, the relationship of various properties with black hole mass and Eddington ratio is much less certain. Wold et al. [2007] found a scattered, positive correlation between variability (measured using the Δm_{ij} criterion described above) and $M_{\rm BH}$. This was also seen by the ensemble study of Bauer et al. [2009], and Giveon et al. [1999] reported a positive correlation between variability and Hβ equivalent width. In contrast, Kelly et al. [2013] found a scattered anticorrelation between their ς^2 variability measure and $M_{\rm BH}$, as well as a weak anticorrelation of variability and Eddington ratio. Simm et al. [2016] found no relationship between variability amplitude and $M_{\rm BH}$, and an anticorrelation of the excess variance and variability amplitude with Eddington ratio. Finally, Zuo et al. [2012] found that whether or not variability and $M_{\rm BH}$ were correlated depended on the Eddington ratio and luminosity.

Having summarized the current state of confusion, we will now present our results, which as stated before should be viewed as the properties of an entirely

different sort of variability than those reported on before.

4.6.2.2 Correlations with Physical Parameters

We have chosen to measure the variability of our light curves via two metrics. Before calculating either of these quantities, we rebin our light curves into 2-day time bins, to mitigate gaps and overcome the effects of noise.

The first measure of variability is the standard deviation of the distribution of values of the difference between subsequent flux measurements. We calculate the distribution of $\Delta F_{ij} = F_i - F_j$ between each set of subsequent flux measurements. We fit this distribution with a gaussian, the width of which is our variability criterion $\sigma_{\Delta \mathrm{F}}$. As an example, Figure 4.11 shows this distribution for KIC 10645722. Our second measure of variability is simply the standard deviation of the binned light curves. Figure 4.12 compares these two metrics for the objects in our sample. Both capture variability and quantify it generally the same way, but there is scatter at low variability. We believe there is value in exploring correlations with both metrics, since there is such a wide variety of homegrown metrics used in the literature. The values of $\sigma_{\Delta \mathrm{F}}$ and the standard deviation are given in Table 4.3.

We first note that our sample, unlike most others, does not show higher variability at higher redshifts. In fact, the opposite is true. This is most likely because our few high-redshift objects are also our most massive black holes, which tend to vary less or at least more slowly than the other objects in our sample. This relationship is shown in Figure 4.13.

Table 4.3: The Variability Properties of the *Kepler* AGN

KIC #	$\sigma_{\Delta F}$ 2 days	$\sigma_{\Delta F}$ 5 days	$\sigma_{\Delta F}$ 10 days	$\sigma_{\Delta F}$ 15 days	Std. Dev. 2 days
10841941	5.8	10.4	11.05	12.5	26
10645722	14.24	26.24	39.9	45.2	49
7175757	9.74	7.97	12.78		17
2694186	9.8	18.04	25.2	30.6	38
6932990	87.58	145.89	241	284	314
2837332	9.42	18.05	29.3	46.24	36
9145961	4.39	8.12	9.09	7.76	20
12401487	24.02	24.02	43.7	169.02	68
5781475	9.13	24.3	53	42	38
8946433	12.8	17.7	5.2		35
11606854	4.1	5.1	8.06	4.9	20
12010193	8.02	21.1	39.7		28
9215110	5.2	9.1	12.6	10.9	32
7523720	9.3	18.8	21.04	26.13	25
12158940	33	73.4	104	115	166
12208602	3.74	3.62	5.48	4.9	26
9650712	36.8	73.67	134.74	170.9	164
10798894	13.2	21.54	18.69	24.32	49
7610713	7.43	16.1	30.4	31.1	42
3347632	9.04	18.9	22.8	35.2	47
11413175	8.85				27

Our two variability metrics given for each object. The first, $\sigma_{\Delta F}$, is the subsequent flux difference distribution width as shown in Figure 4.11, for bins of 2, 10, 15, and 20 days. The second is the standard deviation of the light curve with 2-day bins.

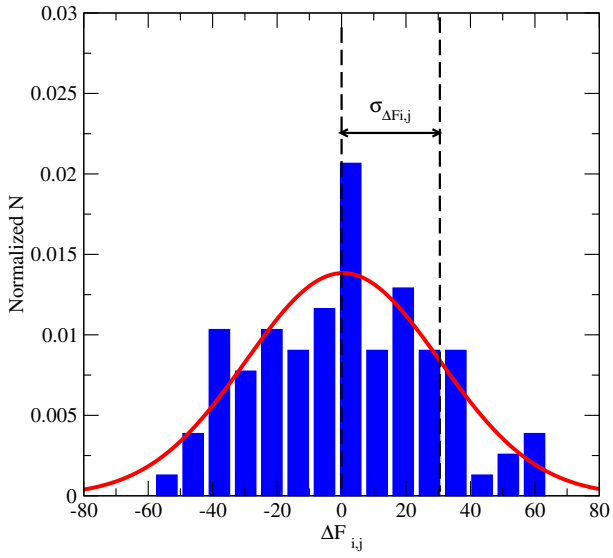

Figure 4.11: Example of the distribution of the difference between subsequent flux measurements ΔF_{ij} used to measure the variability of our light curves; the metric used is the width of the gaussian fit (red). This is the distribution for KIC 10645722.

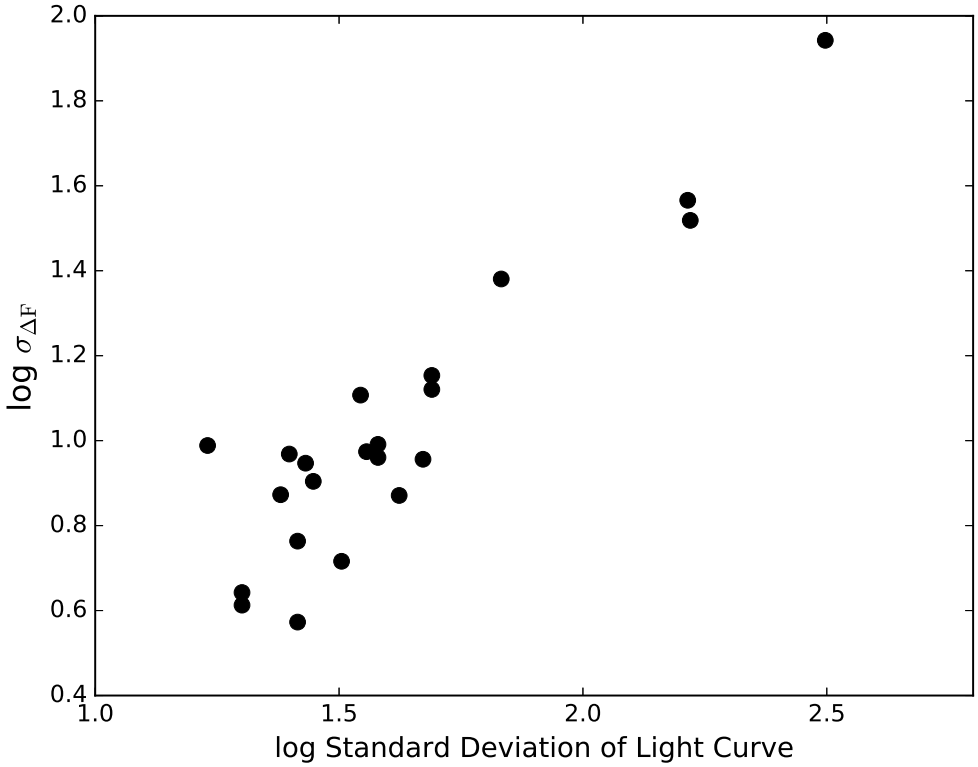

Figure 4.12: Variability metric $\sigma_{\Delta F}$ versus the standard deviation of the light curve. Both are shown for light curves with 2-day binning.

We also see that the *Kepler* data conform to the long-known general anticorrelation of luminosity and variability. Although not a linear correlation, the brighter objects in our sample also tend to be the least variable by both of our metrics, as can be seen in Figure 4.14. We also find that bolometric luminosity is anticorrelated with PSD steepness: brighter objects tend to have shallower PSD slopes. This is shown in Figure 4.15. We do not find any relationship between the high-frequency PSD slope and the Eddington ratio.

Because of the hints in the literature that accretion rate and mass may both be related to the variability, we split our sample into low- and high-Eddington ratio subsets, with $L/L_{\rm Edd} = 0.1$ as the dividing value. This choice was motivated by the possibility that accretion flows with $L/L_{\rm Edd} \sim 10^{-2}$ may be more like advection-dominated flows (ADAFs) than standard thin disks, and because it was a natural value based on the distribution of Eddington ratios in our sample, shown in Figure 4.16.

We find that both measures of variability correlate positively with $M_{\rm BH}$ for low values of Eddington ratio ($L/L_{\rm Edd} < 0.1$), but have no correlation with $M_{\rm BH}$ at high Eddington ratio. Additionally, the strength of the correlation of $M_{\rm BH}$ with $\sigma_{\rm \Delta F}$ depends on the width of the time bins. If instead of 2 days, we rebin our light curve at 5 days, 10 days, and 15 days, we see that the correlation is weaker with larger time bins. This is shown in Figure 4.17. We show the relationship of $M_{\rm BH}$ and the standard deviation in Figure 4.18, with Eddington ratio shown as a color gradient. The sense is the same as for the $\sigma_{\rm \Delta F}$ criterion: a reasonably linear correlation at low Eddington ratio, with no relationship at high ratios or overall.

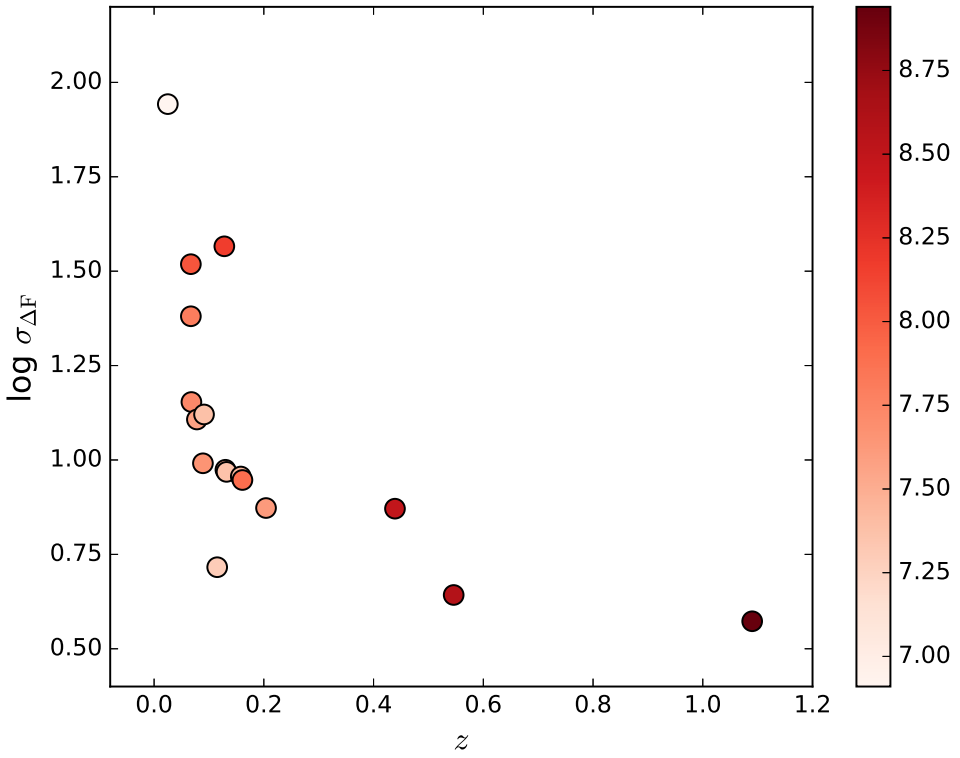

Figure 4.13: Variability metric $\sigma_{\Delta F}$ versus redshift, with log M_{BH} as a color gradient.

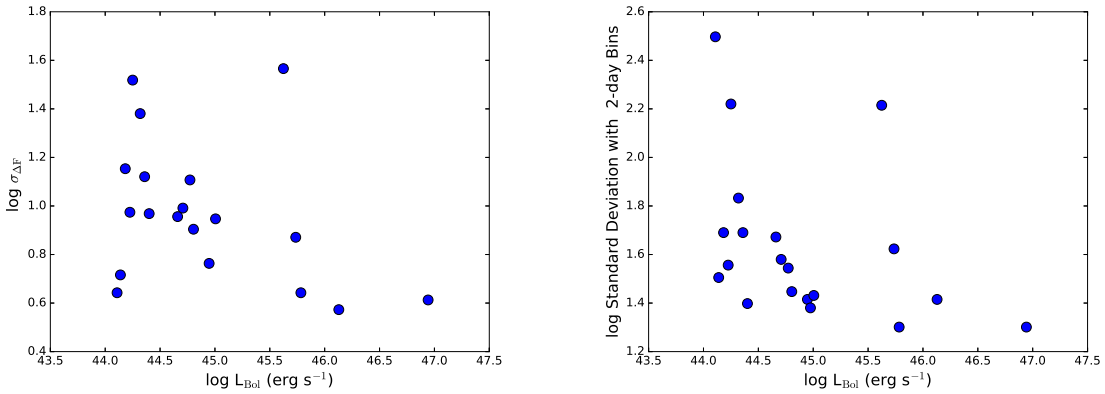

Figure 4.14: Relationship of bolometric luminosity and our two measures of variability: the width of the distribution of $\Delta F_{ij} = F_i - F_j$ between subsequent flux measurements (left), and the standard deviation of the binned light curve (right). We generally duplicate the long-known tendency of brighter objects to be less variable.

It is possible that the relationship between $M_{\rm BH}$ and high-frequency PSD slope, as measured by the best-fitting slope from the method described in Section 4.5, follows a similar pattern. There is a general sense of anticorrelation with PSD steepness, with a possible different trend in low accretion rate objects. This is shown in Figure 4.19. Again, a linear correlation is seen for low $L/L_{\rm Edd}$, with none seen for high $L/L_{\rm Edd}$ or overall. These results are similar to the idea in Zuo et al. [2012] that the correlation with $M_{\rm BH}$ depends on accretion rate.

Finally, we find that $M_{\rm BH}$ is correlated with the break timescale, $\tau_{\rm char}$. The sample is obviously too small to allow physical conclusions, but is consistent with previous results in Collier & Peterson [2001]. This relationship is shown in Figure 4.20.

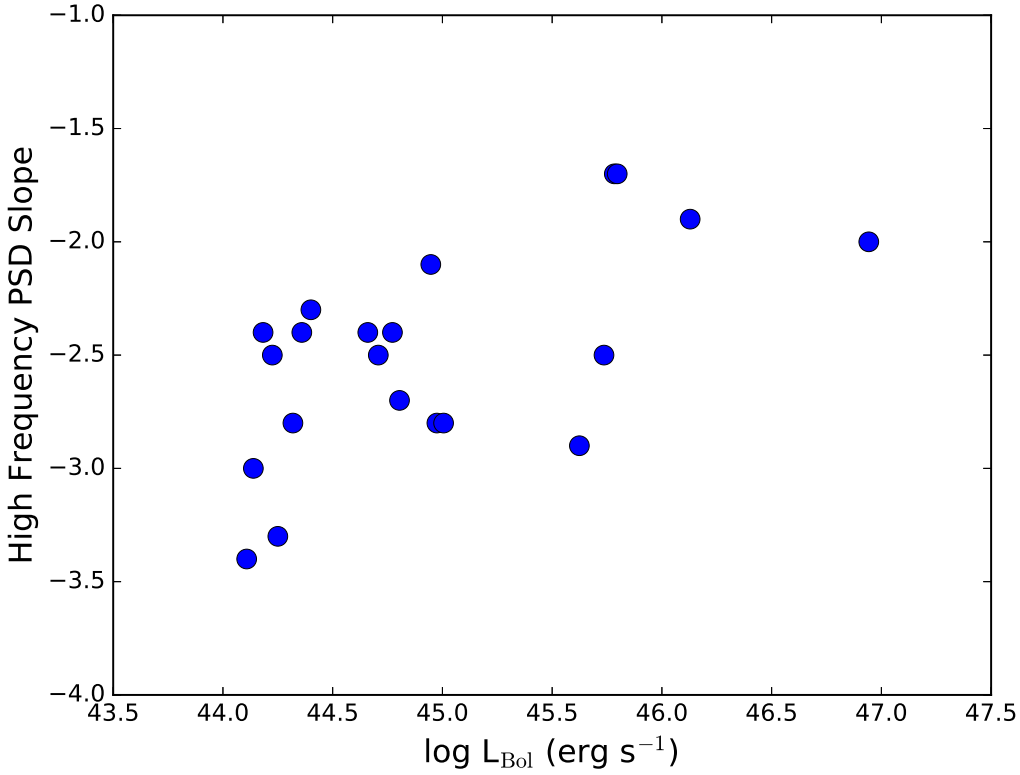

Figure 4.15: Bolometric luminosity versus best-fitting high-frequency PSD slope.

4.6.3 A Candidate Optical QPO

The PSD of KIC 9650712 was poorly fit by single power law and is better described by a broken power law with a characteristic timescale. However, a similar χ^2 value can be achieved by a model consisting of a single power law ($\alpha = -1.9$) and a gaussian component. Such a component could be the signature of a quasi-periodic oscillation. We show the fitted PSD and the fit components in Figure 4.21. We have extracted this light curve carefully omitting a nearby star, in order to avoid false periodicity like that in Figure 4.1. The DSS image of this galaxy and our extraction

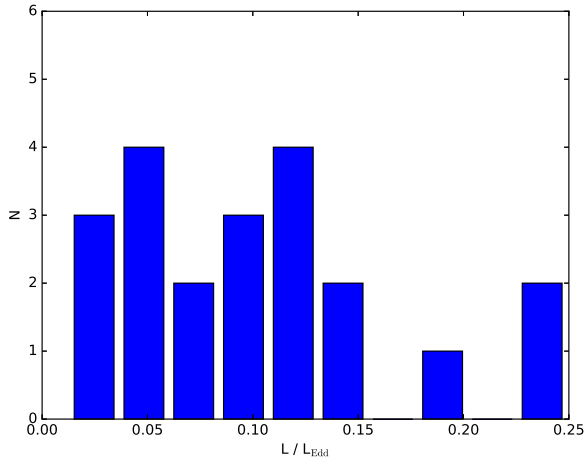

Figure 4.16: Histogram of values of Eddington ratio for *Kepler* AGN with optical spectra.

aperture are shown in Figure 4.22. We have also inspected the J-band image from the UKIRT survey of the *Kepler* field [Casali et al., 2007], which is higher resolution than DSS but is in the infrared. There is no object in this field that could possibly be contaminating the extraction aperture, either. It is of course still possible that there is a faint periodic star convolved with the galaxy, but to the best of our ability we have tried to rule this out.

The best-fitting gaussian model has a central frequency of $\log \nu = -6.53$ Hz, or $t = 39$ days and a width of $\sigma_{\log\nu} = 0.19$. This is wider than known X-ray QPOs, which could be a consequence of the very wide *Kepler* bandpass smearing out the behavior, or of the optical reprocessing of an X-ray QPO across a wide disk surface area physically smearing out the frequency. It is known that high-frequency QPOs in stellar mass black holes have central frequencies that are linearly anticorrelated with M_{BH} [e.g., McClintock & Remillard, 2006]. Although rare, the two candidates

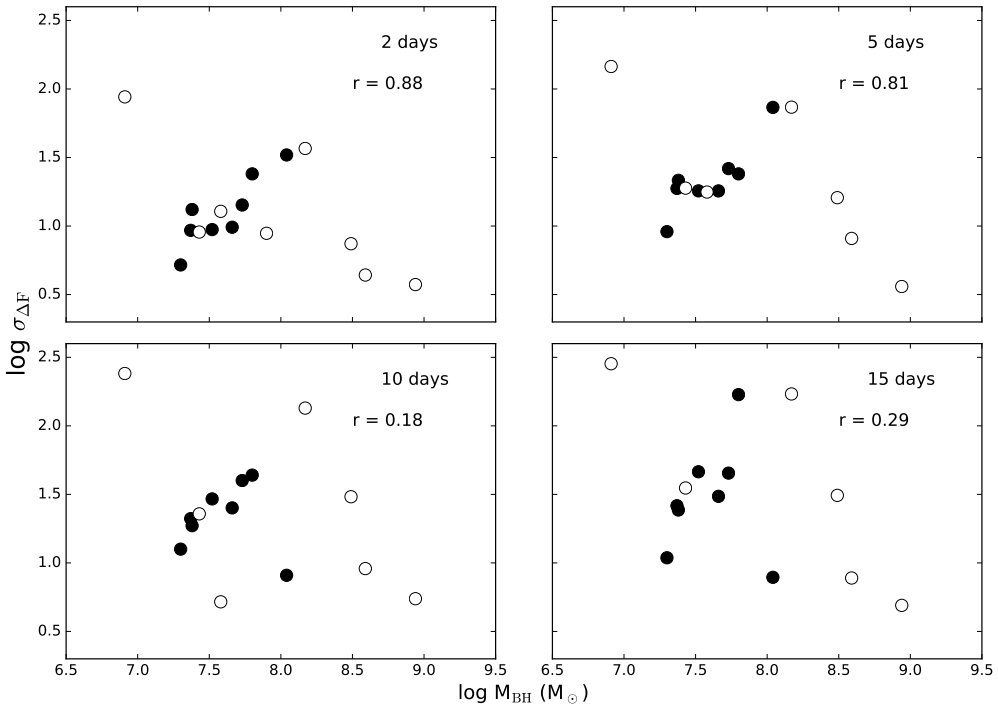

Figure 4.17: The width of the distribution of $\Delta F_{ij} = F_i - F_j$ versus black hole mass for four increasing light curve bin sizes. In each panel, solid circles represent objects with $L/L_{\rm Edd} < 0.1$, and hollow circles represent objects with $L/L_{\rm Edd} > 0.1$. The Pearson correlation coefficient is shown for the trend seen in low Eddington ratio objects.

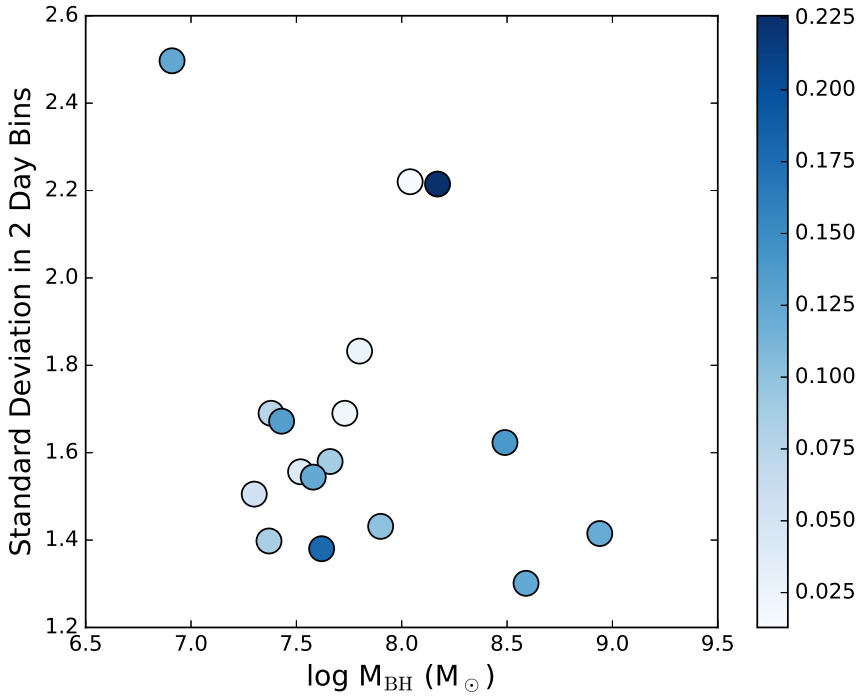

Figure 4.18: The standard deviation of the 2-day binned light curve versus the black hole mass. The Eddington ratio is shown as a color gradient.

for QPOs in intermediate mass black holes, M82 [Pasham et al., 2014] and NGC 5408 [Strohmayer & Mushotzky, 2009] also seem to follow this relation. In Figure 4.23 we show the frequency-mass relation for stellar mass black hole QPOs as found in Table 3 of Strohmayer & Mushotzky [2009], using the mass measurement $M_{\rm best}$, and the two IMBH candidates. We include a linear regressive fit to only the IMBH and stellar mass black holes. Our possible QPO falls very near the expected values of this relation extrapolated across many orders of magnitude in mass. If this QPO candidate proves genuine in future dedicated timing studies, or is duplicated in an X-ray campaign on this object, such continuity has important implications for the

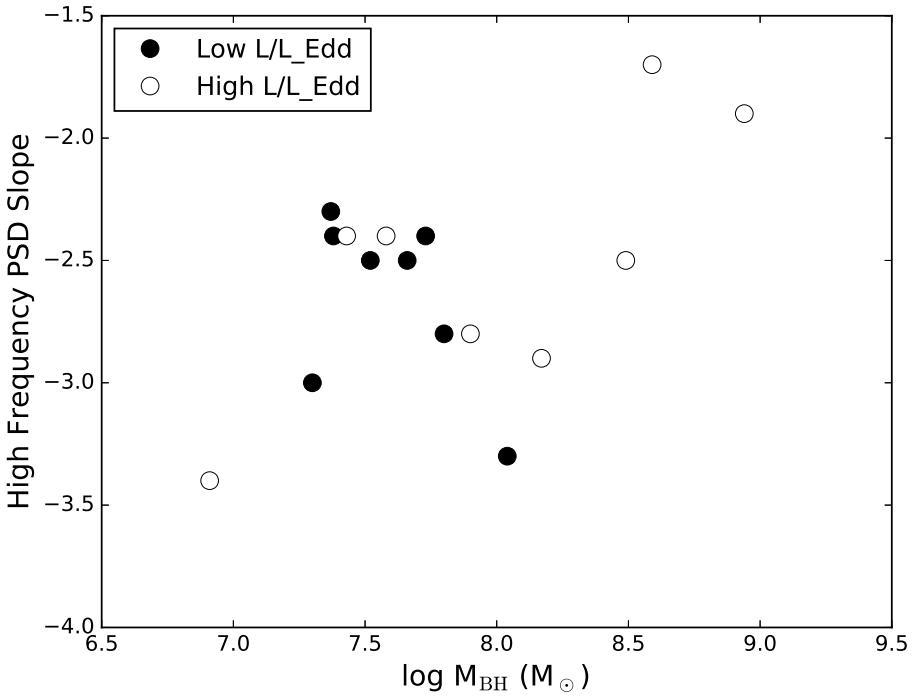

Figure 4.19: Best-fitting high-frequency PSD slope versus black hole mass, divided into low and high Eddington ratio samples.

universality of the accretion process as proposed by, for example, McHardy et al. [2006] and Arevalo & Uttley [2006].

4.6.4 An Unusual AGN Flare

The light curve of the relatively high-redshift AGN KIC 11606854 exhibits a large flare-type outburst at around 200 rest-frame days. This feature is not seen in the light curves of nearby KIC objects, which means it is not likely to be instrumental. Although it is possible that this event is taking place in a star that is convolved with the PSF of our galaxy, it would have to be quite close to the AGN, as there are

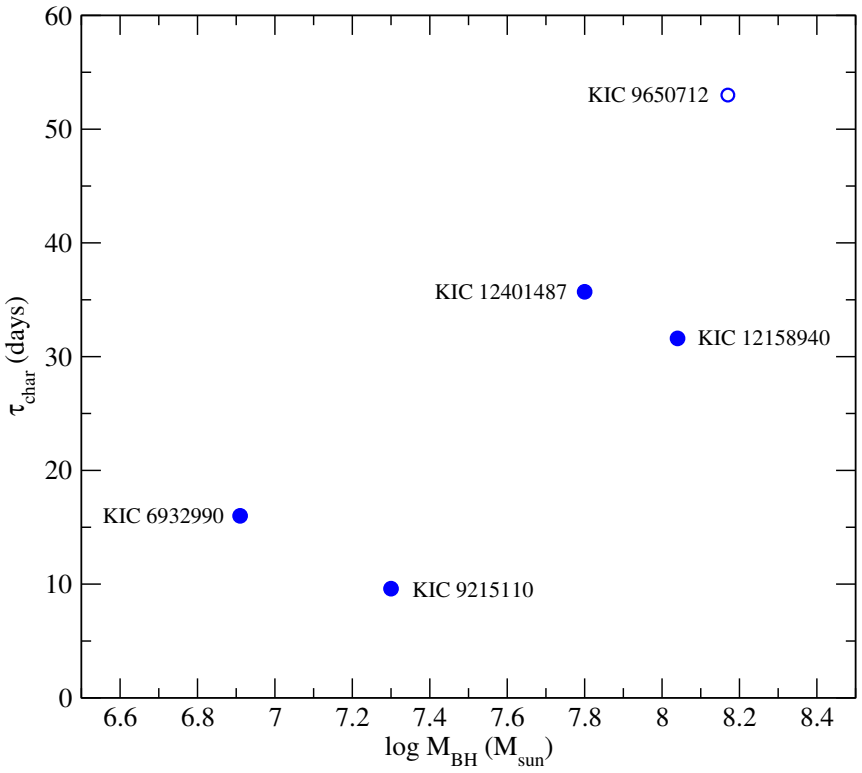

Figure 4.20: Characteristic timescale from the objects with PSDs best-fit by a broken power-law (see Section 4.5) versus black hole mass. The hollow circle shows the object with the "marginal" characteristic timescale.

no objects in the DSS image near enough to have been included in our extraction aperture (see Figure 4.22).

Figure 4.24 shows the flaring portion of the light curve. The flare only lasts for a few days, too short to be a supernova afterglow. Such a feature could indicate a tidal disruption event (TDE) within the accretion disk [e.g., McKernan et al., 2011] or the result of grazing stellar collisions produced by an extreme mass ratio inspiral (EMRI) pair orbiting the central supermassive black hole [Metzger & Stone, 2017].

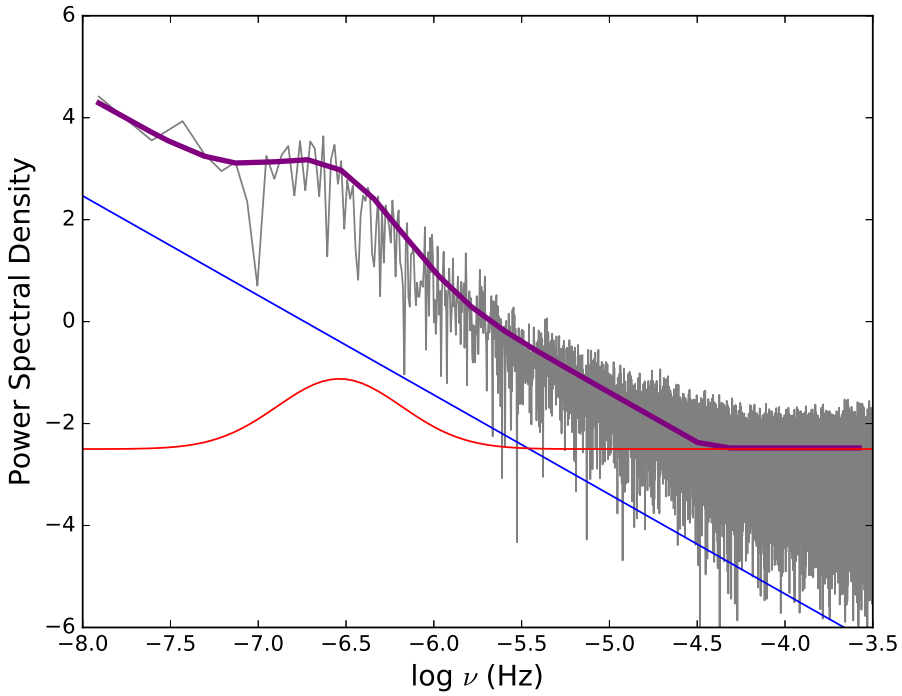

Figure 4.21: The power spectrum of KIC 9650712, our candidate QPO object, with the single power law (red), gaussian (blue), and total combined fit (purple).

We could not get a good fit with the traditional $t^{-5/3}$ profile of a TDE [Komossa, 2015]. Instead, the feature is best fit by an exponential decay, which we show in Figure 4.25. Exponential decays are possible with the EMRI model, but the odd behavior at the flare's peak may be inconsistent with this approach. This remains a mysterious phenomenon.

4.6.5 Physical Implications

As we have stated before, the origin of optical variability in AGN is not known, and many physical models exist. Quantitative, testable predictions are scarce. The

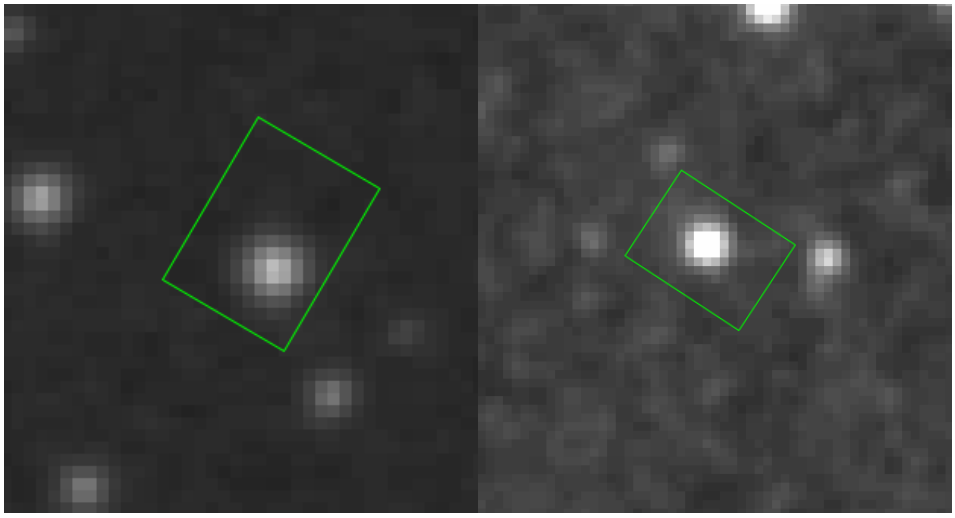

Figure 4.22: The DSS images of our QPO candidate (left) and our flaring object (right), with our custom extraction apertures shown in green.

damped random walk model predicts that the high-frequency portion of the power spectrum should be well-fit by a slope of $\alpha = -2$. Like previous work using this sample [Mushotzky et al., 2011, Kasliwal et al., 2015], we have found that the PSD slopes are in general steeper than allowed by the damped random walk. Two of our sources have slopes shallower than -2, one is best-fit by precisely -2, and the remainder exceed this value, sometimes reaching values as steep as -3.4. We agree, then, that this model is at the very least not sufficient to capture the variability of AGN as seen by *Kepler*, which we again stress is a new regime of variability. It is indeed possible that this model is correct for ground-based quasar light curves, as maintained by Kelly, Bechtold & Siemiginowska [2009], MacLeod et al. [2010] and Zu et al. [2013]; however, some ground-based studies have also found slopes that are steeper than -2 [Simm et al., 2016, Caplar et al. , 2017].

Much of what we have found aligns with an idea put forth by Caplar et al.

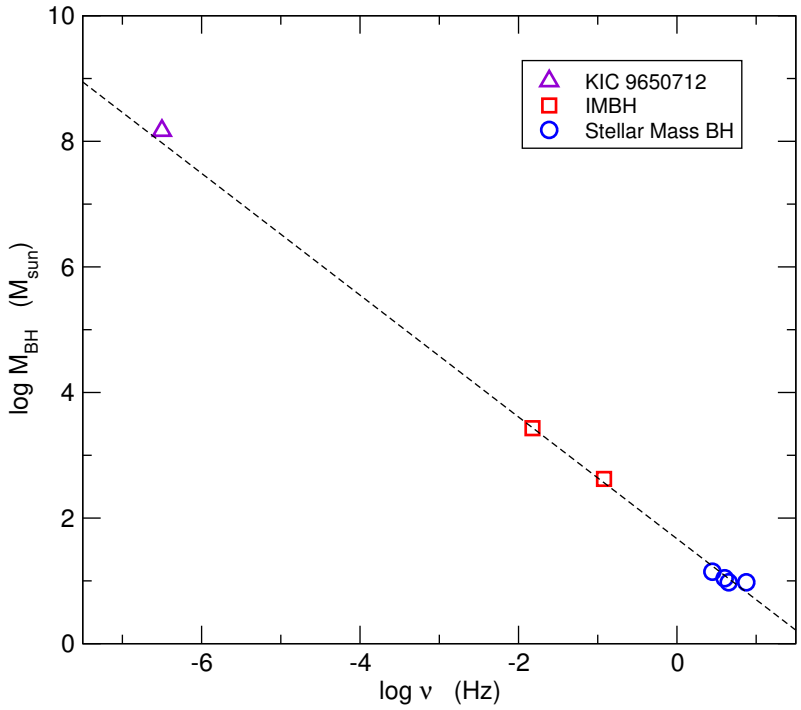

Figure 4.23: The relationship between black hole mass and QPO frequency. The data for the stellar mass black holes are from Strohmayer & Mushotzky [2009], and the intermediate mass black holes are M82 and NGC 5408 (see text for references). The dashed line shows the linear regressive fit to the intermediate and stellar mass samples. Our candidate falls quite near this relation.

[2017]. What if $\tau_{\rm char}$ was the timescale at which the behavior switches from a steep, red variability to a damped random walk or similar? The timescale would need to be correlated with $M_{\rm BH}$ to explain what they see in their ensemble study of ∼28000 Palomar Transient Factory AGN: bins with higher masses tend to have a higher fraction of steep slopes. They observe steepening in their more massive objects, where they are sampling the pre-break timescale, but do not observe steep slopes in their lower-mass objects, where the putative transition frequency is below their sampling rate. Our sample is too small to allow for such binning - we have only one

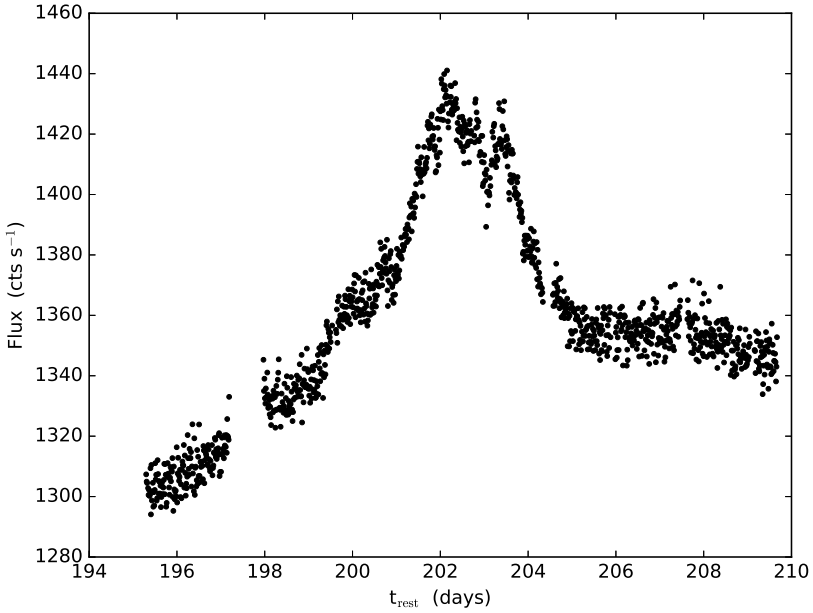

Figure 4.24: An excerpt of the light curve of KIC 11606854 showing the flare-like event.

object that would fall in their highest-mass bin, and it has a shallow slope (as well as the numerous other caveats that we have put forth regarding direct comparison of *Kepler* and ground-based light curves). We realized, however, that we may be able to test an aspect of this model.

Consider that perhaps the PSD of an AGN becomes redder and redder, building towards a critical moment when the behavior switches to a damped random walk. The timescale on which this switch occurs depends on the black hole mass, with longer timescales for larger masses (i.e., larger disks in general). In this case, those objects with observed PSD breaks would have the reddest high-frequency slopes compared to the rest of the sample, which has been caught somewhere in

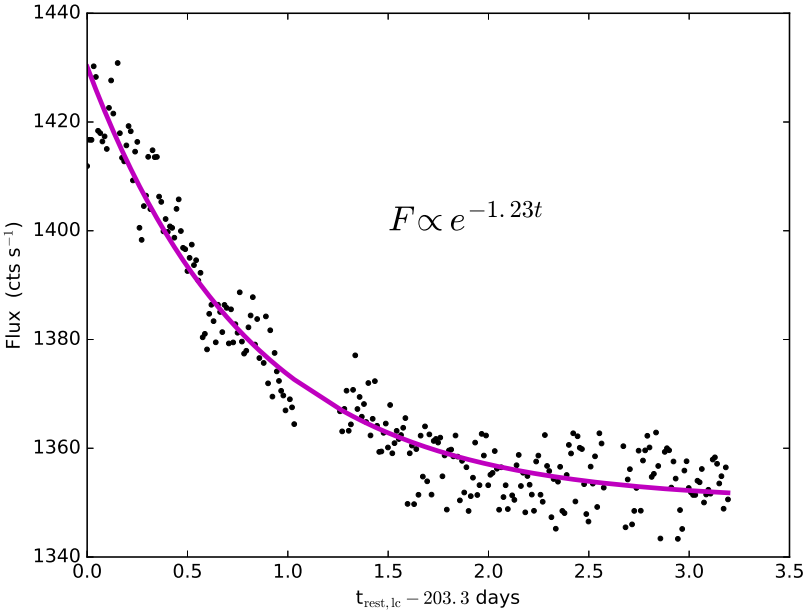

Figure 4.25: The best-fitting model to the decay of the flare-like event in KIC 11606854.

the middle of its reddening phase. This is indeed true in our broken-PSD objects. Five of the six broken-PSD objects have the five steepest slopes in our sample (the exception is best-fit by a slope of -2.7). A histogram of the slopes for each group is shown in Figure 4.26. The mean value for our broken-PSD objects is $< \alpha >= -3.0$, compared to $< \alpha >= -2.3$ for the unbroken sample. In larger upcoming surveys with appropriate cadences (sampling at least as often as 3-5 days), this hypothesis could be better tested.

Next, we note that the paucity of lognormal flux distributions and the total lack of a correlation between the variability and average flux of a given light curve segment places limits on how much of the 0.1%−10% level optical variability can

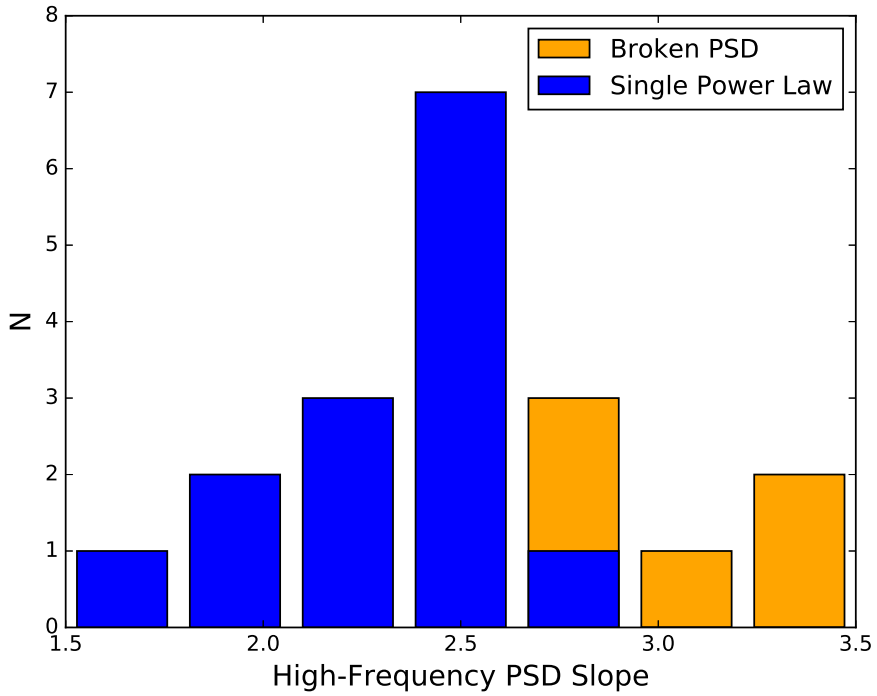

Figure 4.26: Histogram of the best-fitting high frequency PSD slopes for the objects fitted well by a single power law (blue) and a broken power law (orange).

be due to X-ray reprocessing. If reprocessing were an important source of optical variability, we would at least expect objects with high X-ray/optical flux ratios to show these traits. As we stated in Section 4.6.1, we do not see an rms-flux relationship in any of our light curves, and while some of the flux histograms are well-fit by a lognormal distribution, this does not seem to relate to F_X/F_O in any way. We conclude that the variability probed by *Kepler* is not dominated by X-ray reprocessing, and is more likely to be due to properties inherent to the optically-emitting disk.

A physical cause for the anticorrelation of bolometric luminosity and high-

frequency PSD slope is difficult to conjure in the absence of any relationship with Eddington ratio. The bolometric luminosity by itself does not necessarily predict the structure of the disk. It is possible that the phase of a steepening PSD could be accompanied by a general dimming, but it is too early to speculate on why this may happen. We also do not know why the black hole mass should correlate with variability at low Eddington ratios but not overall, and note that this effect may disappear anyway with larger samples that permit stricter and more physically-motivated Eddington ratio binning.

We now turn to the characteristic timescales. There are a number of physical timescales in analytical accretion disk theory. The light-crossing time is too short to be of interest for current optical timing studies and viscous timescales are too long; so we focus here on the orbital, thermal, and freefall timescales. From Edelson & Nandra [1999], the orbital timescale is given by

$$t_{\rm orb} = 0.33\Big(\frac{M}{10^7 M_\odot}\Big)\Big(\frac{R}{10R_S}\Big)^{3/2}{\rm days}, \tag{4.1}$$

the thermal timescale is given by

$$t_{\rm th} = 5.3\Big(\frac{\gamma}{0.01}\Big)^{-1}\Big(\frac{M}{10^7 M_\odot}\Big)\Big(\frac{R}{10R_S}\Big)^{3/2}{\rm days}, \tag{4.2}$$

where γ is the viscosity parameter, and the ADAF accretion timescale is essentially the freefall time [Manmoto et al., 1996]:

$$t_{\rm ff} = 4.62\times10^{-5}\Big(\frac{M}{10M_\odot}\Big)\Big(\frac{R}{1000R_S}\Big)^{3/2}{\rm days}. \tag{4.3}$$

All of these are related to the black hole mass. This makes a correlation of characteristic timescales with mass a natural expectation, which is why its elusiveness is particularly vexing. One complication that afflicts all studies, including and perhaps especially this one, is that the light being monitored comes from a significant range of radii within the disk, diluting the correlation. Collier & Peterson [2001] noted that in their structure function analysis of 13 Sy1 galaxies, higher mass black holes tended to have longer characteristic timescales, but stopped short of calling it a correlation. The relationship they found between M_{BH} and τ_{char} is closest to the theoretical expectation for orbital timescales, but with much scatter. They speculate that timescales on the order of a few to tens of days may have a different physical origin than previously-observed characteristic timescales of hundreds of days. Simm et al. [2016] reported break timescales of hundreds of days in all 90 of the Pan-STARRS light curves of XMM-COSMOS AGN, but saw no correlation of these timescales with any physical parameters including black hole mass.

Many arguments related to characteristic timescale involve the question of whether or not AGN are scaled-up models of accreting stellar-mass black holes; i.e., whether accretion is a universal process across a huge range of masses and relativistic geometries. McHardy et al. [2006] found that after accounting for accretion rate differences, the characteristic timescales in X-ray light curves of stellar mass black holes and AGN are very well correlated with mass, implying a universal accretion scenario. Indeed, the X-ray literature has been far more successful in finding correlations with physical parameters than optical studies. McHardy et al. [2004] found that X-ray break timescales correlated with black hole mass all the way from

Cygnus X-1 to several Seyfert galaxies, although within the Seyfert galaxies there was no correlation. With a larger sample, González-Martín & Vaughan [2012] found that out of 104 XMM power spectra of AGN, 15 were best-fit by broken power laws with characteristic timescales that correlated well with black hole mass. Kelly et al. [2013] found that the amplitude of the high-frequency X-ray power spectrum showed a significant anticorrelation with mass, and could predict masses that agreed well with reverberation mapping values for the same objects. The fact that these relationships have been much less obvious in the optical variability may again speak to the presumably low degree to which optical variations are driven by reprocessing of X-ray variations, or may be due to the fact that the existing body of optical light curves and timing surveys is much more varied than the space-based X-ray light curves of only a few satellites.

Recently, Scaringi et al. [2015] has proposed that the best predictor of characteristic timescales is a combination of the mass, accretion rate, and size of the accreting object. They show that a relationship with the form $\log \nu_b = A \log R + B \log M + C \log \dot{M} + D$ is able to correctly predict ν_b for accretors ranging from young stellar objects (YSOs) and white dwarfs to AGN (using $R_{\rm ISCO}$ with a spin parameter $a = 0.8$ as the "size" of the black holes). According to the results of their grid search, the size is actually the most important parameter. Motivated by this and the desire to determine which of the physical disk timescales best matches our observed break timescales, we have calculated an effective disk radius probed by the *Kepler* light curves, and compared the relationship of our observed timescales with these radii to those expected for the physical timescales described above. Be-

cause calculating a characteristic radius for the very broad bandpass of *Kepler* is somewhat uncertain, we proceed in two ways.

First, we treat the disk locally as a blackbody, and use Wien's Law $\lambda = b/T$ to calculate the temperature at the disk radius probed by *Kepler*, using the central wavelength of the bandpass, 6600Å, as λ. We then use the following equation relating disk temperature and radius from Peterson [1997]:

$$T(r) \approx 6.3 \times 10^5 \left(\frac{\dot{M}}{\dot{M}_{\rm Edd}}\right)^{1/4} \left(\frac{M}{10^8 M_\odot}\right)^{-1/4} \left(\frac{R}{R_S}\right)^{-3/4} {\rm K} \tag{4.4}$$

An alternative way to calculate a characteristic radius is used by Mushotzky et al. [2011], based on the expression for the effective size of the region emitting light at a given frequency from Baganoff & Malkan [1995]:

$$\frac{R_\nu}{R_S} = 7.5 \times 10^{23} \epsilon^{-1/3} \nu^{-4/3} \left(\frac{M}{M_\odot}\right)^{-1/3} \left(\frac{L}{L_{\rm Edd}}\right)^{1/3}, \tag{4.5}$$

where ϵ is the accretion efficiency. Using this relation will predict shorter timescales for the same radius and black hole mass, because it takes into account light from the inner, hotter regions of the disk as contributing to the *Kepler* bandpass, which is physically realistic. However, we note that both the known effect of atmospheric scattering, which requires a color correction that reddens the emission, and the observational evidence (i.e., the 1000Å break seen in quasar spectra) for truncated disks in which hot inner regions do not contribute much to the optical light, would move the effective radius closer to our original, more naive estimate.

In Figure 4.27, we show the regions in the $\tau_{\rm char} - R_{\rm Kep}$ plane described by each

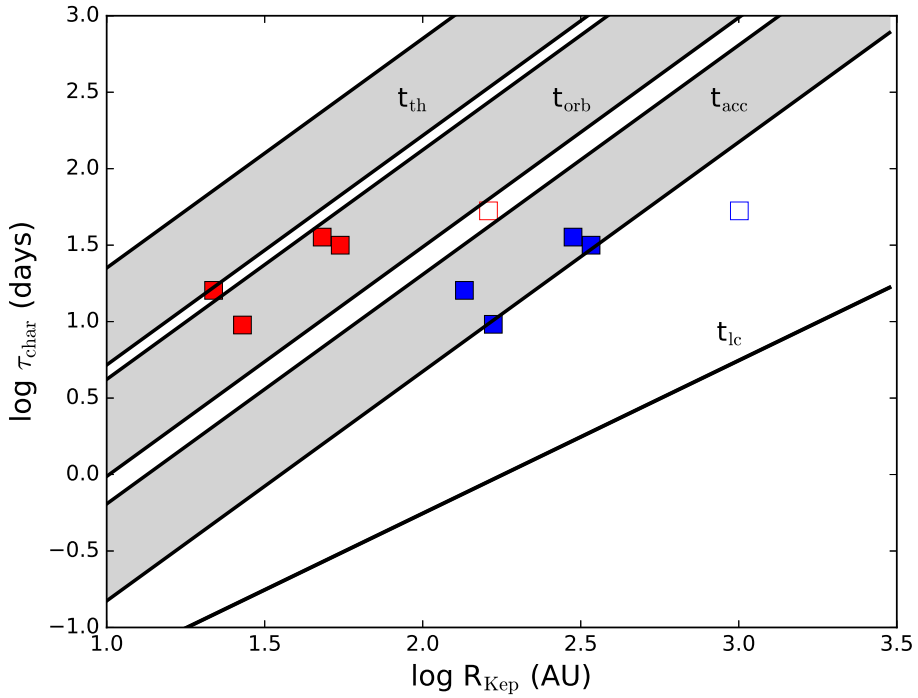

Figure 4.27: The four definite break timescales (solid squares) and one marginal break timescale (hollow square) in the plane of physical timescale and effective radius of the disk probed by the *Kepler* bandpass. Blue symbols are for radii calculated using Equation 4, and red squares for Equation 5.

physical timescale for the range of masses in our broken-PSD sample. If calculated using our blackbody estimation and Equation 4, the timescales are most consistent with the freefall or ADAF accretion timescale. If they are calculated using the effective emitting region size with Equation 5, they are more consistent with orbital timescales. This would be in agreement with the orbital timescale consistency found by Collier & Peterson [2001].

We conclude by noting that, as Scaringi et al. [2015] points out, accreting white dwarfs and stellar-mass black holes have shown identical break timescales

in their optical and X-ray PSDs. This has not been observed in AGN, but this dataset would be a good candidate for X-ray timing follow up. Many X-ray break timescales in the AGN literature are on the same order as our optical timescales, such as those reported by McHardy et al. [2006] and González-Martín & Vaughan [2012]. However, some of the González-Martín & Vaughan [2012] timescales are on the order of minutes to hours, far shorter than we could have seen with these data (white noise begins to dominate our PSDs at around 1 day timescales). Whether or not the X-ray and optical characteristic timescales are identical in a given object would do much towards identifying and disentangling the various sources of variability.

4.7 Summary

We have analyzed a sample of 21 *Kepler* light curves of Type 1 AGN using a customized pipeline and Fourier techniques. Our results are as follows.

1. We have found that the high-frequency PSD slopes are largely inconsistent with the value of $\alpha = -2$ predicted by damped random walk models, in agreement with other studies.

2. Despite the possibility that the *Kepler* space-based optical light curves would be more consistent with X-ray timing studies than optical ground-based surveys, we do not see the lognormal flux distributions or linear rms-flux relationships that characterize X-ray AGN light curves. This holds true even for the highest F_X/F_O objects in our sample, indicating that X-ray reprocessing is unlikely to be a large contributing factor to the 0.1-10% optical variability of AGN.

3. Some of our light curves exhibit bimodal flux distributions, transitioning between what appear to be fixed flux levels. This is possibly the signature of preferred accretion states, but may also be an indication of obscuring material passing along the line of sight.

4. The *Kepler* light curves uphold the general anticorrelation between bolometric luminosity and variability, but do not show an increased variability with redshift. This latter is probably due to the fact that we do not have enough high-redshift AGN to test this properly.

5. Bolometric luminosity is weakly anticorrelated with high-frequency PSD slope.

6. Black hole mass is positively correlated with variability for low Eddington-ratio objects, but there is no correlation with high Eddington objects or overall. The low Eddington correlation weakens with increasing light curve bin size (i.e., probing variability on longer timescales).

7. We put forth two unusual objects, a candidate optical QPO with a frequency of ~ 39 days and a powerful flare with a fading time of ~ 3 days that is best fit by an exponential decay.

8. Six of our AGN show statistically significant PSD flattening, with characteristic break timescales ranging from 9 to 53 days. The black hole mass roughly correlates with these timescales, and objects with break timescales also have the steepest PSD slopes.

9. The characteristic timescales are most consistent with orbital or freefall / ADAF accretion timescales, depending on how the characteristic radius of the disk at the observed wavelengths is calculated.

The results of *Kepler* timing studies were hampered by the premature end of the primary mission. Ongoing space-based optical timing missions like K2 and TESS will have similar cadences to *Kepler* but with significantly shorter monitoring baselines. The data shown in this study can be used to understand how much the statistical properties of variability in K2 and TESS AGN light curves is affected by the shorter baseline, and potentially act as a bridge between K2/TESS and upcoming ground-based surveys like LSST. At the very least, studies of the *Kepler* and upcoming space-based AGN light curves show us that AGN vary at an astounding diversity of timescales and amplitudes, and that with the confluence of all types of surveys in the optical and X-ray, accretion physics will soon be accessible and testable in an entirely unprecedented way.

Acknowledgements

KLS is grateful for support from the NASA Earth and Space Sciences Fellowship (NESSF), which enabled the entirety of this work. KLS also acknowledges Tod Strohmayer and Nathan Roth for helpful discussions regarding QPOs and AGN flares.

Chapter 5: Summary and Future Work

This thesis has explored the central engines of active galaxies through two separate projects, one of which required two stages. First, we have investigated the properties of star formation within a few hundred parsecs of the central supermassive black hole using high resolution radio imaging of a largely unbiased, hard X-ray selected sample of radio-quiet AGN. The imaged star formation had a variety of morphologies including patchy regions, rings, and jets. We have found that despite the potentially different physical environment between the nuclear regions of an active galaxy and star forming regions in normal galaxies, the FIR-radio relation holds after careful decomposition of the AGN and star formation contributions to the flux. In addition to exploring the star formation properties, we have also examined the spatially isolated core radio flux and compared it to the predictions for coronal and scale-invariant jet models from the fundamental plane, and found consistency with both. We have also found that the objects with small nuclear jets seem to lie preferentially below the star forming main sequence, which may be an indication of AGN feedback suppressing star formation in the host at large.

In the second project, we have explored a new regime of optical AGN variability using light curves from the *Kepler* exoplanet-hunting satellite. In order to

achieve this, it was first necessary to obtain a sample of AGN within *Kepler*'s fixed field of view. We conducted an X-ray survey of that region of the sky with the *Swift* X-ray Telescope, dubbed the *Kepler-Swift* Active Galaxies and Stars survey (KSwAGS). The survey discovered 93 significant X-ray sources, which optical spectroscopic follow-up identified as a mixture of AGN and interesting stellar variables. We have also shown that in the absence of spectra, a reliable identification of AGN can be made using the X-ray to optical flux ratio. The KSwAGS survey has now been conducted in three of the K2 fields of view, and the light curves are available for analysis. This survey has identified dozens of new AGN for future study using the rich database of Full-Frame Images in the *Kepler* archive, as well as providing X-ray and UV fluxes or upper limits for any of the tens of thousands of objects in the surveyed modules of the original *Kepler* field.

Although the *Kepler* mission ended prematurely before the bulk of the KSwAGS targets could be investigated, we were able to conduct a time series analysis on a sample of 21 AGN selected using infrared photometry. This analysis required the development of a new pipeline, since the *Kepler* data were optimized for exoplanet science in ways that seriously compromised AGN scientific analysis. The variability seen in the *Kepler* light curves is often at the $0.1 - 1\%$ level, and would be very challenging to detect from the ground. We have found that this variability does not always conform to the noted correlations of the ground-based AGN timing literature, although the gross expectations do hold. We have also found that the *Kepler* variability does not display many of the common timing properties seen in X-ray studies, indicating that reprocessing of X-ray variability is not a major contributor

to optical flux variations. Six of the objects in the sample have significantly detected characteristic timescales, which are consistent with orbital or freefall timescales and are inconsistent with thermal timescales. We note a correlation between the characteristic timescale and the black hole mass, as has been found in X-ray literature. After fitting the power spectral density functions of the *Kepler* AGN with power laws, we find that the high-frequency slopes are generally too steep to support the popular damped random walk flux diffusion model for AGN variability, and find that the slope correlates weakly with bolometric luminosity. The black hole mass correlates with overall variability for objects with a low Eddington ratio, but at higher accretion rates there appears to be no relationship. There is no correlation that is strong enough to allow for reliable mass estimation from optical variability properties in the *Kepler* light curves. We have also found two interesting anomalies, including a possible detection of an optical quasi-periodic oscillation and an unusual flaring event in a quasar, both of which merit further study.

5.1 Future Work: Radio Imaging of Star Formation and Feedback

Based on the results presented in this thesis, we submitted a successful proposal (PI Smith) in 2016 to follow up on two key populations. As can be seen in Figure 2.9, with one exception (Mrk 477) all sources with jet- or core-dominated morphology are either within or well below the main sequence, while objects with nuclear star formation evident in our images reside on the main sequence. Studies of the host galaxies of X-ray selected AGN, and indeed for the *Swift*-BAT AGN

themselves, often find that they lie in the so-called "green valley", morphologically between the blue, star forming galaxy sequence and the "red dead" ellipticals. The interpretation has often been that these galaxies are in the process of transitioning between the two regions through ongoing star formation quenching. Our result that these galaxies tend to have AGN-dominated radio morphologies, including jets and outflows, supports this assumption. However, the sample discussed in this thesis was relatively small, with too few sources to determine a clear relationship between radio flux, morphology, and distance below the main sequence. We requested 1″ imaging of 50 *Swift*-BAT AGN especially chosen to lie $> 1\sigma$ below the main sequence, increasing this population by a factor of five, to test for a prevalence of jet-like or outflow morphologies.

As described in Section 2.3, we created 6″ resolution images using our C-array data for comparison with the full-resolution 1″ images. When we subtracted the flux in the compact 1″ core from the total flux in the 6″ image, there was always some residual flux, even in objects with apparently only compact morphologies. The indication is that while about half of our original sample turned out to have core-dominated 22 GHz morphologies, we have strong evidence that these also have some extended emission. However, this emission was of insufficient surface brightness to be imaged explicitly using the short integration times in our original proposals. Many apparently compact sources have radio fluxes above the prediction from star formation, even once their core flux is removed. These may be low surface brightness outflows or jets, with substantial radio emission from the AGN on scales between 1″ and 6″. There are also many compact sources with extended

radio flux consistent with star formation. Presumably, these will have extended star formation morphologies, which should be apparent with longer integrations. We therefore requested long integration, high sensitivity observations of these sources to examine the morphology of the low surface brightness excess emission. As an added bonus, this will double the sample size for determining the validity of the FIR-radio relation.

Both of these data sets are currently being observed by the JVLA following a successful proposal (PI Smith), and analysis will begin in Fall 2017.

5.2 Future Work: AGN Time Domain Analysis with *Kepler* FFIs, K2, and TESS

We already have a large database of hundreds of K2 target pixel files of AGN from both the second phase of the KSwAGS survey and from archival AGN samples in, for example, SDSS. The lessons learned and software developed during the difficult process of pipelining the *Kepler* data will hopefully enable swifter progress on K2 light curves. One of the first projects after the completion of this thesis will involve testing how accurately the shorter, 70-day duration K2 light curves capture the true behavior in the longer *Kepler* light curves, and whether there are scaling factors between the $\sim$years long variability behavior and that on timescales of a few months. Once these analyses are complete, the K2 sample will vastly improve the number of AGN with $0.1 - 1\%$ monitoring and test the results of this thesis with full statistical significance.

Many pipelines have been developed lately for use on the original *Kepler* field data, including packages that use aperture photometry to create light curves from the Full Frame Images (FFIs). This means that a light curve can be constructed for any object in the field of view, with 30-day cadence. The KSwAGS AGN that came too late for *Kepler* monitoring are an ideal test sample for this analysis.

In 2018, the Transiting Exoplanet Survey Satellite (TESS) will be launched. Considered the successor of *Kepler* and K2, TESS will take full frame images every 2 minutes. The duration of its light curves will range from 27 days near the ecliptic to 351 days at the poles. It is most likely that the bulk of AGN science will need to be done using the longer-baseline light curves near the poles, but testing the properties of the *Kepler* and K2 light curves on shorter timescales will teach us the lowest useful limit on baseline.

Regardless of the source of these future light curves, the search will continue for correlations with physical parameters, and investigations of whether these correlations apply to only certain populations in terms of, say, Eddington ratio. With statistically robust samples, the models of accretion physics will finally be testable, especially considering the rapid progress of simulations. The final goal of these analyses is to prepare us for the truly massive timing database of the upcoming Large Synoptic Survey Telescope (LSST), which should begin operations in 2019 or 2020. LSST is particularly important, since it will monitor $\sim$20 million AGN over the course of ten years.

5.3 Future Work: Supporting Gravitational Wave Science

As we enter the era of gravitational wave astronomy, the *Kepler*, K2 and TESS AGN data sets can provide context for multi-messenger astrophysics. Pulsar timing arrays such as NANOGrav and the space interferometer LISA will search for low-frequency gravitational wave signals from binary systems of supermassive black holes with periods of weeks to decades. Ground-based optical timing studies, especially from the PanSTARRS and Catalina surveys [e.g., Liu et al., 2016], have been a primary source for candidate supermassive binary discoveries with inferred orbital periods accessible to pulsar timing arrays. However, these detections are tenuous because of uncertainties in the interpretation of optical AGN variability. Indeed, quite recently Vaughan et al. [2016] pointed out that the normal stochasticity of AGN light curves can mimic periodic signals, and stress that the community must "carefully assess the methods for identifying periodic candidates from among a population dominated by stochastic variability." Space-based optical timing data has the potential to characterize optical AGN variability in a statistically meaningful way, and enable a robust treatment of ground-based optical timing data in the future. The full *Kepler*-K2 AGN light curve sample will consist of approximately 300 objects by the end of the K2 mission. The plan is to degrade these light curves to match the irregular sampling and photometry of a given ground-based survey, to assess the probable false-positive rate in any search for periodicity in such samples. This will lay the critical groundwork for gravitational wave counterpart detection in LSST, as well as ongoing surveys like PanSTARRS and the PTF/ZTF.

Appendix A: The *Kepler* AGN Light Curves

We present here the full sample of AGN light curves. We display them two ways: first, on different flux axes that are best for each object, to allow distinct features to be easily seen. Second, we show each light curve on identical axes: the range of the ordinate is always 30% of the mean flux ($\pm$15% in each direction), and the abscissa is 1200 rest-frame days, which is the length of our longest light curve. This allows the amount of variability and the baselines to be compared at-a-glance. Each plot displays flux in units of counts sec^{-1} versus time in rest-frame days.

Light Curves of the *Kepler* AGN on Individually Scaled Axes

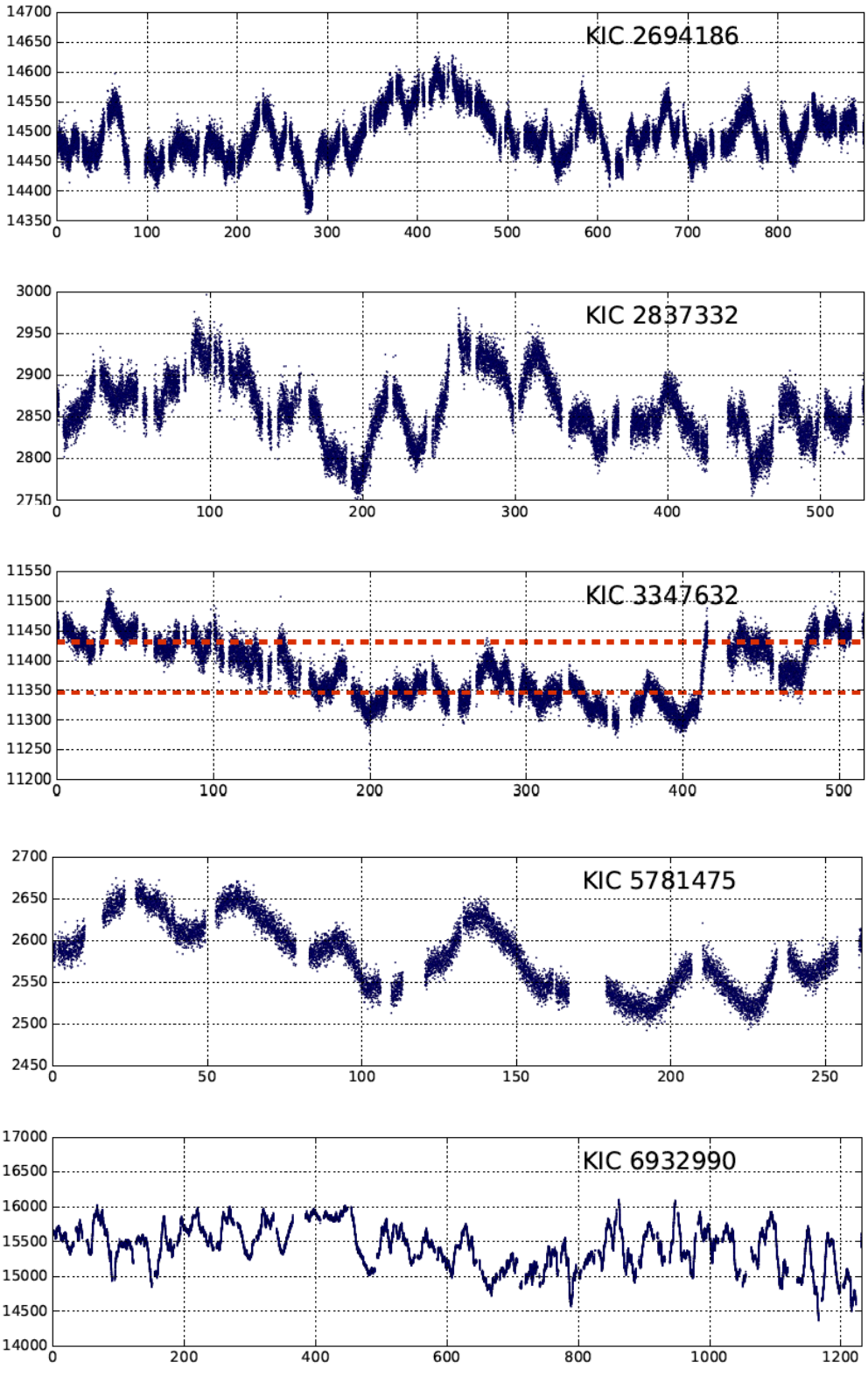

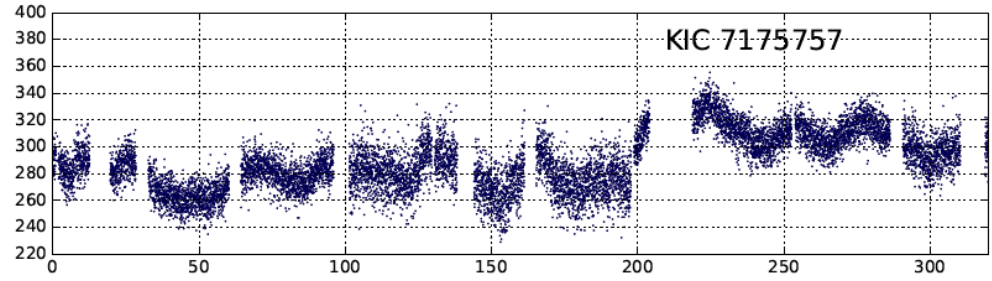
KIC 7175757
400
380
360
340
320
300
280
260
240
220
0
50
100
150
200
250
300

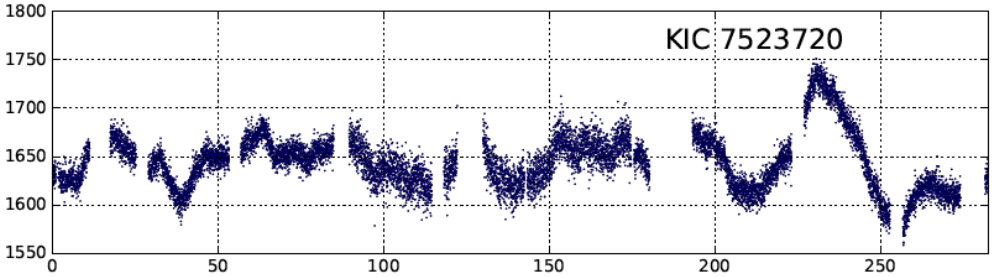
KIC 7523720
1800
1750
1700
1650
1600
1550
0
50
100
150
200
250

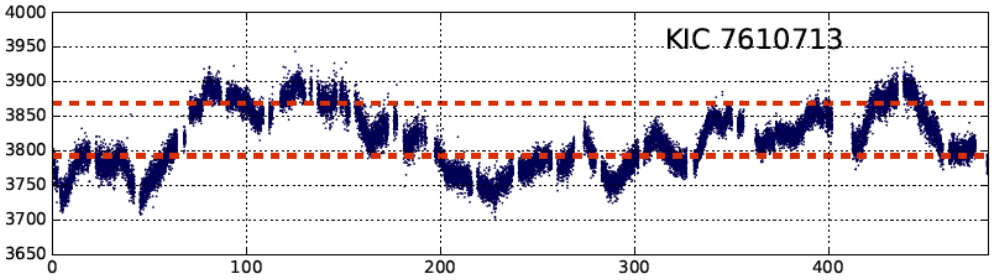
KIC 7610713
4000
3950
3900
3850
3800
3750
3700
3650
0
100
200
300
400

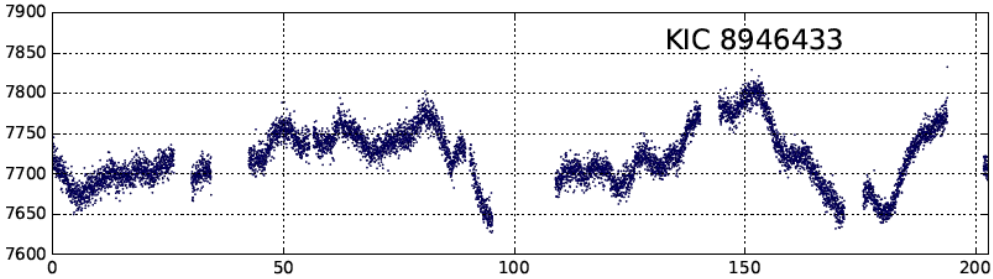
KIC 8946433
7900
7850
7800
7750
7700
7650
7600
0
50
100
150
200

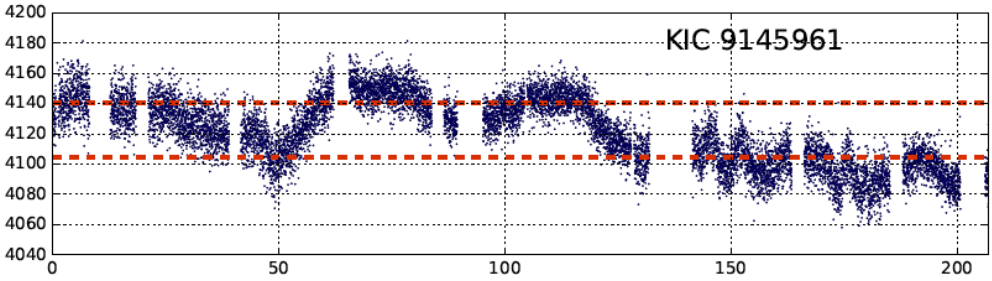
KIC 9145961
4200
4180
4160
4140
4120
4100
4080
4060
4040
0
50
100
150
200

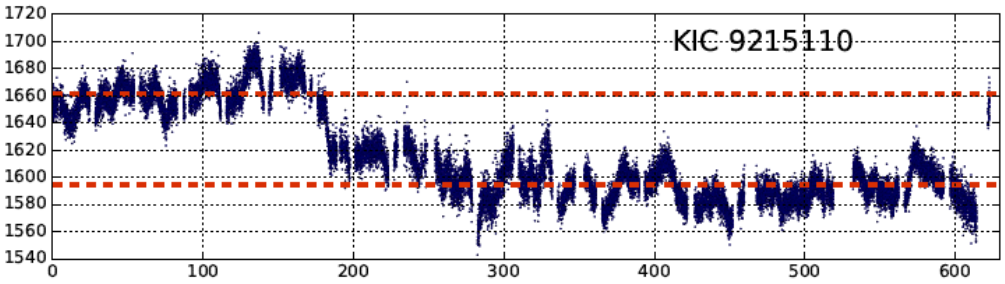
KIC 9215110
1720
1700
1680
1660
1640
1620
1600
1580
1560
1540
0
100
200
300
400
500
600

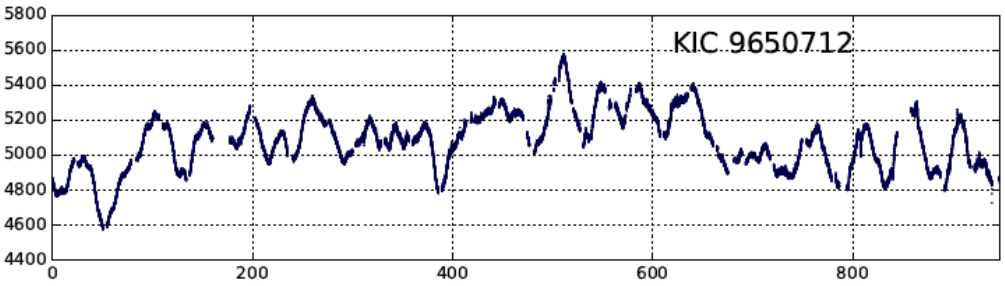
KIC 9650712
5800
5600
5400
5200
5000
4800
4600
4400
0
200
400
600
800

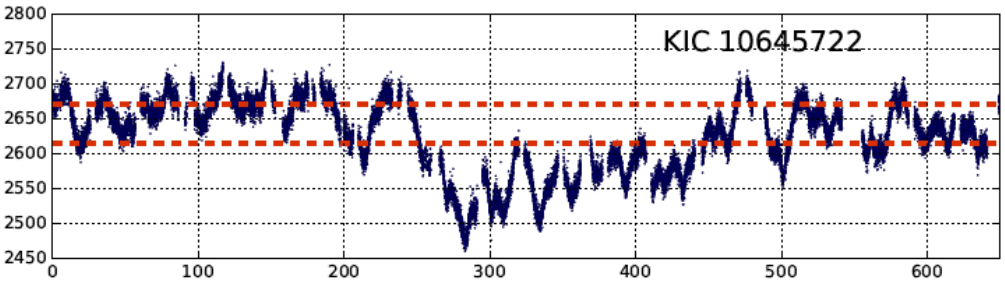
KIC 10645722
2800
2750
2700
2650
2600
2550
2500
2450
0
100
200
300
400
500
600

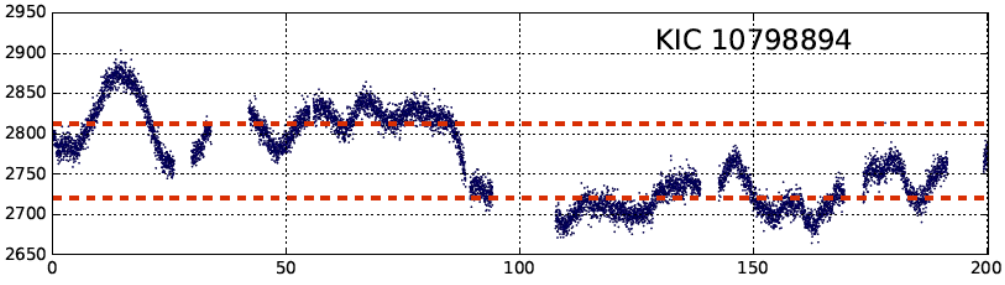
KIC 10798894
2950
2900
2850
2800
2750
2700
2650
0
50
100
150
200

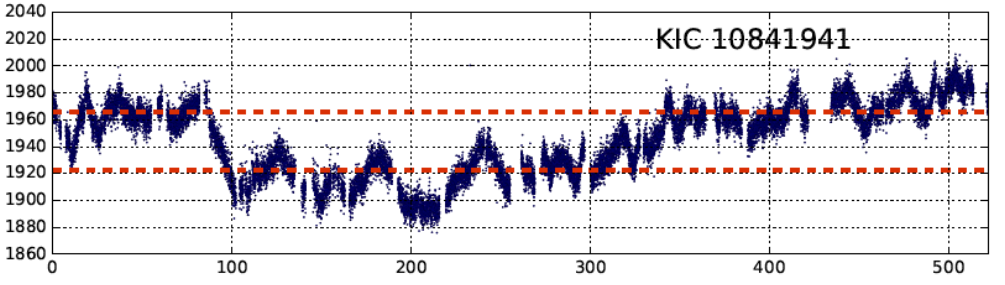
KIC 10841941
2040
2020
2000
1980
1960
1940
1920
1900
1880
1860
0
100
200
300
400
500

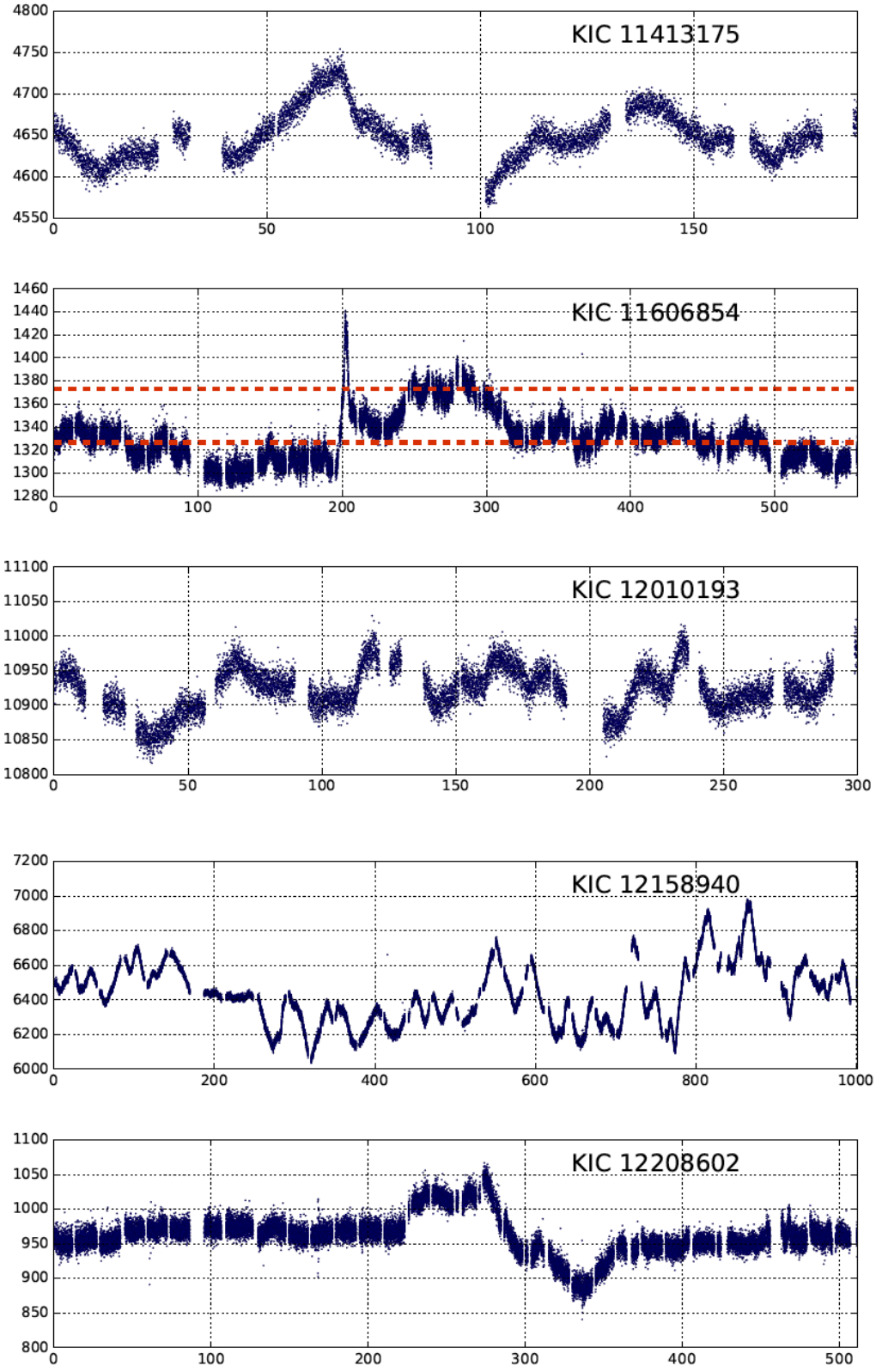
KIC 11413175
KIC 11606854
KIC 12010193
KIC 12158940
KIC 12208602

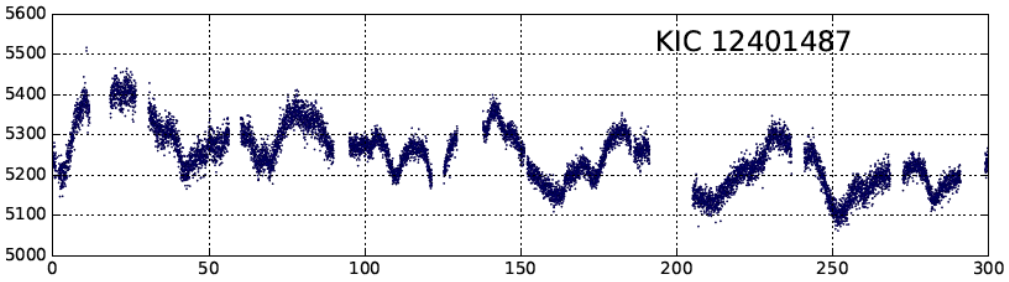

Figure Appendix A.1: Light curves of the *Kepler* AGN with axes scaled to maximize visibility of features for each case. Each plot displays flux in units of counts $\sec^{-1}$ and time in rest-frame days.

Light Curves of the *Kepler* AGN on Identical Axes

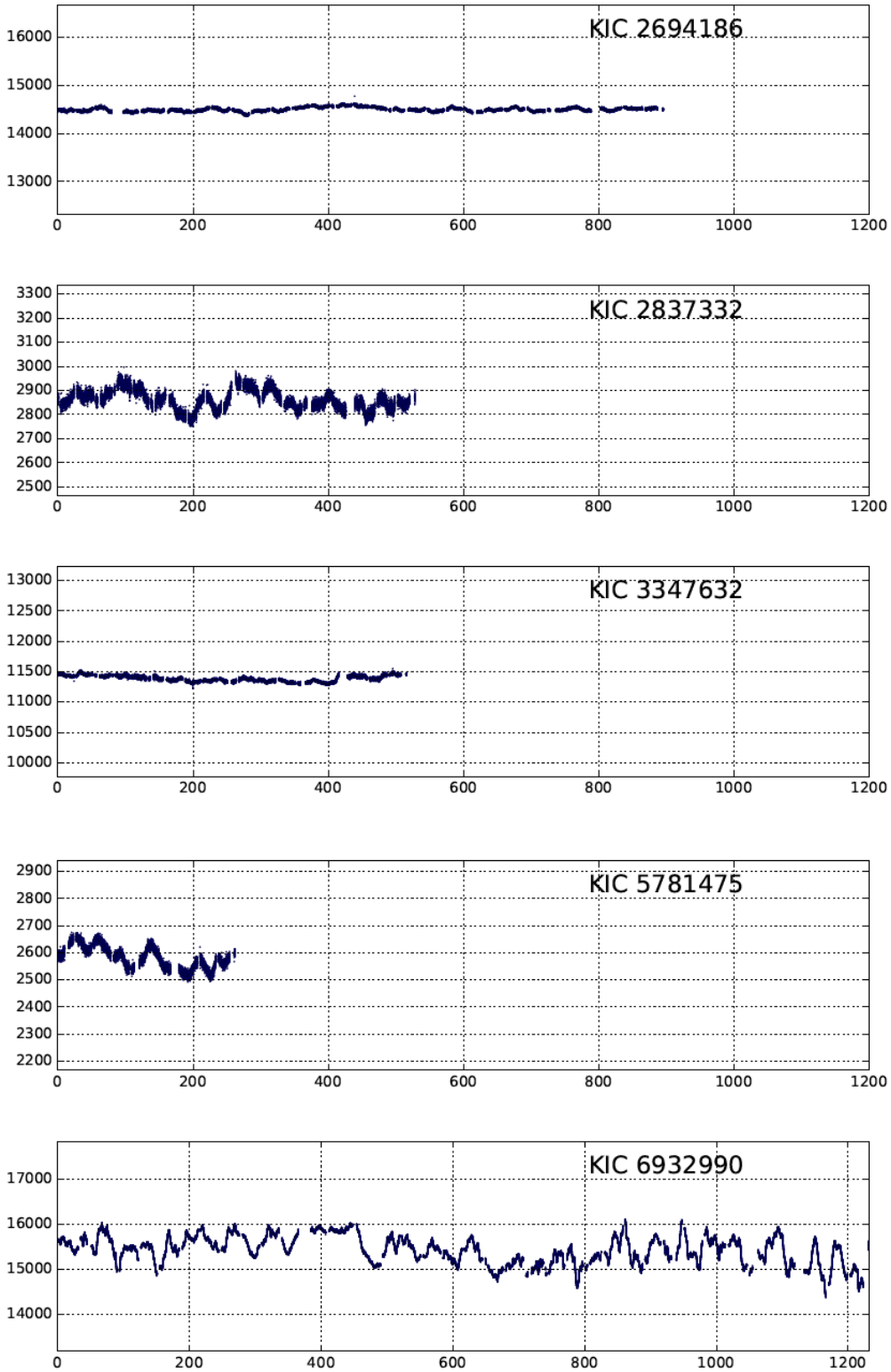

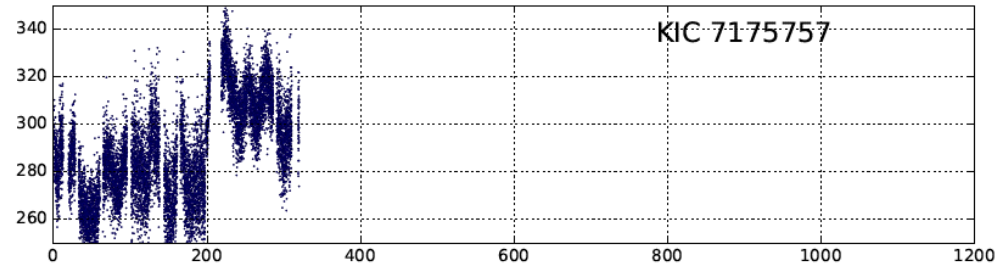
KIC 7175757
340
320
300
280
260
0
200
400
600
800
1000
1200

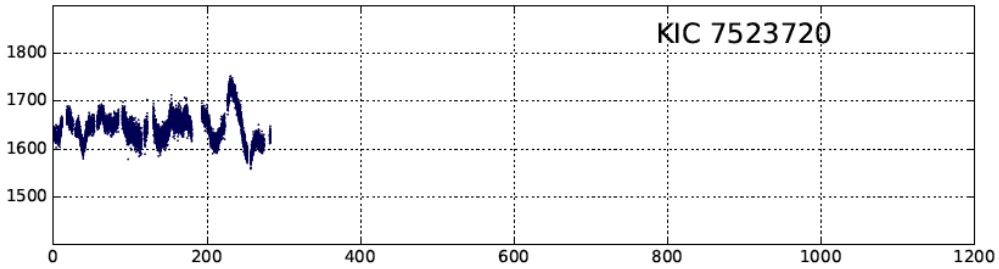
KIC 7523720
1800
1700
1600
1500
0
200
400
600
800
1000
1200

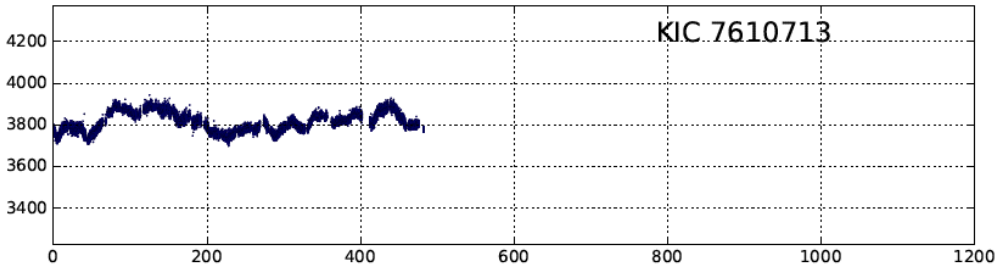
KIC 7610713
4200
4000
3800
3600
3400
0
200
400
600
800
1000
1200

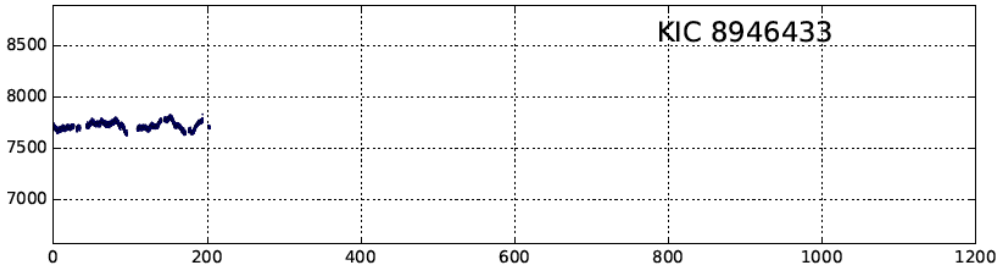
KIC 8946433
8500
8000
7500
7000
0
200
400
600
800
1000
1200

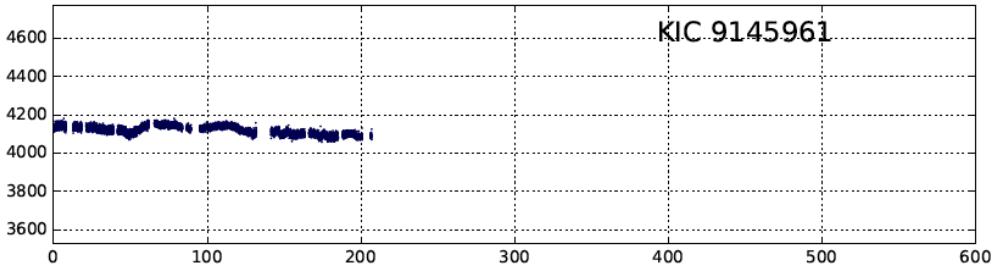
KIC 9145961
4600
4400
4200
4000
3800
3600
0
100
200
300
400
500
600

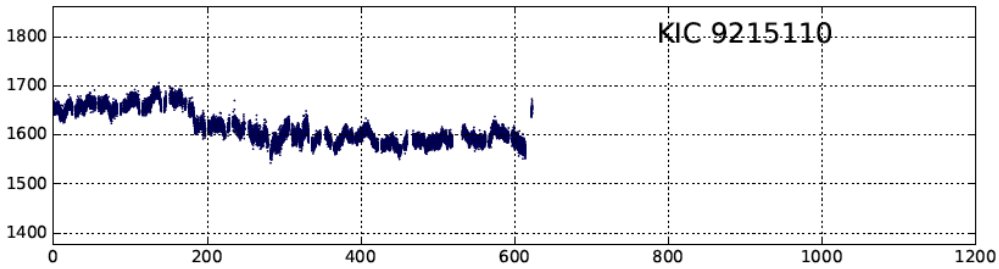
KIC 9215110
1800
1700
1600
1500
1400
0
200
400
600
800
1000
1200

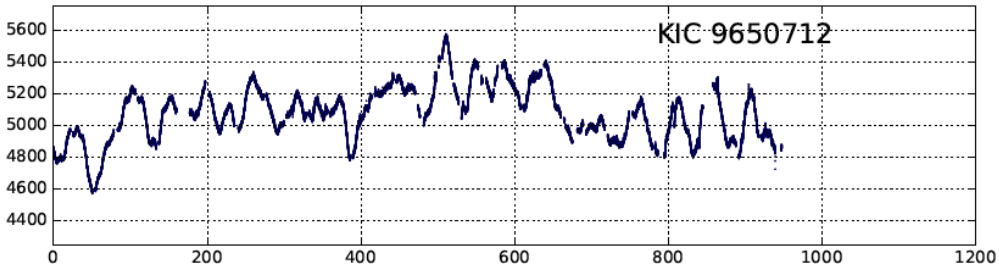
KIC 9650712
5600
5400
5200
5000
4800
4600
4400
0
200
400
600
800
1000
1200

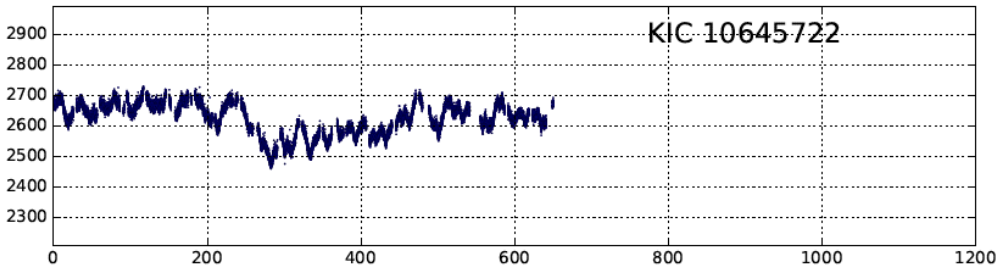
KIC 10645722
2900
2800
2700
2600
2500
2400
2300
0
200
400
600
800
1000
1200

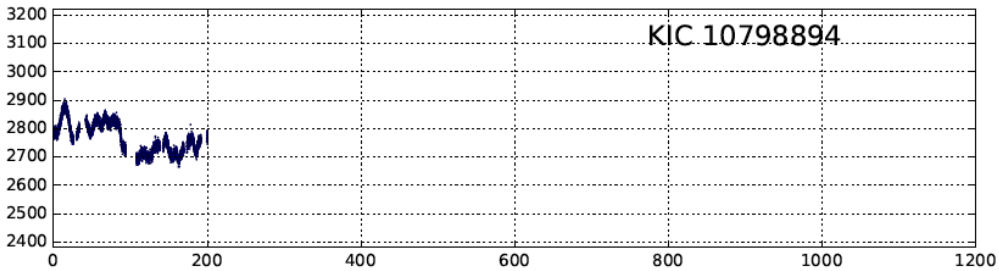
KIC 10798894
3200
3100
3000
2900
2800
2700
2600
2500
2400
0
200
400
600
800
1000
1200

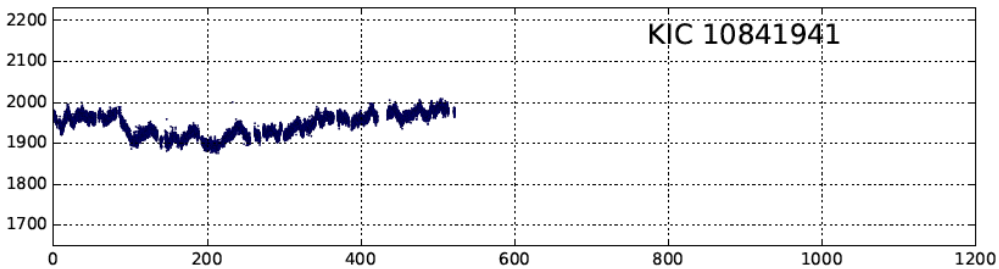
KIC 10841941
2200
2100
2000
1900
1800
1700
0
200
400
600
800
1000
1200

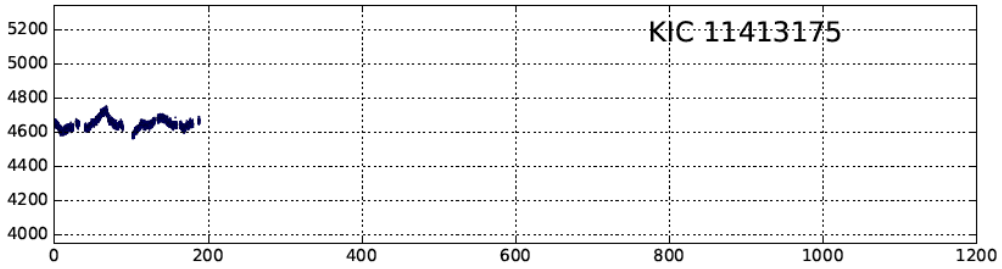
KIC 11413175
5200
5000
4800
4600
4400
4200
4000
0
200
400
600
800
1000
1200

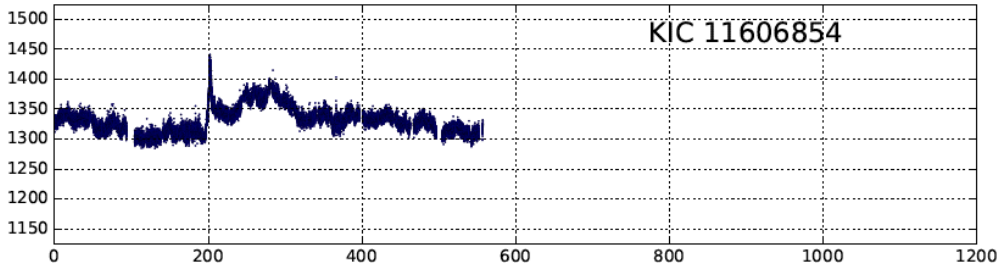
KIC 11606854
1500
1450
1400
1350
1300
1250
1200
1150
0
200
400
600
800
1000
1200

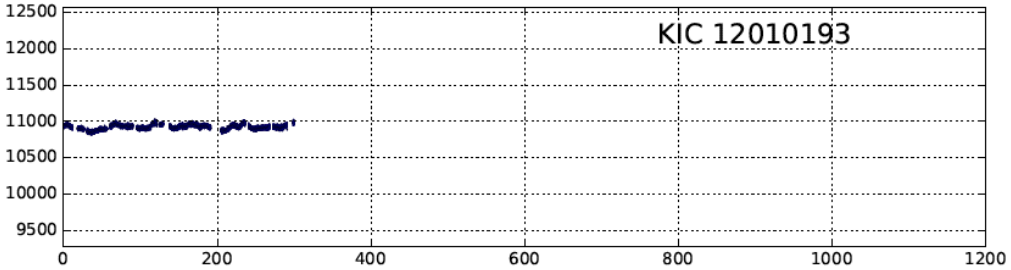
KIC 12010193
12500
12000
11500
11000
10500
10000
9500
0
200
400
600
800
1000
1200

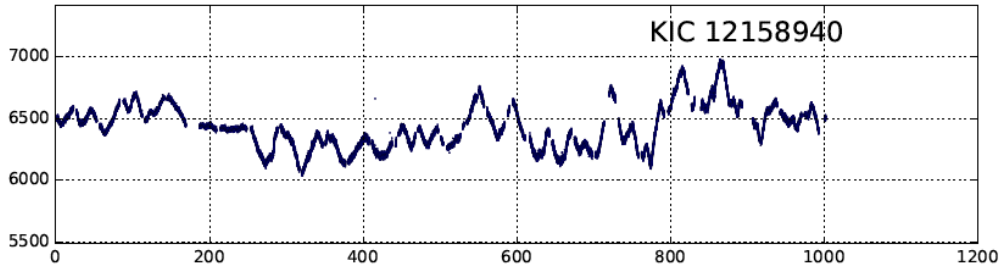
KIC 12158940
7000
6500
6000
5500
0
200
400
600
800
1000
1200

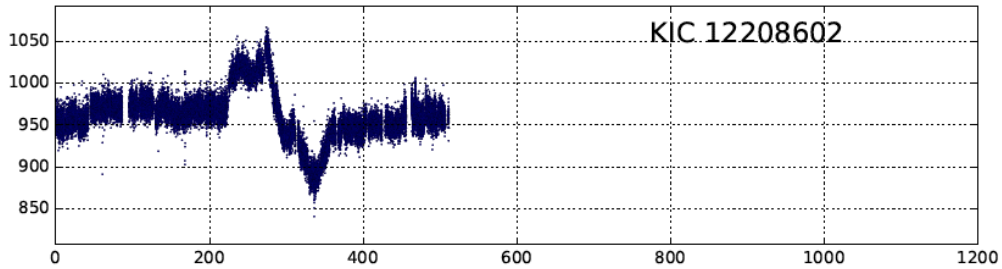
KIC 12208602
1050
1000
950
900
850
0
200
400
600
800
1000
1200

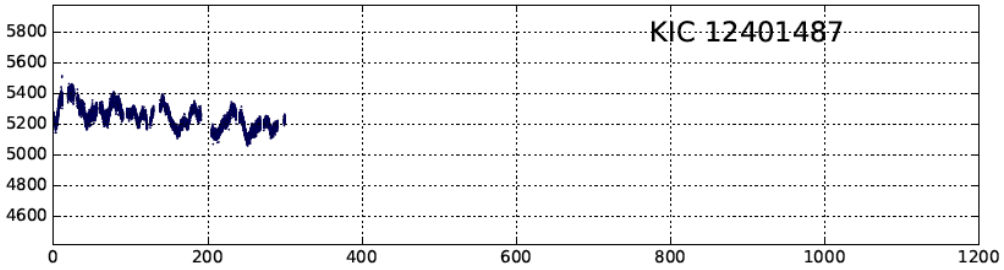

Figure Appendix A.2: Light curves of the *Kepler* AGN with identical flux and time axes. Each plot displays flux in units of counts $\sec^{-1}$ and time in rest-frame days.

Appendix B: PSDs of the *Kepler* AGN

We present here the power spectra and their best-fitting models following the Uttley et al. [2002] method. All power spectra are shown on the same scale, for an immediate indication of the different frequency sampling (due to different time baselines) and power law slopes for each object.

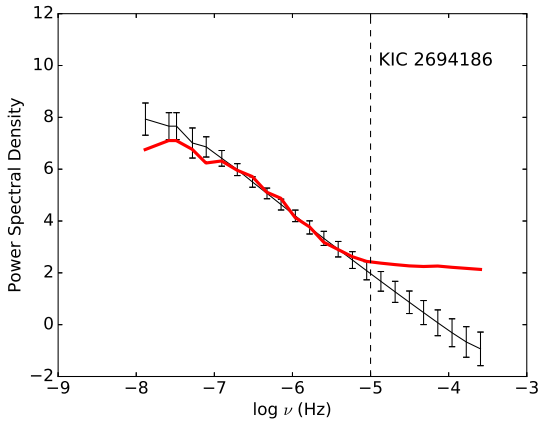
KIC 2694186
Power Spectral Density
log ν (Hz)

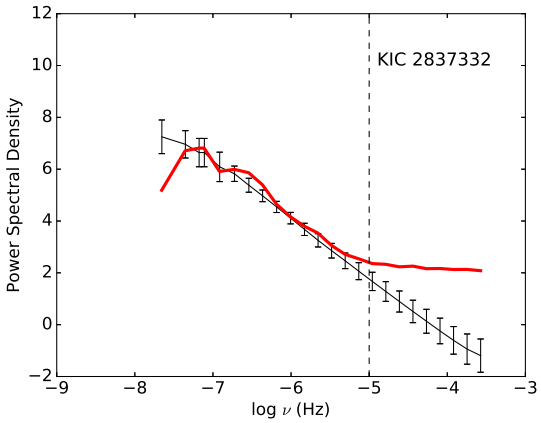
KIC 2837332
Power Spectral Density
log ν (Hz)

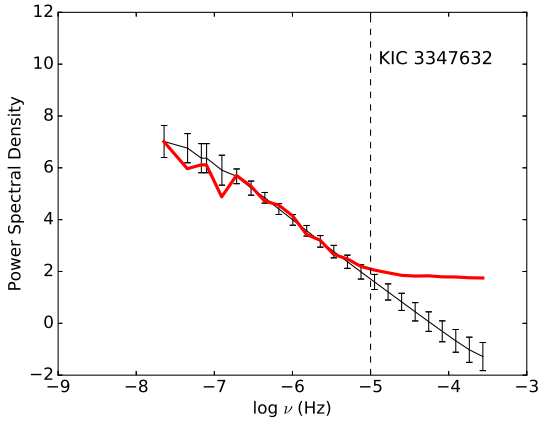
KIC 3347632
Power Spectral Density
log ν (Hz)

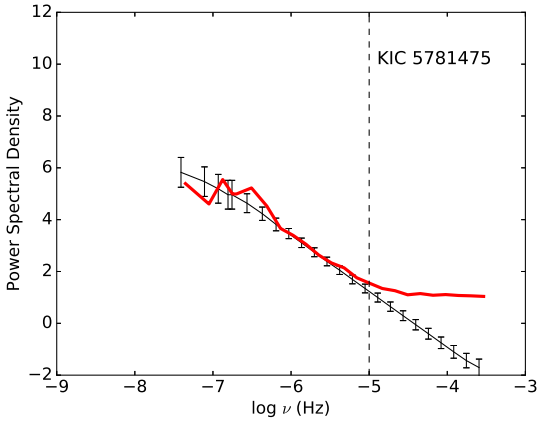
KIC 5781475
Power Spectral Density
log ν (Hz)

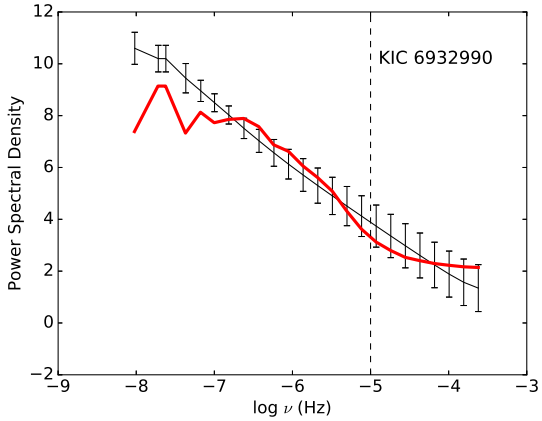
KIC 6932990
Power Spectral Density
log ν (Hz)

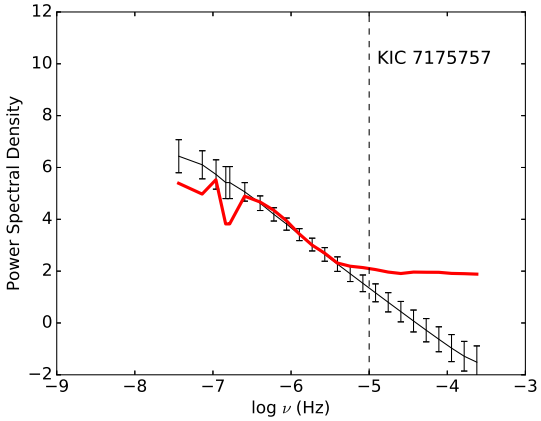
KIC 7175757
Power Spectral Density
log ν (Hz)

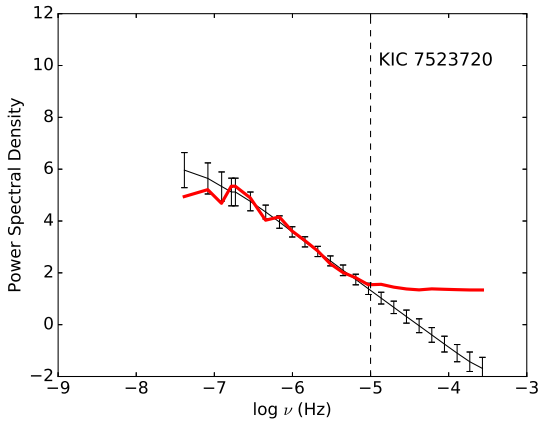
KIC 7523720
Power Spectral Density
log ν (Hz)

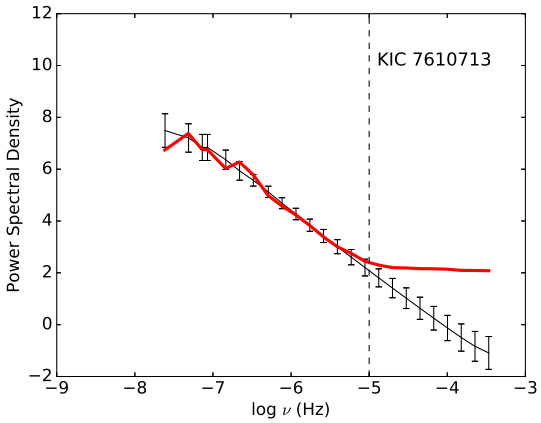
KIC 7610713
Power Spectral Density
log ν (Hz)

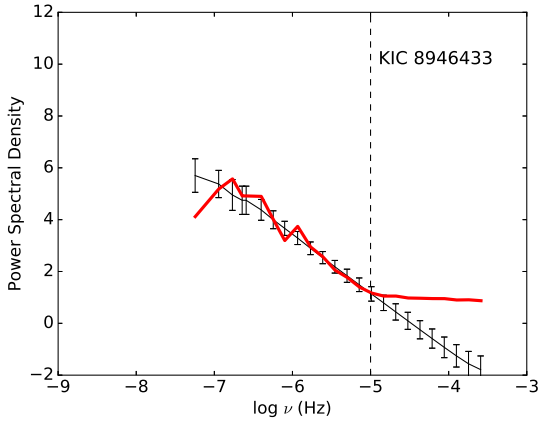
KIC 8946433
Power Spectral Density
log ν (Hz)

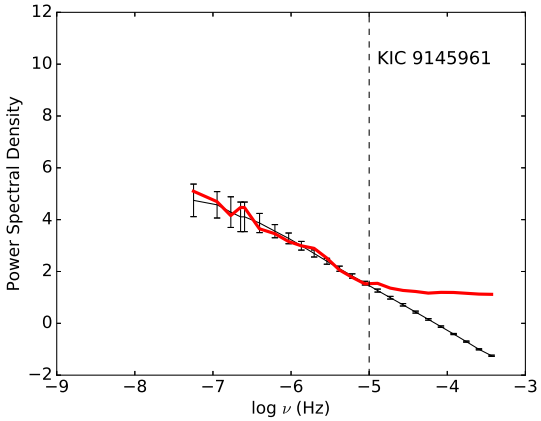
KIC 9145961
Power Spectral Density
log ν (Hz)

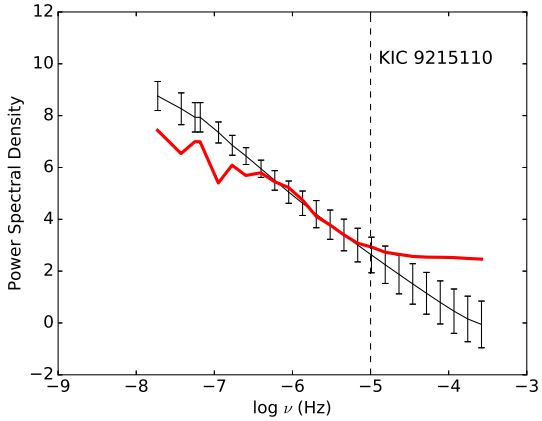
KIC 9215110
Power Spectral Density
log ν (Hz)

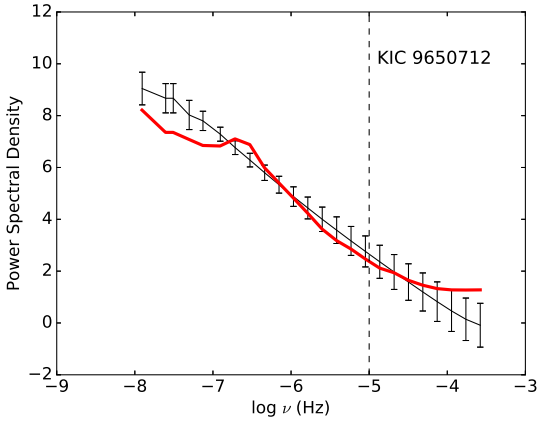
KIC 9650712
Power Spectral Density
log ν (Hz)

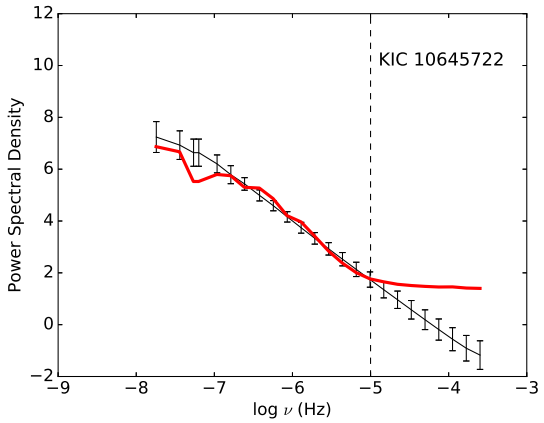
KIC 10645722
Power Spectral Density
log ν (Hz)

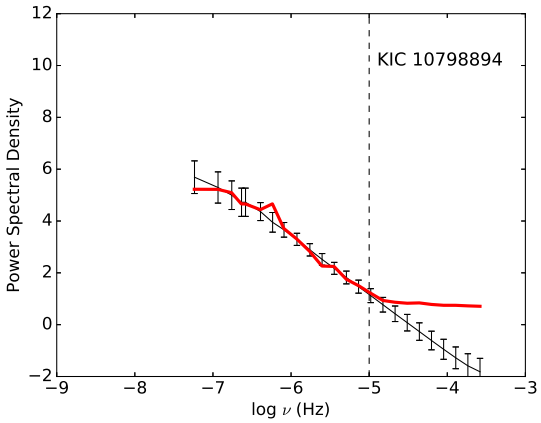
KIC 10798894
Power Spectral Density
log ν (Hz)

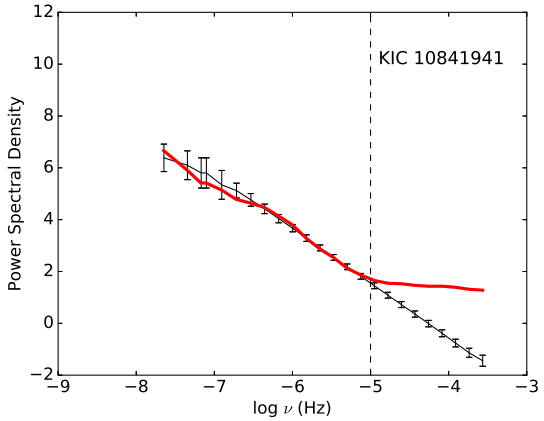
KIC 10841941
Power Spectral Density
log ν (Hz)

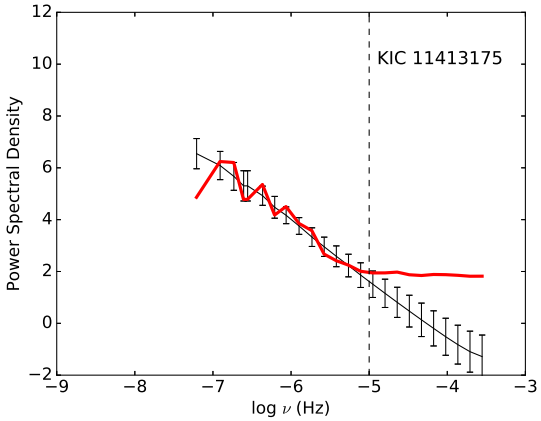
KIC 11413175
Power Spectral Density
log ν (Hz)

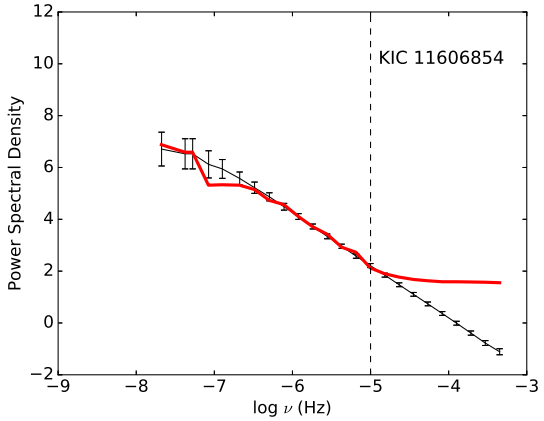
KIC 11606854
Power Spectral Density
log ν (Hz)

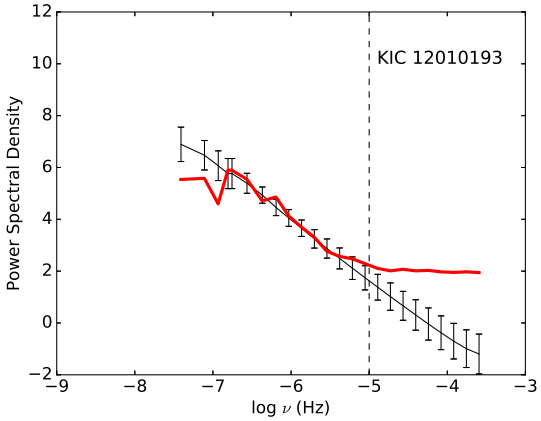
KIC 12010193
Power Spectral Density
log ν (Hz)

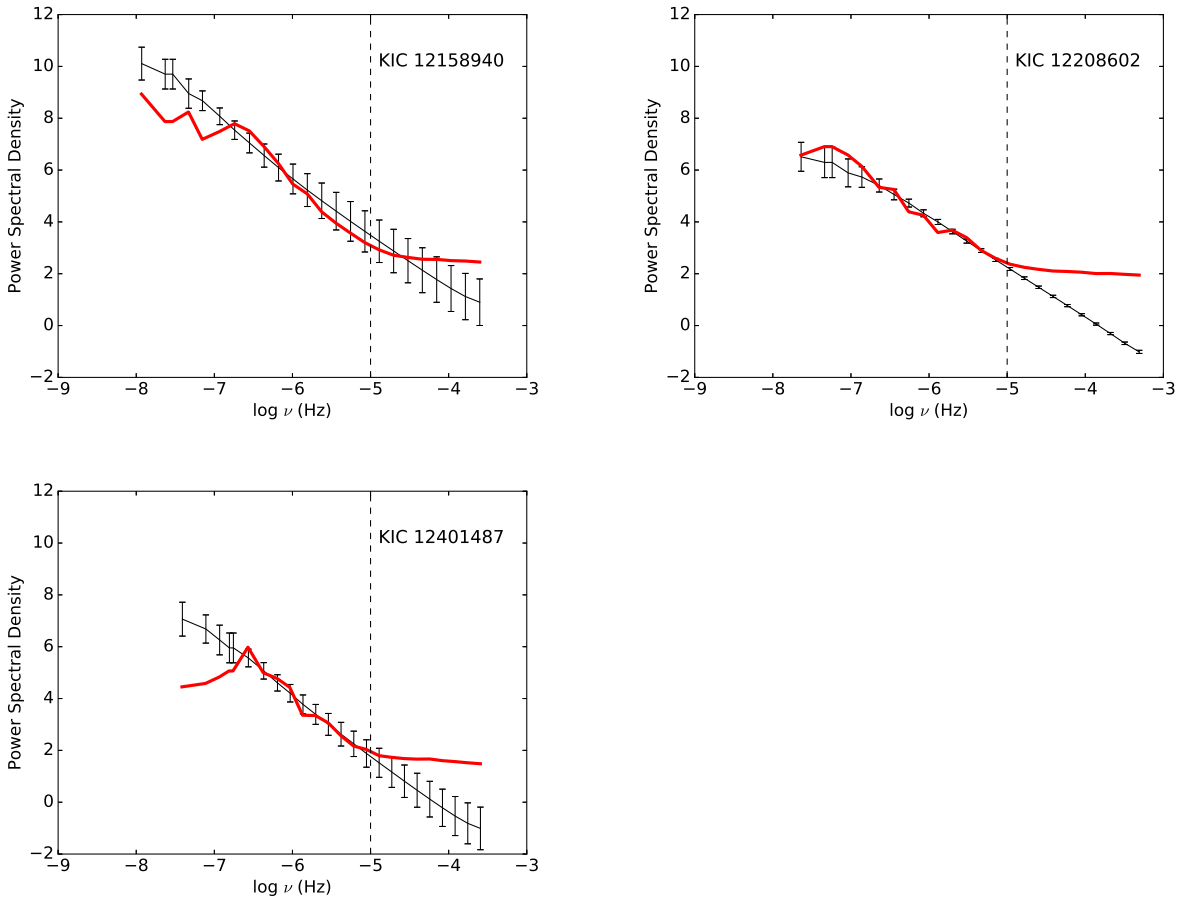

Figure Appendix B.1: Power spectra of the *Kepler* AGN. Red denotes the observed binned power spectra, while black shows the best-fitting model from the Uttley et al. [2002] method with the error bars. Error bars in this case denote the spread in the simulated power spectra; see Section 4.5 for details. Fitting was only performed on frequencies lower than the dashed line, which denotes the point at which Poisson noise begins to dominate. Objects best-fit by broken power laws (e.g., KIC 12401487) are shown here for completeness. The broken power law fits can be seen in Figure 4.9.

Appendix C: Flux Histograms of the *Kepler* AGN

We present here the flux distribution histograms of the *Kepler* AGN light curves, without binning or interpolated points. We have attempted to fit each histogram with a lognormal distribution, but these fits often are not a good match to the data. Many histograms exhibit bimodality, and these are fit with a double-gaussian. In these cases, the centroids of the best-fitting gaussians correspond to the red dashed lines in the light curve images in Appendix A.

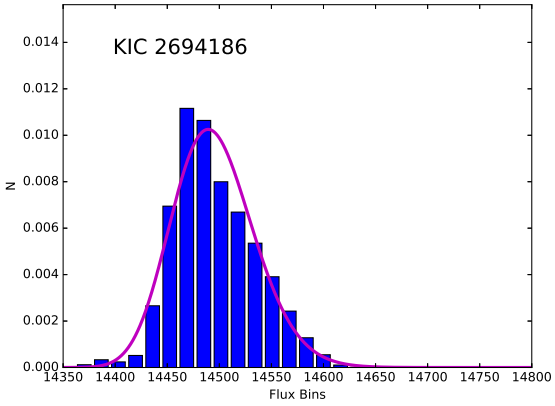
KIC 2694186
N
Flux Bins

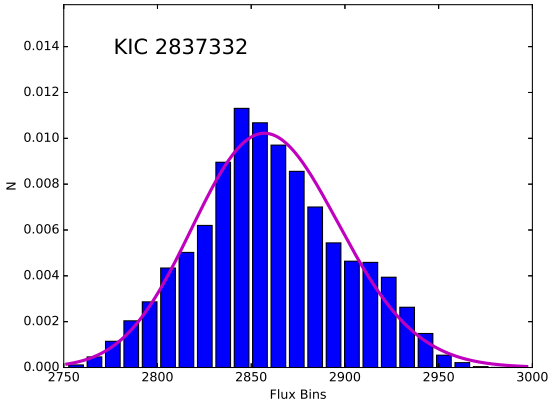
KIC 2837332
N
Flux Bins

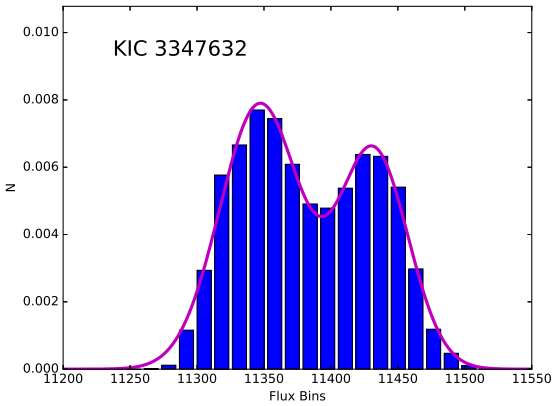
KIC 3347632
N
Flux Bins

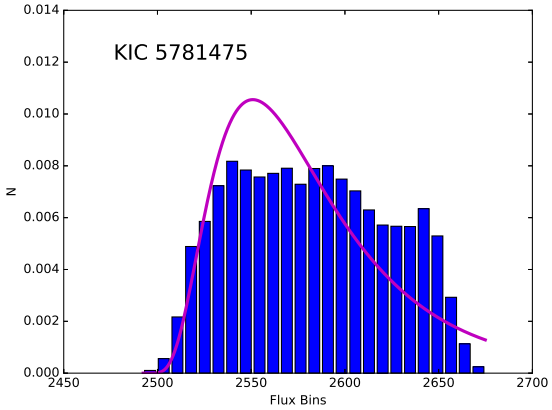
KIC 5781475
N
Flux Bins

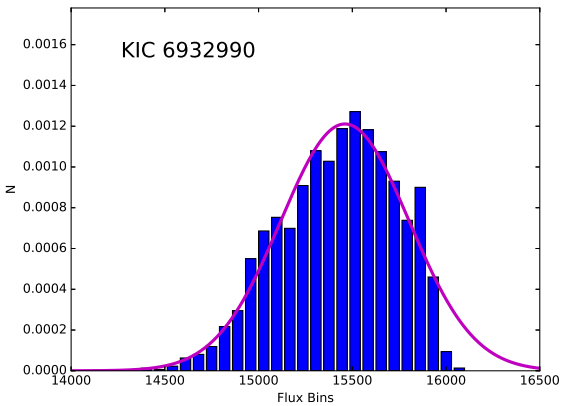
KIC 6932990
N
Flux Bins

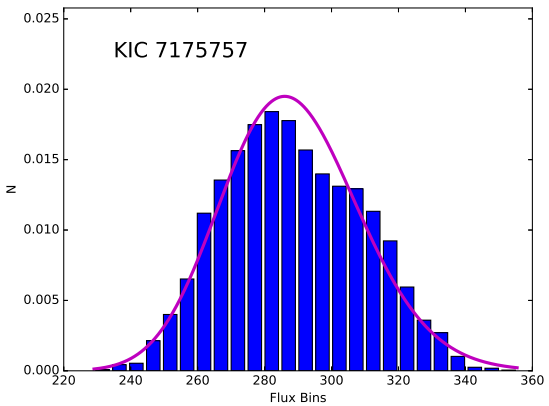
KIC 7175757
N
Flux Bins

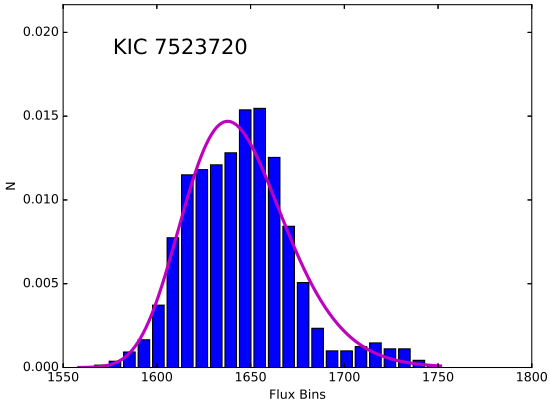
KIC 7523720
N
Flux Bins
0.020
0.015
0.010
0.005
0.000
1550
1600
1650
1700
1750
1800

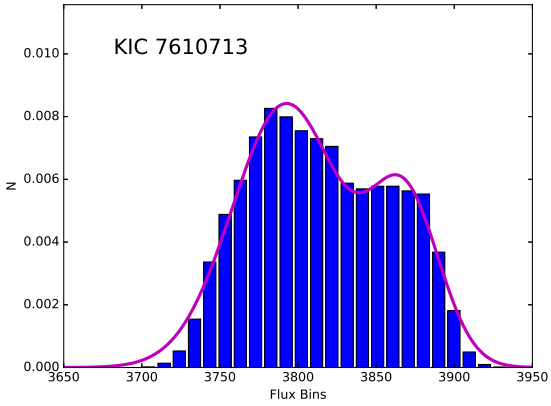
KIC 7610713
N
Flux Bins
0.010
0.008
0.006
0.004
0.002
0.000
3650
3700
3750
3800
3850
3900
3950

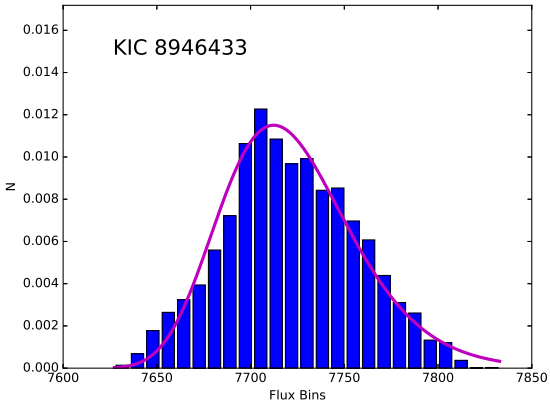
KIC 8946433
N
Flux Bins
0.016
0.014
0.012
0.010
0.008
0.006
0.004
0.002
0.000
7600
7650
7700
7750
7800
7850

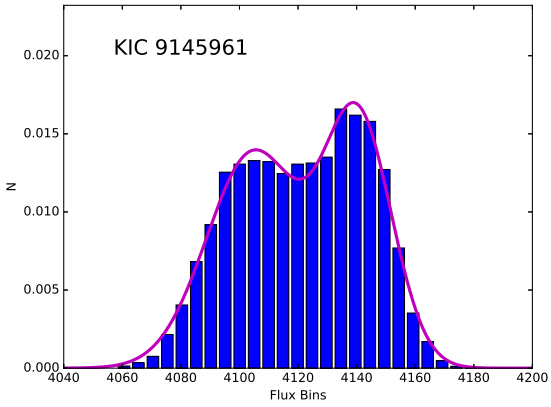
KIC 9145961
N
Flux Bins
0.020
0.015
0.010
0.005
0.000
4040
4060
4080
4100
4120
4140
4160
4180
4200

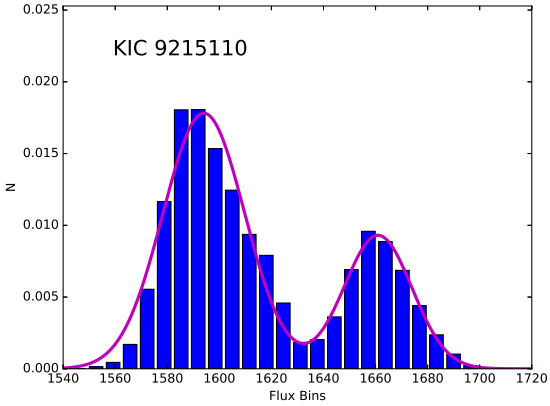
KIC 9215110
N
Flux Bins
0.025
0.020
0.015
0.010
0.005
0.000
1540
1560
1580
1600
1620
1640
1660
1680
1700
1720

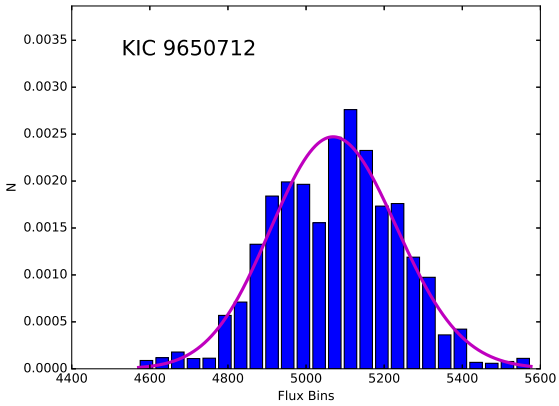
KIC 9650712
N
Flux Bins
0.0035
0.0030
0.0025
0.0020
0.0015
0.0010
0.0005
0.0000
4400
4600
4800
5000
5200
5400
5600

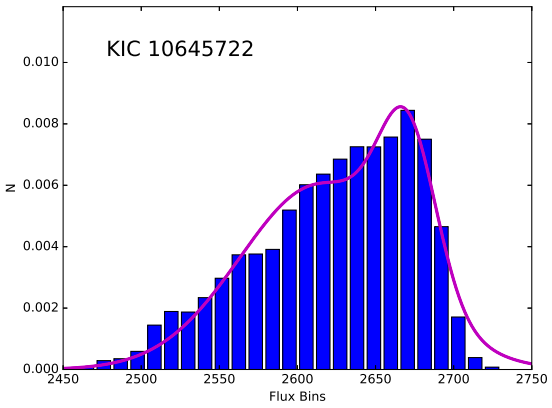
KIC 10645722
N
Flux Bins

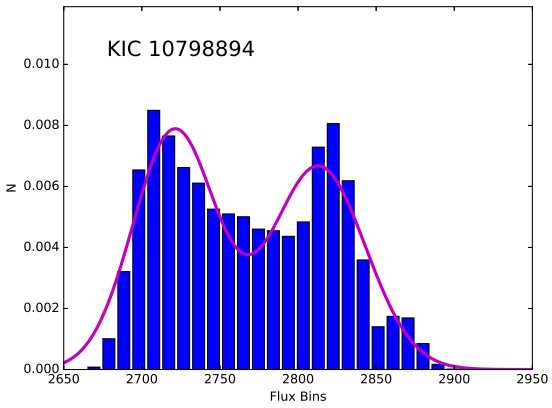
KIC 10798894
N
Flux Bins

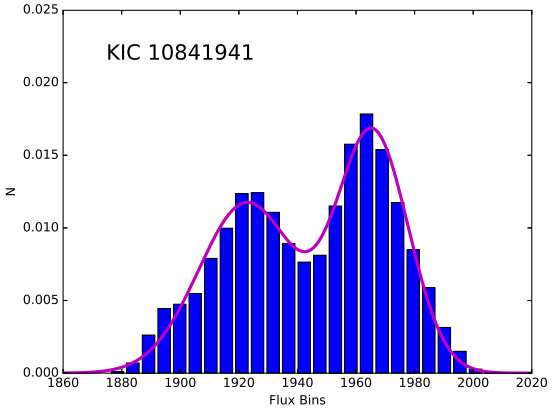
KIC 10841941
N
Flux Bins

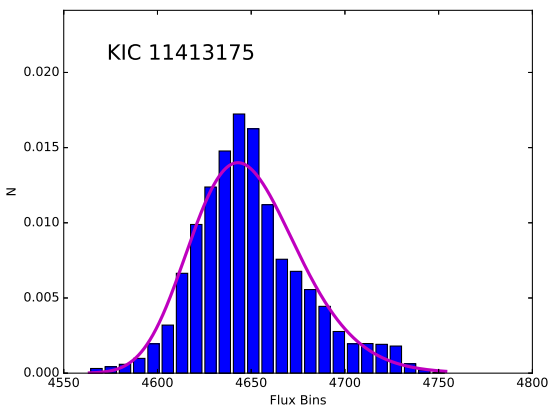
KIC 11413175
N
Flux Bins

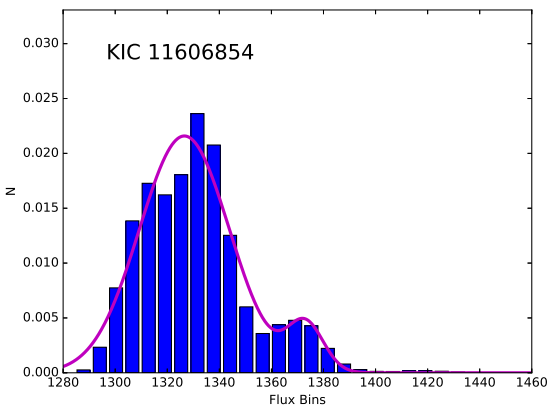
KIC 11606854
N
Flux Bins

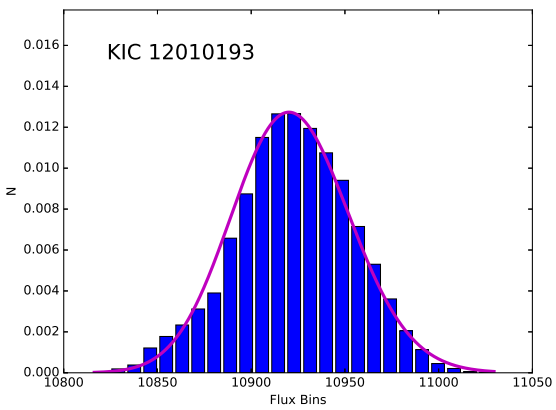
KIC 12010193
N
Flux Bins

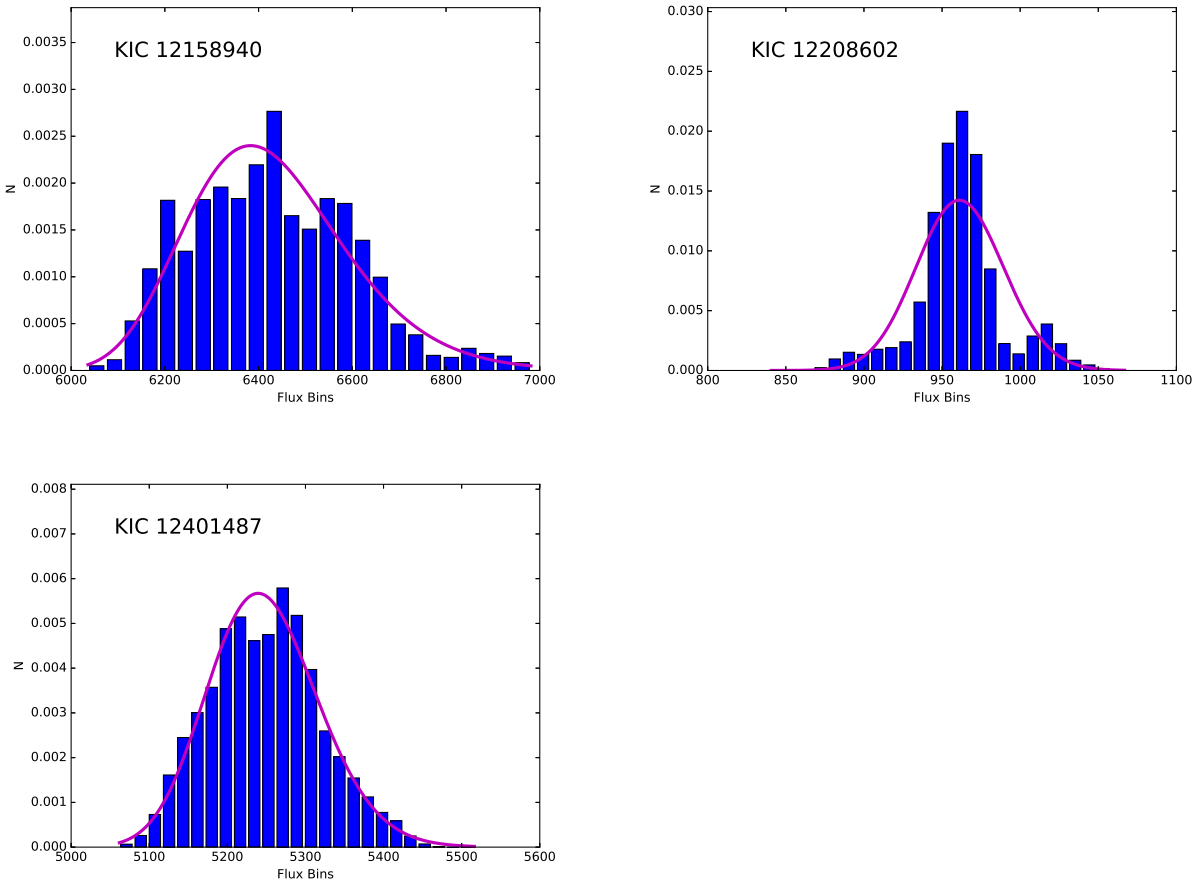

Figure Appendix C.1: Flux distribution histograms, with either lognormal or bimodal gaussian fits (magenta curve).

Bibliography

Alonso-Herrero, A. et al. 2016, MNRAS, 455, 563

Angione, R.J. & Smith, H.-J. 1972, in Evans D.S., Wills D., Wills B.J., eds, Proc. IAU Symp. 44, External Galaxies and Quasi-Stellar Objects. Kluwer, Dordrecht, 171

Antonucci, R.R.J. & Miller, J.S. 1985, ApJ, 297, 621

Aretxaga, I., Cid Fernandes, R. & Terlevich, R.J. 1997, MNRAS, 286, 271

Arevalo, P. & Uttley, P. 2006, MNRAS, 367, 801

Baade, W. & Minkowski, R. 1954, ApJ, 119, 206

Baganoff, F.K. & Malkan, M.A. 1995, ApJL, 444, L13

Balbus, S.A. & Hawley, J.F. 1991, 376, 214

Baldi, R.D., Behar, E., Laor, A. & Horesh, A. 2015, MNRAS, 454, 4277

Ballo, L., Heras, F.J.H., Barcons, X. & Carrera, F.J. 2012, A&A, 545, 66

Balmaverde, B., Capetti, A. & Grandi, P. 2006, A&A, 451, 35

Balona, L.A., Catanzaro, G., Crause, L., Cunha, M.S., Gandolfi, D., Hatzes, A., Uytterhoeven, K. & De Cat, P. 2013, MNRAS, 432, 2808

Balona, L.A. 2012, MNRAS, 423, 3420

Barthelmy, S.D. et al. 2005, SSRv, 120, 143

Barth, A.J. et al. 2011, ApJ, 732, 121

Barth, A.J. et al. 2011, ApJL, 743, L4

Bauer, A., Baltay, C., Coppi, P., Ellman, N., Jerke, J., Rabinowitz, D. & Scalzo, R. 2009, ApJ, 696, 1241

Baum, S.A., O'Dea, C.P., Dallacassa, D., de Bruyn, A.G. & Pedlar, A. 1993, ApJ, 419, 553

Baumgartner, W.H. et al. 2013, ApJS, 207, 19

Becker, R.H., White. R.L. & Helfland, D.J. 1995, ApJ, 450, 559

Behar, E., Ranieri, D.B., Laor, A., Horesh, A., Stevens, J. & Tzioumis, T. 2015, MNRAS, 451, 517

Bell, E.F. 2003, ApJ, 586, 794

Bentz, M.C. et al. 2010, ApJ, 716, 993

Bentz, M.C. et al. 2014, ApJ, 796, 8

Bentz, M.C. & Katz, S. 2015, PASP, 127, 67

Bianchi, S. et al. 2008, MNRAS, 385, 195

Boller, T., Freyberg, M.J., Trümper, J., Haberl, F., Voges, W. & Nandra, K. 2016, A&A, 588, A103

Bolton, C.T. 1972, Nature, 235, 271

Bonchi, A., LaFranca, F., Melini, G., Bongiorno, A. & Fiore, F. 2013, MNRAS, 429, 1970

Boselli, A., et al. 2010, PASP, 122, 261

Botte, V., Ciroi, S., Rafanelli, P. & Di Mille, F. 2004, AJ, 127, 3168

Breeveld, A.A., Landsman, W., Holland, S.T., Roming, P., Kuin, N.P.M. & Page, M.J. 2011, in AIP Conf. Ser. 1358, ed. J.E. McEnery, J.L. Rascusin & N. Gehrels (Melville, NY: AIP), 373

Brinchmann, J., Charlot, S., White, S.D.M., Tremonti, C., Kauffmann, G., Heckman, T. & Brinkmann, J. 2004, MNRAS, 351, 1151

Brinkmann, W., Laurent-Muehleisen, S.A., Voges, W., Siebert, J., Becker, R.H., Brotherton, M.S., White, R.L. & Gregg, M.D. 2000, A&A, 356, 445

Brown, T.M., Latham, D.W., Everett, M.E. & Esquerdo, G.A. 2011, AJ, 142, 112

Burrows, D.N. et al. 2005, SSRv, 120, 165

Butler, N.R. & Bloom, J.S. 2011, AJ, 141, 93

Burbidge, G.R. 1961, Nature, 190, 1053

Cannizzo, J.K., Smale, A.P., Wood, M.A., Still, M. & Howell, S.B. 2012, ApJ, 747, 117

Canosa, C.M., Worrall, D.M., Hardcastle, M.J. & Birkinshaw, M. 1999, MNRAS, 310, 30

Caplar, N., Lilly, S.J. & Trakhtenbrot, B. 2017, ApJ, 834, 111

Carini, M.T. & Ryle, W.T. 2012, ApJ, 749, 70

Casey, C.M., Berta, S., Béthermin, M. et al. 2012, ApJ, 761, 140

Casali, M. et al. 2007, A&A, 467, 777

Chandrasekhar, S. 1960, PNAS, 46, 253

Catanzaro, G. et al. 2011, MNRAS, 411, 1167

Cid Fernandes, R., Sodré, Jr., L. & Vieira da Silva, Jr., L. 2000, ApJ, 544, 123

Cimatti, A. et al. 2013, ApJ, 779, 13

Ciotti, L., Ostriker, J.P. & Proga, D. 2010, ApJ, 717, 708

Cirasuolo, M., Celotti, A., Magliocchetti, M. & Danese, L. 2003, MNRAS, 346, 447

Cleveland, W.S. 1979, Journal of the American Statistical Association, 74, 829

Cohen, M., Wheaton, W.A. & Megeath, S.T. 2003, AJ, 126, 1090

Collier, S. & Peterson, B.M. 2001, ApJ, 555, 775

Collin, S., Kawaguchi, T., Peterson, B.M. & Vestergaard, M. 2006, A&A, 456, 75

Condon, J.J. & Yin, Q.F. 1990, ApJ, 357, 97

Condon, J.J., Cotton, W.D, Greisen, E.W., Yin, Q.F., Perley, R.A., Taylor, G.B. & Broderick, J.J. 1998, AJ, 115, 1693

Condon, J.J., Kellermann, K.I., Kimball, A.E., Ivezić, Z. & Perley, R.A. 2013, ApJ, 768, 37

Condon, J.J. 1992, ARA&A, 30, 575

Cortese, L., Boissier, S., Boselli, A., Bendo, G.J., Buat, V., Davies, J.I., Eales, S., Heinis, S., Isaak, K.G. & Madden, S.C. 2012, A&A, 544, 101

Coughlin, J.L., López-Morales, M., Harrison, T.E., Ule, N. & Hoffman, D.I. 2011, AJ, 141, 78

Cristiani, S., Vio, R. & Andreani, P. 1990, AJ, 100, 56

Cristiani, S., Trentini, S., La Franca, F. & Andreani, P. 1997, A&A, 321, 123

Czerny, B., Doroshenko, V.T., Nikolajuk, M., Schwarzenberg-Czerny, A., Loska, Z. & Madejski, G. 2003, MNRAS, 342, 1222

Dasyra, K.M., Tacconi, L.J., Davies, R.I. et al. 2007, ApJ, 657, 102

Debosscher, J., Blomme, J., Aerts, C. & De Ridder, J. 2011, A&A, 529, 89

Denney, K.D. et al. 2010, 721, 715

DePoy, D.L., Becklin, E.E. & Geballe, T.R. 1987, ApJ, 316, 63

Di Matteo, T., Springel, V. & Hernquist, L. 2005, Nature, 433, 604

Dubois, Y., Gavazzi, R., Peirani, S. & Silk, J. 2013, MNRAS, 433, 3297

Edelson, R. & Malkan, M. 1986, ApJ, 308, 59

Edelson, R. & Nandra, K. 1999, 514, 682

Edelson, R. et al. 2002, ApJ, 568, 610

Edelson, R. & Malkan, M. 2012, ApJ, 751, 52

Edelson, R., Mushotzky, R., Vaughan, S., Scargle, J., Gandhi, P., Malkan, M. & Baumgartner, W. 2013, ApJ, 766, 16

Edelson, R., Vaughan, S., Malkan, M., Kelly, B.C., Smith, K.L., Boyd, P.T. & Mushotzky, R.M. 2014, ApJ, 795, 2

Ellison, S.L., Teimoorinia, H., Rosario, D.J. & Mendel, J.T. 2016, MNRAS, 458, L34

Elvis, M. et al. 1978, MNRAS, 183, 129

Everett, M.E., Howell, S.B. & Kinemuchi, K. 2012, PASP, 124, 316

Fabian, A.C. 2012, ARA&A,50, 455

Falcke, H., Körding, E. & Markoff, S. 2004, A&A, 414, 895

Fanaroff, B.L. & Riley, J.M. 1974, 167, 31

Ferrarese, L. & Merritt, D. 2000, ApJ, 539, 9

Ferrarese, L. & Ford, H. 2005, SSRv, 116, 523

Fritz, J., Franeschini, A. & Hatziminaoglou, E. 2006, MNRAS, 366, 767

Fukumura, K., Kazanas, D., Contopoulos, I. & Behar, E. 2010, ApJ, 715, 636

Ganguly, R. et al. 2007, ApJ, 665, 990

Gaulme, P., McKeever, J., Rawls, M.L., Jackiewicz, J., Mosser, B. & Guzik, J.A. 2013, ApJ, 767, 82

Gebhardt, K. et al. 2000, ApJ, 539, 13

Genzel, R., Eisenhauer, F. & Gillessen, S. 2010, RvMP, 82, 3121

Genzel, R. et al. 2011, ApJ, 733, 101

Gioia, I.M., Maccacaro, T., Schild, R.E., Wolter, A., Stocke, J.T., Morris, S.L. & Henry, J.P. 1990, ApJS, 72, 567

Giveon, U., Maoz, D., Kaspi, S., Netzer, H. & Smith, P.S. 1999, MNRAS, 306, 637

Goad, M.R. et al. 2007, A&A, 476, 1401

González-Martín, O., Papadakis, I., Reig, P. & Zezas, A. 2011, A&A, 526, A132

González-Martín, O. & Vaughan, S. 2012, A&A, 544, 80

Goodman, J. 2003, MNRAS, 339, 937

Greene, J.E. & Ho, L.C. 2005, ApJ, 630, 122

Greene, J.E. et al. 2010, ApJ, 721, 26

Greene, J.E., Seth, A., Lyubenova, M., Walsh, J., van de Ven, G. & Läsker, R. 2014, ApJ, 788, 145

Gu, M.F. & Li, S.-L. 2013, A&A, 554, A51

Guggenberger, E. 2012, Astronomische Nachrichten, 333, 1044

Güdel, M. & Benz, A.O. 1993, ApJ, 405, L63

Gültekin, K., et al. 2009, ApJ, 698, 198

Harrison, C.M., Thomson, A.P., Alexander, D.M., Bauer, F.E., Edge, A.C., Hogan, M.T., Mullaney, J.R. & Swinbank, A.M. 2015, ApJ, 800, 45

Hawkins, M.R.S. 1993, Nature, 366, 242

Hawley, J.F. & Balbus, S.A. 1991, ApJ, 376, 223

Heckman, T.M., Lehnert, M.D., Strickland, D.K. & Armus, L. 2000, ApJS129, 493

Heckman, T.M. 2001, Gas and Galaxy Evolution (ASP Conf. Ser. 240), ed. J.E. Hibbard, M. Rupen & J. H. van Gorkom (San Francisco, CA: ASP), 345

Heinis, S. et al. 2014, MNRAS, 437, 1268

Heinke, C.O., Ruiter, A.J., Muno, M.P. & Belczynski, K. 2008, in AIP Conf. Proc. 1010, 136

Heinz, S. & Sunyaev, R.A. 2003, MNRAS, 343, L59

Hickox et al. 2009, ApJ, 696, 891

Hogg, J.D. & Reynolds, C.S. 2016, ApJ, 826, 40

Hook, I.M., McMahon, R.G., Boyle, B.J. & Irwin, M.J. 1994, MNRAS, 268, 305

Hopkins, P.F., Hernquist, L., Cox, T.J., Di Matteo, T., Robertson, B. & Springel, V. 2006, ApJS, 163, 1

Howell, S.B. et al. 2014, PASP, 126, 398

Howell, S.B., Mason, E., Boyd, P.T., Smith, K.L. & Gelino, D.M. 2016, ApJ, 831, 27

Jiang, Y.-F., Stone, J.M. & Davis, S.W. 2014, ApJ, 796, 106

Kaiser, N. et al. 2010, Proc. SPIE, Vol. 7733, 77330E

Kalberla, P.M.W., Burton, W.B., Hartmann, Dap, Arnal, E.M., Bajaja, E., Morras, R. & Pöppel, W.G.L. 2005, A&A, 440, 775

Kapanadze, B.Z. 2013, AJ, 145, 31

Kasliwal, V.P., Vogeley, M.S. & Richards, G.T. 2015, MNRAS, 451, 4328

Kawaguchi, T., Mineshige, S., Umemura, M. & Turner, E. 1998, ApJ, 504, 671

Kellermann, K.I., Sramek, R., Schmidt, M., Shaffer, D.B. & Green, R. 1989, AJ, 98, 1195

Kelly, B.C., Bechtold, J. & Siemiginowska, A. 2009, ApJ, 698, 895

Kelly, B.C., Sobolewska, M. & Siemiginowska, A. 2011, ApJ, 730, 52

Kelly, B.C., True, T., Malkan, M., Pancoast, A. & Woo, J.-H. 2013, ApJ, 779, 187

Kimball, A.E., Kellermann, K.I., Condon, J.J., Ivezić, Z. & Perley, R.A. 2011, ApJL, 739, L29

Klamer, I.J., Ekers, R.D., Sadler, E.M. & Hunstead, R.W. 2004, ApJ, 612, 97

Klein, U., Wielebinski, R. & Beck, R. 1984, A&A, 135, 213

Kollatschny, W. & Zetzl, M. 2010, A&A, 522, 36

Kolodziejczak, J. et al. 2010, Proc. SPIE, 7742, 38

Komossa, S. 2015, Journal of High Energy Astrophysics, 7, 148

Koss, M., Mushotzky, R.F., Treister, E., Veilleux, S., Vasudevan, R., Miller, N., Sanders, D.B., Schawinski, K. & Trippe, M. 2011, ApJ, 735L, 42

Koss, M., Mushotzky, R.F., Veilleux, S., Winter, L.M., Baumgartner, W., Tueller, J., Gehrels, N. & Valencic, L. 2011, ApJ, 739, 57

Koslowski, S. et al. 2010, ApJ, 708, 927

Koslowski, S. 2016, ApJ, 826, 118

Krautter, J., Zickgraf, F.-J., Appenzeller, I., Thiering, I., Voges, W., Chavarria, C., Kneer, R., Mujica, R., Pakull, M.W., Serrano, A. & Ziegler, B. 1999, A&A, 350, 743

Kristian, J., Sandage, A., & Katem, B. 1974, ApJ, 191, 43

Krolik, J.H. & Begelman, M.C. 1988, ApJ, 329, 702

Law, N.M. et al. 2009, PASP, 121, 1395

Lépine, S. & Gaidos, E. 2011, AJ, 142, 138

Laor, A. & Behar, E. 2008, MNRAS, 390, 847

Law, D.R., Steidel, C.C., Shapley, A.E., Nagy, S.R., Reddy, N.A. & Erb, D.K. 2012, ApJ, 745, 85

Leslie, S.K., Kewley, L.J., Sanders, D.B. & Lee, N. 2016, MNRAS, 455, 82

Lira, P., Videla, L., Wu, Y., Alonso-Herrero, A., Alexander, D.M., Ward, M. 2013, ApJ, 764, 159

Liu, T. et al. 2016, ApJ, 833, 6

Ludlam, R.M., Cackett, E.M., Gültekin, K., Fabian, A.C., Gallo, L. & Miniutti, G. 2015, MNRAS, 447, 2112

Lynden-Bell, D. 1969, Nature, 223, 690

Lyubarskii, Y.E. 1997, MNRAS, 292, 679

MacLeod, C.L. et al. 2010, ApJ, 721, 1014

Maccacaro, T., Gioia, I.M., Wolter, A., Zamorani, G. & Stocke, J.T. 1988, ApJ, 326, 680

Matthews, T.A., Morgan, W.W. & Schmidt, M. 1964, ApJ, 140, 35

McKernan, B., Ford, K.E.S., Lyra, W., Perets, H.B., Winter, L.M. & Yaqoob, T. 2011, MNRAS, 417, L103

Magorrian, J. et al. 1998, AJ, 115, 2285

Maini, A., Prandoni, I., Norris, R.P., Giovannini, G. & Spitler, L.R. 2016, A&A, 589, L3

Manmoto, T., Takeuchi, M., Mineshige, S., Matsumoto, R. & Negoro, H. 1996, ApJL, 464, L135

Marconi, A. & Hunt, L.K. 2003, ApJ, 589, 21

Markowitz, A., Edelson, R. & Vaughan, S. 2003, ApJ, 598, 935

Martin, C. et al. 2003, SPIE, 4854, 336

Massaro, E., Giommi, P., Leto, C., Marchegiani, P., Maselli, A., Perri, M., Piranomonte, S. & Sclavi, S. 2009, A&A, 495, 691

Mateos, S., Alonso-Herrero, A., Carrera, F. J., et al. 2012, MNRAS, 426, 3271

Matthews, T.A. & Sandage, A.R. 1963, ApJ, 138, 30

McClintock, J.E. & Remillard, R.A. *Black Hole Binaries* (2006), pp. 157-213

McHardy, I.M., Uttley, P., Taylor, R.D. & Seymour, N. 2004, AIPC, 714, 174

McHardy, I.M., Koerding, E., Knigge, C., Uttley, P. & Fender, R.P. 2006, Nature, 444, 730

McMullin, J.P., Waters, B., Schiebel, D., Young, W. & Golap, K. 2007, Astronomical Data Analysis Software and Systems XVI (ASP Conf. Ser. 376), ed. R.A. Shaw, F. Hill & D.J. Bell (San Francisco, CA: ASP), 127

McQuillan, A., Mazeh, T. & Aigrain, S. 2014, ApJS, 211, 24

Merloni, A., Heinz, S. & Di Matteo, T. 2003, MNRAS, 345, 1057

Metzger, B.D. & N.C., 2017, arXiv 1705:00643

Miller, J.M., Raymond, J., Fabian, A., Steeghs, D., Homan, J., Reynolds, C., van der Kils, M. & Wijnands, R. 2006, Nature, 441, 953

Mohan, P., Gupta, A.C., Bachev, R. & Strigachev, A. 2016, MNRAS, 456, 654

Morić, I., Smolčić, V., Kimball, A., Riechers, D.A., Ivezić, Ž. & Scoville, N. 2010, ApJ, 724, 779

Morrissey, P. et al. 2007, ApJS, 173, 682

Mukai, K. 1993, Legacy 3, 21-31

Mullaney, J.R., Alexander, D.M., Goulding, A.D. & Hickox, R.C. 2011, MNRAS, 414, 1082

Mullaney, J.R. et al. 2012, ApJ, 753, L30

Murphy, E.J. et al. 2011, ApJ, 737, 67

Mushotzky, R.F. 2004, in Astrophysics and Space Sciences Library, Vol. 308, Supermassive Black Holes in the Distant Universe, ed. A.J. Barger, 53

Mushotzky, R.F., Edelson, R., Baumgartner, W. & Gandhi, P. 2011, ApJ, 743, 12

Mushotzky, R.F., Shimizu, T.T., Melendez, M. & Koss, M. 2014, ApJL, 781, 34

Nagar, N.M., Falcke, H., Wilson, A.S. & Ulvestad, J.S. 2002, A&A, 392, 53

Nandra, K. & Pounds, K.A. 1994, MNRAS, 268, 405

Nandra, K., Georgakakis, A., Willmer, C.N.A., Cooper, M.C., Croton, D.J., Davis, M., Faber, S.M., Koo, D.C., Laird, E.S. & Newman, J.A. 2007, ApJ, 660, 11

Noeske, K.G. et al. 2007, ApJ, 660, L43

Nowak, M.A. et al. 1999, ApJ, 510, 874

Oke, J.B. & Gunn, J.E. 1983, ApJ, 619, L7

Orienti, M. & Prieto, M.A. 2010, MNRAS, 401, 2599

Pacini, F. 1966, Nature, 209, 389

Padovani, P. 2011, MNRAS, 411, 1547

Padovani, P., Bonzini, M., Kellerman, K.I., Miller, N., Mainieri, V. & Tozzi, P. 2015, MNRAS, 452, 1263

Page, K.L., Reeves, J.N., O'Brien, P.T. & Turner, M.J.L. 2005, MNRAS, 364, 195

Panessa, F., Barcons, X., Bassani, L., Cappi, M., Carrera, F.J., Ho, L.C. & Pellegrini, S. 2007, A&A, 467, 519

Panessa, F. & Giroletti, M. 2010, Accretion and Ejection in AGN: a Global View (ASP Conf. Ser. 427), ed. L. Maraschi, G. Ghisellini, R. Della Ceca & F. Tavecchio (Como, Italy:ASP), 377

Pannella, M. et al. 2015, ApJ, 807, 141

Papadakis, I.E. & Lawrence, A. 1993, Nature, 361, 233

Papadakis, I.E. & Lawrence, A. 1995, MNRAS, 272, 161

Pasham, D.R., Strohmayer, T.E. & Mushotzky, R.F. 2014, 513, 74

Perley, R.A., Chandler, C.J., Butler, B.J., & Wrobel, J.M. 2011, ApJL, 739, L1

Peterson, B.M. et al. 1994, ApJ, 425, 622

Peterson, B.M. *An Introduction to Active Galactic Nuclei* (1997)

Peterson, B.M., Wanders, I., Bertram, R., Hunley, J.F., Pogge, R.W. & Wagner, R.M. 1998, ApJ, 501, 82

Peterson, B.M., Ferrarese, L., Gilbert, K.M., Kaspi, S., Malkan, M.A., Maoz, D., Merritt, D., Netzer, H., Onken, C.A., Pogge, R.W., Vestergaard, M. & Wandel, A. 2004, ApJ, 613, 682

Peterson, B.M. 2015, SSRv, 183, 253

Pica, A.J. & Smith, A.G. 1983, 272, 11

Pier, E.A. & Krolik, J.H. 1992, ApJ, 401, 99

Pigulski, A., Pojmanski, G., Pilecki, B. & Szczygiel, D.M. 2009, AcA, 59, 33

Pinsonneault, M.H., An, D., Molenda-Zakowicz, J., Chaplin, W.J., Metcalfe, T.S. & Bruntt, H. 2012, ApJS, 199, 30

Planck Collaboration XIII 2015, arXiv:1502.01589

Prša, A. et al. 2011, AJ, 141, 83

Rakshit, S. & Stalin, C.S. 2017, arXiv:1705.05123

Rauch, K.P. & Blandford, R.D. 1991, ApJL, 381, L39

Reynolds, C.S. & Miller, M.C. 2009, ApJ, 692, 896

Rodighiero, G. et al. 2010, A&A, 518, 25

Roming, P.W.A. et al. 2005, SSRv, 120, 95

Rosario, D.J. et al. 2013, ApJ, 771, 63

Roy, A.L., Norris, R.P., Allen, D.A., Troup, E.R. & Kesteven, M.J. 1992, Relationships Between Active Galactic Nuclei and Starburst Galaxies (ASP Conf. Ser. 31), ed. A.V. Filippenko (San Francisco, CA:ASP), 29

Roy, A.L., Norris, A.P., Kesteven, M.J., Troup, E.R. & Reynolds, J.E. 1998, MNRAS, 301, 1019

Rubin, K.H.R., Prochaska, J.X., Koo, D.C., Phillips, A.C., Martin, C.L., & Winstrom, L.O. 2014, ApJ, 794, 156

Runnoe, J.C., Brotherton, M.S. & Shang, Z. 2012, MNRAS, 422, 478

Sadler, E. et al. 2002, MNRAS, 329, 227

Salim, S. et al. 2007, ApJS, 173, 267

Salpeter, E.E. 1964, ApJ, 140, 796

Salvato, M., Greiner, J. & Kuhlbrodt, B. 2004, ApJ, 600, L31

Sandage, A.R. 1964, ApJ, 139, 416

Saxton, R.D. et al. 2008, A&A, 480, 611

Scaringi, S., Körding, E., Uttley, P., Groot, P.J., Knigge, C., Still, M. & Jonker, P. 2012, MNRAS, 427, 3396

Scaringi, S., Groot, P.J., Verbeek, K., Greiss, S., Knigge, C. & Körding, E. 2013, MNRAS, 428, 2207

Scaringi, S. et al. 2015, Science Advances, 1, e1500686

Schawinski, K., et al. 2009, ApJ, 690, 1672

Schawinski, K., Virani, S., Simmons, B., Urry, C.M., Treister, E., Kaviraj, S. & Kushkuley, B. 2010, ApJ, 692, L19

Schawinski, K. et al. 2014, MNRAS, 440, 889

Schmidt, E.G., Rogalla, D. & Thacker-Lynn, L. 2011, AJ, 141, 53

Schmidt, M. 1963, Nature, 197, 1040

Sesar, B. et al. 2007, AJ, 134, 2236

Seyfert, C.K. 1943, ApJ, 97, 28

Shakura, N.I. & Sunyaev, R.A. 1973, A&A, 24, 337

Sharov, A.S. & Efremov, Y.U. 1963, International Bulletin on Variable Stars, No. 23, Com. 27, IAU

Shimizu, T.T., Mushotzky, R.F., Meléndez, M., Koss, M. & Rosario, D.J. 2015, MNRAS, 452, 1841

Shimizu, T.T. et al. 2017, MNRAS, 466, 3161

Silverman, J.D. et al. 2008, ApJ, 675, 1025

Simm, T. et al. 2015, A&A, 584, A106

Simm, T. et al. 2016, A&A, 585, A129

Skrutskie, M.F. et al. 2006, AJ, 131, 1163

Slawson, R.W. et al. 2011, AJ, 142, 160

Smith, H.J. & Hoffleit, D. 1963, Nature, 198, 650

Smith, M.G. & Wright, A.E. 1980, MNRAS, 191, 871

Smith, K.L. et al. 2010, ApJ, 716, 866

Smith, K.L. et al. 2012, ApJ, 752, 63

Smith, K.L., Koss, M. & Mushotzky, R.F. 2014, ApJ, 794, 112

Smith, K.L. et al. 2015, AJ, 150, 126

Smith, K.L., Mushotzky, R.F., Vogel, S., Shimizu, T.T. & Miller, N. 2016, ApJ, 832, 163

Sopp, H.M. & Alexander, P. 1991, MNRAS, 251, 112

Sramek, R.A. & Weedman, D.W. 1980, ApJ, 238, 435

Stern, D., Assef, R. J., Benford, D. J., et al. 2012, ApJ, 753, 30

Still, M. & Barclay, T. 2012, Astrophysics Source Code Library, ascl:1208.004

Stone, J.M., Hawley, J.F., Gammie, C.F. & Balbus, S.A. 1996, ApJ, 463, 656

Strittmatter, P.A., Hill, P., Pauliny-Toth, I.I.K., Steppe, H. & Witzel, A. 1980, A&A, 88, 12

Strohmayer, T.E. & Mushotzky, R.F. 2009, ApJ, 703, 1386

Tadhunter, C., Marconi, A., Axon, D., Wills, K., Robinson, T.G. & Jackson, N. 2003, MNRAS, 342, 861

Terlevich, R.J., Tenorio-Tagle, G., Franco, J. & Boyle, B.J. 1992, The Nature of Compact Objects in Active Galactic Nuclei. Proc. 33rd Herstmonceux Conf, ed. A. Robinson and R. Terlevich. Cambridge University Press, 209

Timmer, J. & König, M. 1995, A&A, 300, 707

Ulrich, M.-H., Maraschi, L. & Urry, C.M. 1997, ARA&A, 35, 445

Ulvestad, J.S., Antonucci, R.R.J. & Barvainis, R. 2005, ApJ, 621, 123

Uttley, P. & McHardy, I.M. 2001, MNRAS, 323, L26

Uttley, P., McHardy, I.M. & Papadakis, I.E. 2002, MNRAS, 332, 231

Uttley, P. & McHardy, I.M. 2005, MNRAS, 363, 586

Uytterhoeven, K. et al. 2011, A&A, 534, 125

Van Cleve, J.E. & Caldwell, D.A. 2016, *Kepler Instrument Handbook*, KSCI-19033-002

Van der Klis, M. *Statistical Challenges in Modern Astronomy* (1997)

van der Kruit, P.C. 1971, A&A, 15, 110

Vasudevan, R.V. & Fabian, A.C. 2007, MNRAS, 381, 1235

Vasudevan, R.J. et al. 2013, ApJ, 763, 111

Vaughan, S. & Fabian, A.C. 2003, MNRAS, 341, 496

Vaughan, S., Edelson, R., Warwick, R.S. & Uttley, P. 2003, MNRAS, 345, 1271

Vaughan, S. et al. 2016, MNRAS, 461, 3145

Veilleux, S., Bland-Hawthorn, J., Cecil, G., Tully, R.B. & Miller, S.T. 1999, ApJ, 520, 111

Veilleux, S., Shopbell, P.L. & Miller, S.T. 2001, AJ, 121, 198

Veilleux, S. 2002, in "AGN Surveys", Eds. R. F. Green, E. Ye. Khachikian, & D. B. Sanders. San Francisco: ASP Conference Series, 284, p111

Veilleux, S., Cecil, G. & Bland-Hawthorn, J. 2005, ARA&A, 43, 769

Viero, M.P. et al. 2014, ApJS, 210, 22

Voges, W. et al. 1999, A&A, 349, 389

Wang, J.-G. et al. 2009, ApJ, 707, 1334

Webster, B.L. & Murdin, P. 1972, Nature, 235, 37

Wehrle, A. et al. 2013, ApJ, 773, 89

White, R.L., Becker, R.H., Gregg, M.D. et al. 2000, ApJS, 126, 133

Wilhite, B.C. et al. 2008, MNRAS, 383, 1232

Wilson, A.S. 1988, A&A, 206, 41

Wold, M., Brotherton, M.S. & Shang, Z. 2007, MNRAS, 375, 989

Woltjer, L. 1959, ApJ, 130, 38

Wong, I.O., Koss, M.J., Schawinski, K., Kapinska, A.D., Lamperti, I., Oh, K., Ricci, C. & Trakhtenbrot, B. 2016, MNRAS, 460, 1588

Wright, E.L. et al. 2010, AJ, 140, 1868

Yun, M.S., Reddy, N.A. & Condon, J.J. 2001, ApJ, 554, 803

Zakamska, N. et al. 2016, MNRAS, 455, 4191

Zhou, X.-L., Zhang, S.-N., Wang, D.-X. & Zhu, L. 2010, ApJ, 710, 16

Zibetti, S., Charlot, S. & Rix, H.-W. 2009, MNRAS, 400, 1181

Zu, Y., Kochanek, C.S., Kozłowski, S. & Udalski, A. 2013 , ApJ, 765, 106

Zubovas, K. & Nayakshin, S. 2012, MNRAS, 424, 666

Zuo, W., Wu, X.-B., Liu, Y.-Q. & Jiao, C.-L. 2012, ApJ, 758, 104

Zwicky, F. 1965, ApJ, 142, 1293